Tectono-stratigraphic evolution of deep-marine clastic systems in the Eocene Ainsa and Jaca basins, Spanish Pyrenees: petrographic and geochemical constraints

Kanchan DAS GUPTA

Department of Earth Sciences
University College London

Thesis submitted in fulfilment of the requirements for the degree of
Doctor of Philosophy

University of London
October 2008

ProQuest LLC
789 East Eisenhower Parkway
P.O. Box 1346
Ann Arbor, MI 48106-1346

Abstract

The Early-Middle Eocene deep-marine siliciclastic systems of the Ainsa and Jaca foreland basins, Spanish Pyrenees, have been used to develop and support generic models for deep-marine deposits, from process-based to system-based perspectives, and these ideas have been applied globally by academics and industry alike. Despite the considerable amount of research into many aspects of sedimentology of the Ainsa and Jaca basins, the widely-adopted stratigraphic correlation of sandstone systems in the Ainsa and Jaca basins is very poorly-constrained, although the stratigraphy and accurate correlation of sandstone bodies along the basin are paramount to any depositional models that arise from any studies in the Ainsa and Jaca basins. This study used petrography, geochronology, major and trace element geochemistry to better constrain and understand the evolution of the basinal sediments and fingerprint the sandstone bodies within the Ainsa - Jaca basin as a means of correlation. An additional pilot study was carried out on carbon and oxygen isotopic signatures of larger foraminifera from the outcrops.

Three discrete sediment sources are recognised for the deep-marine Early to Mid-Eocene sandstone bodies in the Ainsa and Jaca basins. The arenite composition in the Ainsa and Jaca basins is interpreted to be mainly controlled by synsedimentary tectonic processes that led to changes in sediment sources during basin evolution. Comprehensive petrography data shows that each system of the Ainsa and Jaca basins has a characteristic petrofacies. Three main petrofacies are recognised and on the basis of these petrofacies, a revised correlation of the sandy systems is proposed between the more proximal Ainsa basin, and the more distal Jaca basin sediments, now separated by the Boltaña anticline, across which it is impossible to actually trace out individual beds or sandstone packages between both basins. The new correlation scheme, along with the newly identified sediment provenances, changes the current (published) understanding of the Ainsa and Jaca basins evolution and palaeogeography.

Acknowledgement

Several people have helped me to achieve the goal of completing this PhD, and making this thesis possible. First of all, I would like to express sincere gratitude to my supervisors Prof Kevin T Pickering and Prof Tony Hurford for their encouragement and comments during all stages of my work. I am also indebted to their help regarding matters of academic and non-academic concerns. Special thanks must be given to Dr Andy Carter for his continuous guidance and assistance with the geochronology work. Furthermore, this thesis benefited immensely from the constructive criticism of Prof Rob Hall and Dr Sarah Davies.

I greatly appreciate the help received from several people during data generation for this research. Thanks to UCL deep-water research group members, Tom, Nicole and Clare, for helping me out with the fieldwork. Thanks to the staff and lab in-charge of the following laboratories for assisting me with different laboratory techniques: Wolfson Laboratory for Environmental Geochemistry, UCL for carbon analyses; Bloomsbury Environmental Isotope Facility, UCL and Stable Isotope Laboratories, Royal Holloway University of London (RHUL) for stable isotope analyses; Wolfson Archaeological Science Laboratories, UCL for CL imaging; X-Ray Fluorescence Laboratory, RHUL for XRF analyses. A very special note of thanks is due to Dr Joachim Thomas for helping me with the sample collection in Jaca area.

This PhD project was jointly funded by the Natural Environmental Research Council (NERC) and Scottish Power under the "Dorothy Hodgkin Postgraduate Award" scheme. Additional financial assistance from Prof Tony Hurford, the UCL Graduate School and the International Association of Sedimentologists (IAS) towards laboratory costs and conference expenses are gratefully acknowledged.

Finally, cheers to all my friends in India, Germany and London, who have stood by me through the good and bad times during my PhD, and who have made my stay in UCL (especially Heather, Simon, Tom DJ and Seb) a memorable experience. Last, but not the least, I acknowledge my family for their constant encouragement, enthusiasm and moral support.

Table of Contents

List of Figures

List of Tables

List of Abbreviations

Q: **Q**uartz

F: **F**eldspars

L: **L**ithics (fine-grained)

NCE: **N**on-**C**arbonate **E**xtrabasinal

NCI: **N**on-**C**arbonate **I**ntrabasinal

CE: **C**arbonate **E**xtrabasinal

CI: **C**arbonate **I**ntrabasinal

FT: **F**ission **T**rack

UCC: **U**pper **C**ontinental **C**rust

CHAPTER 1

Introduction

Some 70% of the rocks at the Earth's surface are sedimentary in origin, formed from sediments deposited in the whole range of natural environments that exists today. Deep-marine clastic sedimentary systems constitute a significant proportion of Earth surface environments, and contain extremely large volumes (~ 6 billions km^3) of sediment that have accumulated by a wide range of processes (Fig. 1.1), e.g., turbidity currents, debris flows, sediment slides, pelagic and hemipelagic deposition, and deep-water focussing of tidal currents (Normark & Piper 1991). The down-slope processes that operate to deliver sediment into deep water are varied and complex. Single resedimentation events typically have multiple stages and evolve from one fluid state to another. Such systems are important because they preserve a record of events in the sediment source area, e.g., orogenic events, timing of unroofing of different units and the rate of denudation. The large volume of sediments in the deep-marine environments represent the ultimate 'sink' for sediments prior to metamorphic and tectonic processes that recycle these deposits. Deep-marine deposits are ideal for studying the relationship between tectonism and sedimentation, climate and sedimentation, and for modelling sediment transport processes especially for sediment gravity flows.

Deep-marine clastic systems are also economically important, because large volumes of oil and natural gas (and their estimated reserves) are locked up in deep-marine sandstone bodies e.g., in Gulf of Mexico, Brazilian margin, Nigerian margin, North Sea basin, West-of-Shetland, North Slope off Alaska, Far East deep-water slopes/basins (Fleet and Boldy, 1999). Deep-water turbidite and related reservoirs will be at the forefront of oil and gas exploration and production for at least the next 25 years.

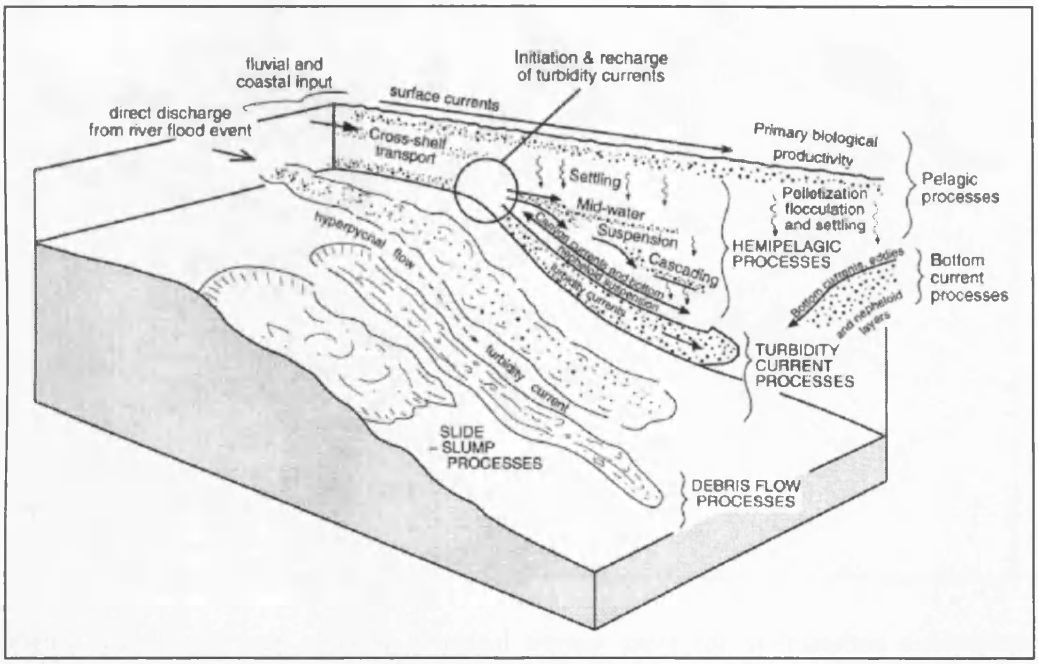

Figure 1.1: Diagram illustrating the range of processes and their interaction that influence the transport and deposition of sediments in deep water environments (Stow and Mayall, 2000).

With increasing technologies that permit successful hydrocarbon recovery in deep water, their importance relative to other sedimentary environments is increasing. This is because most, if not all, of the giant oilfields in non-marine and shallow-marine settings have been discovered, whereas giant oilfields in deep water (which tend to also be ancient deep-marine environments) are still being explored. An estimated 1200 to 1300 oil and gas fields, including discoveries and producing fields, are known from deep-water turbidite and related systems (Stow and Mayall, 2000; Fig. 1.2). In 2003, 57 new deepwater discoveries were announced worldwide which have a total of 11,400 MMBOE (Million Barrels of Oil Equivalent) of reserves. Thus, there are good intellectual and economic reasons for improving our understanding of the nature of deep-water clastic systems.

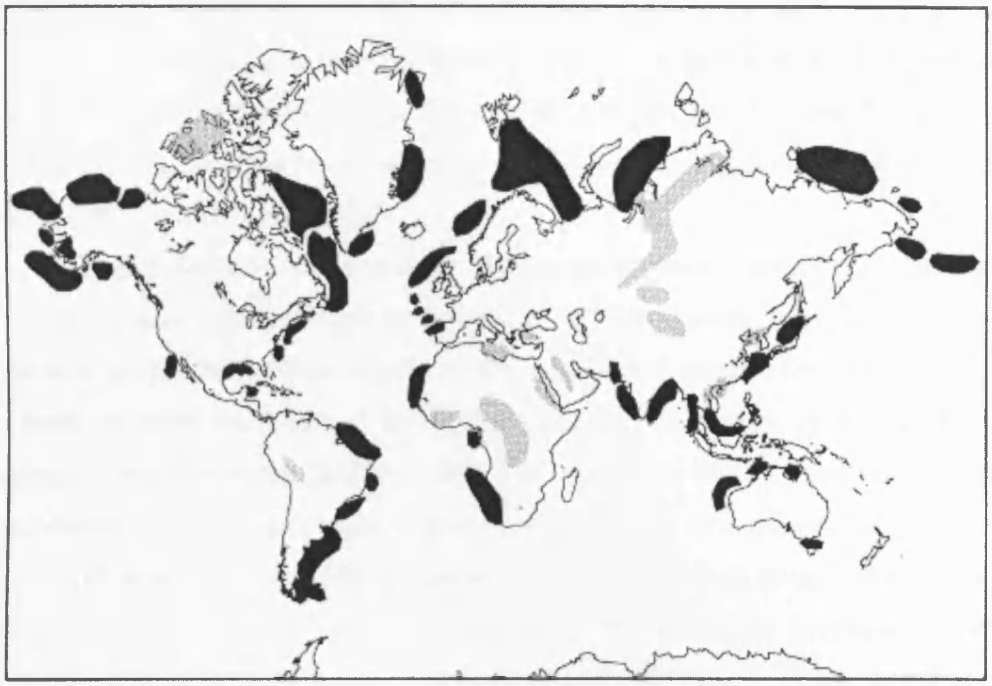

Figure 1.2: World map showing principal frontier areas for hydrocarbon exploration, including the main deep-water provinces (in black), after Stow and Mayall (2000).

1.1 Objectives

The principal aim of this PhD research project is to utilise petrography and geochemistry to provide constraints on the evolution of deep-marine clastic systems within the Ainsa and Jaca basins, south central Pyrenees.

The deep-marine systems of the Ainsa and Jaca basins are internationally recognized as one of the most important natural laboratories for studying deep-marine clastic systems (e.g., Mutti, 1977, 1985; Bentham et al., 1992; Millington and Clark, 1995; Dreyer et al., 1999; Pickering and Corregidor, 2000, 2005; Remacha and Fernandez, 2003; Fernandez et al., 2004; Remacha et al., 2005). They have been used, since 1970's, to develop and support generic models for deep-marine deposits, from process-based to system-based perspectives, and these ideas have been applied globally by academics and industry alike. In particular, the Ainsa and Jaca basins turbidite systems have been used to develop sequence stratigraphic models, with inferences about glacio-eustatic and tectonic controls on stratigraphy, e.g., type I, II and III systems of Mutti (1985). These models have found wide international

application because of their perception as analogues for many deep-marine basins worldwide. Additionally, in terms of practical aspects, the field area has excellent 3D outcrops and, with a few exceptions, has easy accessibility too. All these factors have made the Ainsa and Jaca basins the prime choice for carrying out research on deep-marine clastic systems in Europe.

Despite the considerable amount of research into many aspects of the tectono-stratigraphy and sedimentology of the Ainsa and Jaca basins, there are very few published studies that utilised laboratory data in combination with field observations, in terms of basin analysis and its application to the correlation of the sandstone systems along the entire length of the Ainsa and Jaca basins. However, whilst considerable numbers of detailed studies *have* been made on some systems from the Ainsa and Jaca basins (e.g. Millington and Clark, 1995; Dreyer et al., 1999; Oms et al., 2003; Pickering and Corregidor, 2000, 2005; Remacha and Fernandez, 2003; Remacha et al., 2005), there remains a total lack of published work that includes all the clastic system in a single study.

A pilot study (Robertson Research International report commissioned for UCL Ainsa Project, 1999) on the petrology of an individual system (the Ainsa system) from the Ainsa and Jaca basins have laid the foundation for this project. The pilot study required further and more detailed research on a basin-wide scale covering all the systems – the main focus of this PhD. Before the initiation of this study, the only widely-available literature on petrology from this basin, published in international, peer-reviewed journals, is that of Fontana et al. (1989), who analysed 40 samples across the entire Ainsa and Jaca basins. Another historical problem in the Ainsa and Jaca basins is the over dependence on non-peer reviewed field guide books regarding stratigraphic correlations of sandstone bodies / systems. In an attempt to test and refine the widely adopted, but poorly-constrained, stratigraphic correlations of sandstone bodies between the Ainsa and Jaca basins demonstrated by previous researcher (Mutti et al., 1985; Fontana et al., 1989; Remacha et al., 2003), a detailed petrographic study of sandstone samples from the Ainsa and Jaca basins was planned and carried out.

Similarly, geochemical data (e.g., major/trace elements, stable isotopes) are also very scarce from this area. Perhaps surprisingly there is no geochronology data from the clastic systems of the Ainsa and Jaca basins either. However, it is well

established that geochronology can provide valuable information on various aspects of basin analysis, provenance studies and deciphering hinterland evolution (Hurford et al., 1984; Hurford, 1986; Hurford and Carter, 1991; Carter 1999), e.g., tracing sediment source area and sediment routing systems, establishing temporal relationship between source evolution and sedimentation, reconstructing and constraining palaeogeographic models, reconstructing topographic relief, and interpreting rocks where the petrology indicates derivation from lithologically diverse sources (Kelley and Bluck, 1989; Gehrels et al., 1995; Morton et al., 1996; Stock and Montgomery, 1996; von Eynatten et al., 1996; Gray and Zeitler, 1997; Morris et al., 1998; Carter and Bristow, 2003; Zattin et al., 2003; Li et al., 2004; Bernet et al., 2006; Juez-Larré and Andriessen, 2006). Thus to understand and constrain better the evolution of basinal sediments from the internationally reputed deep-marine clastic systems of Ainsa and Jaca basins, this study has incorporated and combined field evidence with laboratory data.

The objectives of this research can be summarised as follows:

(A) Detailed documentation of petrographic features from each sandy system in the Ainsa and Jaca basins to identify compositional (petrographic) trend and petrofacies;

(B) To undertake combined U-Pb and fission track analysis to obtain thermo-chronometric constraints on basin analysis and provenance;

(C) Whole rock major and trace element analysis in order to obtain constraints on provenance;

(D) A pilot study on stable isotopes to establish an "isotope excursion curve" for comparison with the published global open-ocean curves to unravel any global, for example, eustatic sea-level changes from more regional changes;

(E) Integration of all the laboratory procedures with field evidence to comment on the basin palaeogeography, the basin evolution and correlation of the clastic systems.

1.2 Methods

Methods used in this study can be grouped into two major categories: field work and laboratory work, although the principal focus throughout the study was on laboratory techniques. Three field seasons, spanning about eight weeks in total, were undertaken in and around the Ainsa and Jaca area of Huesca province in Spain, to understand and study the overall geology of the basin, particularly its stratigraphy and sedimentology, although, the principal aim was sample collection for laboratory analysis. Various laboratory techniques have been used in this study:

(i) thin section petrography using transmitted light microscope (TLM),
(ii) fission-track (FT) chronometry on detrital zircon,
(iii) U-Pb dating on detrital zircon using laser-ablation inductively coupled plasma mass spectrometry (LA-ICPMS),
(iv) whole rock major and trace element analysis using x-ray fluorescence (XRF),
(v) stable isotope analysis by ICPMS and TOC /TC (total organic carbon and total carbon) analysis.

All these techniques are briefly discussed in Chapter 3 titled 'Materials and methods'.

1.3 Organisation of the thesis

This thesis is divided into eight chapters and each of these chapters is presented as a self-contained unit. The layout of this thesis is as follows. Chapter 1 is introductory and sets the scene. Chapter 2 provides a background to the research outlining the Eocene epoch, the Pyrenees, the Ainsa and Jaca basins, highlighting the previous work done in these fields by means of a comprehensive literature review. Chapter 3 outline the various methodologies used in this research. This chapter provides a list of the sample material, followed by notes on preparation, observation and data-generation techniques. The following two chapters describe the results obtained in this research. Chapter 4 describes petrography data and Chapter 5 deals with geochronology and geochemistry of the study area. Chapter 6 describes a pilot study

on stable isotopes from the Ainsa basin. Chapter 7 discusses the integration of the results from petrography, geochronology and geochemistry. The final chapter, Chapter 8, is a summation of the overall conclusions in light of the aims and objectives of this study. Some ideas for future work are also presented at the end of this chapter.

CHAPTER 2

Geology of the Study Area

2.1 The Eocene – an overview

This PhD research focuses on the Early to Middle Eocene (i.e., Ypresian and Lutetian stages) deep-marine deposits of the Ainsa and Jaca basins and the study area is located in the south-central Spanish Pyrenees (Fig. 2.1). The Eocene Epoch, which was very significant in the Earth's history, spans about 22 Ma (Fig. 2.2) from 55.8 to 33.9 Ma (Gradstein et al. 2004) and the name comes from the Greek *eos* (dawn) and *ceno* (new) referring to the "dawn" of 'new' or modern mammalian fauna that appeared during the epoch. The Eocene is divided into four stages:

Priabonian (37.2 ± 0.1 – 33.9 ± 0.1 Ma)

Bartonian (40.4 ± 0.2 – 37.2 ± 0.1 Ma)

Lutetian (48.6 ± 0.2 – 40.4 ± 0.2 Ma)

Ypresian (55.8 ± 0.2 – 48.6 ± 0.2 Ma)

The Eocene was crucial in the Earth's evolution history as during this time a rearrangement of tectonic plates resulted in new global palaeogeographical configurations (Fig. 2.3) and ocean circulation patterns, and eventually led to a switch from greenhouse to icehouse global climate. In Europe, the Tethys Sea finally vanished, while the uplift of the Alps isolated the final Tethyan remnant, the Mediterranean, and created another shallow sea with island archipelagos to the north. Though the North Atlantic was opening, a land connection appears to have remained between North America and Europe for sometime since the faunas of the two regions are very similar (Gingerich, 2006). It was also during this Epoch the culmination of the Pyrenean orogeny took place, which gave rise to one of the longest mountain ranges in Western Europe - the Pyrenees.

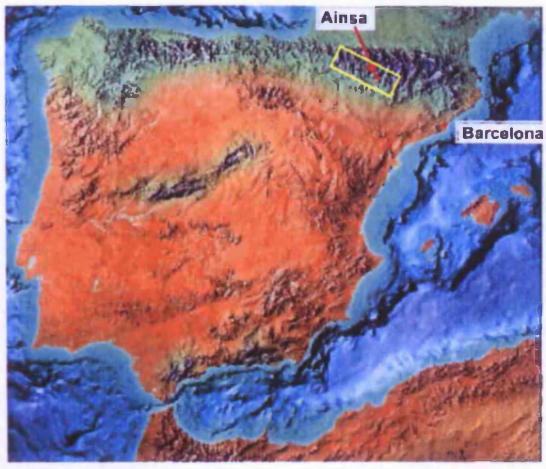

Figure 2.1: Relief map of the Iberian Peninsula, showing approximate location (yellow rectangle) of the study area.

The switch from greenhouse to icehouse condition, in turn, caused regional and global environmental perturbations, including changes in the salinity, turbidity, productivity, temperature and level of seawater (e.g., Bohaty and Zachos, 2003; Coxall et al., 2005; Zachos et al., 2005). At the start of the Eocene, the planet heated up in one of the most rapid and extreme global warming events recorded in the geologic history, currently being identified as the 'Paleocene-Eocene Thermal Maximum' or the 'Initial Eocene Thermal Maximum' (PETM or IETM).

The marine ^{18}O isotope record firmly suggests that the Early Eocene had warm oceans (Fig. 2.2). It was also warm on land as consistently suggested by plant fossil species (or relative of species) that currently found at tropical latitudes were then found at higher latitudes, even after allowing plate motions. Britain at that time was covered in tropical forest. The Thermal Maximum provoked a biotic turnover event that distinguishes Eocene fauna from the ecosystems of the Paleocene, e.g., extinction of up to 50% of benthic foraminifera, the crocodile-like reptile *Champsosaurus* and proprimate mammal *Plesiadapis*; radiation and diversification of coccolithophores (calcareous nannofossil) and sudden appearance of several modern orders of land mammals [Artiodactyla (e.g. deer), Perissodactyla (e.g. horses) and Primates] without any known precursors (Gingerich, 2006 and references therein).

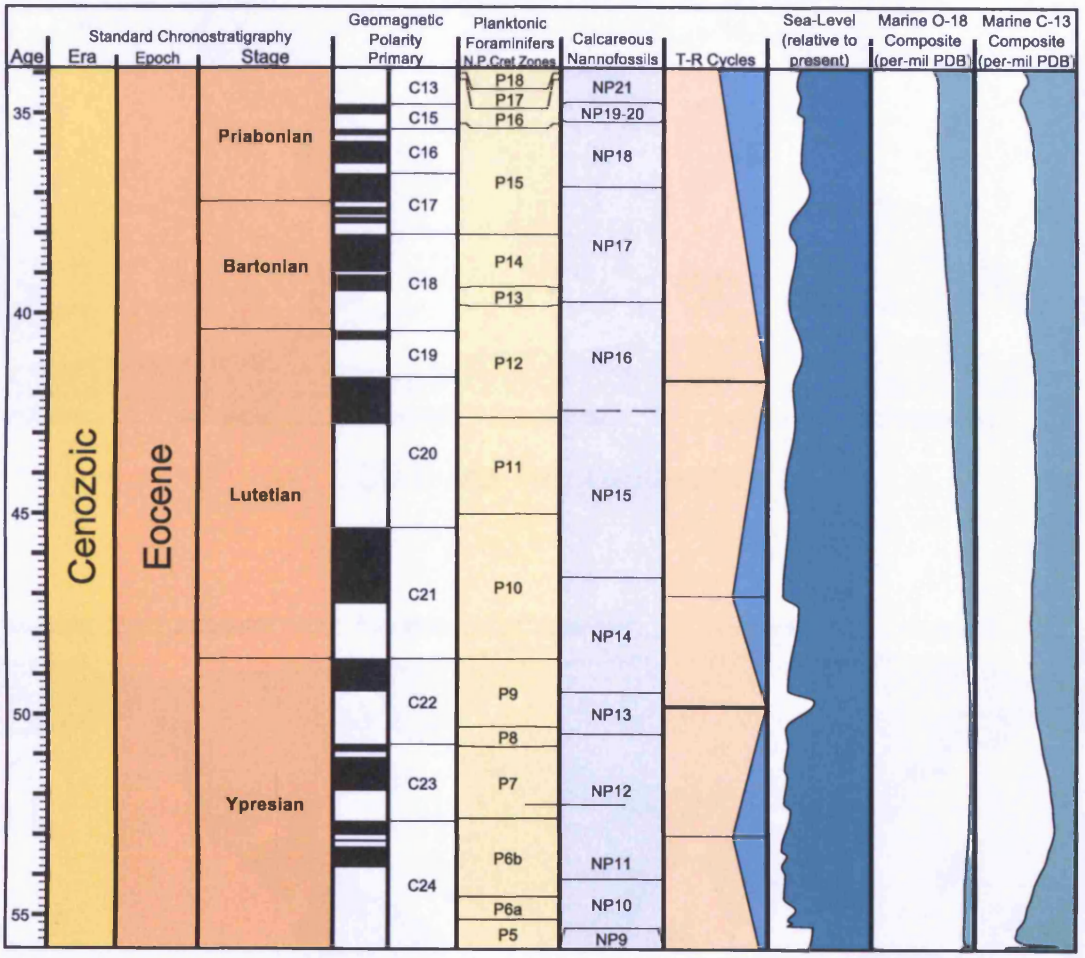

Figure 2.2: An overview of the main bio-, magneto-, chemo-, and other events in the Eocene epoch. The chart was generated by *Time Scale Creator* of International Commission on Stratigraphy and CHRONOS (chronostratigraphy and geomagnetic polarity after Gradstein et al., 2004; Biozones after Berggren et al., 1995; Transgressive-Regressive cycles and sea-level after Hardenbol et al., 1998; marine ^{18}O and ^{13}C after Zachos et al., 2001).

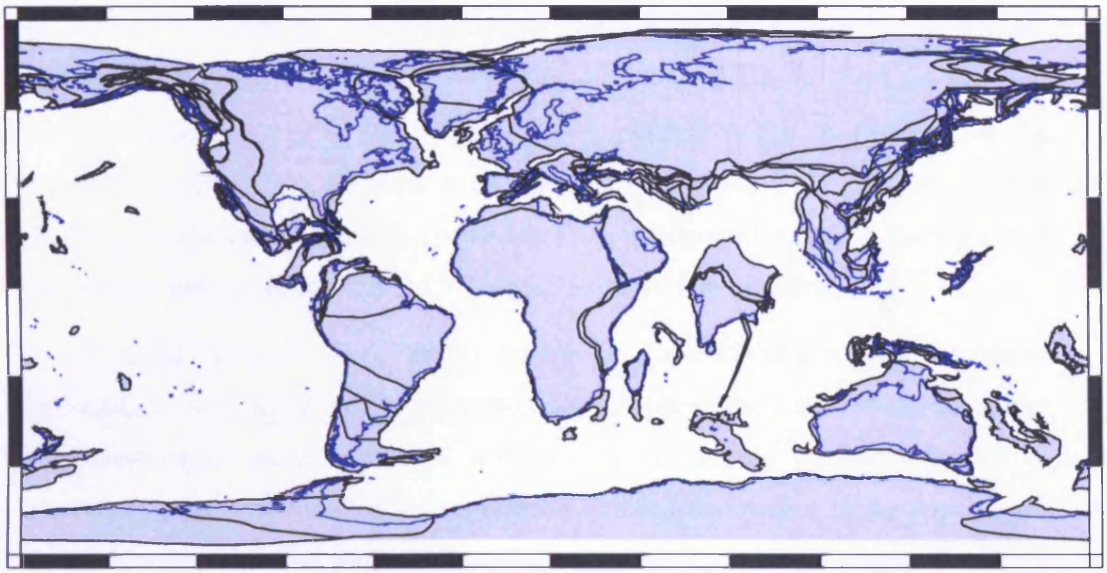

55.8 Ma Reconstruction

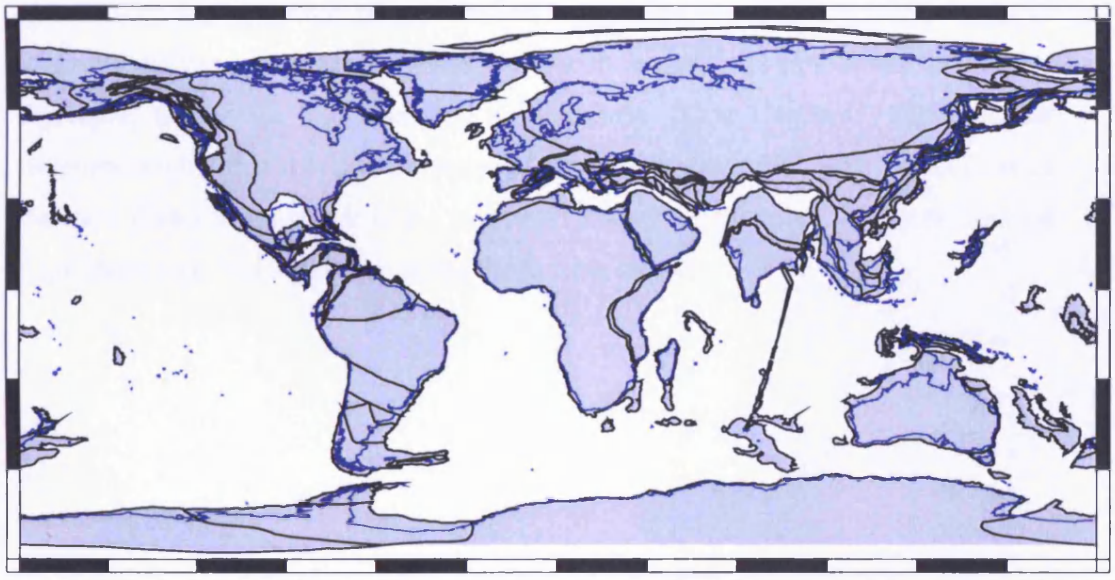

33.9 Ma Reconstruction

Figure 2.3: World palaeogeography during initiation (55.8 Ma) and culmination (33.9 Ma) of the Eocene Epoch. Blue and black lines represent present day shorelines and outline of plate fragments, respectively. Map generated by *ODSN Plate Tectonic Reconstruction Service* after Dercourt et al. (1993), Berggren et al. (1995) and Hay et al. (1999).

Palaeoenvironmental and palaeoceanographic studies on the Eocene Epoch have mainly focused on either the warm climates around the Paleocene–Eocene transition (e.g. Wing et al., 2003; Zachos et al., 2005) or else on the Late Eocene–Early Oligocene interval, when large-scale ice sheets began to develop on the Antarctic continent (e.g. Prothero et al., 2003; Coxall et al., 2005; Dupont-Nivet et al., 2007). In comparison, the Early–Middle Eocene intervening period, during which the climatic deterioration occurred, has received much less attention.

In the Tethyan – Peri-Tethyan realms the Early Eocene may be considered intermediate, in terms of geodynamic evolution, between the Late Cretaceous major reorganisation of plate boundaries and the Middle to Late Eocene inception of continent – continent collision induced by the further convergence of the African and Eurasian plates (Meulenkamp and Sissingh, 2000). This resulted in the uplift of large parts of the northern and southern Peri-Tethys platforms. For at least part of the Cenozoic, the Iberian block with its core of Palaeozoic and Hercynian terranes (Iberian massif) acted as an independent lithospheric microplate. Relative motions of the African and Eurasian plates resulted in the formation of the several Alpine domains and mountain ranges around the Iberian massif, e.g., Cantabrian mountains, Pyrenees, Iberian and Beltic ranges, in the course of the Cenozoic. Early Eocene compressional force resulted in nappe piling and in a roughly W-E orientation of foreland basins at either side of the evolving chain of the Pyrenees. It also reactivated Late Hercynian faults that intersected the Iberian massif.

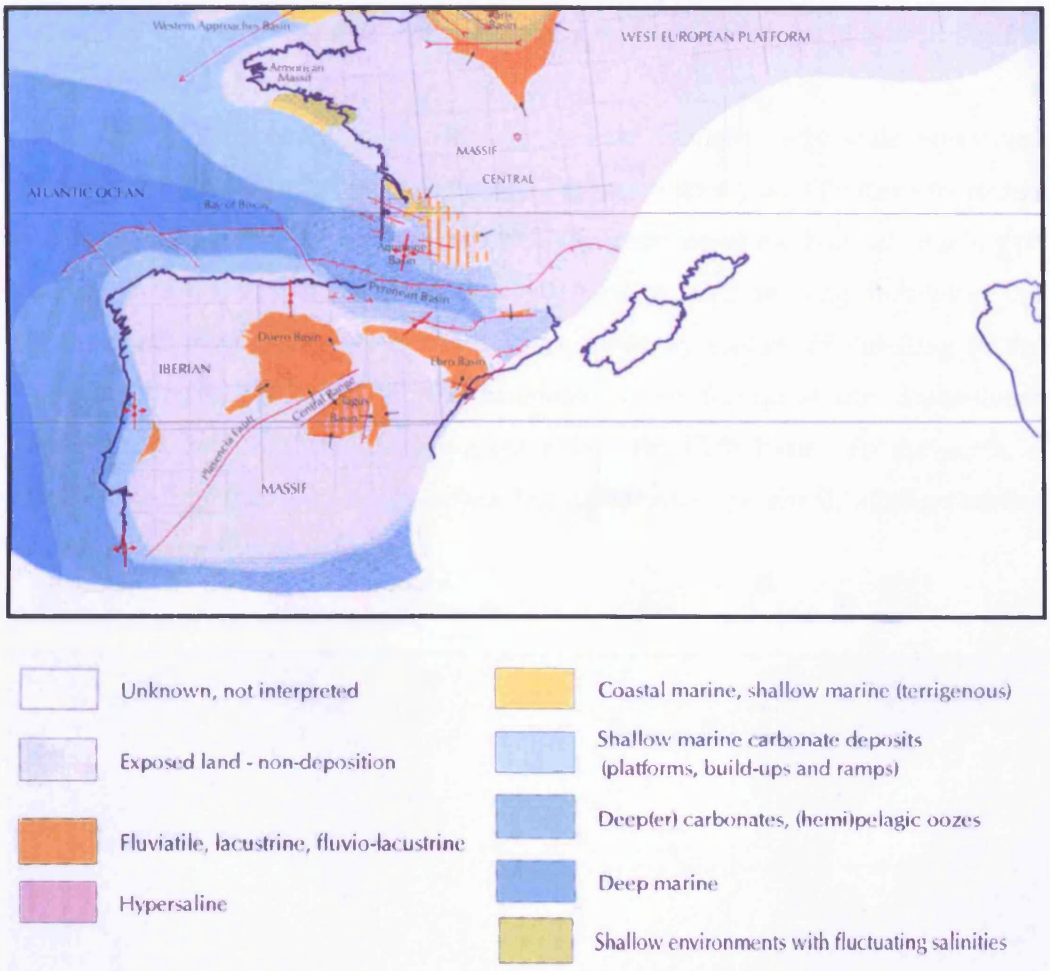

Figure 2.4: Simplified palaeogeographic map (scale 1: 10,000,000) of south-western Europe during the Early to Middle Ypresian (55-51 Ma), after Meulenkamp et al. (2000a).

In the Iberian Peninsula marine sedimentation during the Early Eocene was confined to a W-E oriented southward migrating trough in the Pyrenees region, in which predominantly calcareous turbidites and marls accumulated (Fig. 2.4). This foreland basin was bordered by large carbonate platforms with distal ramps and talus protruding into the basin. Some deltaic complexes developed along the basin margin and the bordering emerged areas provided siliciclastic deposits which formed alluvial fans. The large interior continental basins in the Iberian Peninsula, i.e. Duero, Tagus and Ebro basins, received mainly alluvial sediments, fringing the margins of the basins. The peripheral areas in the west and in the east were the sites of deposition of mainly siliciclastic, non-marine succession. During the Early to Middle Ypresian

period, the marine corridor across the Aquitaine basin connected the Atlantic and Tethyan/Indo-Pacific domains.

During the course of the Middle to Late Eocene, large-scale northward directed latitudinal shifts of the African and Eurasian plates gradually came to an end (Dercourt et al., 1993), in concomitance with the inception of mechanical coupling of the African and Eurasian plates. In the south-west, the still ongoing motions of the African plate relative to Europe were accompanied by southward thrusting of the Pyrenean orogenic belt and by the accumulation of foreland-basin depositional sequences derived from the evolving chain into the Ebro basin. To the north, a narrow foredeep (i.e., Graus-Ainsa-Jaca basin segments) persisted, after an earlier episode of major Pyrenean activity.

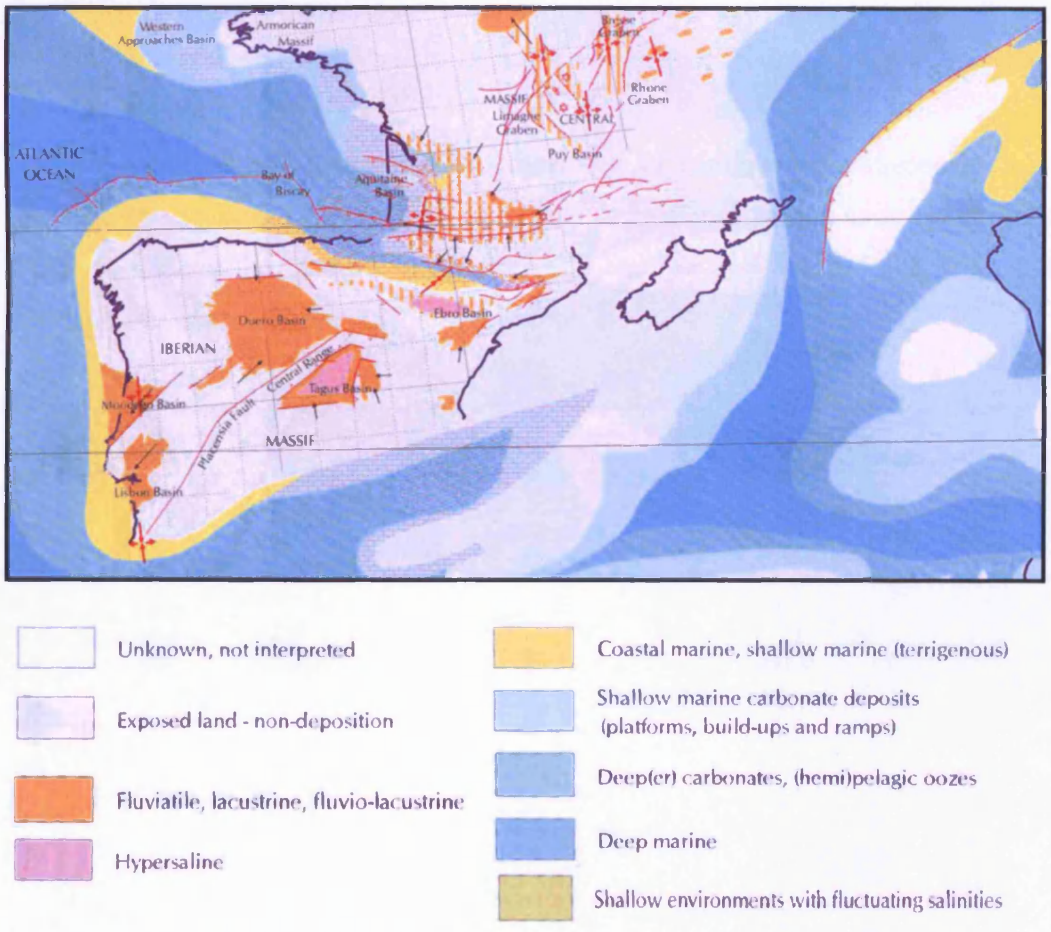

Figure 2.5: Simplified palaeogeographic map (scale 1: 10,000,000) of south-western Europe during the Late Lutetian (44-41 Ma), after Meulenkamp et al. (2000b).

The marine corridor connecting the Atlantic and the Tethys was closed by Late Lutetian time and the distribution of carbonate platforms at either side of the Pyrenean basin became more restricted (Fig. 2.5). However, the marine realm continued to be open towards the Bay of Biscay. The shortening of the foreland basin domains was coupled with a reduction of the extension of carbonate platforms area, but the overall hierarchical organisation of the basins was basically the same as in the Ypresian. Siliciclastic deltaic depositional systems developed and fluvial and alluvial sequences accumulated along the up-thrusted relief. Along the margins of the large interior basins (Duero and Tagus basins) there was predominantly accumulation of alluvial sequences. The separation between the Tagus and Duero basins by the Central Range became more pronounced in response to crustal thickening (Vegas et al., 1990). Displacements along major fault systems (Plasencia fault, Nazare – Lousa fault) in the central and western parts of the Iberian massif are thought to account for the basin evolution in these areas.

By Late Rupelian (Early Oligocene), due to continued emergence of the Pyrenean mountain belt, marine environments had almost ceased to exist on the Iberian block and the Spanish foreland became entirely non-marine with onset of alluvial clastic deposition in the Ebro basin (Fig. 2.6).

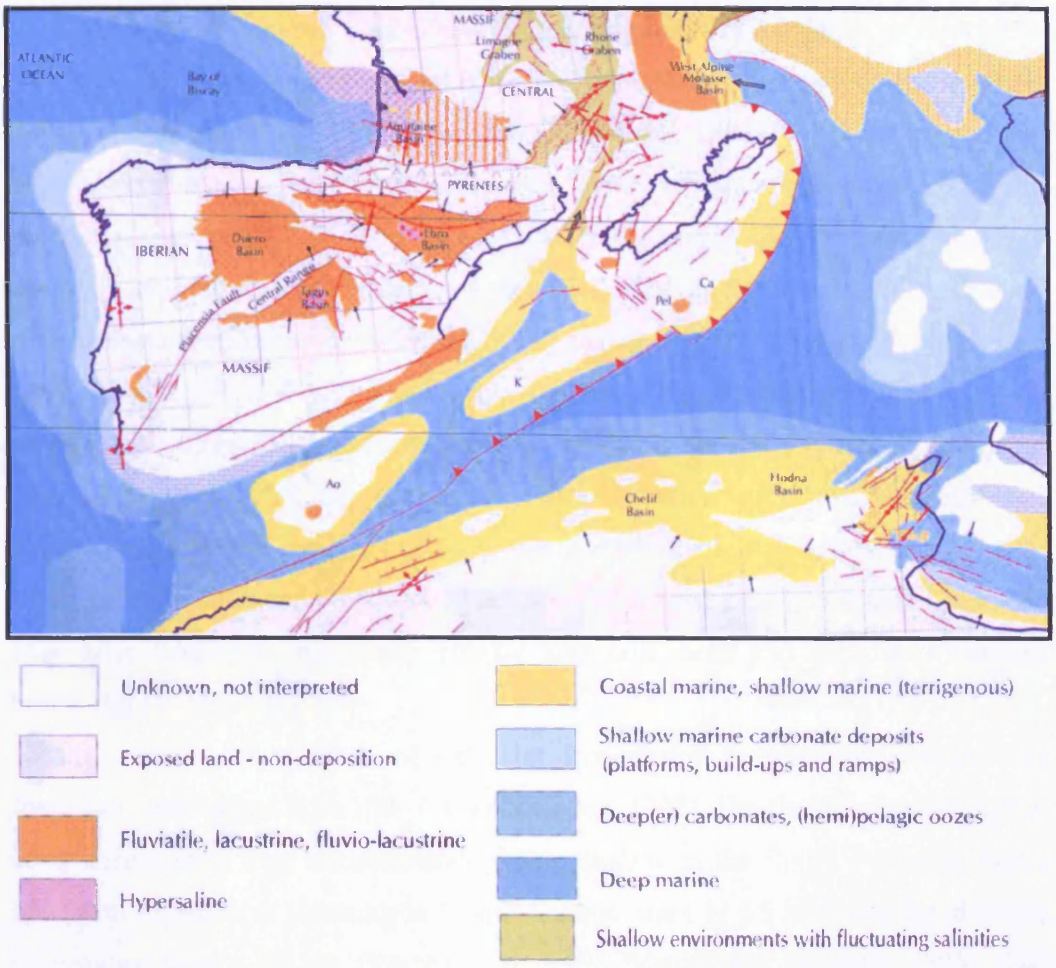

Figure 2.6: Simplified palaeogeographic map (scale 1: 10,000,000) of south-western Europe during the Late Rupelian (32-29 Ma), after Meulenkamp et al. (2000c).

2.2 The Pyrenees

The Pyrenees are 430 km long mountain chain that separates the Iberian Peninsula from France. They extend from the Atlantic Ocean (Bay of Biscay) in northwest Spain (the Cantabrian Mountains) to the Catalunian coast of the Mediterranean at the eastern end. The chain is the westernmost part of the Cenozoic Alpine-Himalayan orogeny, but was profoundly influenced by earlier events, especially the Late Carboniferous Hercynian orogeny (e.g. Zwart 1979).

The chain is the result of the collision of the Iberian microplate with the Eurasian plate at the end of the Mesozoic (Fig. 2.7A). An initial sinistral displacement of Iberia resulted in a series of Triassic to Cretaceous extensional to

transtensional rift systems. This rifting caused the continental crust to be thinned to ~5 km (in thickness) but no evidence for the formation or consumption of oceanic crust has been found (Teixell, 1998; Daignieres et al., 1994). Thick successions of deep-marine deposits, platform sediments, and evaporites accumulated in the associated rift basins. The onset of northward convergence during Late Cretaceous times inverted the east-west trending structures during under-thrusting of the Iberian plate beneath the European plate (ECORS-Pyrenees Team, 1988; Choukroune et al, 1989; Muñoz, 1992). Contemporaneous with these tectono-stratigraphic processes, upper mantle upwelling began under the thinned crust, resulting in the upper mantle material being intruded into the crust as lherzolites and granulites (Vielzeuf and Kornprobst, 1984). Continued convergence and shortening in Oligocene to early Miocene times (Puigdefabregas and Souquet, 1986) established an internal, uplifted axial zone flanked by oppositely vergent fold-thrust belts and associated foreland basins (Fig. 2.7A).

Estimates of amounts of extension-transtension between the Iberian and European plates range from 100- 150 km (Muñoz, 1992). The timing of thrusting has been documented from magnetostratigraphic studies in the South Pyrenean thrust belt, with initiation of thrusting in Lower Eocene times (~ 55 Ma), and rapid thrust propagation until ~ 47 Ma (Vergés et al., 1995, Vergés and Burbank, 1996). The termination of thrusting has been documented using magnetostratigraphic dating of syn- and post-depositional sediments as upper Oligocene (~25 Ma; Meigs et al., 1996; Hogan and Burbank, 1996).

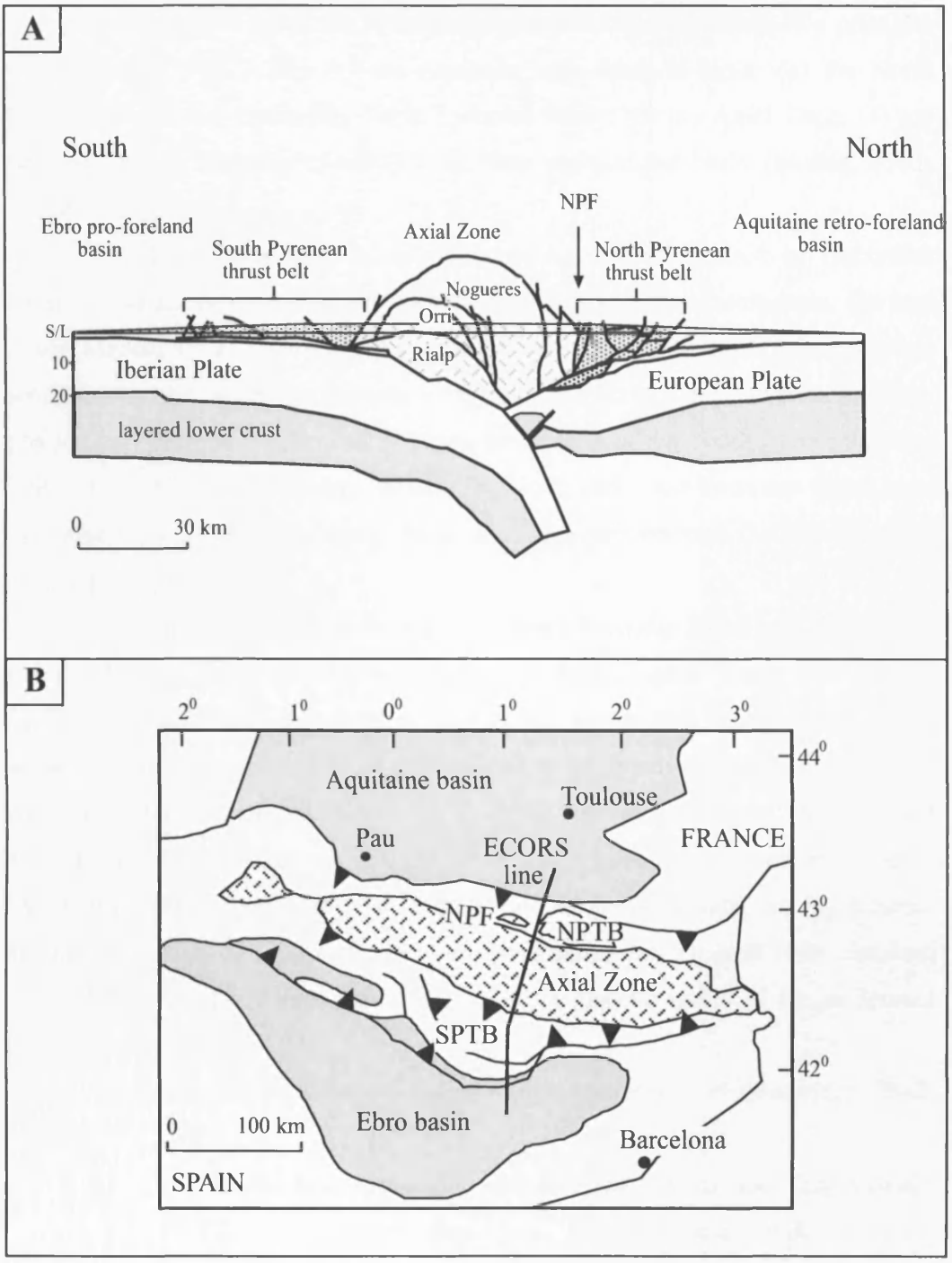

Figure 2.7: (A) Structural cross section along the ECORS Pyrenees line (Muñoz, 1992) highlights the main thrust geometry and, notably, the antiformal stack geometry of the Axial Zone. (B) Simplified structural map of the Pyrenees showing the main tectonic zones from north to south: the Aquitaine retro-foreland basin; the North Pyrenean thrust belt (NPTB); the North Pyrenean Fault (NPF); the Axial Zone; the South Pyrenean thrust belt (SPTB); the Ebro pro (peripheral)-foreland basin. The ECORS Pyrenees line is shown for reference.

From north to south the Pyrenean orogen can be divided into five principal tectonic zones (Fig. 2.7B): (1) the Aquitaine retro-foreland basin; (2) the North Pyrenean thrust belt (including North Pyrenean Fault); (3) the Axial Zone; (4) the South Pyrenean thrust belt; and (5) the Ebro pro-foreland basin (Muñoz, 1992; Vergés et al., 1995).

The Axial Zone (Fig. 2.7A) comprises an antiformal stack of Hercynian basement thrust sheets, which are named, from top to bottom, Nogueres, Ori and Rialp (Muñoz, 1992). The Aquitaine retro-foreland basin is the result of thrust sheet loading from the North Pyrenean thrust belt and the Axial Zone, whereas the Ebro pro-foreland basin is the flexural response to the load of the South Pyrenean thrust belt and the Axial Zone (Brunet, 1986). The North and South Pyrenean thrust belts comprise thrusted Mesozoic and/or basement rocks derived from the European and Iberian plates, respectively.

There are three principal thrusts in the South Pyrenean thrust belt: the Boixols thrust, Montsec thrust and Sierras Marginales thrust, linked along their eastern margin into the Segre oblique ramp fault zone (Vergés and Muñoz 1990). Their western margins, however, are less well defined as the thrusts degenerate into a series of oblique thrusts and anticlines: the Boltaña anticline, Mediano anticline and Cotiella thrust. This western oblique ramp has attracted considerable attention, particularly concerned with the effects of its development on syntectonic sedimentation (e.g. Anadon et al., 1986, Puigdefabregas and Souguet 1986, Bentham et al., 1992). As the thrust system developed, a discrete series of basins formed concomitantly.

The sequence of basin development can be summarized in three stages (Hall, 1997):

(i) Eocene axial prograding depositional system: the Tremp-Graus, Ainsa and inner Jaca (sub) basins. These three thrust-top (piggyback) basins developed in series from east (where the most significant tectonic uplift and shortening occurred) to west.

(ii) Late Eocene and early Oligocene thrust-top basin: the Outer Jaca (sub) basin.

(iii) Oligocene to Miocene alluvial fans: the initiation of the Ebro Basin, south of the Sierras Marginales thrust front. This system developed in response to Oligo-Miocene deformation, which reset

the foreland basin configuration and terminated the axial depositional system.

In the regional context of the study area principally three major rock units are involved: (i) remobilised Hercynian basement, (ii) Mesozoic pre-orogenic succession and (iii) syn-orogenic Late Cretaceous to Cenozoic sedimentary rocks of the contemporaneous basin inversion and foreland basin stages (Morris et al., 1998; Remacha et al. 2003). This unit includes the sediments of the Ainsa and Jaca basins (Fig. 2.8).

2.3 The Ainsa and Jaca basins

The Early-Middle Eocene South Pyrenean foreland basin evolved with mainly non-marine / marginal marine environments in the eastern sectors, whilst farther west there was an overall change from fluvio-deltaic to deep-marine systems in the Ainsa and Jaca basins. The accumulation of the deep-marine sediments in the Ainsa and Jaca basins was broadly contemporaneous with maximum rates of tectonic subsidence in the South Pyrenean foreland basin, and coincident with maximum rates of shortening and thrust front advance (Vergés et al., 1998). The Ainsa and Jaca basins are demarcated by the Mediano anticline to the east and by the Navarre diapirs to the west (Fig. 2.8). Another major structural feature, the Boltaña anticline, occurs within the Ainsa and Jaca basins that separates more confined deposits from less confined deposits (Fig. 2.8).

The Boltaña anticline broadly coincides with the change from more channelised (Ainsa basin) to less confined, more sheet-like deposits (Jaca basin). This Boltaña anticline was a growing seafloor high during accumulation of the deep-marine basin fill, although there was uninterrupted connectivity within the basin throughout most of the depositional history of the South Pyrenean foreland basin (Mutti, 1985; Dreyer et al., 1999; Pickering and Corregidor, 2005).

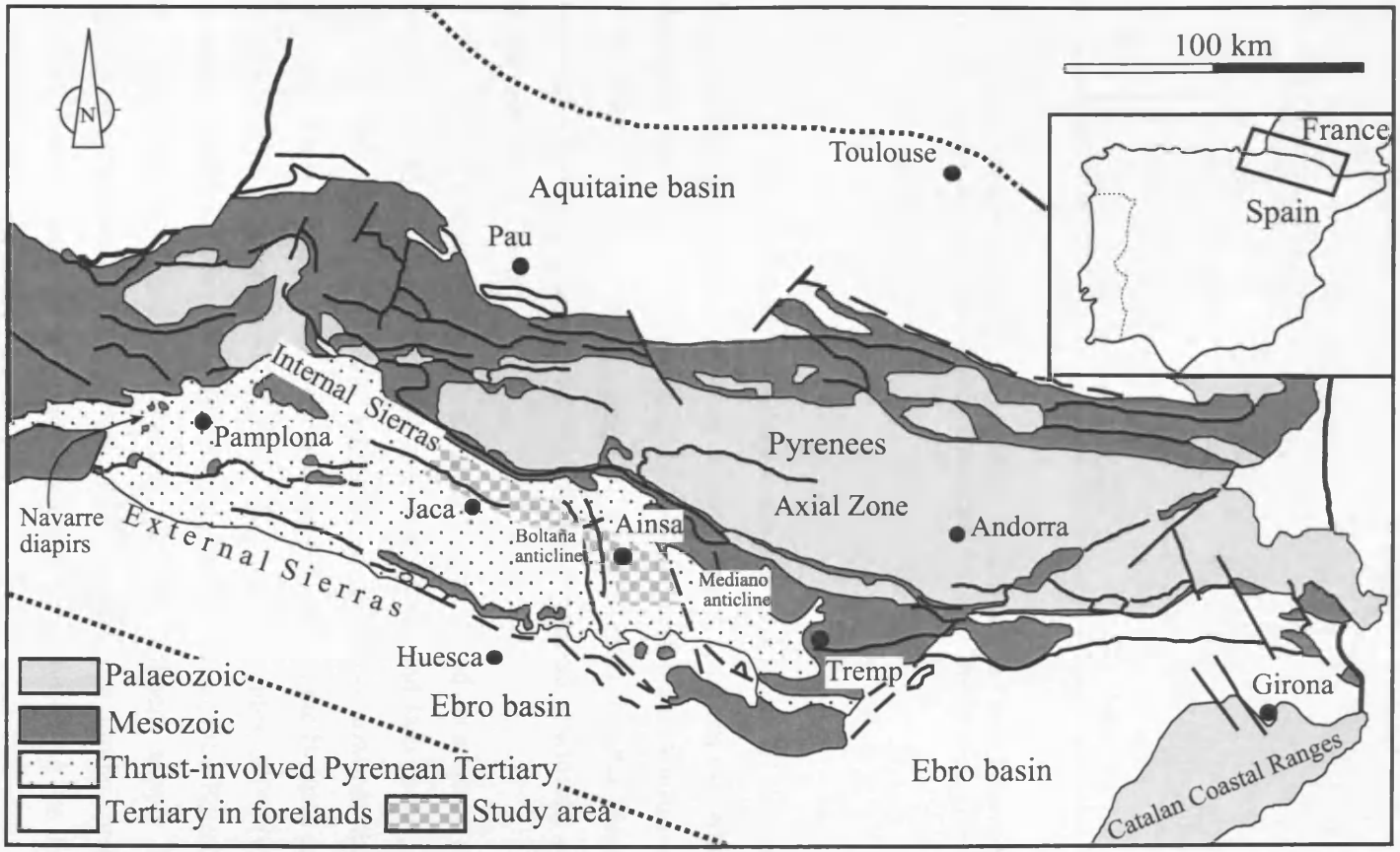

Figure 2.8: Simplified geological map of the Pyrenees and southern foreland basins, also showing location of the study area (the Ainsa and Jaca basins).

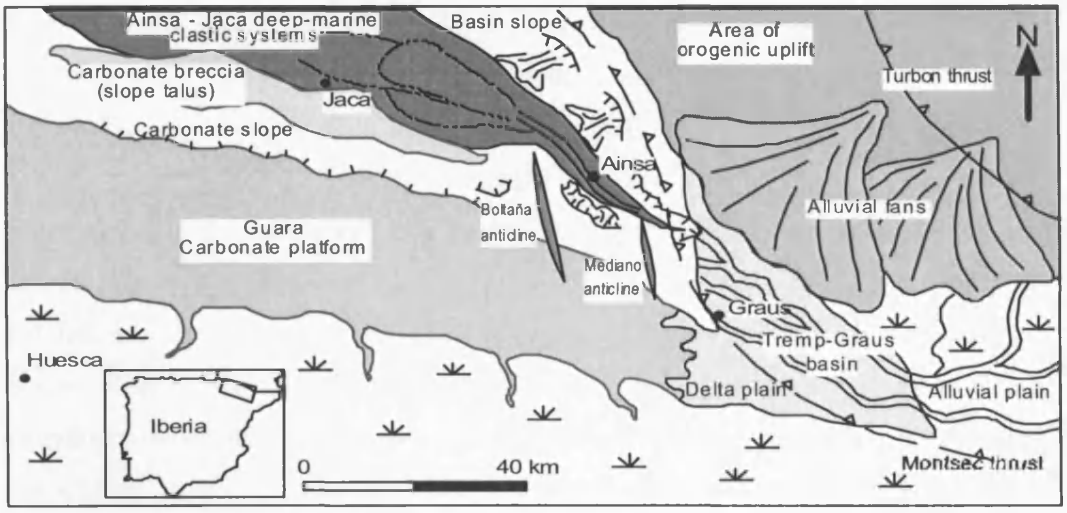

Figure 2.9: Palaeogeographic reconstructions of the Ainsa and Jaca basins and surrounding areas during the early Lutetian. Redrawn and modified after Dreyer et al. (1999).

The Mediano anticline defines the eastern boundary of the Ainsa and Jaca basins and has been interpreted as an asymmetrical detachment fold which was active during the deposition of the deep-marine sediments (Holl and Anastasio 1993; Poblet et al., 1998). Pickering and Corregidor (2005) inferred that the Mediano anticline remained a submarine topographic high that was coincident with the eastern margin of the deep-marine basin.

The deep-marine clastic systems of the Ainsa and Jaca basins appear to have been fed, throughout most of the history of the Ainsa and Jaca basins, from a south-eastern point source, with axial sediment gravity flows towards the NW in the proximal Ainsa basin (~320°), and more westerly across the Boltaña anticline in the relatively distal Jaca basin (~270°) (Pickering and Corregidor, 2005) (Fig.2.9). In the younger, upper Lutetian part of the deep-marine fill, west of the Boltaña anticline in the Jaca basin, an additional northerly-derived sediment supply is recognised (Remacha et al., 2003). Payros et al. (1997) identified a similar, probably coeval, northerly-sourced submarine channel-overbank-levee system in the Pamplona area which is further west of the Jaca basin.

The infill of the Ainsa and Jaca basins comprises cumulatively ~4 km of deep-marine deposits, spanning the Early to Middle Eocene, Ypresian (Cuisian) and

Lutetian stages (Fernandez et al., 2004; Labaume et al., 1985; Payros et al., 1999; Pickering and Corregidor, 2000, 2005; Remacha and Fernandez, 2003; Remacha et al., 2005), and records ~10 million years of deep-marine sedimentation (Pickering and Corregidor 2005). The entire syntectonic Eocene turbidite systems that accumulated in the Ainsa and Jaca basins have been collectively referred to as the "Hecho Group" by Mutti et al. (1972). However, this term has almost become redundant in current usage. The present geographic separation of the Ainsa and Jaca basins deposits by the Boltaña anticline make it impossible for any physical correlation between these two areas. It is, therefore, convenient to informally discuss the infilling of the Ainsa and Jaca basins in terms of the 'Ainsa basin' and the 'Jaca basin'.

2.3.1 Stratigraphy and palaeogeography of the Ainsa basin

The infill of the proximal deep-marine Ainsa basin consists of two unconformity-bound depositional units (Muñoz et al., 1994, 1998; Fernandez et al., 2004) in which the younger unit is both structurally less deformed and shows a south-westward shift in depositional axis (Pickering and Corregidor, 2005) (Fig. 2.10). These "tectono-stratigraphic units" contain seven coarse clastic depositional complexes or systems, each of which is in the order of 100-700 m thick.

The successive depositional systems are separated vertically by several hundred metres of mainly marl deposits with thin-bedded and very thin-bedded sandstone turbidites. Internally, each depositional system contains 2-7 individual sandstone bodies 30-100 m thick, separated by tens of metres of mainly thin-bedded and very thin-bedded sandstones with subordinate marls. Although some sandstone bodies show an aggradational stacking pattern, overall each depositional system (e.g., Banaston, Ainsa) shows a WSW, foreland-stepping pattern (Pickering and Corregidor, 2000, 2005). The bathymetry of the Ainsa basin obtained from foraminiferal assemblage suggests that water depths were at least several hundred metres, probably in the range 400-800 m (Pickering and Corregidor, 2000, 2005).

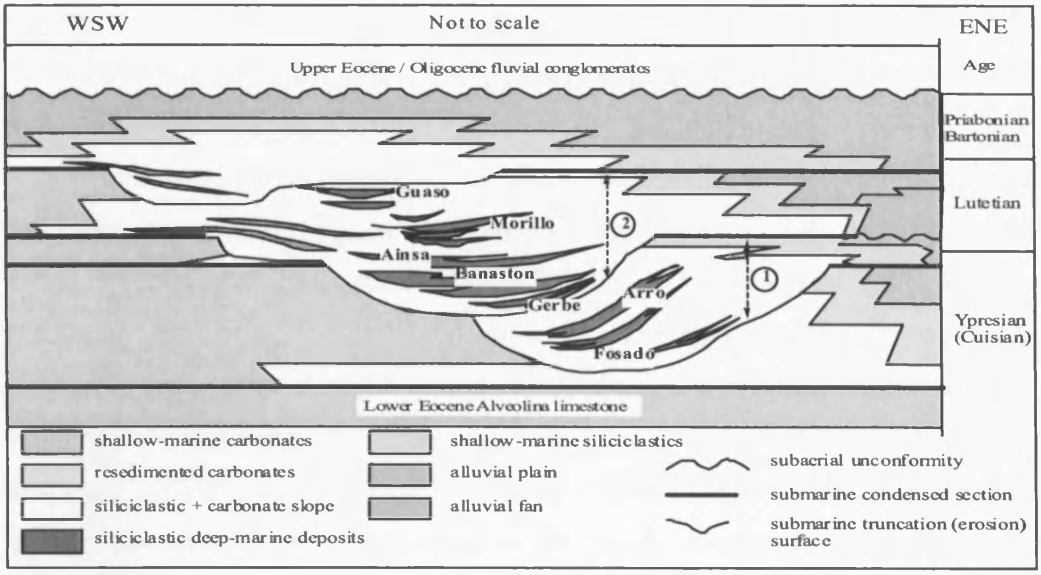

Figure 2.10: General stratigraphy of the Ainsa basin (not to scale), modified after Muñoz et al. (1998). Numbers 1-2 indicate the two unconformity-bounded units.

The seven coarse clastic depositional systems in the Ainsa basin (Fig. 2.10), were deposited in a variety of depositional settings, which from the oldest are: (1) Fosado (two sandstone bodies) = slope channels; (2) Arro / Los Molinos (six sandstone bodies) = erosional slope channels, canyon / base-of-slope channel system; (3) Gerbe (two sandstone bodies) = canyon / lower-slope erosional submarine channel system (Clark and Pickering, 1996); (4) Banaston (seven sandstone bodies) = base-of-slope and proximal basin-floor channel system, but previously interpreted as a canyon system (Clark and Pickering, 1996); (5) Ainsa (three sandstone bodies) = lower-slope erosional channels and proximal basin-floor channelised fan system (Pickering and Corregidor, 2000, 2005); (6) Morillo (three sandstone bodies) = canyon / base-of-slope erosional channel system (Clark and Pickering, 1996), and (7) Guaso (two sandstone bodies) = "structurally-confined clastic ramp" (Pickering and Corregidor, 2005; Sutcliffe and Pickering, *pers. comm.*, 2007).

Within the older part of the Ainsa basin, between the Fosado and Arro systems, there is a discrete sandbody that has not been formally recognised by previous workers as a separate system (and included here within the Arro system). It is ~100 m thick and is separated from the overlying Arro system by ~70 m of thin-bedded, fine-grained turbidites. For this study, and in agreement with Remacha et al.

(2003), the Los Molinos sandbody is grouped with the Arro system (above). The Ainsa basin contains other thin (typically only up to several metres thick), generally heterolithic, sandstone bodies that are not formally defined as sandy systems.

Age-dating of the Ainsa basin is based on micropalaeontological data (mainly foraminifera), and these suggest that the entire deep-marine stratigraphy of the Ainsa basin represents the upper parts of the Ypresian (= Cuisian) and entire Lutetian (Pickering and Corregidor, 2005 and references therein); with the overlying deltaic sediments being Bartonian (Dreyer et al., 1999). Thus, the deep-marine deposits represent ~10 myr (using the timescale of Gradstein et al., 2004). This age dating is consistent with that derived from planktonic foraminifera of the more distal deep-marine sediments in the Hecho Group in the Pamplona and the Jaca basins farther west, which give an age range of Mid- / Late Ypresian to Mid-Lutetian (Payros et al., 1999, their fig. 6). The ~250 m thick Ainsa clastic system was incorrectly cited as having a duration throughout the entire Lutetian and much of the Bartonian stages by Jones et al. (2005).

2.3.2 Stratigraphy and palaeogeography of the Jaca basin

The deep-marine Jaca basin was bordered by active thrust sheets on the hinterland (northern) side and carbonate platforms on the southern cratonic margin. The basin first accumulated turbidites, during the so-called underfilled 'flysch' stage, and then transitional-marine and terrestrial deposits, during the overfilled 'molasse' stage (Payros et al., 1999). The eastern end of the Jaca basin is defined by the Boltaña anticline (Fig. 2.8), and the westernmost preserved parts are exposed in the Pamplona area (Payros et al., 1999, 2006, 2007a). The northern margins of the Jaca basin are delimited by the internal Sierras, and the southern margins by the external Sierras (Fig. 2.8). A distinctive feature of the Hecho Group, in the Jaca basin, is the occurrence of nine very thick megaturbidites (up to 250 m thick) within the terrigenous turbidite succession (Labaume et al., 1983, 1985, 1987). Payros et al., (1999), however, recognises at least thirteen megaturbidites in the entire Jaca and Pamplona basins. These megaturbidites extend for considerable distances along the Jaca basin, and they have been used as marker beds in stratigraphic correlation (*ibid.*)

This study considered the stratigraphy of the Jaca basin separately from the Ainsa basin, now geographically divided by the Boltaña anticline, although previous researchers have considered the stratigraphy of the Ainsa and Jaca basins as a whole (e.g., Mutti et al., 1985, 1988; Labaume et al., 1987; Remacha et al., 1998, 2003; Remacha and Fernandez, 2003). In the Jaca basin, there are several vertically-stacked major sandy turbidite systems (Fig. 2.11), which, from the base up, are the: (1) Torla; (2) Broto; (3) Cotefablo; (4) Banastón (as defined by Remacha et al., 2003, but originally referred to as "Fiscal" by Mutti et al., 1985), and (5) Jaca systems.

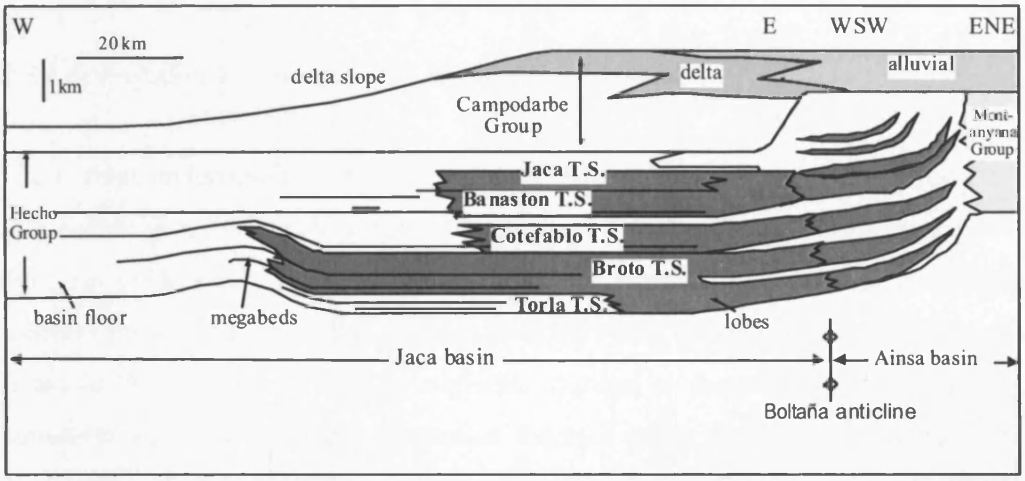

Figure 2.11: Stratigraphy of the Jaca basin (redrawn from Mutti et al., 1985; Labaume et al., 1987); TS: turbidite system.

The Torla and Broto systems represent the first major sand-rich depositional systems in the Hecho Group (Remacha et al., 2003). Remacha et al. (2003), however, show two older heterolithic turbidite systems as present in the Jaca basin, as the Figols and Castigaleu "turbidite systems" (shown as Ypresian / Cuisian in age). As these latter two turbidite systems are poorly exposed, and slightly older than the sandy systems in the Ainsa basin, they shall not be discussed further in this thesis. Furthermore, in agreement with Remacha et al. (1995), the Rapitan channel-levee-overbank deposits reported from the Jaca basin are considered as the youngest part of the Jaca system in this study.

The Jaca basin systems, which represent mainly outer-fan lobe, lobe-fringe, fan-fringe, and distal basin-floor deposits, were fed from single entry points located in the east/southeast except for the latest stages of turbidite sedimentation. In the youngest (upper) parts of the Hecho Group, a new northerly (partly channelised) sediment source is recognised as supplying, coarse clastic systems (Remacha et al., 1991, 1995, 2003). This new sediment provenance has been interpreted as occurring at a time when the Ainsa and Jaca basins temporarily became separated (detached) by the growth of the Boltaña anticline, with sediment supply in the thrust-top Ainsa basin still coming from a southerly source (Remacha et al., 2003).

2.3.3 Correlation framework in the Ainsa and Jaca basins

The current understanding of correlations of the turbidite systems in the Ainsa and Jaca basins have arisen principally from different reports made in non-peer reviewed field-trip guidebooks. Figure 2.12 schematically explains the different correlation schemes involving the turbidite systems from the Ainsa and Jaca basins which can be found in the literature. The older turbidite systems in the Ainsa basin have been correlated with four principal systems in the Jaca basin, namely the Fosado-Torla, Arro-Broto, Gerbe-Cotefablo, and Banaston-Fiscal systems (Mutti et al., 1985). Fontana et al. (1989) reported the same correlation framework as above. In each system, the first name denotes the main outcrop area of the channelised deposits in the Ainsa basin, and the second name the main outcrop area of the depositional lobes in the Jaca basin Remacha et al. (2003) used Banaston turbidite system instead of Fiscal in their figure 10, and it is currently accepted as the latest on Ainsa-Jaca correlations. In order to avoid confusion the same terminology as presented by Remacha et al. (2003) has been used in this study, instead of going back to the original term (i.e., Fiscal system). Mutti et al. (1985) correlated the Jaca system with the turbidite systems in the Ainsa basin and suggested that the Jaca system was equivalent to the Ainsa system. Later, Remacha et al. (1998) suggested that the older part of the Jaca system (Jaca 1 and 2 units) correlates with the Ainsa system (Ainsa 1 and 2 units, respectively), the middle part of the Jaca system (Jaca-3) with the Morillo system, and the upper part of the Jaca system (Jaca-4, Rapitan turbidites) with the Guaso system.

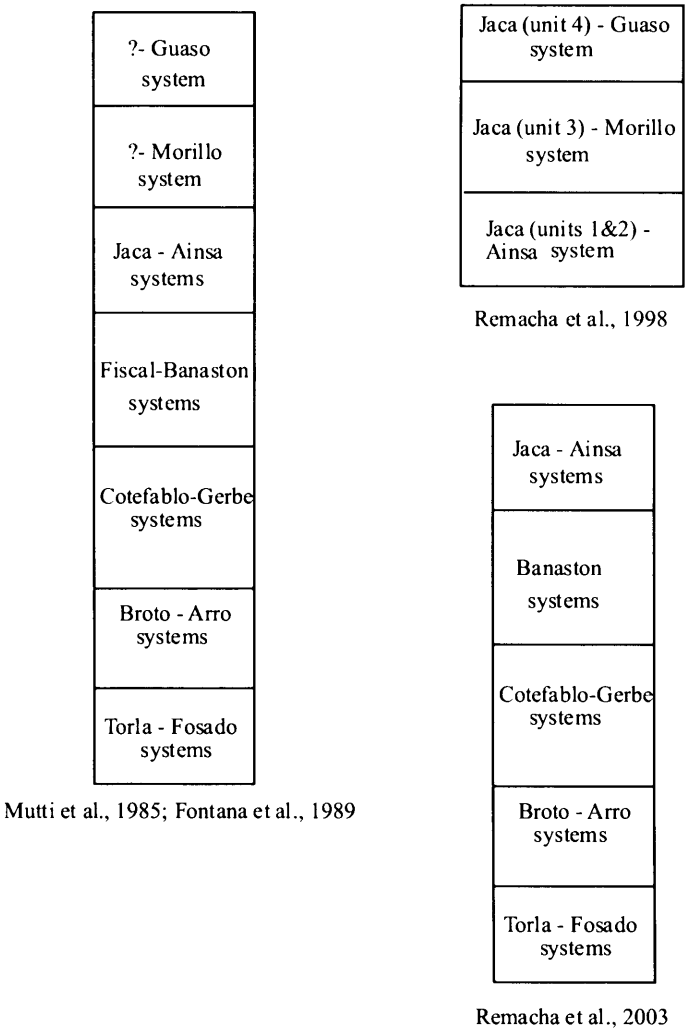

Figure 2.12: Schematic diagram showing different correlations proposed for the turbidite systems of the Ainsa and Jaca basins. The first name denotes the turbidite system from the Jaca basin and the second name denotes its counterpart in the Ainsa basin.

However, in the latest correlation (Remacha et al., 2003), rather surprisingly the entire Jaca system has been correlated with the Ainsa system and there is no formal acknowledgement of the Morillo and Guaso systems counterparts in the Jaca basin. Thus, the current understanding of turbidite system correlation in the entire Ainsa and Jaca basins is non-peer reviewed and inconsistent. In this thesis the latest correlation (Fig. 2.13) by Remacha et al. (2003) have been tested and modified on the basis of petrography (see Chapter 6).

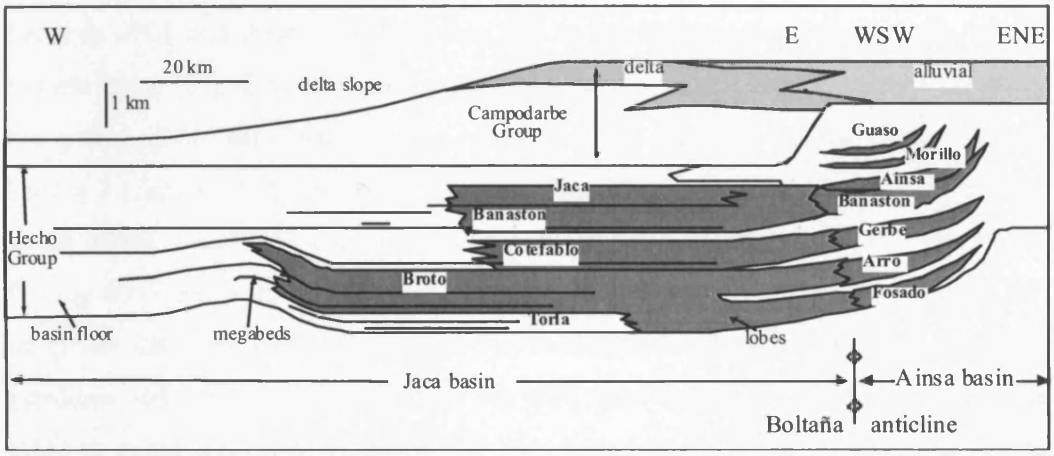

Figure 2.13: Correlation framework of the sandstone (turbidite) systems in the Ainsa and Jaca basins prior to this thesis (redrawn after Mutti et al., 1985; Labaume et al., 1987; Remacha et al., 2003). This correlation have been tested and modified in this thesis (see Chapter 7).

CHAPTER 3

Materials and Methods

3.1 Sample Acquisition

The material for this study includes mainly rock samples and foraminifera, covering the entire stratigraphic units of Ainsa and Jaca basins and ranging from Ypresian to Lutetian in age. These materials were collected during three separate field seasons between 2004 and 2006. The field area lies in the Huesca province, Aragón, north-eastern Spain (Fig. 2.8) with good outcrops occurring in and around many villages in the area, in fact each system in the Ainsa and Jaca basins is named after a village. Figure 3.1 shows a geographical location map of samples and Table 3.1 provides detail of the sampling location, with an aim for providing practical information for finding those locations in the case of re-visit. However, geo-references (latitude and longitude data) for each location are not available due to remoteness of sampling localities and weak signal strength of the GPS used during the fieldwork. Care was taken to avoid collecting weathered samples from outcrops. While collecting, a note on associated sedimentary features and structures was also made. In addition to the outcrop samples, a few core samples were also obtained from the Ainsa system. These cores were collected as part of the UCL - Ainsa Project, an integrated outcrop-subsurface study of deep marine clastic systems (see Pickering and Corregidor, 2005). A systematic sampling of both the larger foraminifera and associated sediment was also undertaken in a vertical profile throughout the Ainsa basin for a pilot study on stable isotopes. Rock samples were collected and sorted out in the field itself for different laboratory techniques, e.g. big blocks (~ 3-5 kg in weight) of coarse gained samples were collected for geochronology study and smaller sample (10 cm x 5 cm in dimension approximately) were kept separate for petrography and XRF analysis.

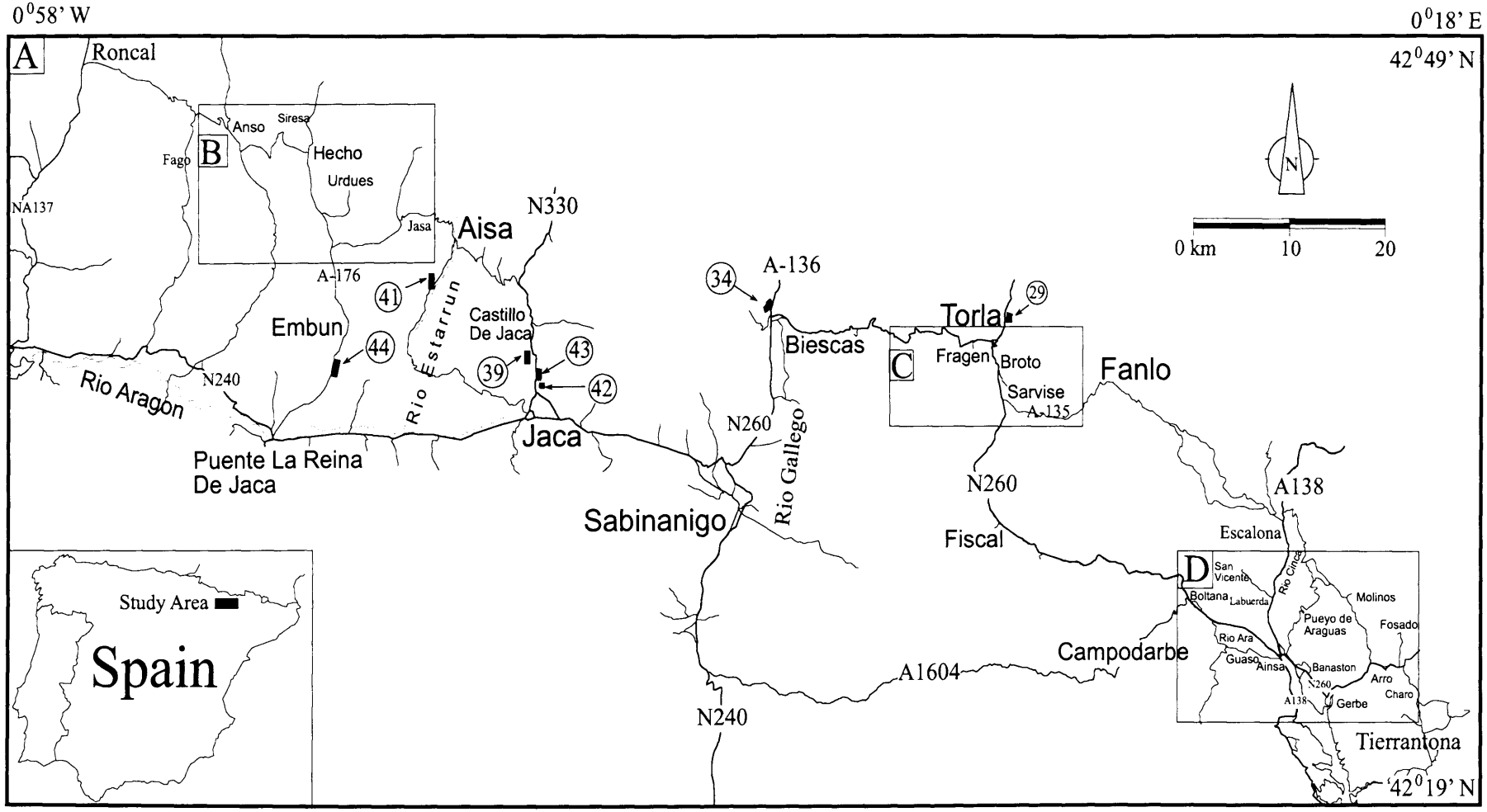

Figure 3.1: (A) Geographical map of the study area, with sampling locations marked by numbers. For location details see Table 3.1. (B) and (C) Sampling locations for the Jaca basin. Note that some sampling locations for the Jaca basin are also shown in A. (D) Sampling locations for the Ainsa basin. Also see figs. 3.2-3.15 for outcrop photographs.

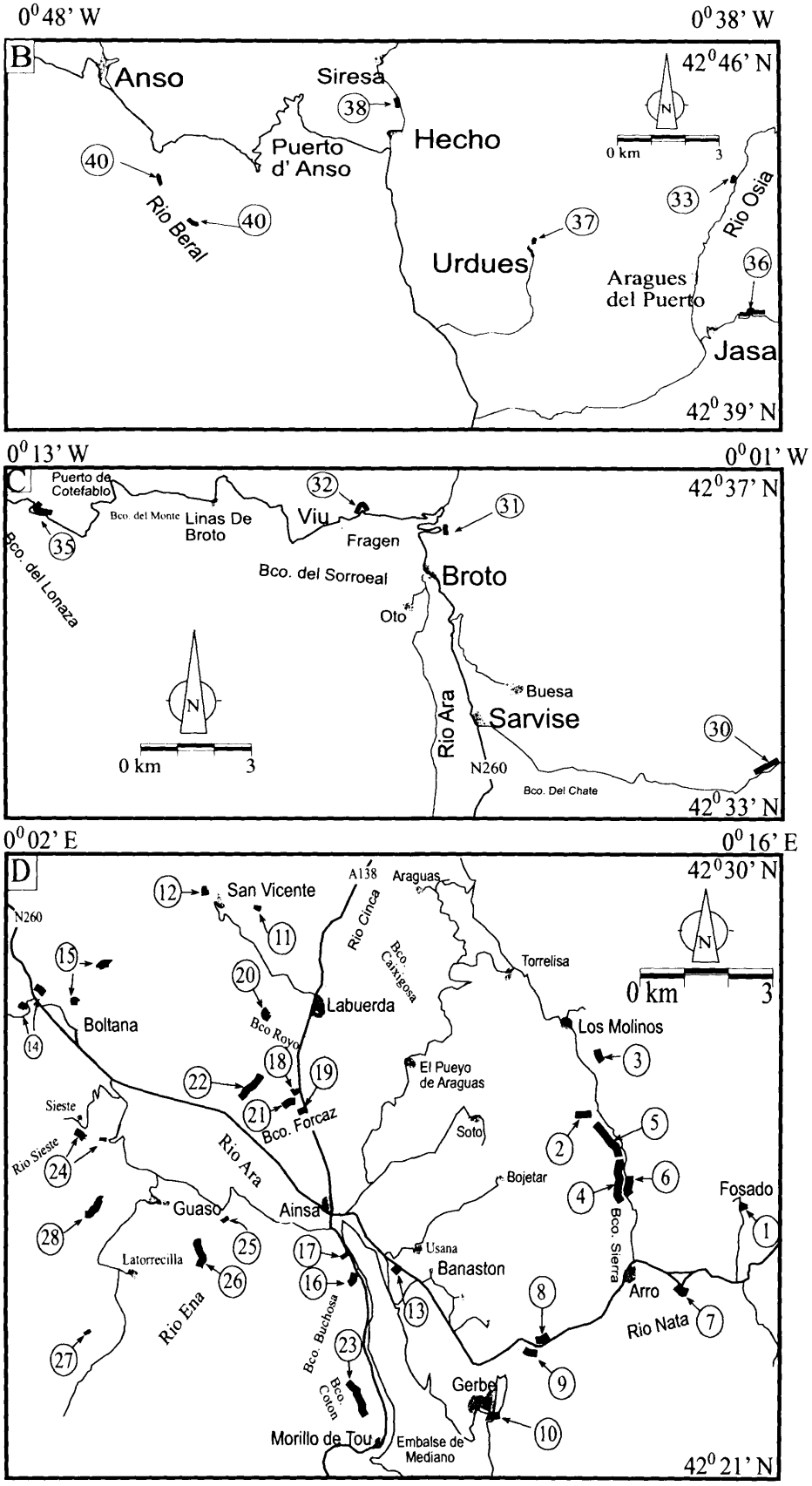

Figure 3.1: *Continued.*

Table 3.1: Details of sampling localities from the Ainsa and Jaca basins (also refer to Figs. 3.1-3.15).

Location	Locality description	System
1	~ 150m south of Fosado village (42°25'N; 0°15'E), on a small cliff face	Fosado
2	~ 300m below the peak of Tozal de Sans, south of Los Molinos village (42°29'N; 0°11'E)	Arro
3	Osposan O Fronton, ESE of Los Molinos village (42°29'N; 0°11'E)	Arro
4	~1.5Km north of Arro village (42°24'N; 0°13'E), along Bco. Sierra	Arro
5	~2Km north of Arro village (42°24'N; 0°13'E), along Bco. Sierra	Arro
6	~1.5Km north of Arro village (42°24'N; 0°13'E), along the road towards Los Molinos	Arro
7	~1Km east of Arro village, the section is on old road along Rio Nata beside the tunnel	Arro
8	~3Km west of Arro village along road N260, the section is a road-cut	Gerbe + Banaston
9	~1Km NE of Gerbe village (42°23'N;0°11'E) along Rio Nata and close to Location 8	Gerbe
10	~200m south of Gerbe village (42°23'N;0°11'E), near Embalse de Mediano	Gerbe
11	~500m east of San Vicente village along Bco. A Pasata	Banaston
12	~50m west of San Vicente village on a road cut	Banaston
13	~800m west of Banaston village (42°24'N; 0°10'E) along road N60	Banaston
14	~1Km west of Boltana village (42°26'N; 0°04'E) along road N260, sections are road-cut	Banaston
15	~1Km north of Boltana village along Bco. San Martin, sections are exposed over one kilometer stretch	Banaston + Ainsa
16	~1Km south of Ainsa village (42°24'N; 0°08'E) along Bco. Buchosa near Ainsa quarry	Ainsa
17	~600m south of Ainsa village (42°24'N; 0°08'E) along road A138	Ainsa
18	~2 Km north of Ainsa village on a track beside Bco. Forcaz, next to an electric tower	Ainsa
19	~1.7Km north of Ainsa village along road A138 and opposite of Pena Montenesa hotel	Ainsa
20	~1Km SW of Labuerda village (42°27'N; 0°08'E) along Bco. Royo	Ainsa
21	~100m westerly of location 19 along Bco. Forcaz	Ainsa
22	~500m NW of location 21 following Bco. Forcaz	Ainsa
23	~500m north of Morillo de Tou (42°22'N; 0°09'E) viallge, along Bco. Cotón	Morillo
24	~150m SSE of Sieste village (42°25'N; 0°03'E) along Rio Sieste	Morillo
25	~1Km east of Guaso village (42°25'N; 0°05'E) along Rio Ena and close to Casa Pelai	Morillo
26	~1.2Km SE of Guaso village (42°25'N; 0°05'E) along Rio Ena	Guaso
27	~2Km SW of La Torrecilla village (42°24'N; 0°05'E) along Rio Ena	Guaso
28	~1.2Km west of Guaso village (42°25'N; 0°05'E)	Guaso
29	At Torla village (42°37'N; 0°06'W)	Torla
30	~5Km east of Sarvise village (42°34'N; 0°06'W) along the road towards Fanlo	Broto
31	~1.5Km north of Broto village (42°36'N; 0°07'W) along Rio Ara	Broto
32	~150m east of Fragen village (42°36'N; 0°08'W), section exposed on a road cut	Broto
33	~3.5Km north of Aragues del Puerto village (42°24'N; 0°40'W), along the road	Broto
34	~1Km north of Biescas village (42°37'N; 0°19'W) along road A-136	Broto
35	~4Km west of Linas de Broto village (42°37'N; 0°10'W) immediate west of Cotefablo tunnel on road N260	Cotefablo
36	~1Km northeast of Jasa village (42°41'N; 0°40'W), section exposed on a road cut	Cotefablo
37	At Urdues village (42°42'N; 0°43'W)	Cotefablo
38	~1Km north of Hecho village (42°44N; 0°45'W) along the road towards Siresa	Cotefablo
39	~400m south of Castillo de Jaca village (42°47'N; 0°33'W) along road N330	Banaston
40	~4Km south of Anso village (42°45'N; 0°49'W), sections are exposed along road cuts parallel to Rio Beral	Banaston
41	~4Km south of Aisa village (42°40'N; 0°37'W), sections exposed along Rio Estarrun	Banaston
42	~1Km north of Jaca town (42°34'N; 0°33'W) along Bco. Salau	Jaca
43	~1Km north of Jaca town (42°34'N; 0°33'W) along road 330	Jaca
44	~1.5Km south of Embun village (42°37'N; 0°43'W) along road A176	Jaca

Although the entire proximal and distal parts of the Ainsa and Jaca basins were sampled for petrography study in this research, geochronology study was carried out mainly on the samples collected from the proximal Ainsa basin. This is because of analytical techniques based limitations for geochronology study which requires abundant zircon grains that are scarce in carbonate rich sediments as in the case for samples of the Jaca basin (Payros et al., 1999; Remacha et al., 2003). As the geochemical (major and trace element) analyses were carried out in order to complement the geochronology data, thereby, it was only undertaken on the samples from the Ainsa basin. The Ainsa basin also represents the 'transfer zone' from shelf to slope depositional environment through which sediments were transported to the Jaca basin throughout most of the Jaca basin infill history (Marzo et al., 1998; Dreyer et al., 1999). Furthermore, scope of the project and financial constraint also limited the flexibility of the research. However, the petrography analysis was performed on all the samples from the entire Ainsa and Jaca basins.

Table 3.2 documents the sandstone samples collected and analysed from the Ainsa and Jaca basins (for sampling location see Fig 3.1 and Table 3.1). Outcrop photographs from the sampling sites are shown in Figs.3.2-3.15. The following sections describe briefly the various laboratory techniques used on the collected samples.

Table 3.2: List of sandstone samples collected from each location along with their grain size in parenthesis (vfs, fs, ms, cs and vcs are very fine, fine, medium, coarse and very coarse sand respectively). The '-' symbol indicates samples were not collected/not analysed from that location. Foraminifera samples where collected are shown in asterisk.

Location	System	Sandstone samples collected for			Foraminifera samples
		Petrography	Geochr.	XRF	
1	Fosado	F2/2 (ms), F2/3 (fs), F2/4 (ms), F2/5 (fs), F2/6 (ms), F2/7 (fs)	-	F/1 (vfs), F/2 (vfs), F/3 (vfs)	*
2	Arro	Ar6/1 (cs)	-	Ar5/1 (vfs), Ar6/1 (cs)	-
3	Arro	-	-	Ar4/1 (vfs), Ar4/2 (vfs)	-
4	Arro	Ar7/1 (ms), Ar7/2 (ms), Ar7/3 (cs), Ar9/1 (fs), AR9/2 (ms), AR9/3 (cs)	-	Ar7/1 (ms), Ar7/2 (ms), Ar7/3 (cs)	*
5	Arro	-	-	Ar8/1, Ar8/2, Ar8/3, Ar8/4 (all vfs)	*
6	Arro	Ar/B (cs), Ar/M (cs), Ar/T (vcs), AR12/1 (ms), AR12/2 (ms), AR12/3 (ms), AR13/1 (cs), AR13/2 (fs), AR13/3 (ms)	Ar/B (cs)	Ar/B (cs), Ar/M (cs), Ar/T (vcs), Ar3/L (vfs)	*
7	Arro	AR10/B (cs), AR11/2 (ms)	-	Ar2/B, Ar2/M, Ar2/T (all vfs)	*
8	Gerbe + Banaston	G1/2 (fs), G1/3 (ms), B-G1/1 (ms)	-	-	-
9	Gerbe	G3/2, G3/3, G3/4 (all fs)	-	G/1, G/2 (all vfs)	*
10	Gerbe	G/T (ms), G/B (ms), G4/1 (ms), G4/2 (fs), G4/3 (ms), G5/1 (fs), G5/2 (fs)	G/T (ms)	G/T (ms), G/M (vfs), G/B (ms)	*
11	Banaston	B1/1 (fs), B1/3 (ms), B1/4 (ms), B3/1 (ms), B3/2 (ms), B3/3 (ms)	-	-	*
12	Banaston	B4/1 (ms), B4/2 (cs), B4/3 (cs), B5/1 (ms), B5/2 (cs)	-	-	-
13	Banaston	B2/1 (fs), B2/2 (ms), B2/3 (vcs)	-	-	-
14	Banaston	B/2 (ms), B6/1 (fs), B6/2 (fs), B6/3 (ms), B6/4 (ms), B7/1 (ms), B7/2 (ms)	B/2 (ms)	B/1 (fs), B/2 (ms), B/3 (fs)	*
15	Banaston + Ainsa	B*/II (ms), B*/3 (ms), Ai III/1 (fs), Ai III/2 (fs), Ai3/2 (ms), Ai3/3 (fs), Ai3/4 (fs), AiIII 2/1 (ms), AiIII 2/2 (ms)		Ai III/1 (fs), Ai III/2 (fs), Ai III/3 (fs), B*/I (vfs), B*/II (ms), B*/2 (vfs), B*/3 (ms)	-
16	Ainsa	Ai I (cs), Ainsa (cs)	Ai I (cs)	Ai I (cs)	-
17	Ainsa	-	-	-	*
18	Ainsa	-	-	-	*
19	Ainsa	-	-	-	*
20	Ainsa	Ai I/1 (ms), Ai I/3 (ms)	-	Ai I/1 (ms), Ai I/2 (vfs), Ai I/3 (ms)	-
21	Ainsa	-	-	-	*
22	Ainsa	-	-	-	*
23	Morillo	MO8/2 (ms), MO9/1 (ms), MO9/2 (ms), MO9/3 (ms), MO5 (ms), MO4/1 (ms), MO4/2 (ms)	-	-	*
24	Morillo	Mo/1 (ms), Mo/2 (ms), Mo/3 (ms), Mo1/1 (cs), Mo1/2 (fs), Mo1/3 (fs), Mo3/1 (ms), Mo3/2 (fs), Mo3/3 (ms), MO6/2 (ms), MO7/1 (cs), MO7/3 (ms), MO7/4 (ms)	Mo/3 (ms)	Mo/1 (ms), Mo/2 (ms), Mo/3 (ms), Mo1/1 (cs), Mo1/2 (fs), Mo1/3 (fs), Mo3/1 (ms), Mo3/2 (fs), Mo3/3 (ms)	*
25	Morillo	MO-Gu/2 (cs), MO-Gu/3 (fs)	-	MO-Gu/2 (cs), MO-Gu/3 (fs)	-
26	Guaso	Gu/ I (fs), Gu1/2 (fs), Gu1/3 (fs), Gu 4/1 (ms), Gu 4/2 (ms), Gu 4/3 (cs)	Gu4/3(cs)	Gu/ I (fs), Gu1/1 (vfs), Gu1/2 (fs), Gu1/3 (fs)	*
27	Guaso	Gu2/1 (cs), Gu2/2 (fs), Gu3/1 (ms), Gu3/2 (fs), Gu3/3 (fs)	-	Gu2/1 (cs), Gu2/2 (fs), Gu3/1 (ms), Gu3/2 (fs), Gu3/3 (fs)	*
28	Guaso	Gu 6/1 (ms), Gu 7/1 (cs), Gu 8/1 (ms)	-		-
29	Torla	T1/1 (fs), T1/2 (fs), T1/3 (ms)	-	-	-
30	Broto	BR2/3 (fs)	-	-	-
31	Broto	BR3/1 (fs)	-	-	-
32	Broto	BR5/2 (fs), BR5/3 (fs)	-	-	-
33	Broto	BR7/0 (fs), BR7/1 (ms), BR7/2 (fs), BR7/4 (fs)	-	-	-
34	Broto	BR6/0 (fs), BR6/1 (ms), BR6/2 (ms), BR6/3 (ms)	-	-	-
35	Cotefablo	CO5/1 (fs), CO5/2 (ms), CO5/3 (ms)	-	-	-
36	Cotefablo	CO1/2 (ms), CO2/1 (fs), CO2/2 (ms), CO2/3 (fs)	-	-	-
37	Cotefablo	CO3/0, CO3/1, CO3/3 (all fs)	-	-	-
38	Cotefablo	CO4/3 (fs)	-	-	-
39	Banaston	BA2/1, BA2/2, BA2/3, BA2/4, BA2/5 (all fs)	-	-	-
40	Banaston	BA4/1, BA4/2, BA5/1, BA5/2 (all fs)	-	-	-
41	Banaston	BA3/2 (fs)	-	-	-
42	Jaca	J4/1, J4/2, J4/3 (all fs)	-	-	-
43	Jaca	J1/1 (fs), J1/2 (ms), J1/3 (fs)	-	-	-
44	Jaca	J3/1 (fs), J3/3 (fs)	-	-	-

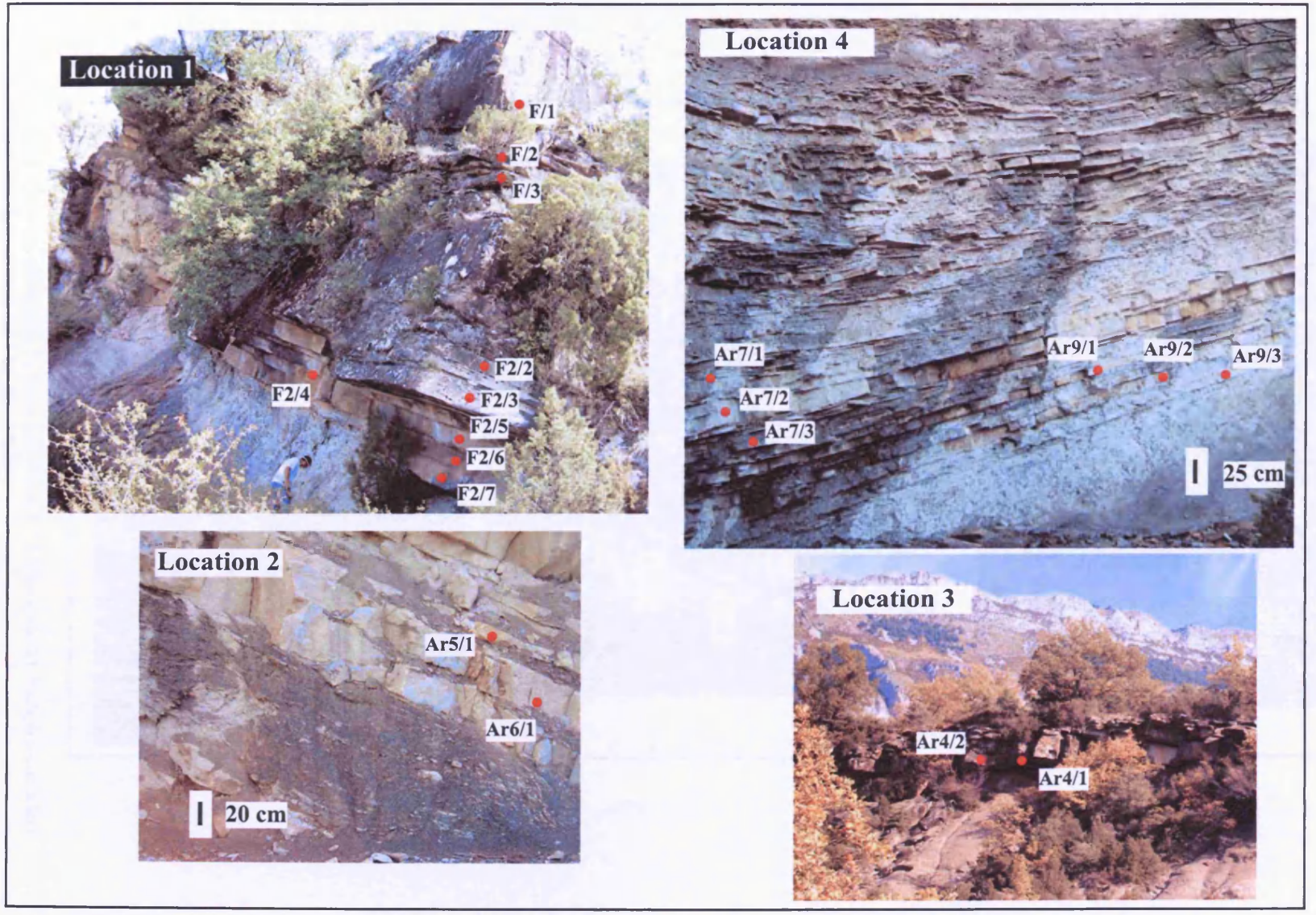

Figure 3.2: Outcrop photographs from Locations1-4. Samples collected from each location are marked by red circles. Location 1: Fosado system; Locations 2-4: Arro system.

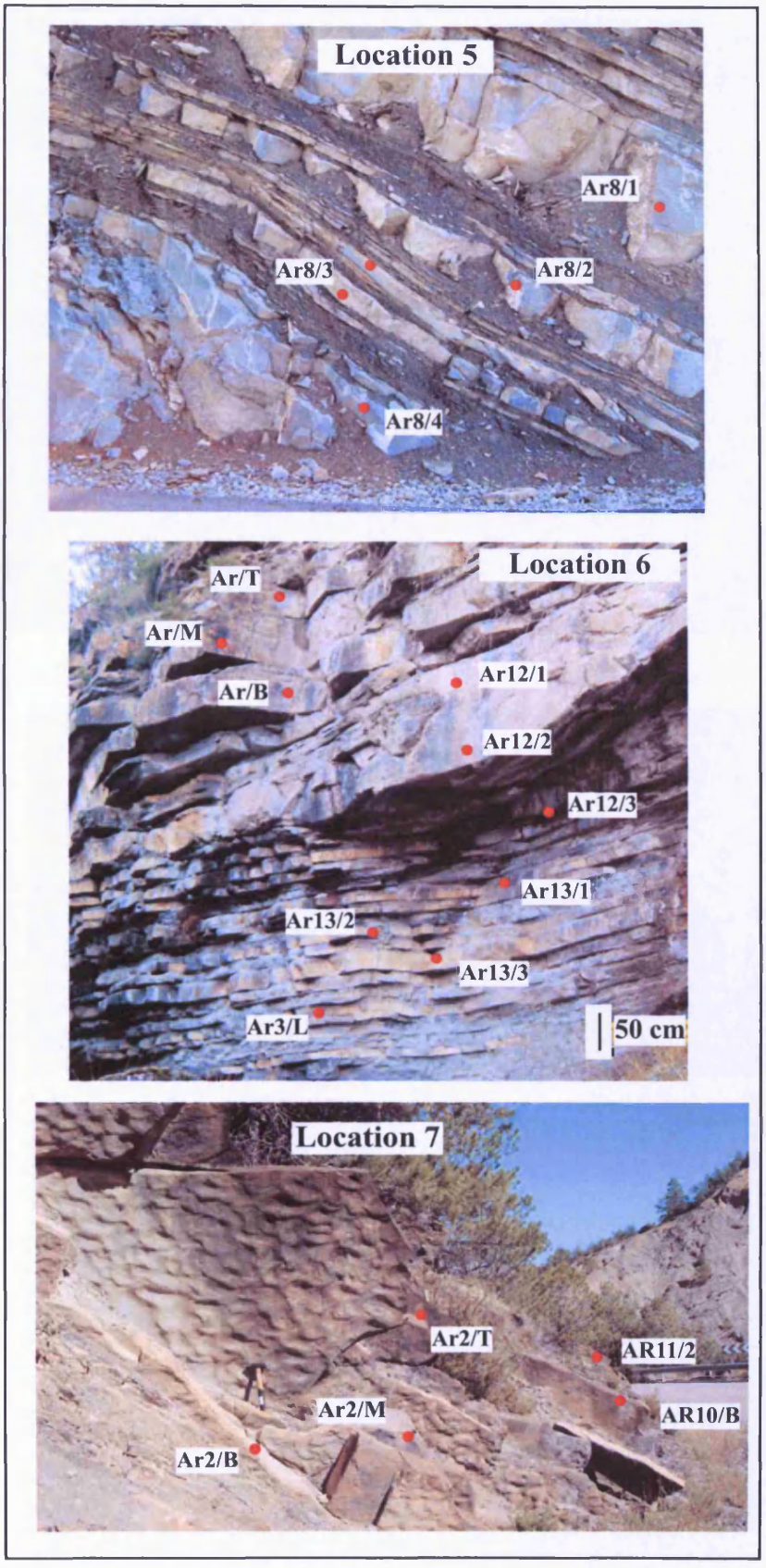

Figure 3.3: Outcrop photographs from Locations 5-7 (Arro system). Samples collected from each location are marked by red circles.

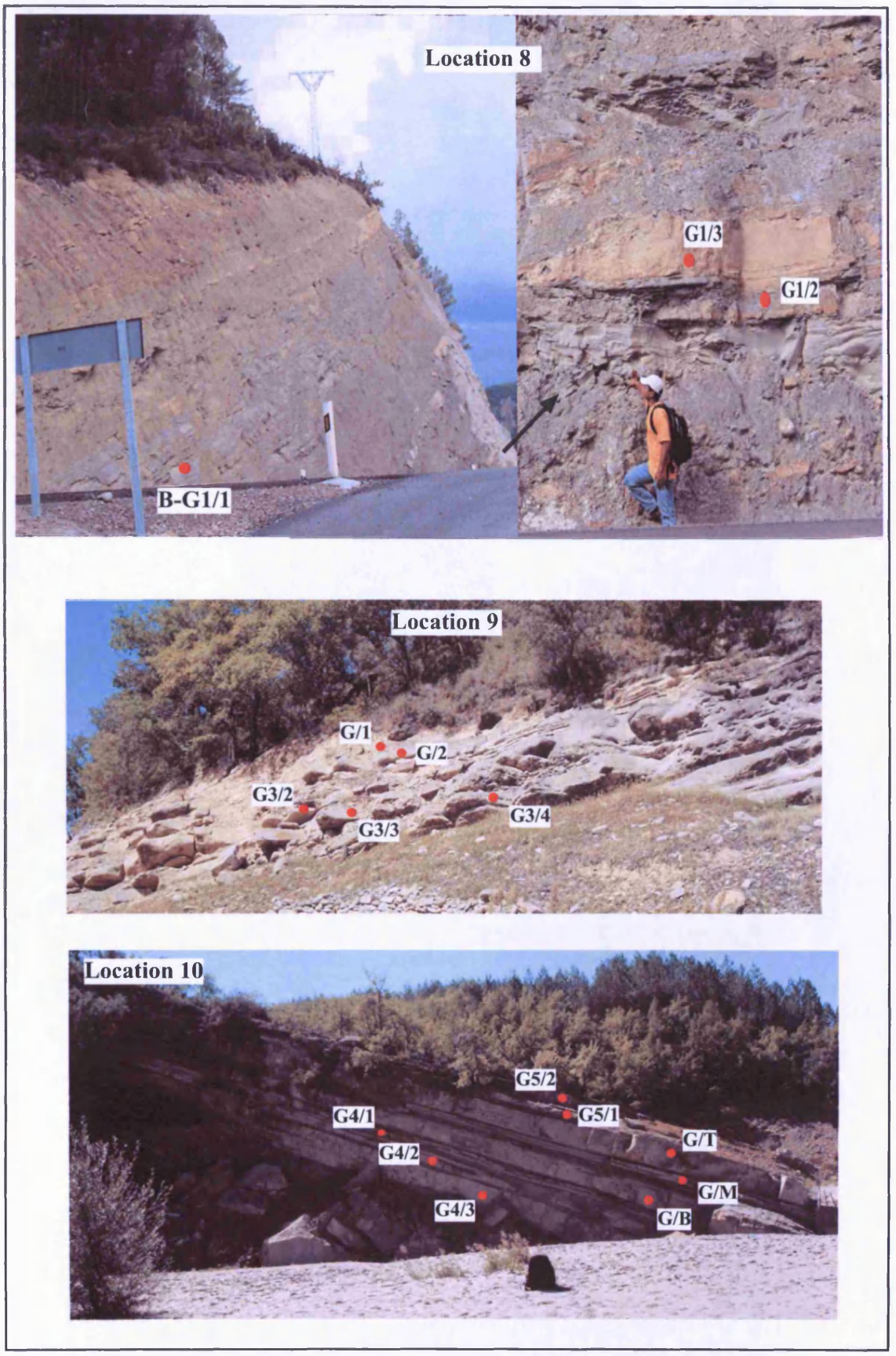

Figure 3.4: Outcrop photographs from Locations 8-10. Samples collected from each location are marked by red circles. Location 8: Gerbe & Banaston system; Locations 9-10: Gerbe system.

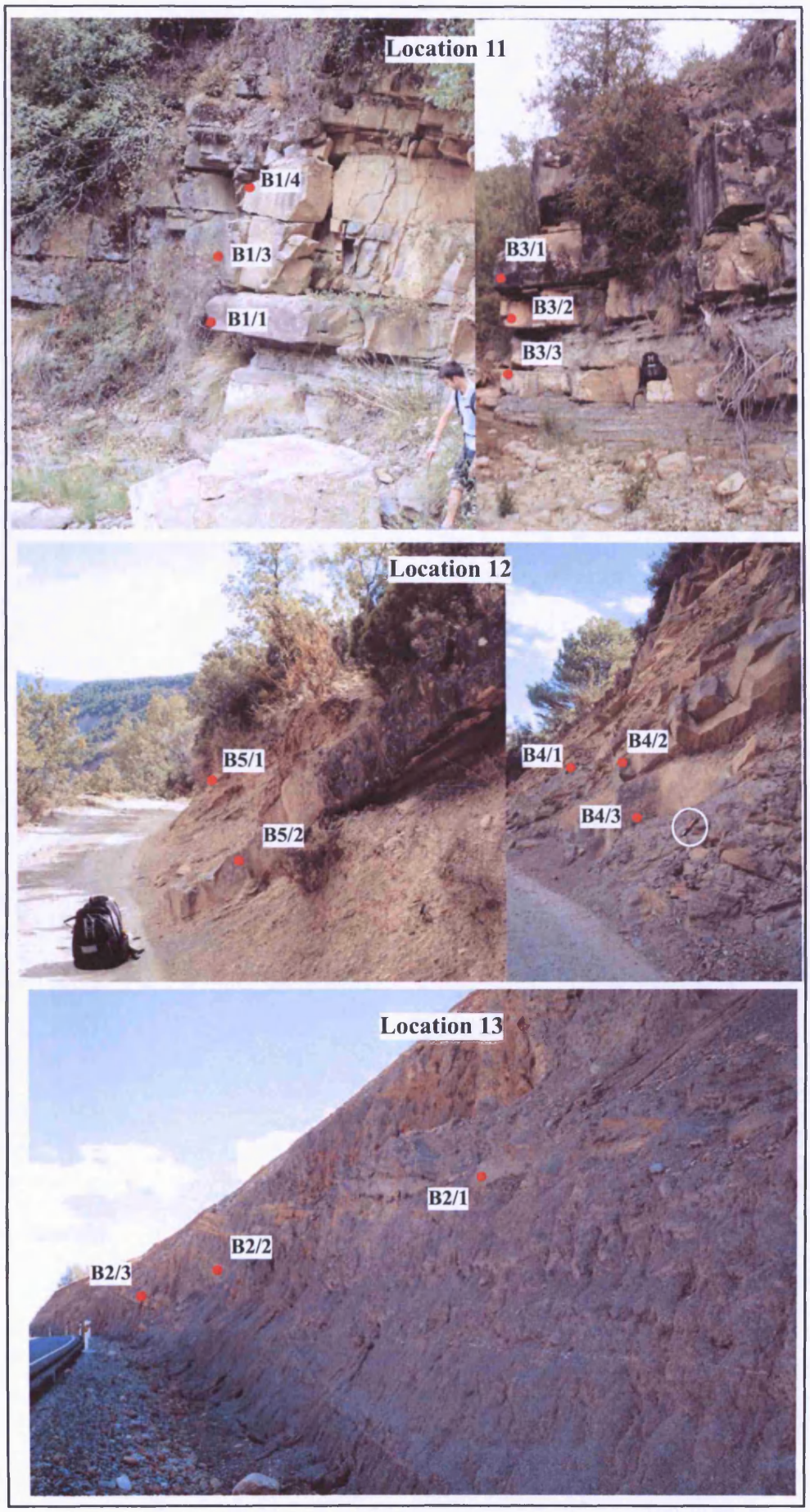

Figure 3.5: Outcrop photographs from Locations 11-13 (Banaston system). Samples collected from each location are marked by red circles.

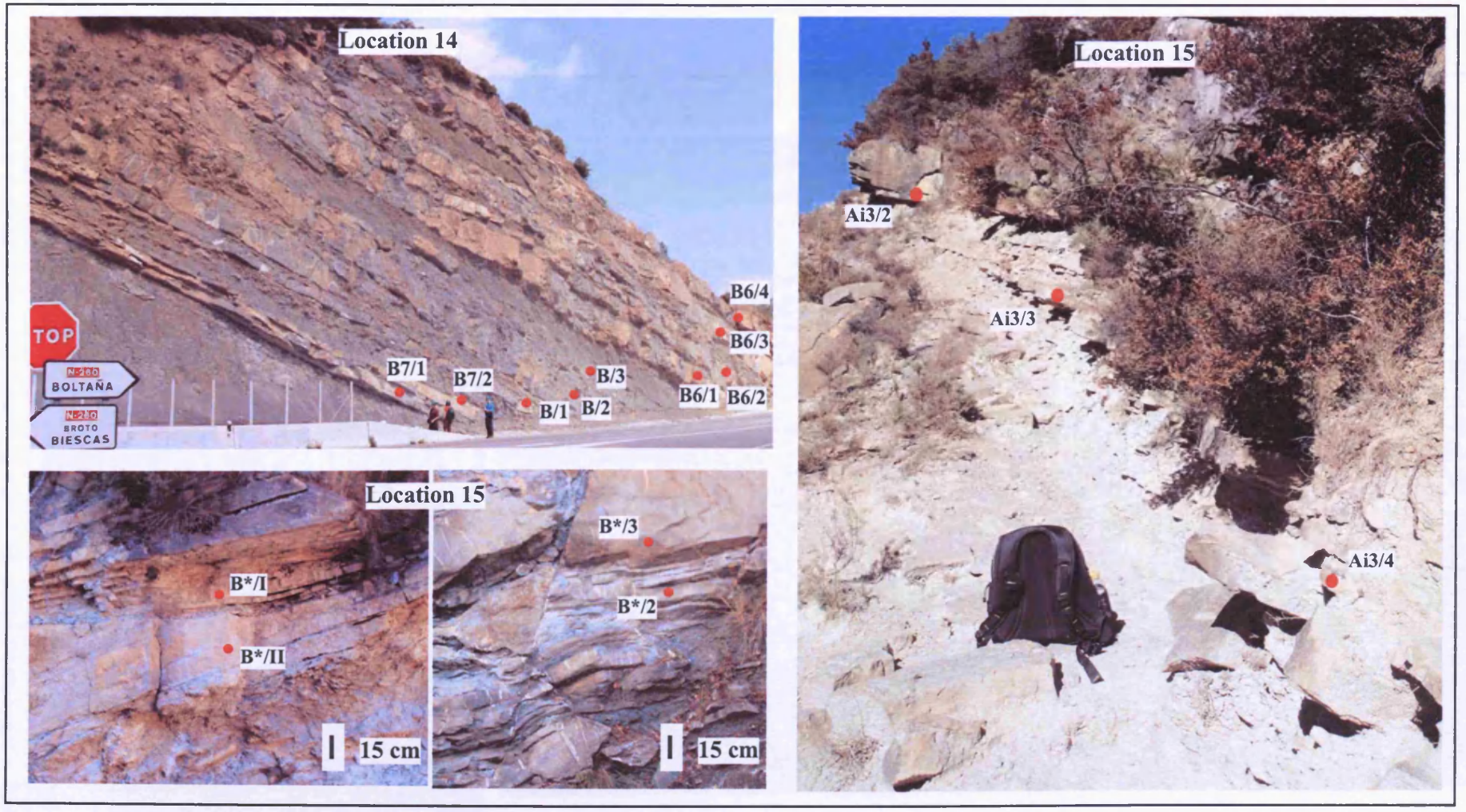

Figure 3.6: Outcrop photographs from Locations 14-15. Samples collected from each location are marked by red circles. Location 14: Banaston system; Location 15: Banaston and Ainsa systems.

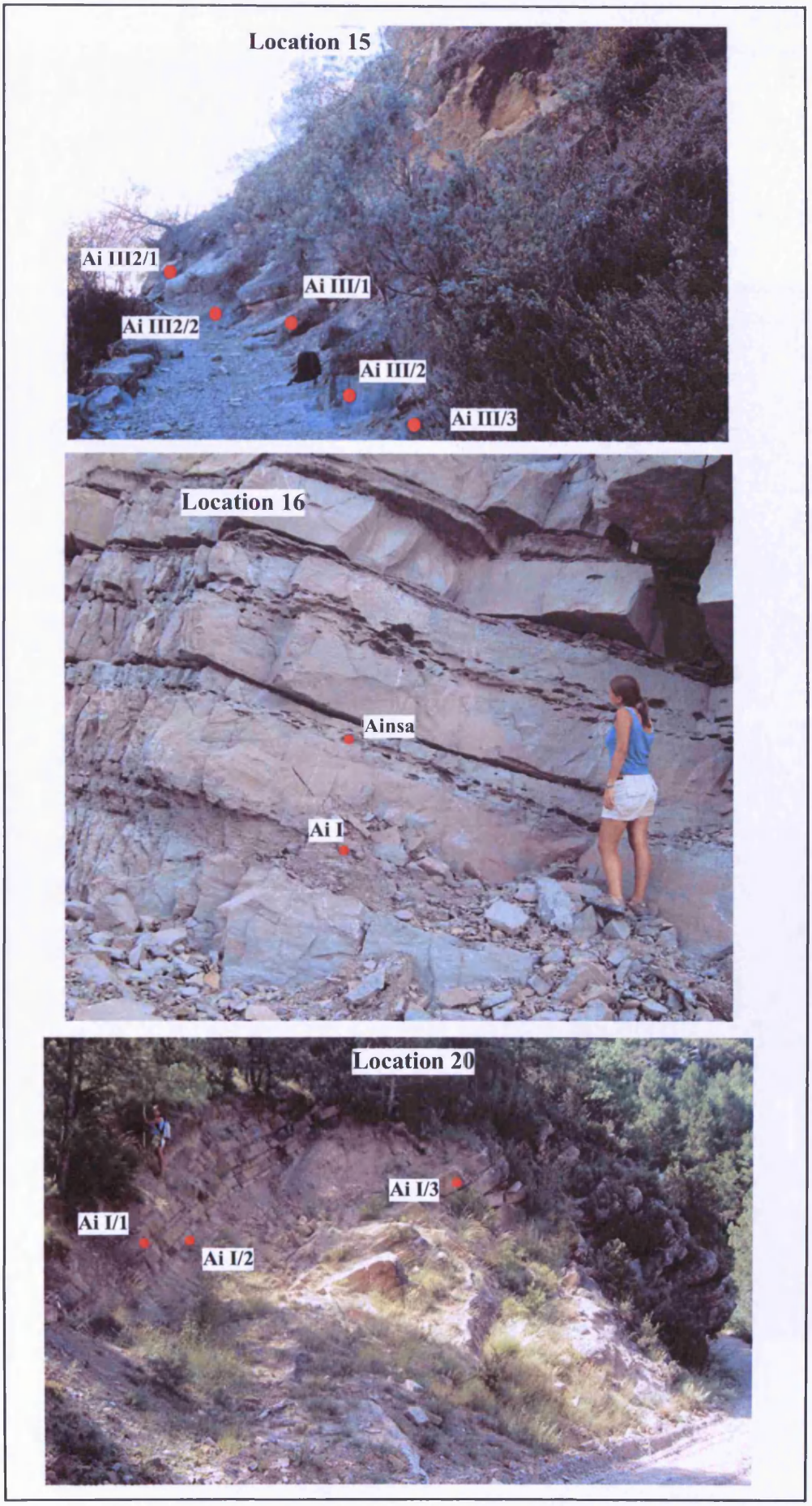

Figure 3.7: Outcrop photographs from Locations 15, 16 and 21 (Ainsa system). Samples collected from each location are marked by red circles.Note some samples from the Ainsa system are also collected from a core.

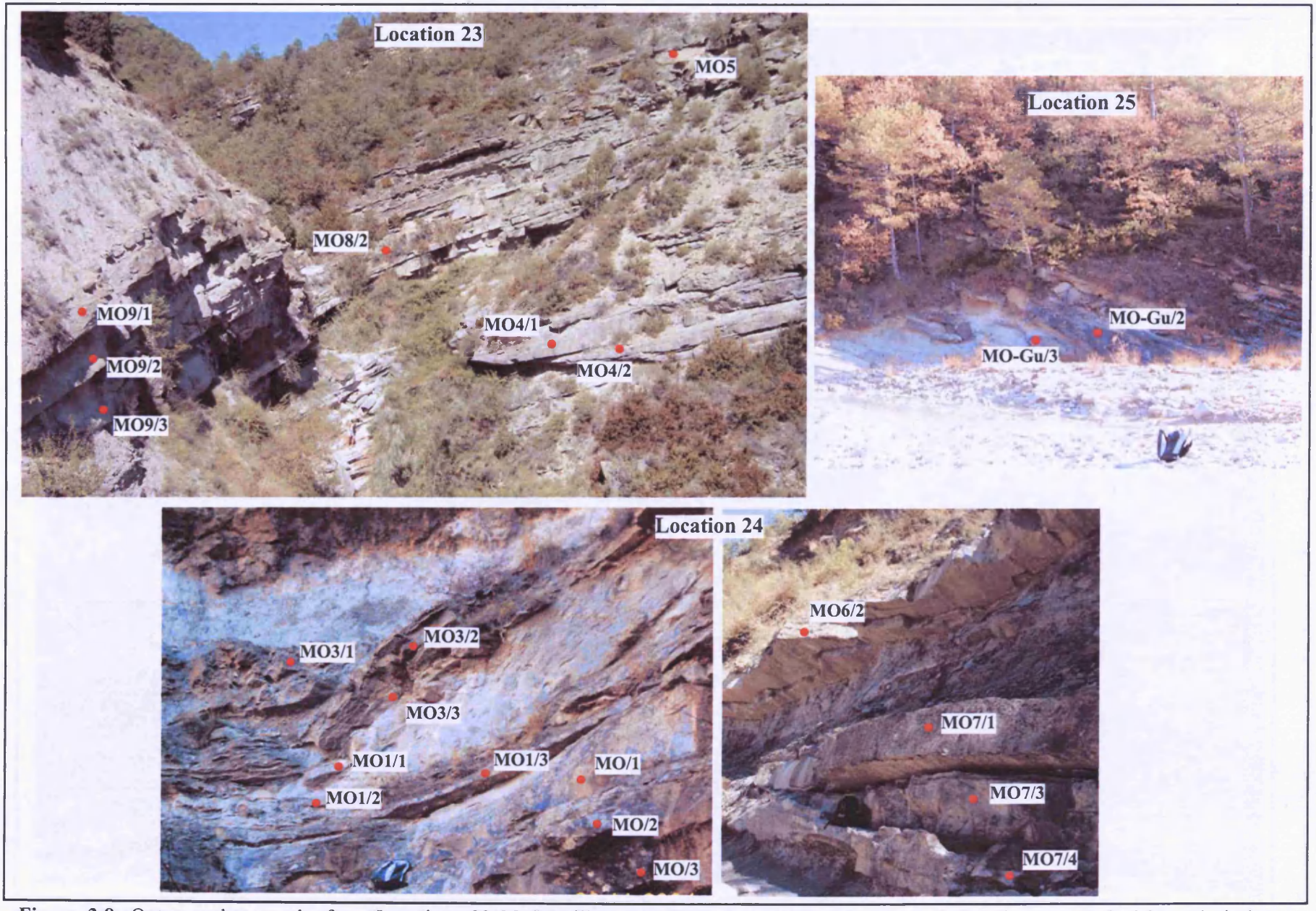

Figure 3.8: Outcrop photographs from Locations 23-25 (Morillo system). Samples collected from each location are marked by red circles.

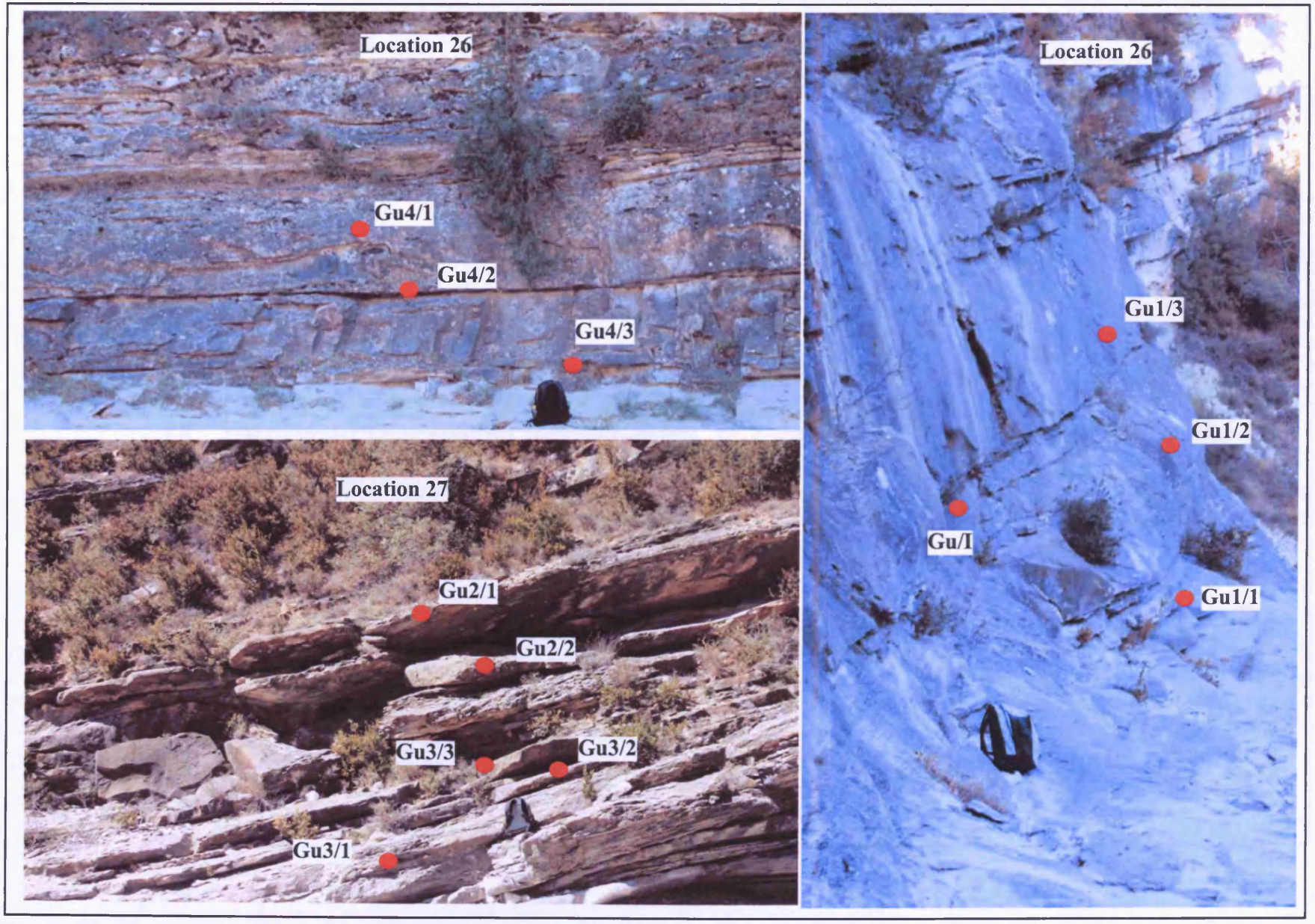

Figure 3.9: Outcrop photographs from Locations 26-27 (Guaso system). Samples collected from each location are marked by red circles.

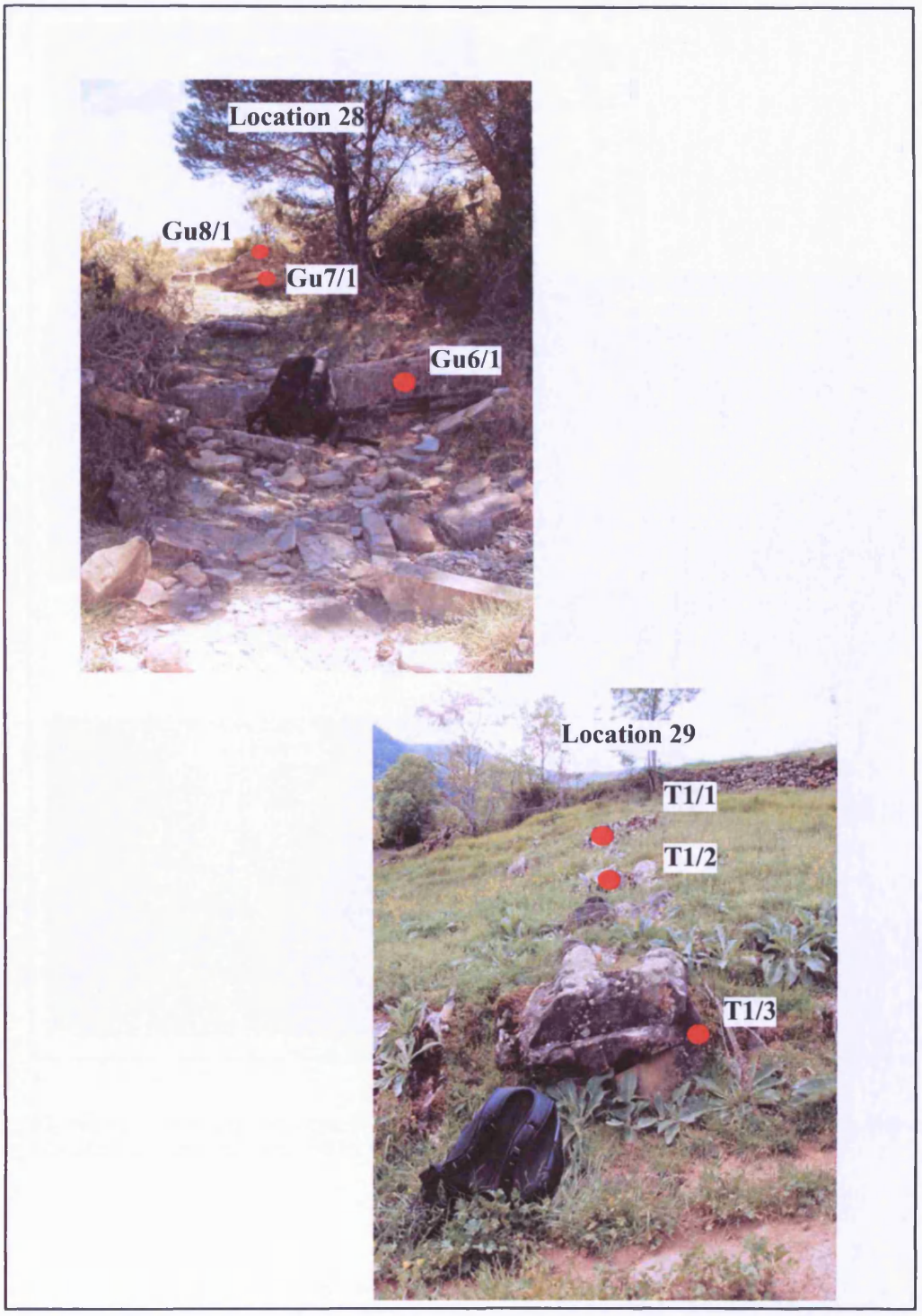

Figure 3.10: Outcrop photographs from Locations 28 (Guaso system) and 29 (Torla system). Samples collected from each location are marked by red circles.

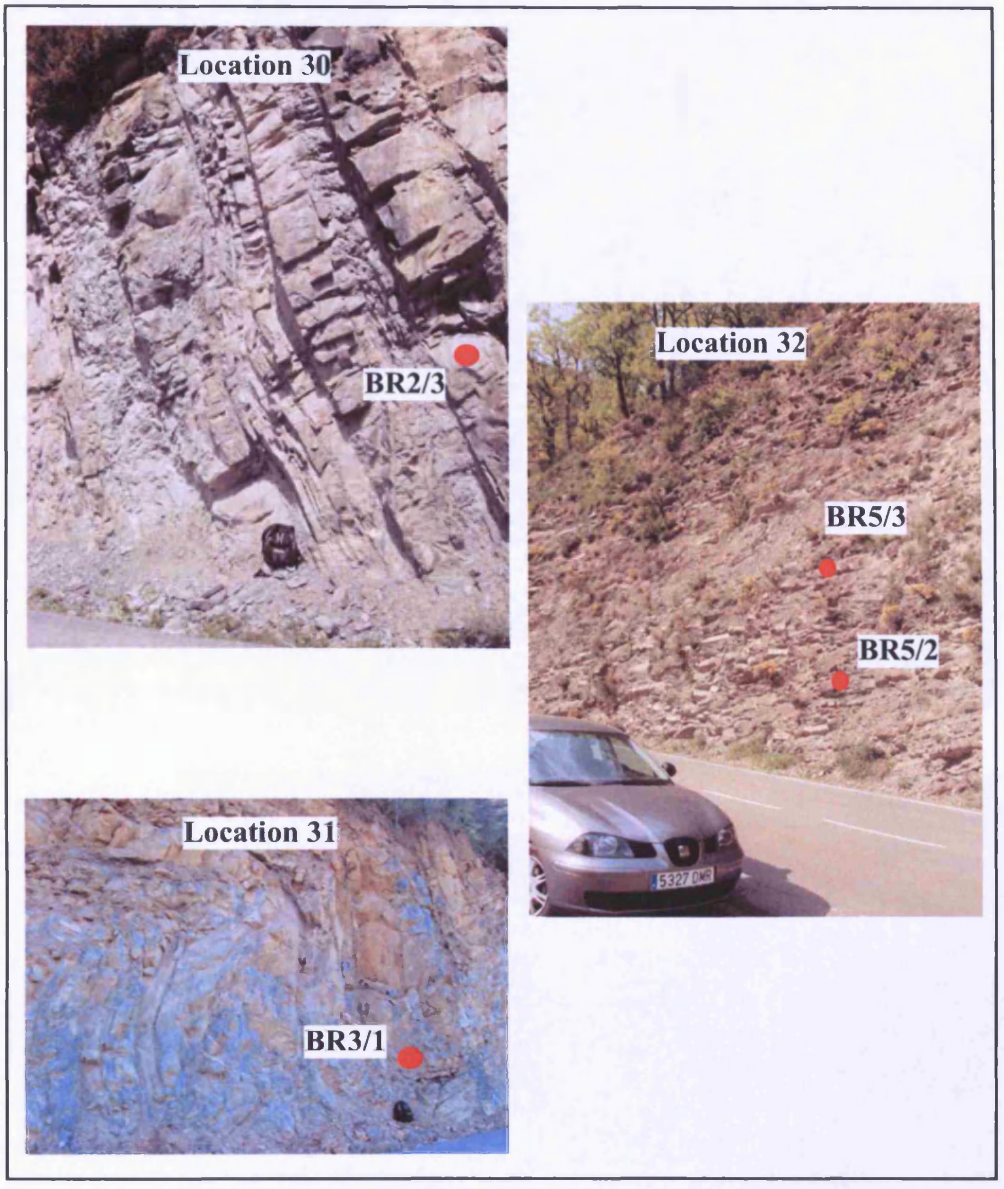

Figure 3.11: Outcrop photographs from Locations 30-32 (Broto system). Samples collected from each location are marked by red circles.

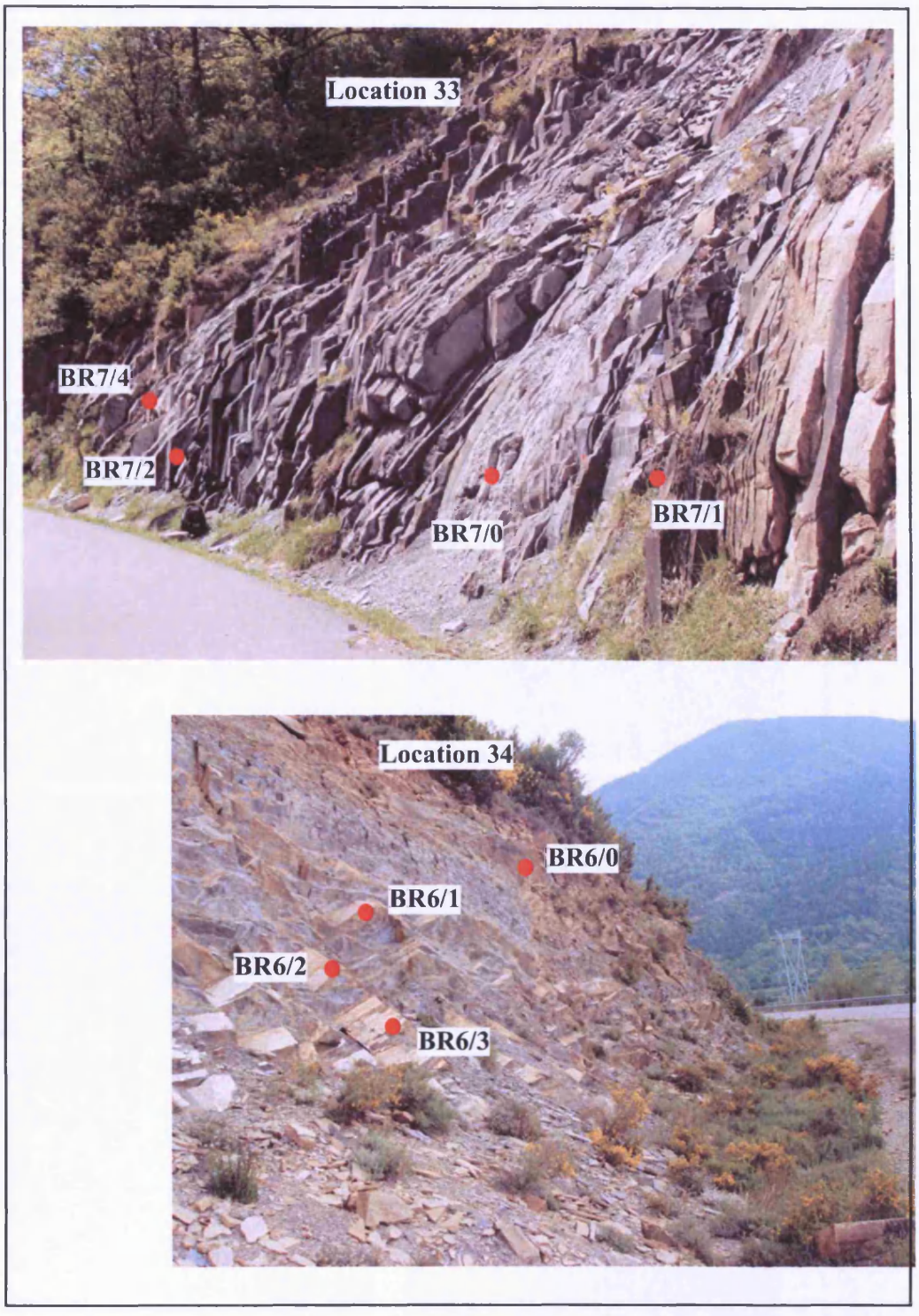

Figure 3.12: Outcrop photographs from Locations 33-34 (Broto system). Samples collected from each location are marked by red circles.

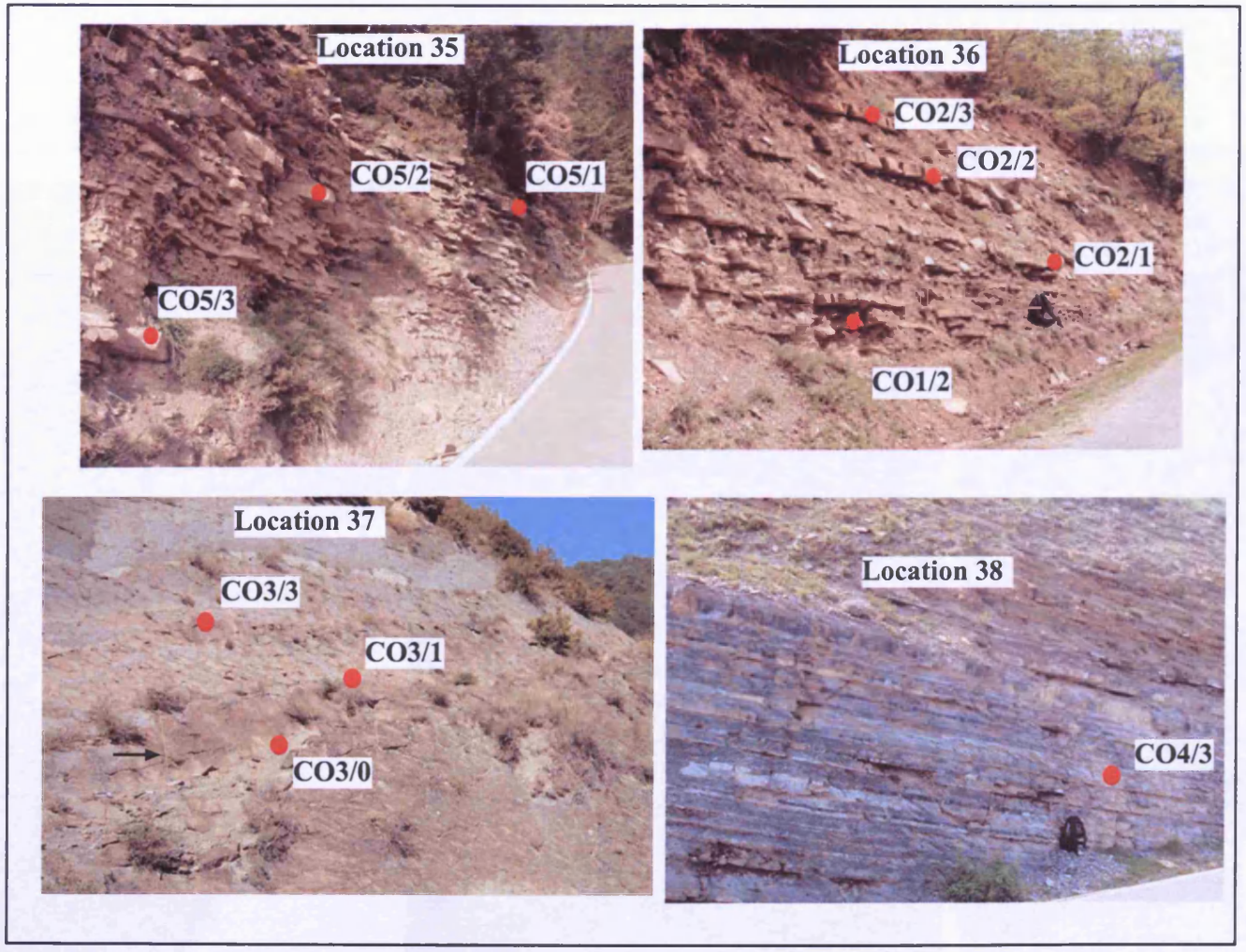

Figure 3.13: Outcrop photographs from Locations 35-38 (Cotefablo system). Samples collected from each location are marked by red circles. The arrow in Location 37 photograph points to a 2m-tape.

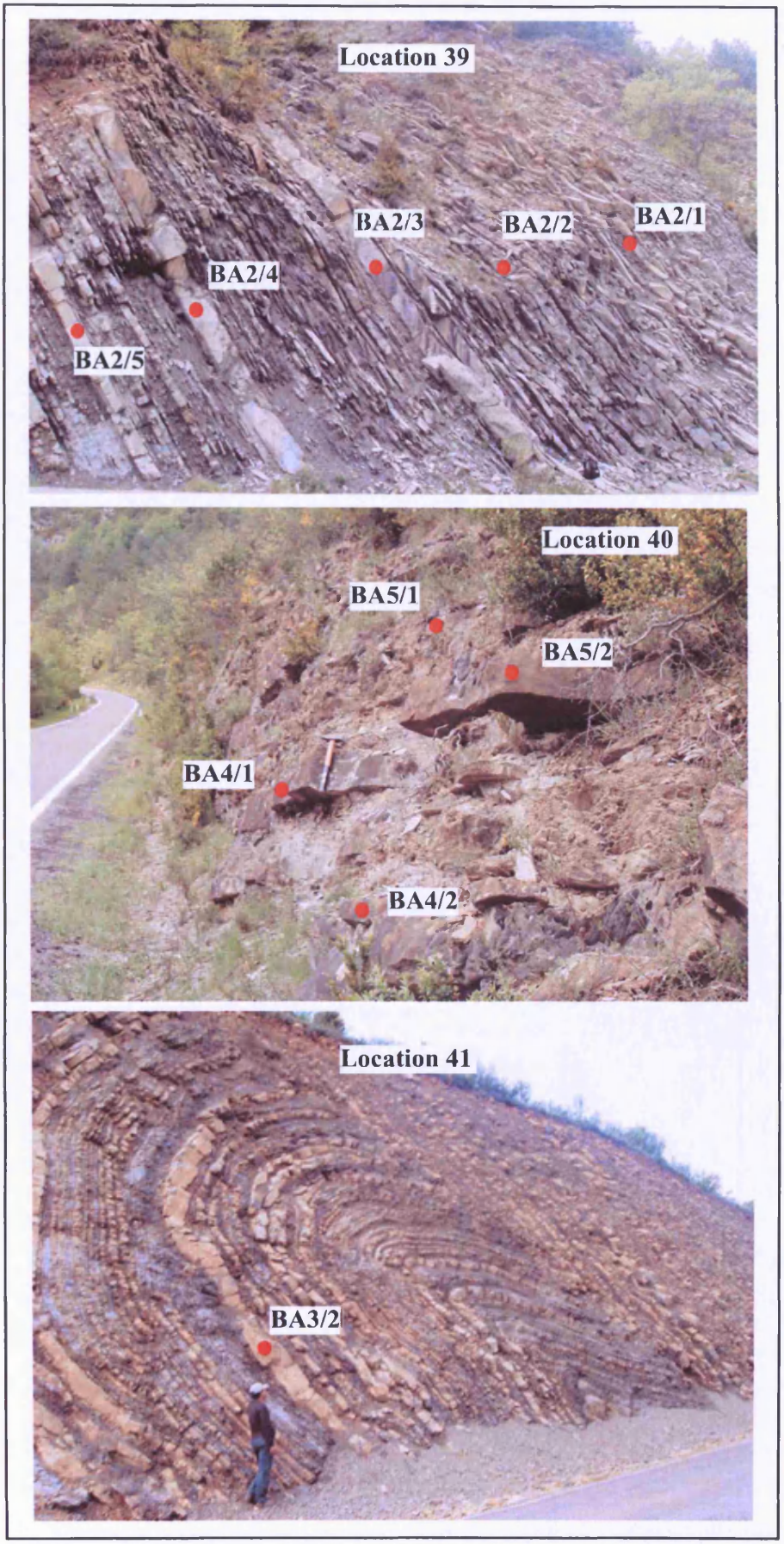

Figure 3.14: Outcrop photographs from Locations 39-41 (Banaston system in the Jaca basin). Samples collected from each location are marked by red circles.

Figure 3.15: Outcrop photographs from Locations 42-44 (Jaca system). Samples collected from each location are marked by red circles.

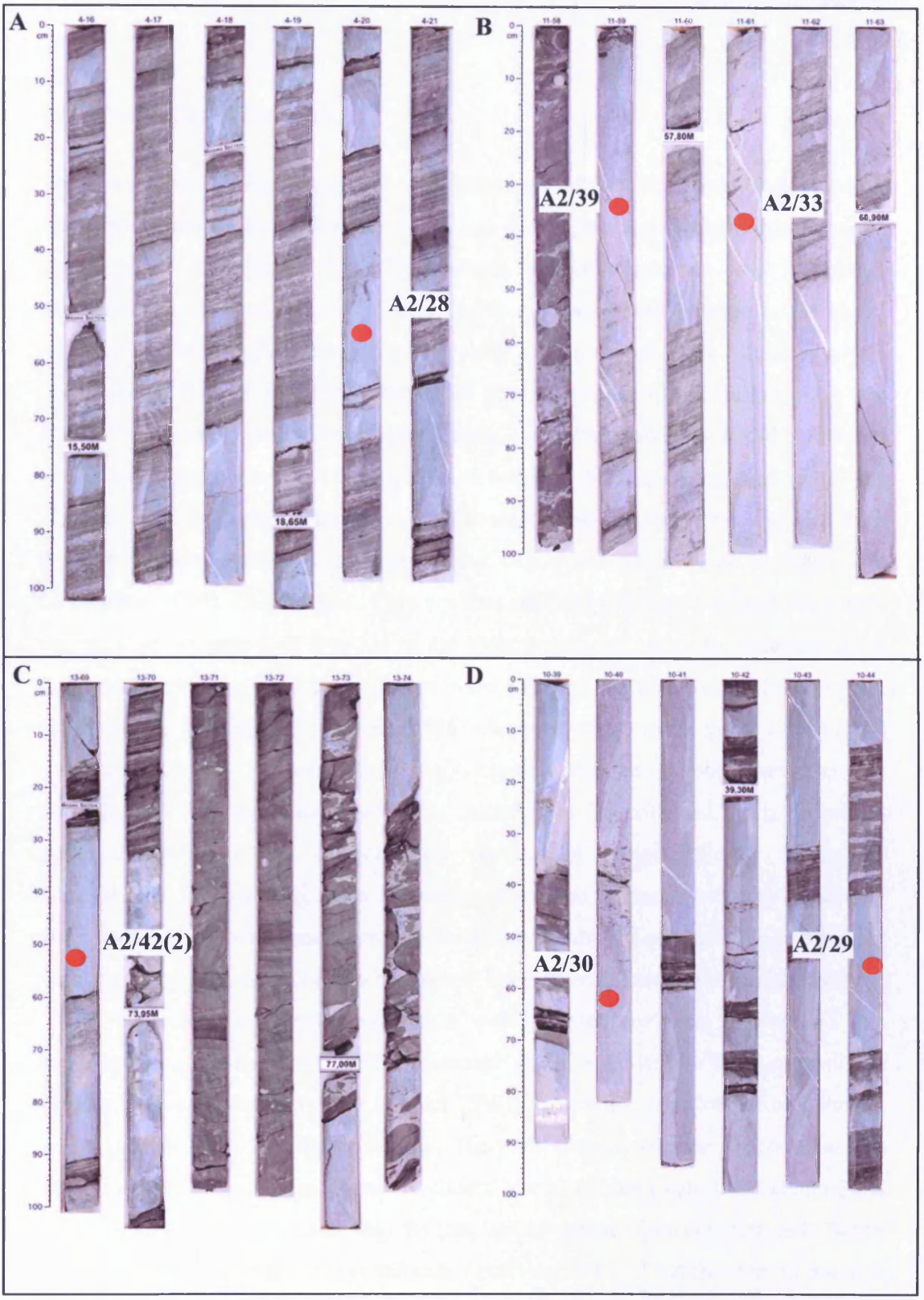

Figure 3.16: Core photographs from the Ainsa system. Samples collected are marked by red circles.

3.2 Petrography Techniques

For petrographic study, a primary field collection of 229 sandstone samples were made from outcrops throughout the Ainsa and Jaca basins, and throughout each sandy system (Fig. 3.1, Table 3.1). The sample selection criterion was to obtain representative samples from each stratigraphic unit or turbidite system in the basin, with the aim of sampling the coarsest-grained sandstone turbidites available within each location (Fig. 3.1), although the upper grain size (mean) limit for sampling was set at 2 mm (i.e., very coarse-grade sand). Care was taken to avoid collecting weathered samples. Out of 229 samples, 166 are from the Ainsa basin area and 63 are from the Jaca basin area. The Ainsa basin samples also include 6 core samples from the Ainsa system collected as a part of the UCL-Ainsa project (see Pickering and Corregidor, 2005). The samples were cut into standard thin sections, and most were stained with Alizarin Red S to aid in the identification of carbonate minerals. After preliminary observations, 157 samples were selected for detailed modal analyses, following the procedure of Valloni (1985). Samples with a mean grain size of <125 μm were discarded. The sampling strategy, together with the sandbody thickness (and accessibility), informed the number of samples to be collected from individual systems, which in turn restricted the number of samples finally taken into consideration for modal analyses. Inevitably, this led to an uneven number of samples from each system, with maximum and minimum number of samples finally analysed from the Banaston system (Ainsa basin) and Torla system (Jaca basin), respectively.

Four hundred framework grains were counted for each of the 157 thin sections using a transmitted light microscope (LEICA DMERX) fitted with digital camera, and a 12-channel point counter (SWIFT MODEL F). Cement and matrix, where present, were counted separately. The point distance chosen for counting was larger than the largest grain fraction included in the analysis (Van der Plas and Tobi, 1965). A 400-point-count embodies the standard deviation of the counting error below 2.5 percentage points for all constituents (meaning that a 5% difference in count is significant at the two sigma level), and holds the counting error to 1 percentage point for constituents present in amounts <10% (Dryden, 1931; Dickinson, *pers. comm.* 2004).

Point counting was performed using the Gazzi-Dickinson technique (Gazzi, 1966; Dickinson, 1970). According to this technique, coarse-grained rock fragments were tabulated by recording the type of crystal below the cross-hair, and the type of rock fragment in which the crystal is contained. For example, a sand-sized plagioclase phenocryst in a volcanic-rock fragment counts as plagioclase, rather than the host lithic grain. Ingersoll et al. (1984) demonstrated that this approach significantly reduces the sensitivity of compositional data to grain size. A brief history of different point counting methods in sedimentary petrography along with their advantages and limitations has been discussed by Weltje (2002).

While counting, particular care was taken to discriminate between the non-coeval extrabasinal and coeval intrabasinal carbonate grains, using the criteria defined by Zuffa (1980; 1985; 1987). Some of the commonly used criteria are shown in Table 3.2. However, it was not always possible to distinguish extrabasinal and intrabasinal grains and in such cases they were counted separately as 'limeclasts'. Effect of undifferentiated limeclasts on the petrography results are discussed in Chapter 4. In total, 51 petrographic classes were recognised for the purpose of point counting, referring to framework grains (48 classes) and matrix / cement (3 classes). The petrographic classes for framework grains were recalculated and these values were plotted on various ternary diagrams (Chapter 5 and 6). For sandstone classification purposes, the schemes of Folk et al. (1970) and Zuffa (1980) were utilised.

3.3 Geochronology Techniques

A variety of methods are in use for geochronology studies. In this particular study, detrital zircon thermochronology using combined fission track (FT) and U-Pb techniques were used. Zircon, being ubiquitous and common to variety of rock types, has been more widely used in provenance-related studies (Gallagher et al., 1998 and references therein) because of its higher temperature stability, generally robust resistance to physical transport and relatively high concentrations of U and Th and low concentration of common Pb (Reiners et al., 2005). The robustness of zircon is reflected by an FT partial annealing zone that occurs at higher temperature than apatite and ranges between ~200 - 310°C, the exact value depending on levels of accumulated alpha radiation damage (e.g. Carter, 1999; Rahn et al., 2004). In contrast,

the inherent strength of the U-Pb dating system lies in its high resistance to thermal overprinting (>700–900 °C, Mezger and Krogstad, 1997), which enables it to effectively "see through" later thermal events. By adopting a dual zircon dating approach (Carter and Moss, 1999), which has the advantage of using each method to constrain provenance interpretation of the other, it is possible to identify underlying age structure of the source terrane and subsequent thermotectonic events. The whole methodology for geochronology comprises three main analyses: heavy mineral separation, FT chronometry and U-Pb dating.

Table 3.3: Criteria used for distinguishing intrabasinal (coeval) and extrabasinal (non-coeval) carbonate particles in modal analysis (after Zuffa 1985).

		Intrabasinal limeclasts	*Extrabasinal limeclasts*
COMPOSITION	Mineralogy	Calcite	Calcite/dolomite/ankerite
	Fauna	Not older than the host sediments; bioclasts may be abundant	Fossils may be present in carbonate rock fragments which are older than the host formation
TEXTURE	Grain size	May be different, typically coarser than terrigenous particle	Generally same as other terrigenous siliciclastic
	Roundness & sphericity	Soft intraclasts occur with irregular and/or sinuous contours; they exhibit also elongated and/or platy shape; skeletal debris is generally angular	Generally rounded, with high values of sphericity
	Fabric	Common fabric of allochemical components; absence of particles with internal veins; absence of recrystallised particles	Particles with coloured, oxidised contours; particles with internal veins; recrystallised particles may be present
INDIRECT EVIDENCE		If bioclasts of the same age as the deposit are present, then other intrabasinal carbonate particles are likely to be present	If dolomite and/or angular chert rock fragments are present, then other extrabasinal carbonate particles are likely to be present

3.3.1 Heavy mineral separation

Samples collected for geochronology are the coarsest available fraction from each outcrop location (Table 3.1). The typical weight of the samples was 3–5 kg and heavy minerals were extracted in the laboratory with standard heavy liquid and magnetic separation techniques. After obtaining the zircon crystals they were processed further for FT and U-Pb dating techniques. The steps for separating heavy minerals, zircon in this case, can be summarised as follows (Bernet and Garver, 2005):

1) Crushing and disaggregating the rock specimen by jaw crusher and disc mill.
2) Separation of the disaggregated sample by size and density using a Wilfley table.
3) Sieving with 500 μm sieves. Only the >500 μm fraction was processed further. The other fractions were stored.
4) Separating heavy minerals from light-mineral contaminates by density separation passing the sample through Bromoform (density = 2.89 gm/cm^3).
5) Passing the heavy fraction, after drying, through the Frantz magnetic separator stepwise at 0.1 – 1.5 amps and different slope settings.
6) Processing the nonmagnetic fraction through another heavy liquid (i.e. Di-iodomethane with a density of 3.25 gm/cm^3). Here zircon crystals will sink owing to higher specific gravity.

3.3.2 Fission track chronometry

When charged nuclear particles travel through insulating solids, they produce linear trails of disrupted atoms. Fission tracks are such damage features, and fission track analysis is the study and characterization of the number and size of these features in minerals. Natural or "spontaneous tracks" in geological samples are produced nearly exclusively by the spontaneous fission of the isotope ^{238}U, as the fission half-lives of all other naturally occurring heavy isotopes such as ^{235}U and ^{232}Th are too long to produce a significant number of tracks. Zircon and apatite have the appropriate trace levels (ppm) of uranium, and so these are the minerals to which fission track chronometry has been principally applied (Hurford & Carter, 1991).The number of fission tracks stored in a host mineral indicates the length of time during which tracks have been accumulating, but is also controlled by the spontaneous fission decay

constant (λ_f) and the uranium content of the mineral. The later is determined by irradiation using thermal (low energy) neutrons to induce fission in ^{235}U, recording these induced fission tracks in a detector (usually of mica) – see Fig. 3.2.

The determination of the ratio of spontaneous to induced track counts for each crystal in a fission track analysis yields an individual age for each grain. This technique is known as the external detector method (Gleadow, 1981) (Fig. 3.2.). This method is also the International Union of Geological Sciences Working Group's recommended approach (Hurford 1990a, b).

For the external detector ζ method, the fission track age equation is written as

$$t = \frac{1}{\lambda_d} Ln\left(\lambda_d \frac{\rho_s}{\rho_i} \rho_d \zeta g + 1\right) \qquad \text{[equation 3.1]}$$

where t is the age; ρ_s and ρ_i are the spontaneous and induced track densities (number of tracks/unit area); λ_d is the α decay constant of ^{238}U; ρ_d is the track density in a dosimeter (a glass of known uranium concentration), which is used to monitor the neutron flux in the reactor; g is known as the geometry factor (which allows for the fact that the spontaneous tracks intersecting the surface of observation represent a sample from twice the effective volume than the induced tracks represent); and ζ is a constant of proportionality made up of the other parameters, including the fission decay constant and neutron capture cross section. The ζ calibration factor is determined from a sample of known age by rearranging Equation 3.1. In practice, an individual analyst will undertake around 30–50 calibrations to determine their own particular ζ value for a given dosimeter. Thus, ζ also absorbs some of the vagaries of the observation process.

After the heavy mineral analysis, samples for zircon fission track analysis were mounted in PTFE Teflon, polished and etched using a binary eutectic of NaOH:KOH at 225°C (Gleadow et al., 1976). Multiple grain mounts were made for each sample and etched for different durations of time to avoid source bias. A mount is considered well etched when the optimum number of zircons has well resolved tracks. Such a median etch time produces grains that are both under-etched and over-etched. Tracks (confined) below the surface can also be revealed if there is a pathway for the etchant (a surface track, cleavage, or fracture). Samples were then packed with

muscovite (uranium-free) external detectors and CN2 glass dosimeters and irradiated in the well thermalised (Cd ratio for Au >100), Hifar Reactor, at Lucas Heights in Australia. Samples are irradiated with low-energy thermal neutron, which induces fission in ^{235}U. During the fission process, some heavy particles cross the interface between the mineral and the mica, producing a mirror image of the original grain.

When the sample is returned to the laboratory, only the mica was etched to reveal the induced tracks. Fission-track densities were measured using an optical microscope at 1250x magnification with an oil objective. These are then fed into Equation 3.1. To avoid bias and to obtain representative and reliable results only a random selection of countable zircons were analyzed, from a randomly mixed suite of zircons in the Teflon mount. Therefore, only grains containing well-etched fission tracks were counted and under-etched or over-etched grains were omitted. In addition, grains with strong zoning, uneven surfaces, cracks, inclusions, or very small counting areas were not counted. Ages ($\pm 1\sigma$) were calibrated by the zeta method (Hurford and Green, 1983), using a zeta factor of 127 ± 4 determined by multiple analyses of zircon age standards.

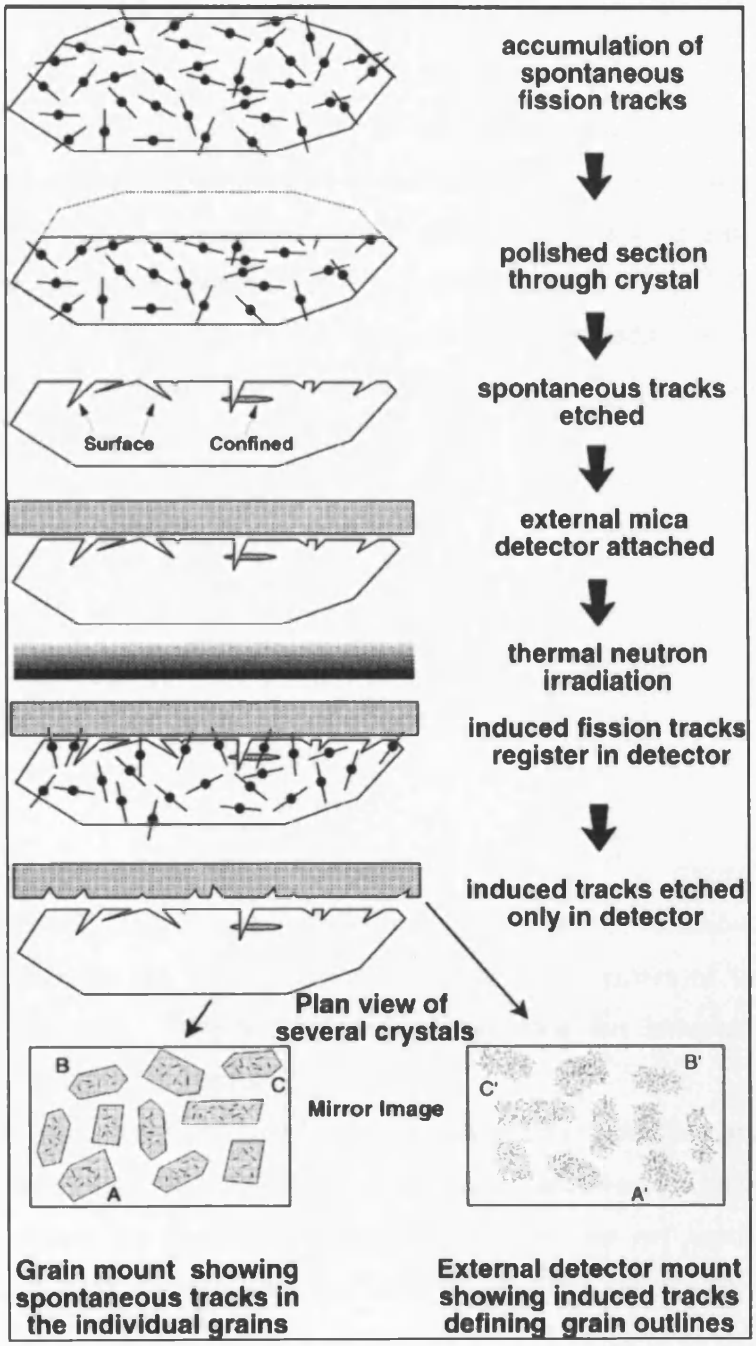

Figure 3.17: The external detector method for fission track analysis (Hurford & Carter, 1991). The surface of zircon is polished and etched to reveal spontaneous (surface) tracks intersecting what was an internal surface. Tracks (confined) below the surface can also be revealed if there is a pathway for the etchant. Then mica (muscovite) detector is sealed against this surface, and the sandwich is sent to a nuclear reactor. The sample is irradiated with low-energy thermal neutrons, which induces fission in ^{235}U. During the fission process, some heavy particles cross the interface between the mineral and the mica, producing a mirror image of the original grain. Upon return, only the mica is etched to reveal the induced tracks. By counting the number of induced tracks in the mica, the parent uranium concentrations are estimated, whereas by counting the numbers of spontaneous tracks in the mineral, the concentration of the daughter product are estimated.

3.3.3 U-Pb analysis

U-Pb dating relies on the equations of U-Pb decay schemes, which are governed by equations derivable from the law of radioactivity ('the rate of decay of an unstable nuclide is directly proportional to the number of atoms remaining at any time'). These equations are written in terms of the atomic $^{206}Pb/^{204}Pb$, $^{207}Pb/^{204}Pb$ and $^{208}Pb/^{204}Pb$ ratios because ^{204}Pb is the only stable non-radiogenic isotope of Pb. The U-Pb dates are calculated by means of following equations and using assumed values of the initial isotope ratios of Pb:

$$t_1 = \frac{1}{\lambda_1} \ln\left[\frac{\left(^{206}Pb/^{204}Pb\right) - \left(^{206}Pb/^{204}Pb\right)_i}{^{238}U/^{204}Pb} + 1\right] \qquad \text{[equation 3.2]}$$

$$t_2 = \frac{1}{\lambda_2} \ln\left[\frac{\left(^{207}Pb/^{204}Pb\right) - \left(^{207}Pb/^{204}Pb\right)_i}{^{235}U/^{204}Pb} + 1\right] \qquad \text{[equation 3.3]}$$

where λ_1 and λ_2 are decay constants of ^{238}U and ^{235}U respectively; $^{238}U/^{204}Pb$, $^{235}U/^{204}Pb$ are ratios of these isotopes calculated from the measured concentrations of U and Pb; and the subscript *i* refers to the initial values of the $^{206}Pb/^{204}Pb$ and $^{207}Pb/^{204}Pb$ ratios. These two equations will result in two independent ages based on each of the two decay series.

The choice of the initial isotope ratios of Pb is a problem only for dating rocks and minerals that have low U/Pb ratios and in addition, are young. The numerical values chosen for the initial isotope ratios of Pb do not significantly affect the calculated U-Pb dates of minerals having high U/Pb ratios (e.g. in zircon, apatite, monazite) because their present isotope ratios of Pb reach large values. Krogh (1973) reported a $^{206}Pb/^{204}Pb$ ratio of 126,000 for crystals of Precambrian zircon. The assumption that the samples being dated remained closed to U-Pb and all intermediate daughter products is satisfied only in rare cases, due to mobility of Uranium in oxidising environments. Also there is a superficial effect from Pb loss on U-Pb ages. Hence U-Pb discordant ages are more common than concordant ages in geological studies. Fortunately, procedures have been devised to overcome these problems which are discussed in detail elsewhere (e.g. Faure and Mensing, 2005).

For U-Pb dating, the zircon grains were separated following the conventional heavy mineral separation methods (discussed in section 3.3.1) and were then mounted in epoxy resin. The grain mount was then photographed, cleaned and carbon coated. Cathodoluminescence (CL) imaging of the mounted zircon grains was carried out on a Philips XL30 Environmental Scanning Electron Microscope (XL30ESEM) to reveal any internal structures. The U-Pb age data were obtained by laser-ablation inductively coupled plasma-mass spectrometry (LA-ICPMS), a relatively modern microprobe technique, using a New Wave 213 aperture imaged frequency quintupled laser ablation system (213nm) coupled to an Agilent 750 quadrupole-based ICP–MS. Real time data were processed using GLITTER software and repeated measurements of external zircon standard PL (Svojtka et al., 2001; TIMS reference age 337.1±0.7 Ma) to correct for instrumental mass bias. CL imaging of zircons was used to guide ablation spot placement. Data were filtered using standard discordance tests with a 10% cut-off and corrected for common lead using the 206 method (e.g. Anderson, 2002).

Grains for analysis were selected randomly from all sizes and morphologies present in the sample mounts, except for avoidance of grains with visible fractures and inclusions. A significant bias in the age distribution of detrital zircons may occur if zircons are selected for analysis on the basis of size and/or optical characteristics (McLennan et al., 2001). Grains <50 μm in diameter were also avoided to ensure that each entire ablation pit was located within a single zircon grain. For each U-Pb and zircon FT dataset the principal detrital source age modes were extracted using the approach of Sambridge and Compston (1994), incorporating the method of Galbraith and Green (1990).

3.4 Geochemical Techniques

3.4.1 X-ray fluorescence (XRF) analysis

A total of 62 sandstone samples were collected for compositional determination using conventional XRF analysis from the Ainsa basin only (Table 3.2). Care was taken to avoid collecting weathered samples from outcrops. Samples were crushed to <1400 μm, avoiding weathered surfaces, and reduced to powder in an agate TEMA mill.

Bulk rock analyses of the major and most of the trace elements were determined by conventional XRF technique, using the Philips model PW1480 XRF spectrometer of the London University facility at Royal Holloway College.

Principally, this spectrometric technique utilises Bragg's law of X-ray diffraction in which the elements in a sample are caused to emit their characteristic X-rays. The excitation can be accomplished by several means such as bombardment of target by high-energy electrons or accelerated charged particles or by irradiation with X- rays. A diffracting crystal (or a set of crystals) diffracts (angular dispersion) the polychromatic X-ray fluorescent beam to resolve it into its component wavelengths and hence allows the sequential (or simultaneous with special arrangements) detection of characteristic X-ray emitted by the elements in the sample. In terms of Bragg's equation ($n\lambda = 2d \sin\theta$), the wavelength λ is detected for an assumed value of n (order of reflection, generally n=1), known value of d (dispersing crystal lattice spacing) and measured incidence angle θ.

Major elements were analysed on fused glass disks, prepared from 1.5-2 gm sample powder which were pre-ignited at 1,100 ^{0}C for 20 minutes to remove volatiles. Then the loss on ignition (LOI) was determined prior to major element analysis, so that major element results are reported on a volatile-free basis. Spectroflux 105 was used as flux while preparing the fused glass disks. The XRF was calibrated using 24 international standards largely from USGS and CRPG to ensure accuracy and the calibration was periodically monitored using 4 internal standards. Recommended values are from Govindaraju (1989) supplemented by isotope dilution data run at RHUL. Additionally, a synthetic CaO-SiO_2 standard was prepared to check concentrations up to 60% CaO, and concentrations were adjusted slightly using a quadratic relationship. The reproducibility of the major element data is <0.2% absolute. For trace element analysis, pressed pellets were made from ~7 gm of sample powder. Matrix corrections for the trace elements were calculated from the major element compositions. Drift, accuracy, and precision were monitored with the international standards. A few samples with low major oxide totals (<97%) were excluded from the final data set.

3.4.2 Stable isotope analysis

Forty-four samples of larger foraminifera were collected from locations throughout the Ainsa basin for a pilot study to determine their stable isotope (C and O) concentrations. The aim of this pilot study was to compare global open-ocean stable isotope curve with that derived from the foraminifera of the Ainsa basin. The collected foraminifera were washed with water and anhydrous sodium carbonate (Na_2CO_3), and dried overnight at room temperature. To reduce the effects of dissolution and secondary crystallisation on the stable isotope values, the foraminiferal individuals with cleaner external surfaces and none or minor calcite overgrowth on tests were selected. Specimens were initially examined under stereo-zoom microscope to obtain samples with minimum alteration. Few foraminifera samples were cut into thin section for identification. The tests of foraminifera were micro-drilled using MicroMill fitted with a LEICA GZ6T binocular stereo-zoom microscope, to obtain material from the inner test in order to avoid any surfacial weathering. Most of the drilled powder samples (26) were analysed by a VG Prism Series II isotope ratio mass spectrometer (fitted with Isocarb automated single acid bath analysis system) at the Stable Isotope Laboratories, Royal Holloway College. The rest of the samples were analysed at the Bloomsbury Environmental Isotope Facility of UCL by Delta V Advantage isotope ratio mass spectrometer connected with a Gas Bench. To evaluate external precision, NBS-19 and BDH (an in-house standard) were measured. Analytical precision ranges between 0.03 – 0.1‰ (1σ) for both $\delta^{13}C$ and $\delta^{18}O$ ratios and consistency of data between the two laboratories were checked by analysing few common samples.

3.4.3 Carbon analysis

Twenty seven sediment samples associated with foraminifera from the Ainsa basin were analysed for total organic carbon (TOC) and total carbon (TC) content, as a part of the pilot study mentioned above, using a LECO CS-200 Carbon and Sulphur Analyser at the Wolfson Laboratory (University College London). For TOC analyses, ~ 0.7 g of crushed sample was weighed in a sterilised standard LECO crucible and treated with 10 % hydrochloric acid to remove inorganic carbonates, then washed with distilled water and dried overnight at 50 ^{0}C. The dried samples, covered in iron

chip accelerator were combusted in the LECO induction furnace at 800 ^{0}C for ~10 minutes. The released CO_2, which was passed through purifying agents, were measured by the carbon detector unit of the LECO Analyser.

TC was determined in a similar way by analysing 0.15 - 0.25 g of crushed sample covered in iron chip accelerator and fed straight into the furnace without any pre-treatment. Total inorganic carbon was calculated from TOC and TC contents. The precision of the measurements are ±3.1%.

Table 3.4: Summary of laboratory techniques used in the research.

Technique	Raw material	Outcome
Modal analysis	Rock sample (thin section)	Detailed petrography (e.g., mineral abundance, textural relationship)
Fission Track chronometry	Zircon grain	Age (exhumation)
U-Pb dating	Zircon grain	Age (zircon formation)
XRF	Rock sample (powder)	Major and trace element compositions
Stable isotope analysis	Foraminifera	Stable isotope ratio of C and O (δ^{13}C and δ^{18}O)
Carbon analysis	Marl sample	Total organic carbon and total carbon contents

CHAPTER 4

Petrography of the Ainsa and Jaca basins

4.1 Introduction

Sandstone composition is influenced by the character of the sediment provenance, the nature of the sedimentary processes within a depositional basin, and the nature of the sediment dispersal pathways that link the sediment source (provenance) to deposition in the receiving basin. Petrographic studies are essential to any understanding and interpretation of sediment provenance, tectonic setting, hydrodynamically-controlled and diagenetically-influenced sediment composition associated with sediment transport and deposition, and likely stratigraphic correlations in clastic sediments (Hiscott, 1978; Ingersoll, 1978, 1990; Dickinson and Suczek, 1979; Dickinson, 1985; Valloni, 1985; Zuffa, 1985, 1987, 1991; Pettijohn et al., 1987; Underwood et al., 1993, 1995; Uddin and Lundberg, 1998; Marchesini et al., 2000; Underwood and Hoke, 2000; Ryu, 2003; Weltje and von Eynatten, 2004; Yuste et al., 2004).

The petrographic study of sandstones from the Ainsa and Jaca basins and the modal analyses data show compositional variability of the clastic systems. One-hundred and fifty-seven thin sections were analysed with comprehensive details. The sandstones are composed of framework grains, matrix and authigenic cements. Many of the sandstones have significant carbonate content in their framework grains and as cements. Framework grains are the dominant component followed by cements and matrix. In total, 51 petrographic classes (Table 4.1) were recognised for the purpose of point counting, referring to framework grains (48 classes) and matrix / cement (3 classes). The framework grains of the sandstones are divided into four principal categories having different genetic and compositional significance, adopting the criteria of Zuffa (1980): (i) non-carbonate extrabasinal; (ii) carbonate extrabasinal; (iii) non-carbonate intrabasinal; and (iv) carbonate intrabasinal.

Table 4.1: Key to counted petrographic classes and recalculated parameters.

NCE (Non -Carbonate Extrabasinal)

- **Q**
  - Monocrystalline quartz (non-undulatory); Qmnu
  - Monocrystalline quartz (undulatory); Qmu
  - Polycrystalline quartz (unstrained); Qpnu
  - Polycrystalline quartz (strained); Qpu
  - Polycrystalline quartz with 2-3 crystal units per grain; Qp2–3
  - Polycrystalline quartz with >3 crystal units per grain; Qp>3
  - Quartz in sedimentary rock fragment
  - Quartz in metamorphic rock fragment
  - Quartz in plutonic rock fragment
  - Carbonate replacement of quartz; CQ
- **P**
  - Plagioclase
  - Plagioclase in sedimentary rock fragment
  - Plagioclase in metamorphic rock fragment
  - Plagioclase in plutonic rock fragment
  - Carbonate replacement of Plagioclase; CP
- **K**
  - K-feldspar
  - K-feldspar in sedimentary rock fragment
  - K-feldspar in metamorphic rock fragment
  - K-feldspar in plutonic rock fragment
  - Carbonate replacement of K-feldspar; CK
- **L**
  - Shale
  - Siltstone
  - Sandstone
  - Chert
  - Low-grade metamorphic lithic fragment
  - Volcanic lithic fragment
  - Carbonate replacement of fine lithics; CL
- **M**
  - Muscovite
  - Biotite
  - Chlorite
  - Micas and chlorites in rock fragments
- Other minerals

CE (Carbonate Extrabasinal)

- Dolostone and Limestone
- Dolomitic limestone
- Micritic limestone
- Sparitic limestone
- Fossil

NCI (Non-Carbonate Intrabasinal)

- Iron oxides
- Glauconite

CI (Carbonate Intrabasinal)

- Intraclast
- Oolite
- Peloid
- Bioclasts

Lc

- Limeclast

Calcite
Alterites
Carbonate replacement of undetermined grains; CX
Indeterminate

Carbonate cement
Silica cement
Matrix

4.2 Framework grains

4.2.1 Non-Carbonate Extrabasinal (NCE)

Quartz (Q), feldspars (F), fine-grained lithics (L) and phyllosilicates constitutes the NCE group. Quartz occurs as monocrystalline and fine- to coarse-grained polycrystalline grains (Figs. 4.1A and B). Undulose and non-undulose varieties are present among both types of quartz. Monomineralic quartz grains are monocrystalline non-undulatory (Qmnu), monocrystalline undulatory (Qmu), and the polycrystalline varieties are Qp2-3 (2-3 crystal units per grain) and Qp>3 (>3 crystal units per grain), following the criteria of Basu et al. (1975) (Figs. 4.1A and B). Qmnu is the most abundant quartz type, commonly constituting more than 50% of total quartz grains. K-feldspar and plagioclase are subordinate, and generally do not exceed 25% of the total detrital components. Both feldspars are also present in coarse-grained rock fragments. Sericitization and calcite replacement are present in all the analyzed samples. Muscovites and biotites represent the majority of the phyllosilicates, whereas chlorite is quite rare. Non-carbonate lithic fragments (L) are fine-grained (< 0.062 mm), and include sedimentary rock fragments (Fig. 4.1D), low-grade metamorphic rock fragments represented by quartz-mica phyllites (Fig. 4.1E) and volcanic rock fragments (Fig. 4.1F). Sedimentary rock fragments include shales, siltstones and chert. Among these lithic fragments, sedimentary rock fragments are most common. In rare occurrences heavy minerals like zircon and apatite were observed in thin-section. Carbonate replacements of feldspars, quartz and lithics were also included in these groups (Table 4.1).

4.2.2 Non-Carbonate Intrabasinal (NCI)

NCI grains are present in very small proportions, ranging from 0.5 to 10%. They mainly comprise pellets of iron oxides and, rarely, of glauconites (Figs. 4.1G and H).

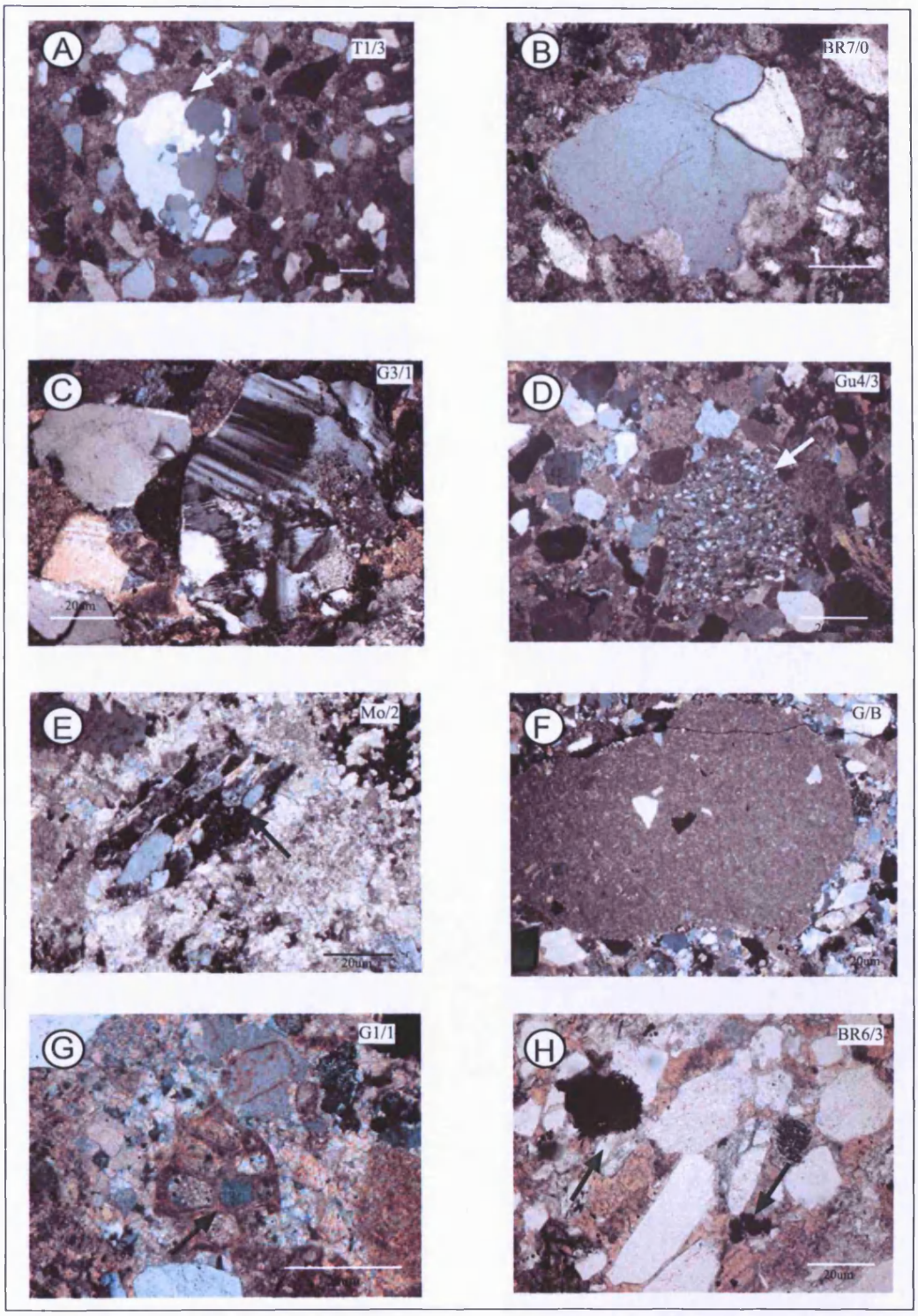

Figure 4.1: Thin-section photomicrographs showing different non-carbonate extrabasinal (NCE) and intrabasinal (NCI) grains from the Ainsa and Jaca basins arenites. The scale bar is 20 micron. (A) Polycrystalline quartz, pointed by arrow, with >3 crystal units (Qp>3) and several monocrystalline quartz; NCE, crossed polar. (B) Polycrystalline quartz with 2 crystal units (Qp2-3); NCE, crossed polar. (C) A coarse plagioclase feldspar, right; NCE, crossed polar. (D) Sedimentary (sandstone) rock fragment; NCE, crossed polar. (E) Low-grade metamorphic (quartz-mica phyllite) rock fragment; NCE, crossed polar. (F) Volcanic rock fragment; NCE, crossed polar. (G) A bioclast cavity filled with glauconite; NCI, crossed polar (thin-section stained for calcite). (H) Pellets of opaque (iron oxide); NCI, plane polar.

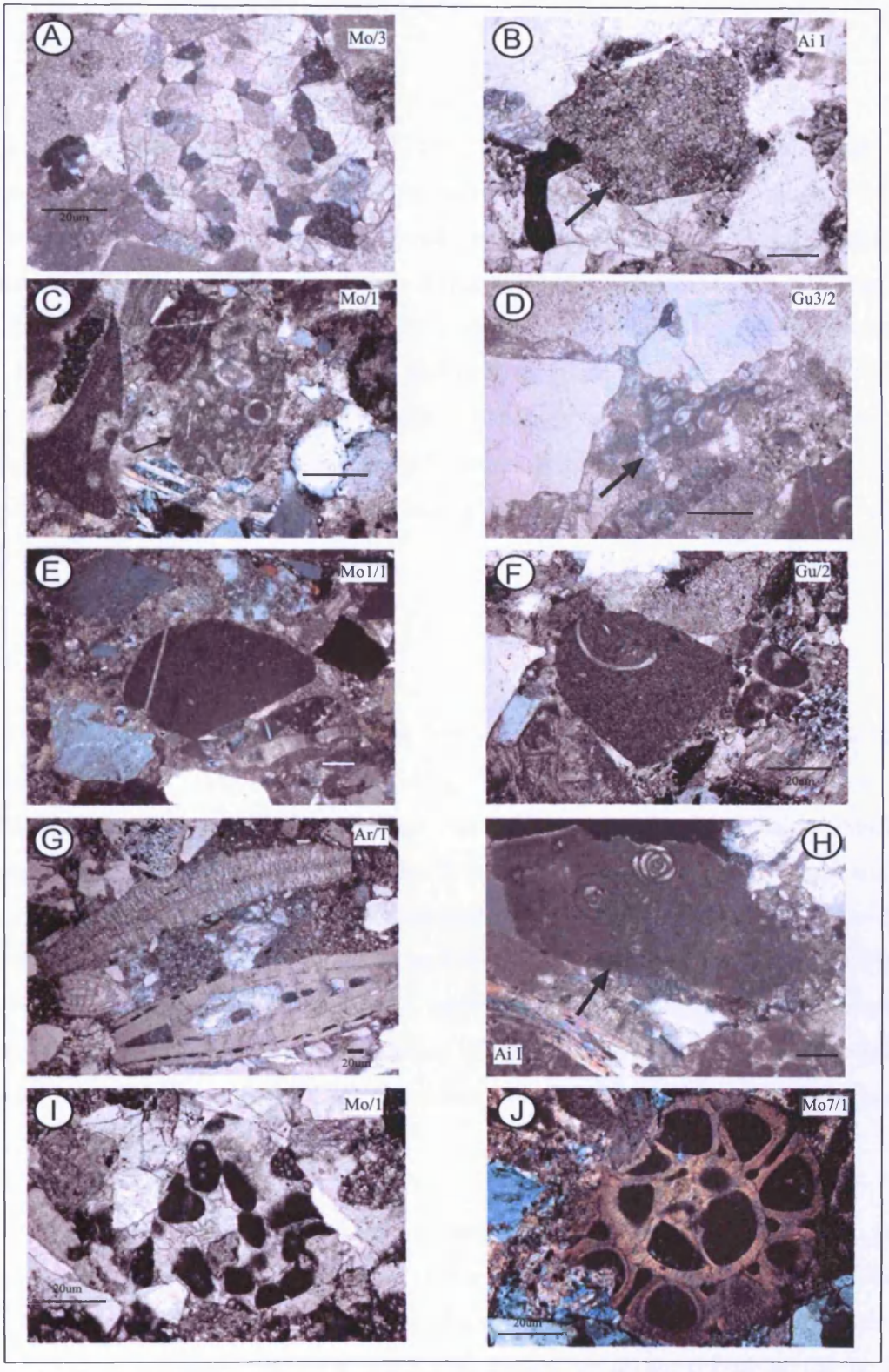

Figure 4.2: Thin-section photomicrographs showing different carbonate extrabasinal (CE) and intrabasinal (CI) grains from the Ainsa and Jaca basins arenites. The scale bar is 20ìm. (A) Coarse-grained dolostone; CE, crossed polar. (B) Fine-grained dolostone; CE, plane polar. (C) and (D) Micritic limestone with Late Cretaceous Pithonellid tests (arrowed); CE, crossed polar. (E) Micritic limestone showing good roundness and an internal vein; CE, crossed polar. (F) Rounded micritic limestone clast containing a shell fragment; CE, crossed polar. (G) Single bioclasts of Eocene larger foraminifera (*Nummulites*, lower and *Discocyclina*, upper); CI, plane polar. (H) Micritic limestone clast with irregular contour, soft appearance and containing Miliolid foraminifera; CI, crossed polar. (I) Sparitic limestone clast (arrowed) containing peloids (pelsparite); CI, plane polar. (J) Bioclast cavities filled with micrites; CI, crossed polar (thin-section stained for calcite).

4.2.3 Carbonate Extrabasinal (CE)

This component ranges from 1.5 to 25% of the bulk rock and comprises fine- to coarse-grained dolostones (Figs. 4.2A and B), single detrital dolomite crystals, reworked micritic, fossiliferous, limestones with Pithonellid tests (Figs. 4.2C and D), and micritic, microsparitic limestones displaying textural evidence of a terrigenous origin (Figs. 4.2E and F). The extrabasinal grains exhibit a high degree of roundness, a lithified appearance, internal veins, and oxidised grain boundaries (also see Table 3.2). Pithonellids, present within some micritic limestone clasts, are a group of pelagic calcispheres that reached their acme simultaneously worldwide in late Albian- Coniacian times and progressively declined in post-Coniacian times (see Dias-Brito, 2000)

4.2.4 Carbonate Intrabasinal (CI)

These constituents range from 0.2 to 40% of the bulk rock, and comprise mainly single bioclasts (Fig. 4.2G), including Eocene larger foraminifera, such as *Nummulites, Alveolina*, *Discocyclina,* and bioclasts of other shallow-marine organisms like miliolids and textularian foraminifera, echinoderms, bivalve (mainly oyster) shells, algal grains, and indeterminate shell fragments. Additionally, the CI category includes intraclasts, peloids and oolites (Figs. 4.2H, I and J), all showing evidence of an intrabasinal origin, e.g., having a soft appearance, irregular contours, elongated and/or platy shape, an absence of internal veins or recrystalised particles (also see Table 1 of Zuffa, 1985). In some samples, Eocene bioclasts were found within the intraclasts.

There are some other varieties of framework grains, which do not fit into any of the four categories described above (Table 4.1). Those grains are: single crystals of calcite, patchy calcite, fully-altered grains ("alterites"), carbonate replacement of unknown grains and carbonate clasts that cannot be distinguished as CE or CI ("limeclasts"). However, single calcite crystals and patchy calcite are not very common. Corrections for the limeclasts and calcite replacement (Section 4.8) have been applied for the interpretation of the petrographic data. In addition to the petrographic classes discussed above, some other classes are used to evaluate matrix

and cements (carbonate, quartz and Fe-oxide). Matrix is almost negligible. Carbonate cement is present among all samples, ranging from 1% to 5% of the total rock volume. Silica cement, in the form of overgrowth, is rare and Fe-oxide cements are almost negligible.

Table 4.2 shows the complete point-count data. Table 4.3 lists the statistical comparisons between the various sandy systems in the Ainsa and Jaca basins, based on widely used univariate statistical methods. Employing univariate methods for a multivariate compositional dataset is inappropriate in a strict sense (Weltje, 2002, 2006). In this context, compositional data are those which contain relative information only, or in other words, they are parts of some whole. Generally compositional data are recorded as statistically closed data, i.e. data summing to a constant such as 100%. They are always positive and range from 0 to 100 (or any other constant), when given in closed form. Such data are widespread in the geosciences discipline and include classical whole rock-geochemical and petrography modal analyses data.

Standard statistical techniques, in contrast, are designed to be used with data that are free to range from $-\infty$ to $+\infty$. However, these statistical techniques may give apparently interpretable results which are at best approximations (Pawlowsky-Glahn and Egozcue, 2006; Weltje, 2006) and need to be treated with considerable amount of non-statistical (e.g., geological) evidences while interpreting. As the goal of the petrographic analyses in this research is to compare the results both with published petrographic data from the Ainsa and Jaca basins (Fontana et al., 1989) and the vast literature on petrographic studies of sandstones (e.g., Hiscott, 1978; Ingersoll, 1978, 1990; Dickinson and Suczek, 1979; Dickinson, 1985; Valloni, 1985; Zuffa, 1985, 1987, 1991; Pettijohn et al., 1987; Underwood et al., 1993, 1995; Uddin and Lundberg, 1998; Marchesini et al., 2000; Underwood and Hoke, 2000), and in common with these researchers, univariate statistical methods were used. It is beyond the scope of this research to investigate multivariate statistical analyses on those vast amounts of original compositional data reported by previous researchers.

Table 4.2: Synthesis of modal point-count data of arenites from the Ainsa and Jaca basins. See Table 4.1 for explanation of abbreviations.

		Quartz; Q							Feldspars; F					Lithic fragments; L					CE	CI			NCI					
Sample No.:	Loc.	Qmnu	Qmu	CQ	Qpnu	Qpu	Qp2-3	Qp>3	Plag	CP	K-spar	CK	M	Sed	Chert	Met.	Volc.	CL	CE	CI grains	Bioc-last	Lc	Iron oxide	Glauc-onite	Other mineral	Indeter-minate	Alter-ites	CX	Calcite (single +patchy)
Fosado System																													
F2/2	1	25.2	2.5	0.5	6.7	6.7	5.0	8.5	1.8	0.3	17.8	0.8	2.7	13.3	0.8	0.0	0.0	0.2	5.5	2.0	0.0	2.5	4.8	0.0	0.0	0.8	0.3	2.5	2.5
F2/3	1	23.8	2.8	0.0	11.7	9.2	7.8	13.3	1.7	0.0	12.2	0.0	0.2	18.2	0.0	0.0	0.0	0.2	3.2	1.8	0.0	3.5	3.8	0.0	1.0	0.5	1.3	1.8	3.3
F2/4	1	26.7	1.5	0.0	13.5	10.0	8.8	14.8	3.2	0.0	13.7	0.0	3.7	15.0	0.2	0.0	0.0	0.2	1.5	1.2	0.0	2.5	2.5	0.0	0.7	0.0	0.0	1.5	2.0
F2/5	1	28.5	4.5	0.0	7.0	5.5	4.8	7.5	2.3	0.8	14.5	0.0	4.2	20.5	0.7	0.0	0.0	0.2	0.2	1.7	0.0	2.5	3.7	0.0	0.0	0.0	0.0	0.5	2.5
F2/6	1	26.0	1.5	0.3	13.5	8.7	7.5	14.8	3.2	0.0	18.7	0.0	2.7	12.8	0.8	0.0	0.0	0.0	0.7	0.3	0.0	1.3	3.3	0.0	1.0	0.0	0.3	3.0	2.0
F2/7	1	37.7	2.5	0.5	6.7	6.7	6.8	6.8	1.3	0.3	12.7	0.0	4.5	11.7	1.0	0.0	0.0	0.0	1.5	0.5	0.0	1.0	6.5	0.0	0.3	0.3	0.0	2.5	1.8
Arro System																													
Ar/B	6	25.8	4.8	1.0	11.0	2.5	6.0	7.5	2.8	1.8	10.0	1.2	4.7	8.7	0.5	0.0	0.0	0.2	3.7	2.5	3.0	3.2	2.8	0.0	0.0	0.3	0.8	5.0	3.8
Ar/M	6	17.2	1.3	0.8	4.5	3.5	3.3	4.8	1.0	0.2	5.2	2.0	0.7	7.2	0.5	0.3	0.0	0.8	3.2	2.0	37.7	0.7	3.3	0.0	0.0	0.5	0.5	4.3	2.5
Ar/T	6	25.5	2.0	0.7	6.2	5.0	6.0	5.3	2.7	0.0	12.3	0.3	0.2	9.5	0.0	0.0	0.0	0.7	8.7	2.2	14.0	2.5	2.3	0.0	0.0	0.2	1.0	3.8	0.0
Ar6/1	2	27.5	4.7	1.5	2.7	3.0	2.8	3.0	2.8	0.8	9.7	0.5	3.2	12.7	1.5	0.0	0.0	1.2	3.0	2.0	0.2	5.2	5.0	0.0	0.0	0.0	2.0	7.8	2.8
Ar7/1	4	28.0	1.7	3.0	8.7	2.2	5.8	5.3	2.5	1.0	8.8	1.3	0.5	4.5	0.2	0.0	0.0	0.2	2.5	1.8	20.2	4.3	1.8	0.0	0.0	0.3	0.3	4.3	2.0
Ar7/2	4	22.8	2.3	0.5	6.7	2.0	5.8	3.0	3.2	0.0	11.3	1.8	0.2	7.8	0.3	0.3	0.0	0.8	2.5	0.0	28.7	2.0	1.0	0.0	0.0	0.0	0.3	4.5	1.3
Ar7/3	4	23.0	2.5	1.0	8.2	3.2	4.0	7.5	1.5	0.0	9.0	0.7	0.2	13.5	0.0	0.3	0.0	0.8	1.5	1.5	24.5	1.0	4.3	0.0	0.0	0.5	0.3	1.3	1.3
Ar9/1	4	39.8	1.3	0.0	4.0	2.0	3.3	2.8	2.0	0.0	15.5	0.0	3.0	4.5	0.2	0.0	0.0	0.2	1.2	3.5	3.0	3.2	1.8	0.0	0.0	0.5	1.3	8.8	4.5
Ar9/2	4	37.0	1.0	0.0	15.3	3.3	6.7	12.0	6.0	0.0	15.7	0.3	2.0	7.0	0.3	0.0	0.0	0.6	1.0	2.0	0.6	2.0	1.0	0.0	1.0	0.0	0.6	2.3	0.6
Ar9/3	4	29.3	0.8	0.0	15.0	5.2	6.3	14.0	2.5	0.0	11.2	0.0	1.2	9.0	1.2	0.2	0.0	0.0	1.0	0.8	9.7	2.3	2.3	0.0	0.0	0.0	0.3	4.5	3.5
AR10/B	7	39.7	3.0	0.0	8.0	1.2	5.0	4.3	4.5	1.2	13.3	0.8	0.5	7.5	0.7	0.0	0.0	0.5	0.0	0.5	4.7	3.0	1.0	0.0	1.0	0.0	0.5	6.7	1.5
AR11/2	7	34.2	1.5	0.0	5.0	2.5	4.5	3.0	2.3	1.8	15.5	1.5	1.0	8.2	0.5	0.0	0.0	0.2	1.5	2.0	5.0	5.0	2.0	0.0	0.2	0.0	1.5	5.5	3.0
AR12/1	6	29.0	1.5	0.0	16.2	5.2	10.8	10.8	7.0	0.0	14.3	0.3	1.5	6.7	0.0	0.0	0.0	0.7	1.5	1.8	3.0	2.8	0.3	0.0	0.8	0.3	0.5	4.5	2.3
AR12/2	6	27.2	0.5	0.0	3.0	4.7	3.0	5.0	3.5	1.0	16.8	0.3	4.0	13.5	1.0	0.0	0.0	0.0	0.5	3.0	8.2	2.0	2.5	0.0	0.0	0.0	1.3	4.3	2.8
AR12/3	6	23.2	2.5	0.0	12.7	7.7	7.5	13.0	5.3	0.3	16.0	0.5	0.7	5.0	0.7	0.0	0.0	0.5	1.5	3.0	6.0	2.7	2.5	0.0	0.0	0.0	0.8	5.8	2.5
AR13/1	6	23.0	1.0	0.0	5.0	2.0	2.6	4.0	3.3	0.0	7.3	0.0	1.0	14.3	0.0	0.0	0.0	0.0	0.6	4.3	29.6	1.7	1.7	0.0	0.0	0.0	0.3	4.0	0.6
AR13/2	6	35.2	2.0	0.0	6.0	3.0	4.8	4.3	2.5	0.0	17.3	0.8	2.2	7.2	1.0	0.3	0.0	0.3	1.0	2.8	2.5	2.8	1.5	0.0	0.5	0.0	1.0	5.8	4.5
AR13/3	6	19.0	0.6	0.0	2.3	1.3	2.3	1.3	2.3	0.3	8.7	0.3	0.3	4.7	0.3	0.0	0.0	0.3	0.3	0.3	49.0	3.0	1.0	0.0	0.0	0.0	1.3	3.7	0.6
Gerbe System																													
G/T	10	21.5	3.2	0.5	8.2	8.5	3.8	13.0	1.0	0.0	20.7	0.0	0.5	7.3	2.3	0.5	0.8	1.0	2.5	1.5	2.2	0.0	2.3	0.0	0.3	0.3	0.8	4.5	9.8
G/B	10	38.0	8.0	0.2	6.7	9.5	2.8	13.5	1.2	0.0	15.0	0.5	0.5	2.8	3.3	0.0	0.5	1.0	1.7	0.2	0.0	0.5	2.5	0.0	0.5	0.0	1.8	4.3	1.3
G1/2	8	29.2	2.0	1.0	7.5	6.7	4.5	9.8	0.5	0.0	17.0	0.7	1.5	14.8	1.8	0.3	0.0	0.3	3.0	0.3	0.2	2.8	3.5	0.0	0.0	0.0	0.8	4.0	2.3
G1/3	8	33.3	1.8	0.0	7.5	6.2	4.8	8.8	2.5	0.0	20.2	0.0	0.7	11.2	1.0	0.0	0.0	0.2	2.0	1.5	0.5	3.2	2.8	0.0	0.3	0.0	0.8	2.3	2.0
G5/1	10	28.8	2.8	0.0	9.2	8.5	5.0	13.0	1.0	0.0	19.5	1.0	2.7	9.8	2.3	0.0	0.0	0.0	1.2	0.8	0.0	3.8	4.5	0.0	0.0	0.0	1.0	2.0	1.3
G5/2	10	33.0	0.2	0.0	11.2	7.0	9.3	8.5	1.0	0.0	21.5	0.0	4.0	9.0	0.5	0.0	0.0	0.2	1.5	1.0	0.0	2.5	2.0	0.0	0.5	0.0	0.3	3.3	1.3
G4/1	10	34.2	1.5	0.0	13.0	8.0	7.8	13.3	1.2	0.0	19.8	0.3	2.7	5.7	1.0	0.0	0.0	0.7	2.0	0.0	0.0	1.7	1.0	0.0	1.3	0.3	0.0	4.3	1.3
G4/2	10	26.0	1.2	0.0	13.5	12.0	10.3	15.0	1.8	0.3	24.2	0.5	2.2	6.8	0.8	0.0	0.0	0.0	1.7	0.7	0.0	2.5	1.8	0.0	0.0	0.5	0.8	1.8	1.0
G4/3	10	27.7	0.5	0.0	12.5	5.5	8.5	9.0	1.5	0.0	22.8	0.3	1.5	5.5	1.7	0.0	0.0	0.5	2.0	0.0	0.0	4.5	6.0	0.0	0.5	0.3	0.0	4.8	2.0
G3/2	9	26.0	1.5	0.0	9.5	11.0	8.8	12.0	1.7	0.0	20.2	0.5	3.0	11.5	0.5	0.0	0.0	0.5	3.2	0.5	0.0	4.2	0.8	0.0	1.0	0.5	0.3	2.8	0.8

		Quartz; Q							Feldspars; F					Lithic fragments; L						CE	CI			NCI					
Sample No.:	Loc.	Qmnu	Qmu	CQ	Qpnu	Qpu	Qp2-3	Qp>3	Plag	CP	K-spar	CK	M	Sed	Chert	Met.	Volc.	CL	CE	CI grains	Bioc-last	Lc	Iron oxide	Glauc-onite	Other mineral	Indeter-minate	Alter-ites	CX	Calcite (single +patchy)
G3/3	9	35.0	1.7	0.0	9.0	8.7	3.5	14.5	3.2	0.0	13.0	0.0	1.2	10.3	1.8	0.0	0.0	0.0	1.5	0.7	0.0	3.0	1.3	0.0	0.0	0.3	3.0	3.5	2.8
G3/4	9	26.2	1.0	0.5	11.5	8.2	6.0	12.5	1.3	0.3	15.7	0.0	2.5	10.0	1.5	0.0	0.0	1.0	2.2	0.8	0.0	6.3	1.0	0.0	1.3	0.5	1.3	4.5	2.5
Banaston System																													
B-G1/1	8	16.7	1.5	0.0	9.5	9.2	2.8	16.0	1.0	0.2	9.5	0.0	1.2	11.5	10.0	0.0	0.0	0.0	1.5	9.5	9.7	4.7	1.0	0.5	0.0	0.5	0.5	0.8	0.8
B/2	14	30.5	3.0	0.5	5.5	5.2	3.3	7.5	2.2	0.0	13.7	0.0	0.5	11.0	2.0	0.8	0.0	1.5	2.7	3.5	3.7	2.0	0.8	0.0	0.0	0.5	1.5	6.0	2.8
B*/II	15	16.3	0.8	0.5	2.0	1.2	1.3	2.0	1.0	0.0	7.7	0.0	0.2	16.7	1.0	0.0	0.0	0.5	2.0	4.0	32.2	1.2	3.5	0.0	0.0	0.5	0.5	3.5	4.5
B*/3	15	18.5	3.0	0.0	4.2	1.7	2.0	4.0	0.2	0.0	7.5	0.2	0.2	19.0	0.5	0.0	0.0	0.0	3.2	2.2	28.7	0.0	1.3	0.0	0.0	0.5	0.8	5.8	2.3
B1/1	11	29.5	3.2	1.0	6.5	4.2	5.0	5.8	0.8	0.3	10.5	0.0	2.7	11.8	1.3	0.0	0.0	0.0	3.5	3.3	0.2	3.3	4.3	0.3	0.0	0.0	0.3	11.0	2.3
B1/3	11	29.8	2.5	1.3	5.0	7.5	4.3	8.3	1.3	0.3	15.0	2.0	0.7	5.0	2.2	0.0	0.0	1.0	3.0	2.7	5.7	4.5	0.8	0.0	0.0	0.3	1.3	7.0	1.3
B1/4	11	25.3	3.0	1.3	7.5	6.7	6.5	8.0	2.2	0.5	10.7	0.5	1.0	7.3	2.8	0.5	0.0	0.5	0.7	1.8	17.0	2.3	0.3	0.0	0.0	0.3	0.0	5.8	2.3
B2/1	13	43.0	2.0	0.2	5.0	3.5	3.8	5.0	0.5	0.0	5.5	0.0	2.0	10.2	0.0	0.0	0.0	0.2	0.5	0.5	3.7	2.0	9.0	0.0	0.3	0.3	0.5	10.5	0.5
B2/2	13	34.8	1.8	0.3	4.7	2.5	4.5	2.8	1.0	0.2	14.0	0.7	1.0	8.0	0.5	0.0	0.0	0.2	1.2	3.8	3.7	3.8	3.5	0.0	0.3	0.3	0.5	10.3	3.0
B2/3	13	14.0	0.2	0.0	6.0	3.0	3.8	5.5	2.0	0.0	6.7	0.0	0.2	17.0	1.0	0.0	0.0	0.0	7.2	2.0	30.0	3.2	0.5	0.0	0.0	0.5	0.0	4.8	1.3
B3/1	11	33.7	2.0	0.5	9.5	7.2	5.2	11.5	1.7	0.0	11.0	0.2	3.2	5.7	1.5	0.0	0.0	1.2	1.2	4.3	2.5	2.8	1.0	0.0	0.0	0.0	1.3	5.8	3.5
B3/2	11	28.0	1.5	0.0	9.2	9.2	6.3	12.5	2.0	0.0	20.5	0.0	1.0	5.8	0.8	0.2	0.0	0.5	4.5	3.5	0.7	4.0	0.5	0.3	0.0	0.5	0.0	5.0	2.3
B3/3	11	25.0	0.2	0.0	7.2	7.7	5.8	9.5	1.2	0.0	15.5	0.2	0.7	10.5	3.5	0.3	0.0	0.3	7.0	2.2	7.5	3.5	0.8	0.0	0.5	0.5	0.3	4.5	0.8
B4/1	12	28.5	2.5	0.2	14.7	10.2	8.3	16.8	4.2	0.0	18.0	0.0	1.5	3.3	2.3	0.2	0.0	0.5	2.7	1.7	0.5	2.0	0.3	0.0	0.0	0.0	0.3	5.0	1.3
B4/2	12	24.2	1.5	0.0	17.0	5.0	7.5	14.3	4.7	0.0	23.5	0.2	0.7	5.0	2.7	0.2	0.0	0.0	2.0	3.2	1.7	1.5	0.8	0.0	2.0	0.5	0.0	2.5	0.8
B4/3	12	22.5	2.2	0.0	13.0	7.0	6.5	13.5	2.7	0.5	17.0	0.2	0.0	6.0	3.0	0.2	0.0	0.5	3.2	6.3	1.2	8.3	0.8	0.0	0.5	0.0	0.8	3.5	0.5
B5/1	12	38.7	1.5	0.0	4.2	5.0	2.5	6.5	3.0	0.0	12.8	0.3	2.2	3.7	1.0	0.7	0.0	2.0	4.2	3.8	2.2	4.8	1.0	0.0	0.3	0.0	0.0	5.5	3.0
B5/2	12	27.2	1.0	0.0	5.0	5.0	2.5	7.5	0.7	0.0	11.3	0.3	1.0	5.0	2.7	1.5	0.0	1.0	11.2	7.5	1.2	7.5	0.0	0.5	0.0	0.5	1.5	7.5	0.7
B6/1	14	33.5	0.7	0.0	6.0	5.7	5.0	6.8	0.5	0.0	14.0	0.0	2.2	3.0	1.0	0.0	0.0	0.2	2.7	7.3	0.7	7.8	1.5	0.0	1.0	0.0	0.0	6.8	5.3
B6/2	14	38.5	1.0	0.0	4.0	3.5	2.8	4.5	1.2	0.0	14.0	0.0	5.0	5.5	0.0	0.0	0.0	0.7	3.0	4.3	0.5	5.8	3.3	0.0	1.3	0.0	0.0	3.5	5.0
B6/3	14	33.8	2.3	0.0	9.2	5.0	7.8	6.5	0.7	0.0	18.0	0.0	0.5	7.7	1.0	0.2	0.0	0.5	0.7	8.3	2.2	3.3	1.0	0.0	0.0	0.3	0.3	4.0	1.0
B6/4	14	30.8	0.8	0.0	7.7	4.7	4.3	8.3	0.7	0.0	14.8	0.3	0.2	3.5	1.0	0.0	0.0	0.2	4.0	8.0	1.7	8.2	2.8	0.0	0.5	0.3	0.3	5.3	4.3
B7/1	14	34.2	2.0	0.0	8.2	6.7	6.5	8.5	1.0	0.0	16.7	0.0	1.5	3.0	0.5	0.0	0.0	0.0	0.5	5.0	1.7	8.5	1.0	0.0	0.8	0.0	1.0	5.3	2.3
B7/2	14	32.8	1.8	0.3	13.2	4.7	7.3	10.8	1.5	0.0	11.5	0.0	0.7	3.2	1.0	0.0	0.0	0.2	1.5	7.0	6.2	5.5	0.5	0.3	0.3	0.0	0.5	5.0	2.3
Ainsa System																													
Ai I/1	20	29.5	3.5	0.0	5.5	2.0	4.8	2.5	4.2	0.0	17.8	1.8	1.2	15.7	1.0	0.0	0.0	0.7	1.5	2.0	0.5	0.2	3.3	0.0	0.0	0.0	1.3	7.0	1.3
Ai I/3	20	27.7	2.0	0.0	14.2	7.0	12.0	9.3	3.5	0.0	11.0	0.0	2.2	10.3	1.3	0.5	0.2	0.0	5.3	10.0	1.3	2.3	1.0	0.0	0.0	0.3	0.0	0.0	0.0
Ai III/1	15	36.5	3.5	0.0	5.2	3.5	4.0	4.8	2.5	0.0	13.7	0.0	2.2	11.7	1.0	0.0	0.2	0.0	5.0	4.8	0.3	6.5	2.8	0.0	0.0	0.3	0.3	0.0	0.0
Ai III/2	15	35.2	3.2	0.0	3.5	2.7	2.8	3.5	2.0	0.0	9.0	0.0	1.5	14.2	0.5	0.2	1.0	0.0	5.3	17.3	0.5	0.0	2.8	0.0	0.0	0.0	0.3	0.0	0.0
Ai I	16	20.8	4.3	2.5	12.7	5.0	8.0	9.8	2.2	0.5	9.0	1.8	2.0	10.5	1.5	0.3	0.5	1.3	16.5	1.5	3.0	0.5	0.5	0.0	0.0	0.0	1.0	2.3	0.0
Ai3/2	15	24.2	1.5	0.0	6.0	2.5	4.3	3.0	3.5	0.0	18.5	0.0	1.2	3.0	1.5	0.0	0.0	1.0	3.7	5.2	11.0	4.5	1.3	0.3	0.3	0.0	0.5	8.3	2.0
Ai3/3	15	30.8	4.3	0.0	4.0	5.0	3.8	5.0	4.7	0.0	13.2	0.0	1.2	5.5	1.0	0.5	0.0	0.5	2.7	3.5	0.5	6.2	2.3	0.0	0.5	0.0	0.5	9.5	3.5
Ai3/4	15	28.3	2.8	0.0	8.2	4.7	6.5	6.5	2.5	0.2	12.7	0.0	4.2	12.8	1.3	0.0	0.0	0.2	1.7	3.0	1.0	3.7	1.0	0.0	0.5	0.0	0.5	8.8	1.8
AiIII 2/1	15	24.3	2.3	0.0	3.5	3.0	3.3	3.0	3.0	0.0	14.2	0.0	0.5	7.3	0.8	0.0	0.0	0.5	5.7	5.5	2.5	9.7	0.8	0.0	1.0	0.0	1.0	8.0	6.5
AiIII 2/2	15	25.2	1.0	0.0	5.0	3.0	5.5	2.5	5.2	0.0	14.5	0.0	1.0	6.8	1.8	0.3	0.0	0.8	2.7	6.3	4.5	9.8	1.5	0.0	0.2	0.0	0.5	7.5	2.5

		Quartz; Q							Feldspars; F					Lithic fragments; L						CE	CI			NCI					
Sample No.:	Loc.	Qmnu	Qmu	CQ	Qpnu	Qpu	Qp2-3	Qp>3	Plag	CP	K-spar	CK	M	Sed	Chert	Met.	Volc.	CL	CE	CI grains	Bioc-last	Lc	Iron oxide	Glauc-onite	Other mineral	Indeter-minate	Alter-ites	CX	Calcite (single +patchy)
Ainsa	16	23.3	3.3	0.0	1.2	4.2	8.8	6.8	3.2	0.0	15.5	0.0	0.7	9.8	1.8	0.0	0.0	0.0	5.5	5.3	4.7	5.8	1.0	0.0	0.0	0.0	0.2	2.5	2.0
A2/42(2)	core	23.3	1.3	0.0	10.2	4.5	7.8	7.0	7.2	0.0	11.0	0.0	2.2	11.3	0.8	0.0	0.0	0.5	6.7	1.5	2.2	7.0	1.3	0.0	0.0	0.3	1.5	4.5	2.7
A2/39	core	16.2	2.5	0.0	3.7	3.2	3.8	3.3	2.7	0.0	5.5	0.0	0.7	20.5	2.2	0.0	0.0	0.5	6.0	3.3	15.0	7.3	1.8	0.0	0.0	0.0	2.8	4.5	1.3
A2/33	core	22.5	2.3	0.0	9.2	6.0	7.8	7.5	5.0	0.0	10.2	0.0	1.7	13.3	0.8	0.0	0.0	1.2	1.2	4.3	0.7	10.5	2.8	0.0	0.0	0.0	0.3	5.5	2.5
A2/30	core	23.2	2.5	0.0	8.2	3.7	4.5	7.5	3.5	0.0	7.5	0.0	1.5	13.5	1.0	0.0	0.0	1.0	4.2	3.5	7.5	6.0	1.8	0.0	0.0	0.0	1.0	6.3	4.0
A2/28	core	29.0	1.2	0.0	8.2	3.5	4.8	7.0	3.5	0.2	9.0	0.0	1.0	12.2	1.0	0.0	0.0	0.0	6.2	4.8	3.8	6.3	1.3	0.0	0.0	0.0	2.0	4.3	2.5
A1/29	core	20.3	1.3	0.0	4.5	4.5	4.8	4.5	6.7	0.0	9.0	0.0	0.0	16.5	0.7	0.0	0.0	0.0	6.7	2.7	10.5	8.0	2.3	0.0	0.3	0.0	1.5	3.8	0.8
Morillo System																													
Mo/1	24	16.0	1.8	1.3	5.5	4.2	3.8	6.0	2.2	0.0	8.5	0.5	1.0	11.3	1.8	0.2	0.5	0.5	21.7	2.0	1.2	5.7	0.8	0.0	0.0	0.5	3.3	9.5	0.0
Mo/2	24	25.7	2.8	2.3	4.5	5.5	3.0	5.8	4.5	0.5	10.0	0.8	2.7	6.5	1.0	1.3	0.0	0.3	17.5	0.8	1.7	5.3	1.0	0.0	0.0	0.3	2.3	3.0	0.0
Mo/3	24	17.2	2.3	1.3	6.2	7.0	3.8	9.5	2.7	0.5	7.2	0.0	1.0	8.7	1.5	0.2	0.0	0.5	25.7	2.0	1.7	2.5	1.5	0.0	0.3	0.3	4.0	5.5	0.0
Mo1/1	24	23.8	4.0	1.3	4.0	4.5	3.0	5.5	2.2	0.0	13.5	0.5	2.0	7.3	0.8	0.0	0.0	0.0	17.5	2.2	7.2	2.5	0.8	0.0	0.0	0.0	2.3	3.8	0.0
Mo1/2	24	26.3	3.8	3.0	1.5	3.0	1.3	3.3	0.7	0.0	7.0	0.2	4.5	7.8	0.3	0.0	0.0	0.0	22.7	1.7	0.5	3.5	6.8	0.0	0.0	0.0	2.8	3.8	0.0
Mo1/3	24	30.2	0.5	5.0	2.2	2.2	2.5	2.0	1.8	0.3	8.5	0.5	5.2	8.0	0.0	0.3	0.5	0.3	10.5	1.7	0.5	2.5	7.8	0.0	0.5	0.8	2.0	8.3	0.0
Mo3/1	24	17.3	4.8	1.5	2.5	3.7	2.5	4.0	1.7	0.0	10.2	0.0	1.5	13.5	0.3	0.2	0.5	0.5	23.2	1.7	0.5	6.0	1.8	0.0	0.0	0.5	3.0	6.0	0.0
Mo3/2	24	27.3	3.0	4.3	2.0	4.0	2.3	3.8	0.5	0.8	8.2	0.5	4.5	8.7	0.0	0.0	0.0	0.2	11.0	0.2	0.7	1.5	4.3	0.0	0.0	1.0	5.0	5.3	7.0
Mo3/3	24	20.5	4.0	2.5	2.0	6.0	2.3	5.8	1.5	0.0	13.5	0.0	3.5	10.8	0.8	0.5	0.3	1.0	11.2	2.0	0.7	4.5	2.0	0.0	0.3	0.3	4.0	3.5	4.8
MO-Gu/2	25	13.0	6.5	0.7	3.2	6.0	3.8	5.5	3.2	0.0	11.3	0.8	1.7	8.7	2.0	0.7	0.5	1.0	20.7	3.0	1.0	4.5	1.5	0.0	0.0	0.0	3.8	4.3	1.8
MO-Gu/3	25	24.0	5.0	2.2	0.5	3.2	1.3	2.5	3.0	0.0	12.5	0.5	3.2	6.8	0.8	0.0	0.0	0.2	12.7	0.8	0.7	3.8	2.8	0.0	0.3	0.3	1.5	7.0	8.3
MO7/1	24	19.7	3.5	0.0	6.2	3.0	3.5	5.5	5.2	0.0	13.5	0.0	0.5	6.8	0.8	0.0	0.0	1.0	9.2	5.0	8.2	6.0	0.7	0.0	1.3	0.0	0.0	7.5	1.8
MO7/3	24	28.3	1.8	0.0	4.2	3.7	3.3	4.5	2.2	0.0	16.2	0.0	1.7	8.0	0.2	0.5	0.0	0.5	10.7	2.0	0.2	9.5	2.0	0.0	0.8	0.0	0.5	3.8	3.0
MO7/4	24	26.8	2.8	0.0	4.7	2.0	4.8	2.0	4.2	0.0	19.2	0.0	3.7	8.0	2.0	0.3	0.0	1.3	5.5	1.2	0.5	6.0	1.3	0.0	0.3	0.0	1.0	6.8	2.5
MO8/2	23	20.7	2.5	0.0	5.2	3.0	3.5	4.8	1.7	0.0	17.2	0.0	2.0	9.0	0.5	0.2	0.0	0.5	11.7	3.3	2.7	5.8	1.5	0.0	0.5	0.0	2.0	7.3	2.5
MO9/1	23	31.0	1.2	0.0	4.0	1.2	2.8	2.5	3.5	0.0	23.2	0.0	2.5	7.2	0.5	0.0	0.0	1.0	4.2	2.3	0.2	10.8	0.5	0.0	0.8	0.0	0.3	2.5	3.0
MO9/2	23	24.2	1.0	0.0	6.0	3.5	3.5	5.5	4.5	0.0	18.5	0.0	2.0	8.5	1.0	0.0	0.0	1.0	7.0	2.8	1.5	11.3	0.0	0.0	0.8	0.0	0.5	4.0	1.8
MO9/3	23	30.7	2.5	0.0	4.5	3.0	3.8	3.8	4.0	0.0	21.2	0.0	1.0	9.7	1.0	0.0	0.0	0.5	5.2	2.3	0.0	8.3	1.3	0.0	0.0	0.0	0.0	2.8	2.0
MO5	23	26.5	1.7	0.0	6.5	3.5	3.3	6.5	3.7	0.0	20.2	0.0	2.5	6.5	0.7	0.8	0.0	1.3	5.7	2.5	3.5	6.7	1.5	0.0	0.0	0.0	0.0	5.0	1.0
MO6/2	24	26.8	1.3	0.0	3.2	2.7	2.5	3.5	3.7	0.0	19.2	0.0	1.0	7.8	0.8	0.0	0.0	0.2	11.5	0.7	1.7	9.0	1.3	0.0	0.3	0.3	1.5	3.8	3.3
MO4/1	23	31.2	0.5	0.0	7.7	3.0	4.8	5.8	4.7	0.0	13.5	0.0	4.5	8.0	0.5	0.0	0.0	1.7	3.5	1.8	1.0	9.8	0.5	0.0	0.5	0.0	0.0	4.3	3.3
MO4/2	23	24.8	0.8	0.0	5.7	2.2	3.5	4.5	3.0	0.0	16.0	0.2	2.2	5.3	0.8	0.0	0.0	1.7	13.2	4.5	0.2	8.7	0.5	0.0	0.0	0.0	1.3	4.0	4.8
Guaso System																													
Gu/ I	26	35.5	2.5	1.2	3.5	1.7	1.8	3.5	1.0	0.0	11.8	0.3	6.0	9.7	0.0	0.3	0.0	0.3	5.5	0.3	0.2	1.3	3.5	0.3	0.3	0.0	2.3	6.5	6.3
Gu1/2	26	31.5	3.8	1.8	2.7	2.0	2.8	2.0	1.0	0.2	4.7	0.0	2.2	18.5	0.5	0.0	0.0	0.2	3.7	0.7	0.2	2.5	9.5	0.0	0.5	0.0	2.0	6.5	5.0
Gu1/3	26	25.0	4.3	2.3	3.0	2.0	1.8	3.3	0.8	0.3	8.0	0.2	2.2	22.2	0.5	0.0	0.0	0.7	6.2	0.7	0.0	1.5	9.8	0.0	0.0	0.0	1.5	5.3	3.5
Gu2/1	27	20.3	1.8	1.0	2.2	2.5	1.5	3.3	1.2	0.0	7.2	0.5	1.0	8.5	1.2	0.2	0.0	0.5	21.0	5.2	0.2	3.5	5.5	0.0	0.5	0.3	4.3	6.3	5.0
Gu2/2	27	22.3	2.3	1.0	3.0	3.2	2.3	4.0	1.3	0.3	11.5	1.0	2.5	13.5	0.5	0.0	0.0	1.2	14.2	2.3	0.2	3.8	3.8	0.0	0.3	0.3	1.8	4.5	5.5
Gu3/1	27	28.7	2.8	1.3	3.5	2.0	3.3	2.3	2.8	0.3	14.3	0.3	1.0	5.5	0.2	0.0	0.0	1.2	12.7	2.0	0.7	3.2	4.3	0.0	0.0	0.5	2.0	5.0	5.8
Gu3/2	27	28.7	2.0	2.0	2.5	3.2	2.0	3.8	0.8	0.3	7.5	1.0	1.7	19.8	0.3	0.0	0.0	0.7	6.0	0.0	1.0	2.0	7.0	0.0	0.0	0.3	2.5	6.0	4.8

		Quartz; Q							Feldspars; F					Lithic fragments; L					CE	CI			NCI					
Sample No.:	Loc.	Qmnu	Qmu	CQ	Qpnu	Qpu	Qp2-3	Qp>3	Plag	CP	K-spar	CK	M	Sed	Chert	Met.	Volc.	CL	CE	CI grains	Bioc-last	Lc	Iron oxide	Glauc-onite	Other mineral	Indeter-minate	Alter-ites	CX	Calcite (single +patchy)
Gu3/3	27	25.2	1.3	0.8	3.7	2.0	3.3	2.5	1.5	0.0	13.2	1.0	2.2	10.5	0.2	0.0	0.0	1.5	11.7	1.8	0.0	6.3	2.8	0.0	0.0	0.0	1.8	5.8	6.8
Gu 4/1	26	27.0	0.2	0.0	5.0	1.5	3.3	3.3	2.7	0.0	13.2	0.0	1.5	3.8	0.3	0.0	0.0	1.7	14.7	5.2	0.7	11.5	1.0	0.3	0.0	0.0	0.5	6.7	2.3
Gu 4/2	26	24.5	2.5	0.0	7.2	3.5	5.3	5.3	3.5	0.0	14.0	0.0	2.0	9.0	1.5	0.0	0.0	0.7	11.5	4.2	0.2	6.0	0.8	0.0	0.8	0.0	0.5	5.5	2.0
Gu 4/3	26	24.0	0.7	0.0	7.2	2.0	4.5	5.0	5.2	0.0	8.5	0.0	1.5	7.5	0.7	0.0	0.0	1.2	11.7	3.5	2.7	11.0	0.0	0.0	0.8	0.0	1.5	8.3	1.8
Gu8/1	28	25.7	3.0	0.0	5.2	4.2	3.0	6.5	6.2	0.0	12.7	0.0	4.5	4.7	0.0	0.2	0.0	1.5	3.2	2.0	1.0	14.2	1.8	0.0	0.0	0.3	0.3	6.0	3.0
Gu7/1	28	18.0	2.3	0.0	11.6	2.6	2.6	11.6	7.6	0.0	10.0	0.0	1.6	5.3	0.0	0.3	0.0	1.3	13.3	8.0	0.0	11.3	0.6	0.0	0.0	0.0	0.6	3.0	2.0
Gu6/1	28	23.3	2.3	0.0	3.5	2.7	1.8	4.5	8.0	0.0	9.7	0.0	1.7	10.0	0.2	0.0	0.0	1.5	6.5	4.8	0.0	14.3	1.0	0.0	0.3	0.0	0.3	5.5	4.5
Torla System																													
T1/1	29	59.5	3.0	0.0	6.2	4.0	6.0	4.0	1.2	0.0	6.5	0.0	1.0	7.0	0.2	0.0	0.0	0.0	0.0	0.2	1.5	2.0	6.3	0.0	0.8	0.0	0.0	0.5	0.0
T1/2	29	46.7	2.5	0.0	5.7	4.5	6.5	3.8	0.2	0.0	3.7	0.0	0.2	0.0	0.5	0.0	0.0	0.0	0.5	6.3	19.0	6.8	0.8	0.0	0.0	0.0	0.0	1.8	0.8
T1/3	29	46.0	2.0	0.0	4.0	5.2	4.3	6.3	0.7	0.0	4.5	0.0	0.0	0.3	0.3	0.0	0.0	0.0	0.2	3.5	19.2	5.7	1.3	0.0	0.0	0.0	0.5	4.5	2.0
Broto System																													
BR2/3	30	35.7	2.5	0.0	2.5	5.2	3.5	4.3	7.0	0.0	9.7	0.0	2.2	15.7	1.0	0.0	0.0	0.0	1.2	2.8	0.0	2.3	3.8	0.0	1.0	0.0	0.3	5.8	1.3
BR3/1	31	31.7	2.5	0.0	5.0	6.0	4.8	6.3	11.7	0.0	4.2	0.0	2.5	15.7	2.0	0.0	0.0	0.5	1.0	2.5	0.2	2.0	2.8	0.0	0.8	0.0	0.3	7.5	1.0
BR5/3	32	33.8	1.8	0.0	1.5	4.2	1.8	4.0	13.0	0.0	7.5	0.0	2.7	10.7	1.5	0.5	0.0	1.3	1.5	1.3	0.2	4.8	1.0	0.0	0.5	0.0	0.3	8.0	4.0
BR6/0	34	34.2	3.5	0.0	5.2	3.0	3.8	4.5	9.0	0.0	6.7	0.0	3.0	7.0	1.5	0.3	0.0	2.5	1.0	2.0	0.2	4.2	2.5	0.0	1.0	0.0	0.5	10.0	2.2
BR6/1	34	35.5	5.5	0.2	5.5	5.5	4.3	6.5	16.0	0.0	6.2	0.0	1.5	3.5	4.0	0.0	0.0	0.7	1.2	1.8	1.2	2.0	1.0	0.0	0.3	0.0	1.3	5.8	1.3
BR6/2	34	34.0	3.0	0.0	5.5	6.0	5.3	6.3	10.0	0.5	7.0	0.2	1.5	8.2	2.0	0.5	0.0	1.5	2.7	3.3	0.5	2.8	2.5	0.0	0.3	0.0	1.3	5.2	1.5
BR6/3	34	34.7	2.0	0.0	4.7	6.7	4.0	7.5	12.2	0.0	7.8	0.3	2.0	8.7	1.0	0.0	0.0	0.7	3.0	2.0	1.5	3.0	2.8	0.0	0.5	0.0	0.8	4.5	1.0
BR7/0	33	31.5	1.8	0.0	5.7	6.2	5.0	7.0	9.0	0.5	4.7	0.0	4.0	9.0	2.7	0.5	0.0	1.7	2.2	0.7	1.2	3.5	5.0	0.0	1.0	0.3	1.3	6.0	1.3
BR7/1	33	33.0	3.2	0.0	7.5	8.5	8.8	7.3	10.5	0.2	4.2	0.0	6.0	9.5	1.7	0.0	0.0	1.0	2.0	0.2	0.2	1.5	2.3	0.0	0.8	0.0	0.0	6.8	0.8
BR7/4	33	32.0	1.7	0.0	4.0	4.7	4.7	4.0	10.2	0.0	7.0	0.0	3.0	12.3	1.3	0.0	0.0	0.5	4.0	0.3	0.2	4.3	2.3	0.3	0.8	0.0	0.5	10.3	0.5
BR5/2	32	39.0	1.0	0.0	2.2	4.7	2.7	4.2	8.7	0.0	7.2	0.0	3.2	9.3	1.3	0.0	0.0	0.0	0.5	1.5	0.5	3.5	3.5	0.0	0.8	0.0	0.5	11.5	1.0
BR7/2	33	31.3	0.8	0.0	2.7	5.0	3.5	4.2	8.5	0.2	7.0	0.0	2.0	12.0	0.2	0.2	0.0	2.0	2.5	4.0	0.5	3.5	4.3	0.0	0.5	0.0	0.8	10.0	2.0
Cotefablo System																													
CO1/2	36	34.3	1.3	0.0	4.7	2.5	2.3	5.0	9.5	0.0	5.0	0.0	0.7	6.8	3.3	0.2	0.0	1.5	2.2	5.5	8.2	6.7	1.8	0.0	0.0	0.0	0.0	4.3	1.5
CO2/2	36	28.3	1.3	0.0	7.0	2.0	4.0	5.0	8.2	0.0	4.2	0.0	0.7	7.0	0.7	0.3	0.0	0.3	2.2	12.5	7.0	8.0	2.8	0.0	0.5	0.0	0.5	5.7	0.8
CO2/3	36	28.5	1.0	0.0	3.0	3.7	2.5	4.0	5.0	0.0	5.5	0.0	1.2	2.8	1.3	0.0	0.0	1.0	3.2	13.3	4.2	10.5	2.8	0.0	1.0	0.0	1.3	9.5	1.3
CO3/0	37	29.3	1.8	0.0	3.7	2.5	3.0	3.0	8.7	0.0	9.7	0.0	1.2	8.3	0.8	0.0	0.0	0.7	2.5	2.8	1.0	12.0	3.5	0.0	1.3	0.0	1.0	7.0	2.3
CO3/1	37	33.5	3.5	0.0	3.0	4.5	3.0	4.3	7.2	0.0	5.7	0.0	2.5	4.5	0.8	0.0	0.0	1.0	2.5	6.8	4.2	5.5	4.5	0.0	2.3	0.0	0.5	5.0	2.5
CO3/3	37	41.0	3.0	0.0	4.5	3.2	3.8	4.0	12.2	0.0	5.7	0.0	2.0	7.0	1.5	0.2	0.0	0.5	1.5	1.8	0.7	3.8	3.3	0.0	0.5	0.0	0.8	5.7	1.0
CO4/3	38	26.8	1.3	0.0	3.0	5.5	3.3	5.3	5.7	0.0	5.5	0.0	1.2	5.8	1.3	0.0	0.0	1.7	4.0	5.3	1.0	10.5	3.0	0.0	0.3	0.0	0.5	15.0	2.8
CO5/1	35	34.5	0.7	0.0	2.7	2.2	2.5	2.5	8.7	0.0	6.0	0.0	2.2	8.2	1.0	0.0	0.0	0.0	1.7	3.0	4.2	6.7	5.3	0.0	1.0	0.0	0.5	9.2	1.8
CO5/2	35	19.0	1.2	0.0	8.5	3.0	5.0	6.5	6.5	0.0	1.5	0.0	1.0	5.7	1.0	0.5	0.0	0.0	1.7	8.8	20.2	8.8	2.5	0.0	0.0	0.0	3.8	5.0	1.3
CO5/3	35	29.7	3.5	0.0	5.5	5.5	5.0	6.0	12.7	0.0	5.7	0.0	1.2	4.0	1.0	0.0	0.0	0.0	0.5	6.0	5.7	7.5	3.0	0.0	0.0	0.0	1.0	4.7	2.5
CO2/1	36	38.2	2.0	0.0	3.0	1.7	2.2	2.5	5.5	0.0	8.7	0.0	2.7	8.2	0.0	0.0	0.0	0.0	2.0	1.2	1.2	6.0	6.0	0.0	0.0	0.0	0.8	11.2	1.3
Banaston* System																													
BA2/1	39	17.5	0.8	0.3	2.0	5.2	2.5	4.8	4.0	0.0	3.7	0.0	0.5	10.3	0.3	0.0	0.0	1.2	6.5	13.5	0.0	12.5	3.3	0.0	1.0	0.0	2.3	11.0	4.3

		Quartz; Q							Feldspars; F					Lithic fragments; L					CE	CI			NCI					
Sample No.:	Loc.	Qmnu	Qmu	CQ	Qpnu	Qpu	Qp2-3	Qp>3	Plag	CP	K-spar	CK	M	Sed	Chert	Met.	Volc.	CL	CE	CI grains	Bioc-last	Lc	Iron oxide	Glauc-onite	Other mineral	Indeter-minate	Alter-ites	CX	Calcite (single +patchy)
BA2/2	39	25.2	1.5	0.0	5.2	1.7	3.3	3.8	7.5	0.0	5.5	0.0	1.5	9.3	0.8	0.0	0.0	2.7	4.5	5.5	1.5	10.5	1.5	0.0	1.8	0.0	1.5	9.5	3.3
BA2/3	39	30.0	1.5	0.0	2.2	1.8	2.4	2.0	10.2	0.0	4.4	0.0	3.5	12.8	0.4	0.0	0.0	1.0	0.8	8.6	0.0	4.5	3.6	0.0	0.8	0.0	0.4	8.0	5.4
BA2/4	39	17.8	0.8	0.0	1.7	1.7	1.3	2.3	6.0	0.0	4.5	0.0	2.2	6.0	0.2	0.3	0.0	1.3	8.0	12.0	8.2	11.2	1.5	0.0	0.5	0.0	1.5	9.5	5.0
BA2/5	39	26.3	0.8	0.0	1.7	2.2	2.0	2.0	5.7	0.0	4.0	0.0	3.2	11.0	0.2	0.0	0.0	0.5	2.0	10.5	5.5	9.0	2.8	0.0	0.3	0.0	1.0	10.2	3.0
BA3/2	41	23.5	0.2	0.0	2.0	2.7	1.0	3.8	6.7	0.0	2.2	0.0	1.2	11.0	1.5	0.0	0.0	1.0	1.7	16.3	1.2	9.3	3.3	0.0	0.0	0.0	0.8	10.5	4.8
BA4/1	40	20.8	0.3	0.0	0.7	0.5	0.8	0.5	4.7	0.0	6.2	0.0	1.2	20.0	0.2	0.0	0.0	0.0	3.0	9.5	0.5	5.0	7.5	0.0	1.3	0.0	0.5	15.0	3.0
BA4/2	40	19.2	1.0	0.0	0.7	0.5	0.3	1.0	5.0	0.0	8.5	0.0	2.7	13.5	0.0	0.0	0.0	0.7	6.7	11.3	0.2	6.8	6.5	0.0	0.3	0.3	0.8	13.0	2.3
BA5/1	40	26.2	0.5	0.0	1.7	2.5	1.0	3.3	7.2	0.0	5.5	0.0	1.5	13.3	0.3	0.0	0.0	0.5	5.5	9.8	1.5	6.5	1.5	0.0	1.0	0.0	0.5	11.8	2.8
BA5/2	40	23.8	0.3	0.0	3.2	0.7	1.3	2.8	10.2	0.0	9.7	0.0	0.2	6.3	0.3	0.3	0.0	1.3	3.7	12.8	6.5	6.8	0.8	0.0	0.5	0.0	1.5	10.0	1.3
Jaca System																													
J1/1	43	25.7	1.5	0.0	3.5	4.5	3.3	4.8	4.5	0.0	17.0	0.0	6.0	16.0	0.5	0.0	0.0	0.0	0.2	1.3	1.2	2.3	2.5	0.3	0.0	0.0	1.5	7.5	4.0
J1/2	43	15.3	1.3	0.0	2.7	3.2	1.0	5.0	5.0	0.2	8.5	0.0	4.5	7.5	1.0	0.0	0.0	0.2	4.5	6.8	11.7	5.3	5.0	0.0	0.5	0.0	5.3	8.8	2.8
J1/3	43	24.7	2.0	0.0	2.5	3.5	1.8	4.3	5.7	0.0	12.2	0.0	3.0	14.2	0.5	0.0	0.0	0.2	1.2	2.5	3.5	5.5	3.8	0.0	0.5	0.0	0.8	11.8	1.8
J3/1	44	22.8	0.8	0.0	2.2	2.5	2.8	1.8	2.2	0.0	12.5	0.0	3.2	11.5	0.7	0.0	0.0	0.7	2.5	4.8	0.7	7.5	6.3	0.0	1.3	0.0	1.5	11.8	4.5
J3/3	44	21.0	0.7	0.0	2.0	3.0	2.5	2.8	1.0	0.0	12.5	0.0	1.2	8.2	0.5	0.0	0.0	1.2	0.7	6.0	17.0	6.0	6.5	0.5	0.8	0.0	1.5	8.0	1.5
J4/1	42	29.5	4.0	0.0	2.2	3.0	2.5	2.8	0.7	0.0	10.2	0.0	4.0	12.5	2.0	0.0	0.0	0.2	0.7	5.0	1.7	5.2	4.8	0.0	0.5	0.3	0.8	10.5	2.0
J4/2	42	21.2	1.5	0.0	7.5	3.2	4.8	6.0	2.5	0.0	10.2	0.0	3.5	15.8	1.8	0.2	0.0	1.0	2.0	4.0	1.2	5.2	5.3	0.0	0.3	0.0	2.5	10.0	1.0
J4/3	42	27.0	1.7	0.0	3.2	5.5	4.3	4.3	3.2	0.0	5.7	0.0	3.7	21.2	0.5	0.0	0.0	0.2	0.7	2.3	1.0	5.8	9.0	0.0	0.8	0.0	0.3	6.5	1.5
Note: Qp2-3 and Qp>3 are not used for final modal calculation as they are just another variety of Qpnu and Qpu.																													

Table 4.3: Summary of framework grain modes of arenites from the Ainsa and Jaca basins.

	NCE	NCI	CE	CI	Q	F	L
Fosado system							
AM	84.8	4.1	2.1	1.2	48.4	17.5	15.9
E	4.3	1.4	2.0	0.7	4.5	3.2	3.3
MAX	88.6	6.5	5.5	2.0	54.1	21.9	21.4
MIN	79.0	2.5	0.2	0.3	41.6	13.9	12.7
Arro system							
AM	69.0	2.1	2.0	15.9	41.6	16.4	9.4
E	12.6	1.2	2.0	14.1	9.0	4.5	3.3
MAX	88.5	5.0	8.7	49.3	56.6	22.0	15.4
MIN	40.4	0.3	0.0	2.2	23.2	8.4	4.9
Gerbe System							
AM	84.2	2.4	2.0	0.9	50.5	21.0	10.8
E	4.0	1.6	0.6	1.0	5.5	3.3	2.9
MAX	89.1	6.0	3.2	3.7	62.4	26.7	17.0
MIN	75.9	0.8	1.2	0.0	41.9	16.2	7.4
Banaston system (in the Ainsa basin)							
AM	70.6	1.7	3.1	11.3	43.9	15.2	10.3
E	9.4	1.9	2.5	9.4	9.1	5.2	5.1
MAX	86.0	9.0	11.2	36.2	56.1	28.4	21.5
MIN	47.8	0.3	0.5	2.2	20.7	6.0	3.5
Ainsa system							
AM	69.9	1.7	5.1	9.0	39.2	15.9	13.3
E	7.6	0.8	3.5	5.1	6.9	4.0	4.2
MAX	82.8	3.3	16.5	18.3	50.9	23.7	23.2
MIN	57.7	0.5	1.2	2.5	25.6	8.2	5.5
Morillo system							
AM	65.6	1.9	12.8	3.7	35.8	17.2	10.1
E	6.7	2.0	6.7	2.8	3.9	5.4	2.1
MAX	78.1	7.8	25.7	13.2	42.4	26.7	15.0
MIN	55.1	0.0	3.5	0.9	28.7	7.9	7.7
Guaso system							
AM	64.1	3.7	10.1	3.4	35.8	13.9	12.1
E	6.8	3.2	5.1	2.4	4.4	4.1	5.6
MAX	73.6	9.8	21.0	8.0	44.4	18.9	23.4
MIN	48.0	0.0	3.2	0.5	27.7	5.9	5.7
Torla system							
AM	71.8	2.8	0.2	16.6	63.1	5.6	2.7
E	14.5	3.0	0.3	12.9	8.4	1.9	3.9
MAX	88.6	6.3	0.5	25.3	72.7	7.7	7.2
MIN	62.9	0.8	0.0	1.7	57.2	3.9	0.5
Broto system							
AM	79.1	2.8	1.9	2.4	46.1	17.0	12.3
E	3.8	1.2	1.0	1.2	3.9	2.6	2.8
MAX	85.3	5.0	4.0	4.5	52.2	22.2	18.2
MIN	71.8	1.0	0.5	0.4	39.7	14.2	8.2
Cotefablo system							
AM	64.2	3.5	2.2	11.3	40.7	14.1	8.8
E	9.1	1.3	0.9	8.2	5.5	3.5	3.3
MAX	80.8	6.0	4.0	29.0	51.7	18.4	16.7
MIN	47.9	1.8	0.5	2.4	31.7	8.0	5.0
Banaston system (in the Jaca basin)							
AM	54.5	3.2	4.2	13.5	27.8	12.1	12.8
E	7.3	2.2	2.4	4.6	5.0	3.5	3.5
MAX	67.8	7.5	8.0	20.2	35.5	19.9	20.2
MIN	42.3	0.8	0.8	7.0	21.4	7.7	7.7
Jaca system							
AM	64.5	5.5	1.6	8.8	31.8	14.2	14.8
E	10.4	1.9	1.4	7.6	5.6	3.9	4.4
MAX	79.2	9.0	4.5	23.0	38.7	21.5	21.9
MIN	49.3	2.8	0.2	2.5	22.4	8.9	8.7

Note: AM - arithmetic mean; E - error estimates based on univariate statistical methods; MAX - maximum; MIN - minimum. See text for explanation of other abbreviations.

4.3 Petrography of the Ainsa basin systems

4.3.1 Fosado system

Framework grains of the Fosado depositional system range from fine to lower medium grain-size. They are moderately sorted and well packed with long grain contacts. Most of the grains are sub-rounded to sub-angular in shape. NCE grains are the most abundant with mean value of 85% and include quartz, K-feldspar, plagioclase, phyllosilicates (biotite and muscovite), sedimentary lithic fragments like shale and chert. Both monocrystalline and polycrystalline quartz are mostly non-undulatory. Alteration of feldspar is quite common in all the samples. The Plagioclase to K-feldspar (P/K) ratio is <1. There are few intrabasinal carbonate clasts (mean value 1.2%) and opaque minerals (mean value of NCI 4%), but rarely extrabasinal carbonate clasts (mean value 2%), although there are traces of dolostones in the sediment.

The sandstones from the Fosado system can be classified as subarkose arenite with a mean of $Q_{58}F_{21}L_{21}$. Taking into account the relative proportions of CI-NCE-CE, the arenites are non-carbonate extrarenites.

4.3.2 Arro system

The principal grain size in the samples from the Arro system ranges from fine-grained sand (upper division) to very coarse-grained sand (lower division), but the majority are medium-grained. The framework grains are moderate to poorly sorted, sub-rounded to sub-angular, and mainly with tangential grain-to-grain contacts. Quartz, feldspars, and lithic fragments (sedimentary and metamorphic) constitute NCE grains, which account for about 69% (mean value) of all the framework grains. Sedimentary lithic fragments include shale and chert, whereas quartz-mica phyllites represent the metamorphic lithic fragments. There are few examples of quartz overgrowths with abraded boundaries (Fig. 4.3A), broken quartz grains (Fig. 4.3C), and heavy mineral inclusions in quartz. The plagioclase feldspars are mainly altered, although rare examples of unaltered grains were observed (P/K ratio <1). These sandstones contain relatively large amounts of CI grains, represented by single

bioclasts of larger foraminifera, such as *Nummulites, Discocyclina* and *Alveolina*, oyster shell fragments, algal grains (*Konickopora*?) and intrabasinal carbonate clasts. There are also rare occurrences of oolitic limestone (oomicrite) fragments. Some of the bioclasts show post-depositional alteration, for example, dissolution and compaction (Fig. 4.3E). The CI grains have a mean value of 16%, but can be as high as 49%. In contrast, the CE grains are rare (mean value 2%), and represented only by fine-grained dolostones. Calcite cement is generally Fe-rich. Opaque (iron oxides) pellets represent the NCI component, but also occur as interstitial pore filling material.

According to QFL ratios, the sandstones from the Arro depositional system can be classified as subarkose arenite with a mean of $Q_{60}F_{24}L_{16}$. Taking into account the relative proportions of CI-NCE-CE, the arenites from the Arro system can be considered as hybrid arenites.

4.3.3 Gerbe system

The sandstones from the Gerbe system are fine- (upper division) to medium-grained, moderate to poorly sorted, sub-rounded to sub angular, and with grain contacts varying from tangential to long. NCE grains are the most abundant (mean of 84%), and include quartz, K-feldspar, plagioclase, phyllosilicates (chlorite, biotite and muscovite), sedimentary lithic fragments (shale, chert and sandstone fragments). Alteration of feldspar is quite common in all samples, although there are some traces of unaltered plagioclase grains (P/K ratio <1). NCI (represented by glauconite and opaque minerals), CI and CE grains are very low in abundance, with a mean value of 2.4%, 2%, and 0.9%, respectively. There are rare occurrence of deformed foraminifera shell, doloclasts and poikiloptic calcite cement.

On the basis of QFL ratios, the sandstones from the Gerbe system can be classified as subarkose arenite, with a mean of $Q_{60}F_{25}L_{15}$. Considering the relative proportions of CI-NCE-CE, the sandstones from the Gerbe system are non-carbonate extrarenites.

4.3.4 Banaston system

At the start of the Banaston system, there is a substantial and significant influx of reworked intrabasinal carbonate clasts, including large carbonate olistoliths up to metres in maximum dimension. Samples from the Banaston system range from fine- to coarse-grained, but most are medium-grained. Sorting mainly varies from moderate to poor, with few well-sorted samples. The framework grains are mainly sub-rounded to sub-angular in shape with tangential grain-to-grain contacts, although angular grains are common. Quartz, feldspars, and lithic fragments (sedimentary and metamorphic) constitute the NCE grains, which accounts for about 71% (mean value) of all framework grains. Sedimentary lithic fragments include shale and chert, whereas quartz-mica phyllites represent the metamorphic lithic fragments. There are few heavy mineral inclusions in quartz. Feldspars are mainly altered, although there are minor amounts of unaltered grains of plagioclase and microcline (P/K ratio <1). These sandstones also contain relatively large amounts of CI grains (mean of 11%). They are represented by *Nummulites, Discocyclina,* oyster shell fragments, algal grains (*Konickopora*?), peloidal limestone fragments and intrabasinal carbonate clasts. Some of the bioclasts show evidences of dissolution. The CE grains, however, are rare, with a mean value of 3%, and represented by dolostones and single dolomite crystals. Pellets of opaque (iron oxides) and glauconite characterise the NCI components. Replacements of framework grains by chlorite were also observed.

The sandstones from the Banaston system can be classified as subarkose arenite with a mean of $Q_{61}F_{21}L_{18}$. On the basis of the relative proportions of CI-NCE-CE, the arenites from Banaston system can be classified as hybrid arenites.

4.3.5 Ainsa system

The principal grain size in the sandstones from the Ainsa system is medium sand, although they range from fine- to coarse-grained. Sorting is moderate, with mainly sub-rounded to sub-angular grains and tangential grain-to-grain contacts. Pressure solution contacts among grains were also observed in some grains (Fig. 4.3D). NCE grains account for about 70% of the total framework grains. Monocrystalline and polycrystalline quartz are almost exclusively non-undulatory. In some samples, monocrystalline quartz contains heavy mineral inclusions. The P/ K ratio is <1 with

some traces of unaltered feldspars. Lithic fragments contain shale, chert, sandstone fragments, weakly metamorphosed sandstones and volcanic rock fragments. Micas, in some cases, are deformed and/or squeezed by the surrounding grains. CE grains (mean of 5%) contain mainly fine-grained dolostones, and micritic fossiliferous limestones, rarely with Pithonellid tests. Single bioclasts, intraclasts and micritic grains represent the CI category, which accounts for ~ 9% of all the framework grains. Few intraclasts contain Eocene foraminifera. Also, in some bioclasts, the cavities are filled with opaque (iron-oxide) pellets.

The sandstones from the Ainsa system can be classified as sublitharenite ($Q_{53}F_{22}L_{25}$), and also as hybrid arenites on the basis of CI-NCE-CE contents.

4.3.6 Morillo system

Samples from the Morillo system are clast-supported (in common with other systems) and well packed. The grain-size ranges from fine- to coarse-grained, but most are medium-grained. Sorting mainly varies between moderate and poor, with a few well-sorted samples. The framework grains are mainly sub-rounded to sub-angular in shape with long to tangential grain-to-grain contacts. Quartz, feldspars, phyllosilicates, sedimentary and metamorphic lithic fragments constitute the NCE grains, which account for ~66% (mean value) of all framework grains. Sedimentary lithic fragments include shale and chert, whereas quartz-mica phyllites represent the metamorphic lithic fragments. There are few evidences of broken quartz grains and heavy mineral inclusions in quartz. Feldspars are mainly altered, although some unaltered grains were also noted (P/K ratio <1). In all the samples, the CE grains are relatively high in abundance with a mean value of 13%, but reaching ~25% in some samples. They are represented by both coarse- and fine-grained dolostones, micritic limestones with/without Pithonellid tests. The dolostones, however, are generally more abundant than the micritic limestones. CI grains are comparatively quite low in abundance, accounting for only 4% (mean value) of all the framework grains, and consist of peloidal limestone clast, micritic intraclasts typically containing Miliolids and single bioclasts of Eocene larger foraminifera (that commonly have a micrite-filled cavity). NCI grains (opaque and glauconite) constitute ~2%.

The Morillo system sandstones can be classified as feldspathic litharenites, with a mean of $Q_{47}F_{23}L_{30}$. On the basis of the CI-NCE-CE content, these sandstones are carbonate extrarenites (calcilithites).

4.3.7 Guaso system

Sandstones from the Guaso system are moderately sorted, sub-rounded to sub-angular grains with tangential grain-to-grain contacts. The grain-size ranges from fine- (upper division) to medium-grained. Quartz, feldspars, micas, shales and sandstone fragments constitute the NCE grains (mean of 64%). There is little evidence of broken quartz grains, or heavy mineral inclusions in quartz. Feldspars are mainly altered, along with a few unaltered grains (P/K ratio <1). In common with the sandstones from the Morillo system, the CE grains are relatively high in abundance with a mean of 10%, but reaching as high as 21%. They are represented by both coarse- and fine-grained dolostones, micritic limestones with/without Pithonellid tests. CI grains are comparatively low in abundance, accounting for only ~3% (mean value) of all the framework grains, and they comprise peloidal limestone clast, micritic intraclasts and single bioclasts. In some samples, the intraclasts are squeezed between other clastic grains. NCI grains (opaque and glauconite) comprise ~4%.

The Guaso system sandstones can be classified as feldspathic litharenites with a mean of $Q_{50}F_{19}L_{31}$, while on the basis of the CI-NCE-CE components, they are carbonate extrarenites (calcilithites).

4.4 Petrography of the Jaca basin systems

4.4.1 Torla system

Sandstones from the Torla system are mainly fine-grained, with poor sorting. Most of the framework grains are sub-rounded to sub-angular with tangential grain-to-grain contacts. Carbonate cements are scarcely present in all the samples. NCE grains dominate the framework grain population, as in the systems of the Ainsa basin, with a mean of 72%. The fine-grained lithic fragments are rare among the NCE grains and the P/K ratio is <1. CE grains are almost negligible (mean 0.2%). CI grains, however,

account for ~17% of the total framework grains, and they are represented mainly by single bioclasts, e.g., foraminifera and micritic limestones. NCI grain abundance is also low (mean 3%).

Sandstones from the Torla system can be classified as quartz arenites ($Q_{88}F_8L_4$). On the basis of CI-NCE-CE contents, they are hybrid arenites.

4.4.2 Broto system

Sandstones from the Broto system are generally fine-grained, with a few medium-grained samples. Sorting is moderate to poor, with grain roundness ranging from sub-rounded to sub-angular. There is no evidence of compaction and/or deformation as the framework grains are mainly in tangential grain-to-grain contacts. NCE grains have a mean value of 79% and are represented by quartz, feldspars, micas and fine-grained lithic fragments, e.g., shale, chert, mudstones and rarely metamorphic lithic fragments. The P/K ratio is >1. All other framework components (CE, CI and NCI grains) are relatively low in abundance and almost equal in mean proportions. The mean value of CE, NCI and CI are ~2%, 3%, and 2%, respectively.

The sandstones from the Broto system can be classified as subarkose arenite ($Q_{60}F_{22}L_{18}$) depending on the QFL ratio. On the basis of CI-NCE-CE contents, they are non-carbonate extrarenites.

4.4.3 Cotefablo system

In the Cotefablo system, the sandstones are generally fine-grained, with a few samples that are medium grained. Generally, the sandstones are moderately sorted, sub-rounded to sub-angular shaped, and mainly with tangential grain-to-grain contacts. Quartz, feldspars, micas, shales and sandstone fragments constitute the NCE grains, with a mean value of 64%, which is relatively lower than for other systems in the Jaca basin. There is some evidence of broken quartz grains, and heavy mineral inclusions in quartz. Feldspars are mainly altered, although some unaltered grains were observed. The P/K ratio is >1. The next most abundant constituents are CI grains (mean 11%), represented by foraminifera and micritic intraclasts. In this system, opaque pellets solely constitute the NCI grains, which accounts for ~3% of the framework grains and are slightly more abundant than CE grains (mean 2%).

The Cotefablo system sandstones can be classified as subarkose arenite ($Q_{62}F_{21}L_{17}$), whereas on the basis of the CI-NCE-CE content, they are hybrid arenites.

4.4.4 Banaston system

In the Banaston system in the Jaca basin, the sandstones are uniformly fine-grained, and show varying degrees of grain sorting, from well sorted to moderate to poorly sorted. The framework grains are sub-rounded to sub-angular, mainly with tangential grain-to-grain contacts and, commonly, with long contacts. Quartz, feldspars, micas, shale, sandstone and low-grade metamorphic rock fragments constitute the NCE grains, with a mean of 55%, the lowest among all the sandy systems in the Jaca basin. The P/K ratio ratio is >1. The second most dominant are CI grains (mean 14%), represented by micritic limestone fragments and foraminifera. The CE grains have a mean of 4%, and they are mainly dolostones fragments, which are greater in abundance than the opaque minerals (NCI grains; mean 3%).

According to QFL ratio the sandstones from the Banaston system can be classified as feldspathic litharenite, with a mean of $Q_{49}F_{21}L_{30}$. On the basis of their CI-NCE-CE content, these arenites can be classified as hybrid arenites.

4.4.5 Jaca system

Sandstones from the Jaca system are mainly fine-grained, with moderate sorting. Most of the framework grains are sub-rounded to sub-angular with tangential grain-to-grain contacts. Carbonate cements are scarcely present in all the samples. NCE grains (mean of 65%) are represented by quartz, feldspars, micas and fine-grained sedimentary lithic fragments, e.g., shale, chert, and mudstones. The P/K ratio is <1. CE grains are the least common (mean 2%) among all framework components, and they are represented by fine-grained dolostones. CI (foraminifera and micritic limestones) and NCI (only opaque minerals) grains have a mean abundance of ~9% and 5%, respectively.

The sandstones from the Jaca system can be classified as feldspathic litharenites ($Q_{51}F_{23}L_{26}$) and on the basis of their CI-NCE-CE content, they are hybrid arenites.

Table 4.4: Summary of arenite varieties identified in the Ainsa and Jaca basins. Q: Quartz; F: Feldspars; L: Lithics; NCE: Non-carbonate Extrabasinal; CE: Carbonate Extrabasinal; CI: Carbonate intrabasinal.

System	Q-F-L classification (Folk et. al, 1970)	NCE-CE-CI classification (Zuffa, 1980)
	Ainsa basin	
Guaso	feldspathic litharenites ($Q_{50}F_{19}L_{31}$)	carbonate extrarenites
Morillo	feldspathic litharenites ($Q_{47}F_{23}L_{30}$)	carbonate extrarenites
Ainsa	sublitharenites ($Q_{53}F_{22}L_{25}$)	hybrid arenites
Banaston	subarkose arenites ($Q_{61}F_{21}L_{18}$)	hybrid arenites
Gerbe	subarkose arenites ($Q_{60}F_{25}L_{15}$)	non-carbonate extrarenites
Arro	subarkose arenites ($Q_{60}F_{24}L_{16}$)	hybrid arenites
Fosado	subarkose arenites ($Q_{58}F_{21}L_{21}$)	non-carbonate extrarenites
	Jaca basin	
Jaca	feldspathic litharenite ($Q_{51}F_{23}L_{26}$)	hybrid arenites
Banaston	feldspathic litharenites ($Q_{49}F_{21}L_{30}$)	hybrid arenites
Cotefablo	subarkose arenites ($Q_{62}F_{21}L_{17}$)	hybrid arenites
Broto	subarkose arenites ($Q_{60}F_{22}L_{18}$)	non-carbonate extrarenites
Torla	quartz arenites ($Q_{88}F_8L_4$)	hybrid arenites

4.5 Diagenesis

In any modal analyses, it is important to evaluate any post-depositional modifications that affect the framework grains and, therefore, diagenetic factors that might distort any potential interpretation of the original sandstone petrography. For palaeogeographic and palaeotectonic reconstructions, a better understanding of diagenetic modifications is essential in determining the original composition of the arenite framework (Helmold, 1985; McBride, 1985). The major diagenetic processes that affected the arenites of the Ainsa and Jaca basins are widespread calcite cementation, and siliciclastic grain replacements and alterations. Minor amounts of silica cements as are observed in some of the arenites (Fig. 4.3A), however, quartz overgrowths are almost absent in the arenites from the Jaca basin. Dolomite replacement and de-dolomitization are rare in the Ainsa and Jaca basins arenites. The

effects of compaction appear to be negligible in almost all cases, as indicated by the rare occurrence of pressure solution (Fig. 4.2D) and very long grain-to-grain contacts. It is most likely that the early introduction of calcite as a cement prevented substantial grain compaction.

Calcite is the most common authigenic mineral, occurring both as pore-filling material cement (Fig. 4.3B) and as a replacement of framework grains. Mostly, non-ferroan calcites are observed, but there are also some occurrences of ferroan calcite, identified by a blue tinge on stained calcites (Fig. 4.3F). Opaque minerals can occur as pore-filling material. Partial to total replacement of framework grains by calcite is very common (Fig. 4.3F). Table 4.2 shows the amount of identified framework grains, together with the unidentified grains in the case of total replacement. In general, the arenites in the Jaca basin show more calcite replacement than their counterparts in the Ainsa basin. This is possibly due to relatively finer grain size of the sediments in the Jaca basin, as the surface to volume ratio in case of fine grain is higher than coarse grains, accelerating chemical reactions. Partial feldspar alteration is also common. However, unaltered feldspar grains of both plagioclase and K-feldspar can be identified. Sericitization is the major alteration process in the feldspar (Figs. 4.3G and H), while feldspar replacement by chlorite is subordinate.

In some samples, framework grains are wholly replaced by calcite and, in such cases, it is difficult to identify the original grain. Those grains were counted as a separate class during modal analyses (Carbonate replacement of undetermined grains; CX). In accordance with Fontana et al. (1989), the carbonate replacements of undetermined framework grains were reapportioned according to the frequency of the recognised replacement, which affected the main groups (Table 4.2), i.e., CX is redistributed among the CQ/CK/CP/CL classes (Table 4.1) according to their modal proportion and each class recalculated accordingly.

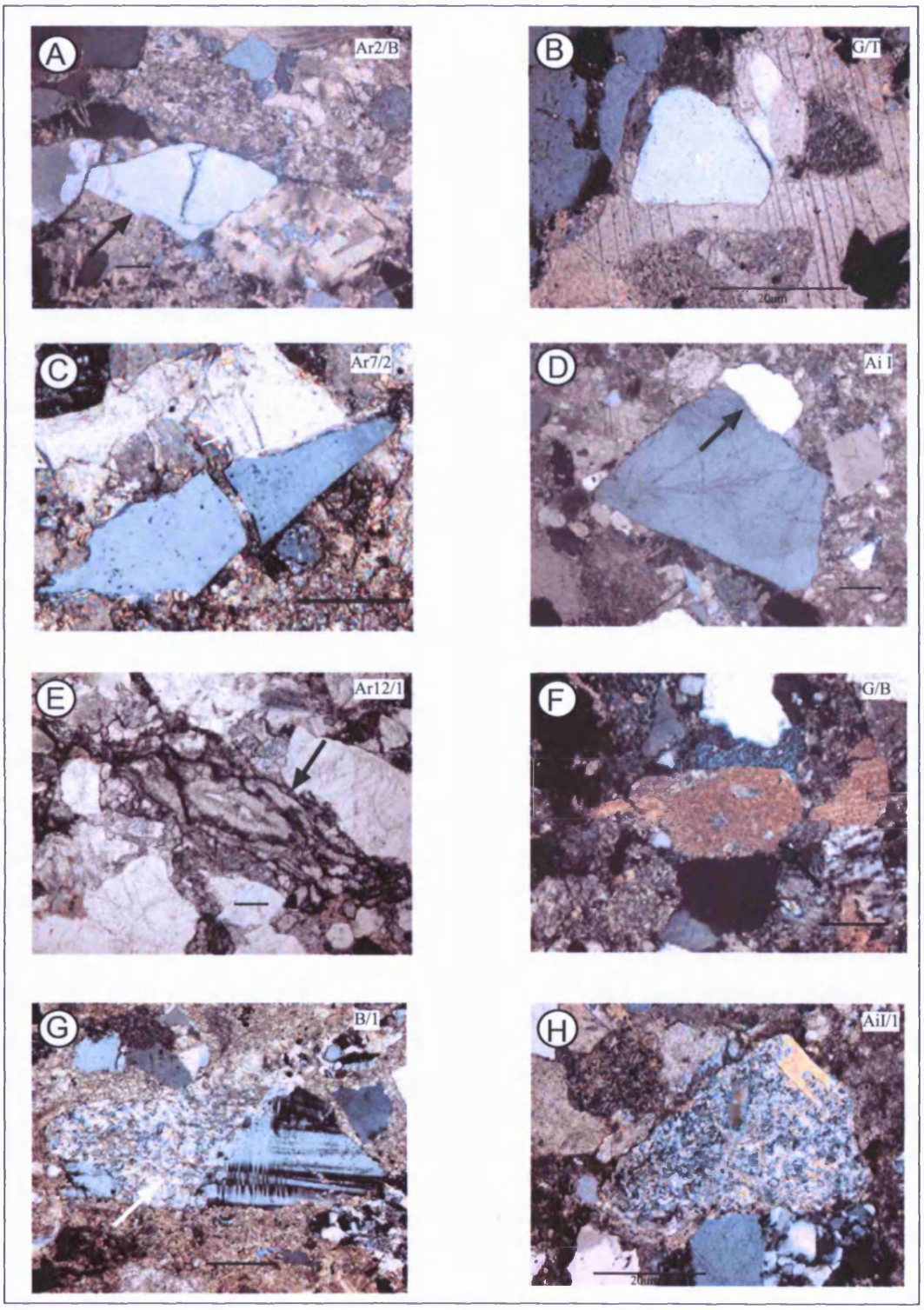

Figure 4.3: Thin-section photomicrographs showing cement varieties and post-depositional modifications in the Ainsa and Jaca basins arenites. The scale bar is 2 micron. (A) Silica cements as quartz overgrowth (fairly uncommon); crossed polar. (B) Calcite cement is more common, occasionally cement crystals envelope many detrital grains resulting in a poikilitic texture; crossed polar. (C) Broken quartz grain, crossed polar. (D) Pressure-solution contact between quartz grains; crossed polar. (E) Compaction and dissolution of a bioclast (Nummulites); plane polar. (F) Calcite (stained pink) replacing a siliciclastic grain, also showing interstitial ferroan calcite (stained blue); crossed polar. (G) Partially altered K-feldspar grain (sericitization); crossed polar. (H) Totally replaced feldspar grain; crossed polar.

4.6 Petrofacies

Contrasting ternary plots (Figs. 4.4 – 4.7) for the arenites of the Ainsa and Jaca basins are drawn in order to identify any compositional trend using the parameters outlined above. Figure 4.4 shows the nature of the arenites from each system in terms of their Q-F-L ratios. It is clearly evident that on the standard QFL diagram (Fig. 4.5A) all the samples from the Ainsa basin group together in the same field, which is the recycled orogen field of Dickinson and Suczek (1979). This is also the case for the Jaca basin arenites (Fig. 4.5A). The standard QFL petrography shows no clear compositional trend, nor does it permit any discrimination between the different systems. This implies that the siliciclastic fraction alone is insufficient to distinguish between the different depositional systems and to recognise any compositional trends. However, a better discrimination is obtained when the terrigenous carbonate grains (CE) are included in the L pole (Fig. 4.5B). Using this QFL+CE diagram, it is at least possible to separate out the Morillo and Guaso samples, which now plot more towards the L+CE pole.

By plotting the samples on the NCE-CE-CI diagram proposed by Zuffa (1980), the clearest discrimination of the Ainsa basin arenites is obtained. The same parameters are also used to plot the Jaca basin arenites. Individual compositional plots for each system of the Ainsa and Jaca basins are presented in Fig. 4.6. It is apparent that the individual systems are occupying different parts of the NCE-CE-CI diagram although there are zones of overlap. Figure 4.7 is a summary diagram showing all the data on one plot along with the mean composition of each system in NCE-CE-CI space. All the arenites group broadly into three petrofacies, which is consistent with the study on the Hecho Group turbidite system by Fontana et al. (1989). As previously mentioned univariate statistical methods (e.g., arithmetic mean) for a multivariate compositional data set are not suitable in a strict sense (Weltje, 2002, 2006), nonetheless, these statistical techniques may give apparently interpretable results which are at best approximations.

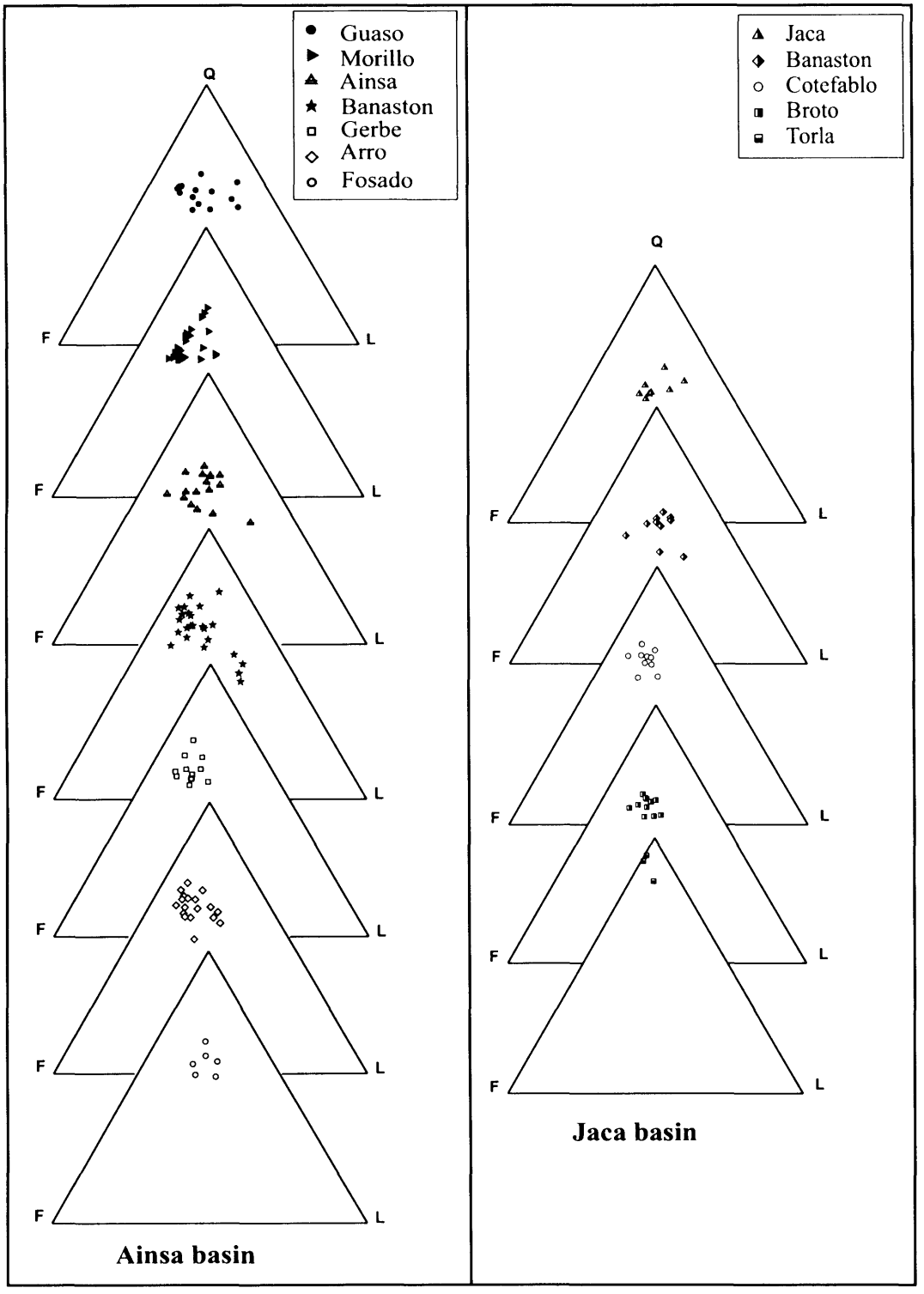

Figure 4.4: Standard QFL plot (extrabasinal siliciclastic components) for each system of the Ainsa and Jaca basins. Q- Total quartz; F- Total feldspar; L- Lithics

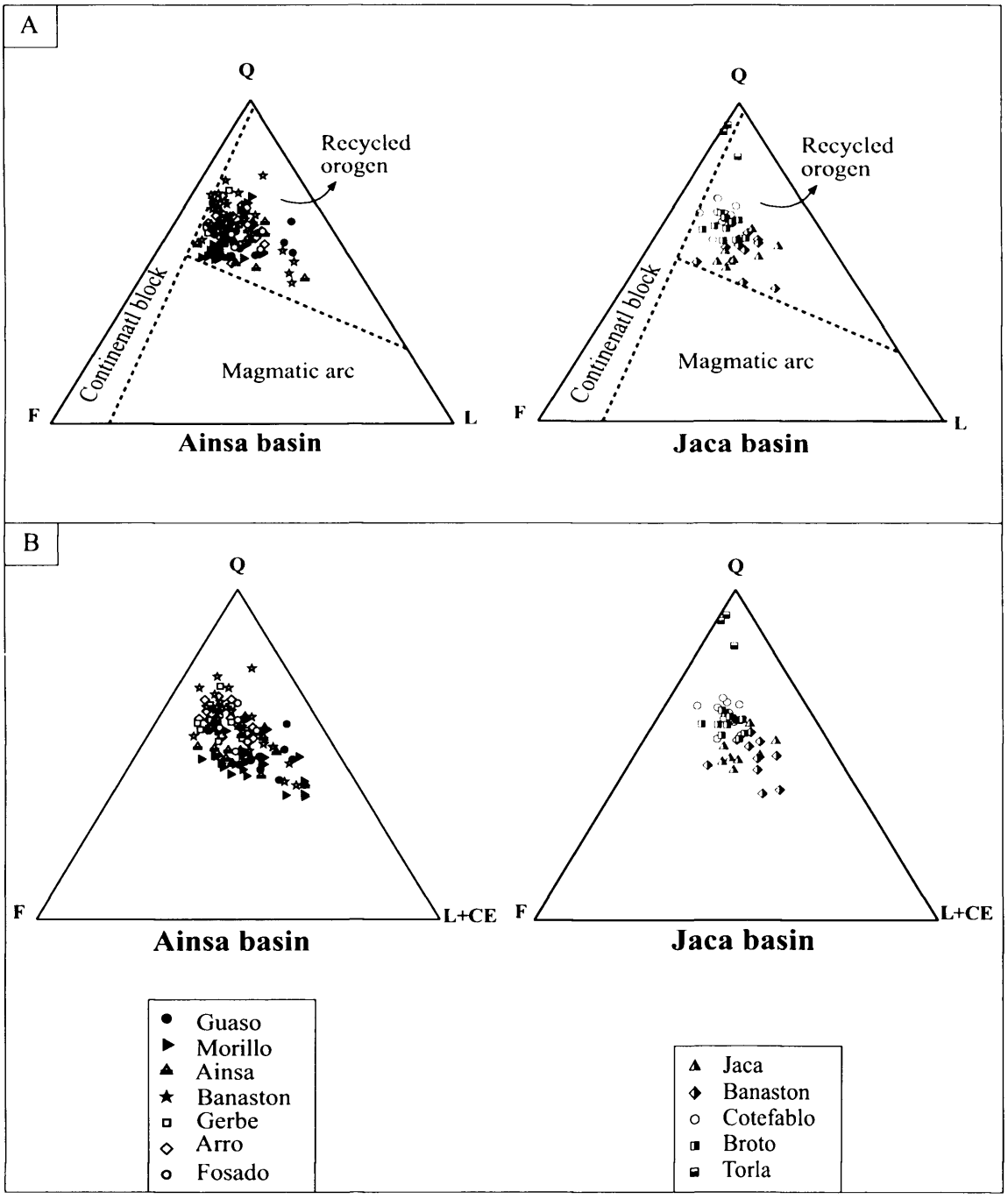

Figure 4.5: Compositional plots of the arenites from the Ainsa and Jaca basins: (A) Standard QFL plot (extrabasinal siliciclastic components) which fails to show any petrographic trends. (B) Q-F-L+CE classification (extrabasinal siliciclastic + carbonate components).
Q- Quartz; F- Feldspars; L- Fine-grained siliciclastic lithics; CE- Carbonate extrabasinal.

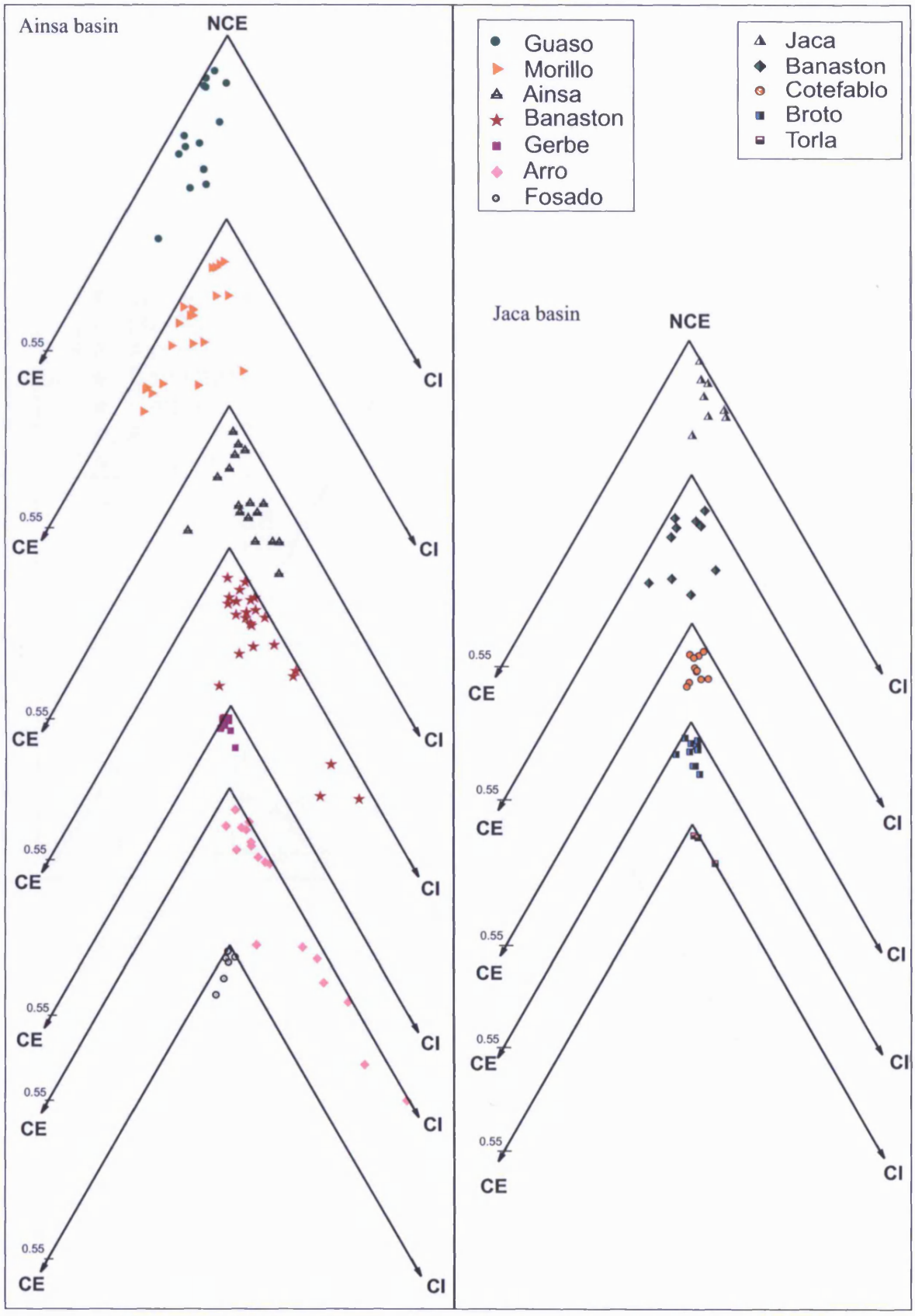

Figure 4.6: NCE-CI-CE plot for each system of the Ainsa and Jaca basins. NCE: non-carbonate extrabasinal grains; CI: carbonate intrabasinal grains; CE: carbonate extrabasinal grains.

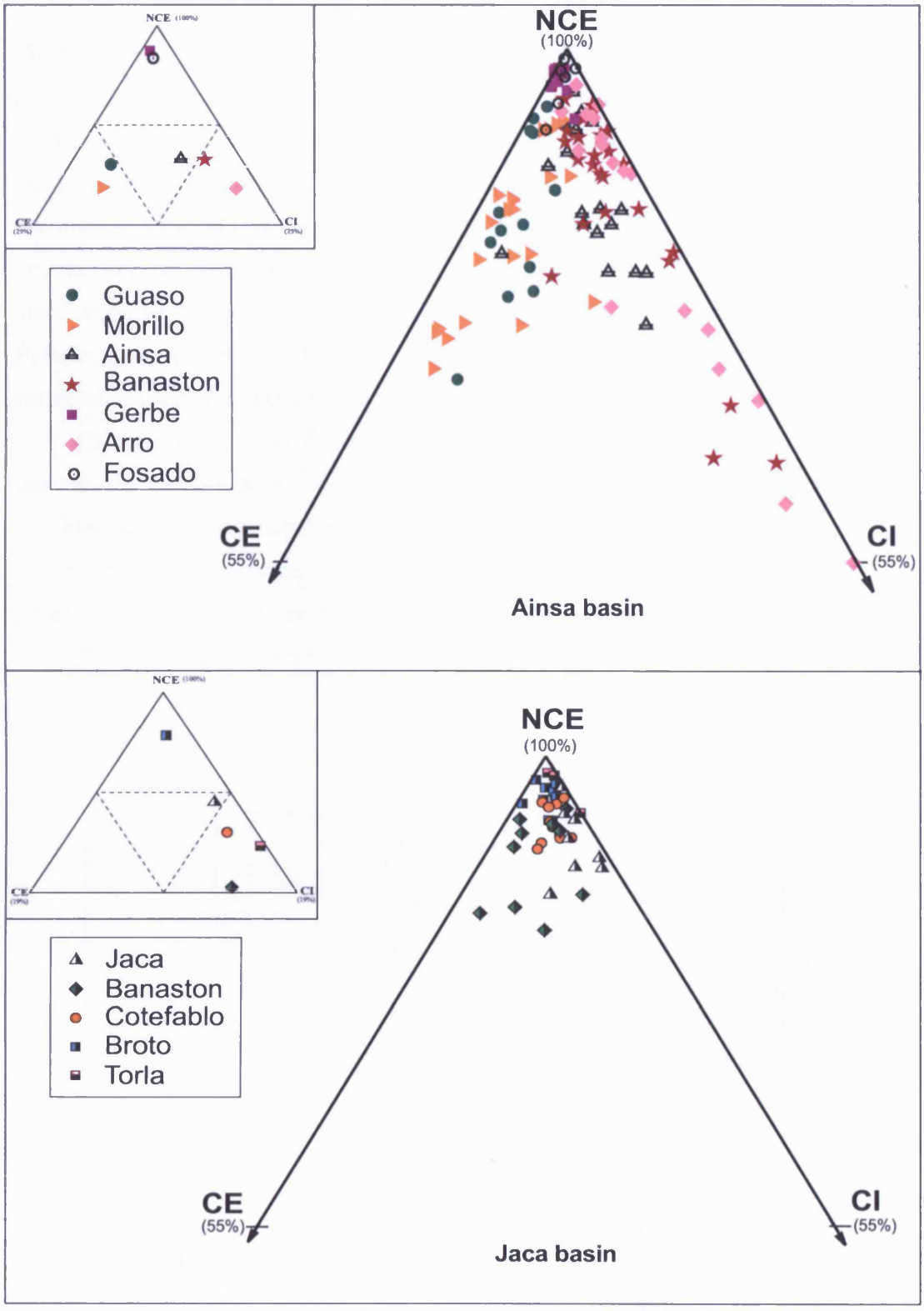

Figure 4.7: Summary diagram for NCE-CI-CE classification of arenites from the clastic systems of the Ainsa and Jaca basins. This compositional plot provides the best discrimination among the arenites. Mean NCE-CI-CE plot for each system is shown in inset. Three petrofacies can be identified in the Ainsa basin, but in the Jaca basin only two petrofacies are present. NCE: non-carbonate extrabasinal grains; CI: carbonate intrabasinal grains; CE: carbonate extrabasinal grains. See Table 4.1 for nomenclature details.

The three petrofacies identified in the Ainsa and Jaca basins are:

Petrofacies 1: sandstone (sensu Zuffa, 1980) or non-carbonate extrarenites. The framework of these rocks is mainly composed of siliciclastic grains (~ 80% or more) and total carbonate grains are negligible (~ 4% or less).

Petrofacies 2: hybrid arenites (sensu Zuffa, 1980). A distinctive characteristic of this petrofacies is the significant presence of intrabasinal carbonate grains (~10% or more) as framework phases.

Petrofacies 3: calcilithite. These rocks contain relatively abundant (~10% or more) extrabasinal carbonate framework grains.

The Fosado and Gerbe arenites have typical sandstone framework grains, whereas the arenites from the Morillo and Guaso systems are mainly calcilithites. The arenites, however, from the Arro, Banaston and Ainsa systems have mainly signatures of hybrid arenites containing both siliciclastic and intrabasinal carbonate grains. The Ainsa depositional system, however, show some arenites that suggest a transitional phase between the hybrid arenite and calcilithite petrofacies.

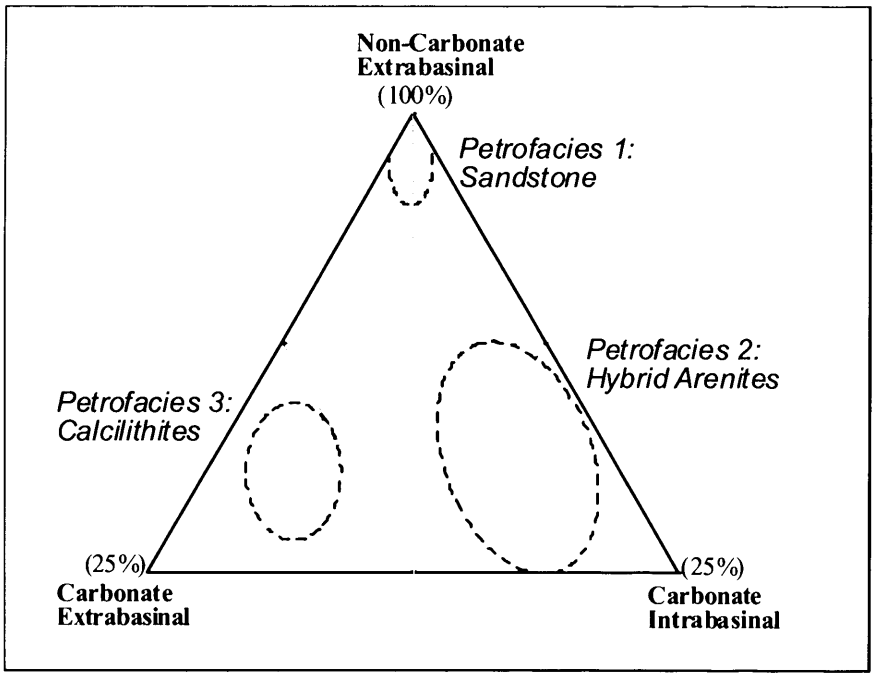

Figure 4.8: A schematic sketch showing the three petrofacies identified in the arenites of the Ainsa and Jaca basins based on the mean sandstone composition.

While considering discrete samples from individual depositional systems, it is quite common to find that one depositional system transgress from one petrofacies field to another (Fig. 4.7).

In the Jaca basin, the arenites are relatively fine grained compared with those in the Ainsa basin, because they represent the more distal part of the deep-marine basin. On the basis of NCE-CI-CE composition, the Jaca basin arenites show only two petrofacies, unlike in the Ainsa basin that shows all three petrofacies. All the turbidite systems in the Jaca basin, apart from the Broto system, fall within the hybrid arenite petrofacies (Fig. 4.7). The Broto arenites show a typical sandstone composition. Within the Jaca basin, however, there is no comparable representative of the calcilithite petrofacies.

4.7 Compositional trends

Figure 4.9A shows how the different depositional systems in the Ainsa basin have changed compositionally with vertical stratigraphic position. The oldest system (Fosado system) has a petrographic composition dominated by NCE grains. It is overlain by the Arro system, which has a totally contrasting petrographic composition, being enriched in CI grains. The overlying Gerbe depositional system has a similar composition to that of the Fosado system. The succeeding Banaston system shows enrichment in CI grains, similar to that observed in the Arro system, and with relatively more NCE grains. During the accumulation of the oldest four depositional systems, there is, therefore, an oscillating compositional shift between sandbodies rich in NCE grains and those rich in CI grains. In contrast, the Ainsa system, although relatively rich in CI grains, shows an intermediate (mixed) composition, with a tendency for a compositional shift away from the CI corner. In the youngest two systems (the Morillo and Guaso systems) the arenite composition changes substantially to arenites enriched in CE grains. However, there is a subtle difference in composition between these two youngest systems, the Guaso system is relatively rich in NCE grains compared with the Morillo system.

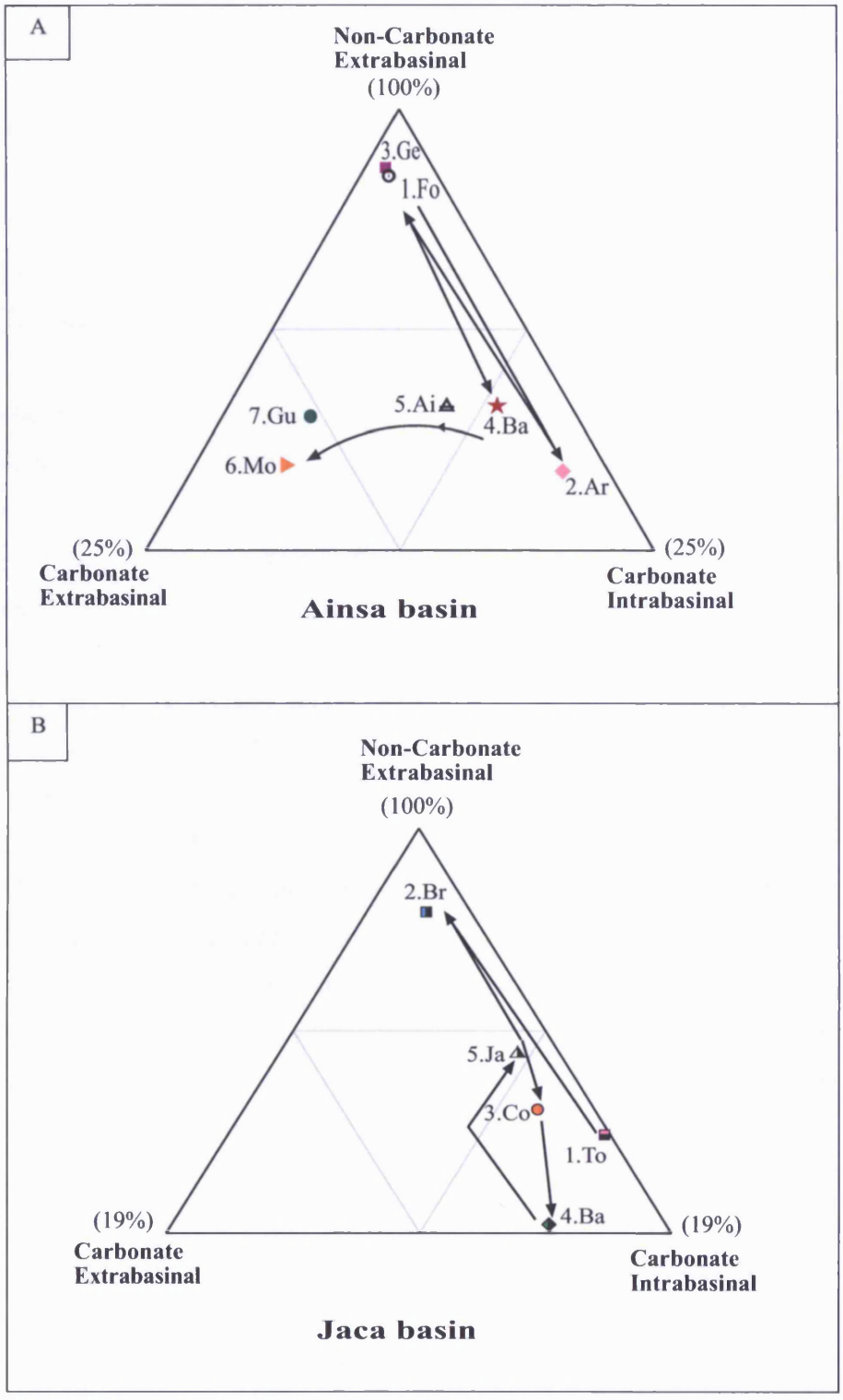

Figure 4.9: Compositional changes observed in: (A) Ainsa basin systems, and (B) Jaca basin systems. Ainsa basin: Fo: Fosado; Ar: Arro; Ge: Gerbe; Ba: Banaston; Ai: Ainsa; Mo: Morillo; Gu: Guaso. Jaca basin: To: Torla; Br: Broto; Co: Cotefablo; Ba: Banaston; Ja: Jaca. Numbers refer to chronological order of systems in basin.

Perhaps surprisingly, the oldest system in the Jaca basin (the Torla system) contains more CI grains and is not rich in NCE grains unlike the oldest (Fosado) system in the Ainsa basin. These very different petrographic characteristics cannot be reconciled with correlating the channelised Fosado and lobe-like Torla systems (cf. Mutti et al., 1985; Remacha et al., 2003). Here, these differences most likely can be explained by the relatively thin Fosado system shaling out before reaching the Jaca basin and, therefore, having no more distal correlative.

The Broto system, overlying the Torla system, contains mainly NCE grains. In contrast, all the overlying systems in the Jaca basin (i.e., Cotefablo, Banaston and Jaca) contain greater amounts of CI grains as a framework component. In the Cotefablo system, the CI grains increase in abundance, and reach a maximum in the Banaston system, then again show a decrease into the Jaca system. It is noteworthy that, in the Jaca basin, CI grains constitute mainly intraclasts rather than single bioclast grains. Within the Jaca basin, however, there is no system, which contains enough CE grains in the framework to allow for its inclusion within the calcilithite petrofacies. Hence, no system in the Jaca basin can be considered as a likely counterpart to the Morillo and Guaso systems in the Ainsa basin. This suggests that the Jaca basin probably contains no distal correlatives of the Morillo and Guaso systems.

The ternary plot involving different quartz varieties after Basu et al. (1975) (Fig. 4.10) displays negligible differences between each depositional systems in terms of quartz typology. Figure 4.10A suggests that quartz grains from all the systems in the Ainsa basin are exclusively of igneous (plutonic) origin. This is also true for the Jaca basin quartz grains (Fig. 4.10B). In very few cases, essentially only for samples from the Morillo system, the approach of the graph is towards the boundary of metamorphic provenance indicating the possibility of metamorphic origin for few quartz grains. The relatively high proportion of monocrystalline quartz grains (Table 5.2) may also be attributed to the igneous origin of the quartz grains. Mainly two varieties of polycrystalline quartz grains are observed in the whole assemblage: Qp2-3 (2-3 crystal units per grain) and Qp>3 (>3 crystal units per grain). The second type indicates an origin from metamorphic source rocks (Blatt et al., 1980; Asiedu et al., 2000). Polycrystalline quartz grains with a bimodal size distribution of individual crystals were also noticed which might have been derived from a gneissose source (Blatt et al., 1980; Abdel-Wahab, 1992). Some quartz grains

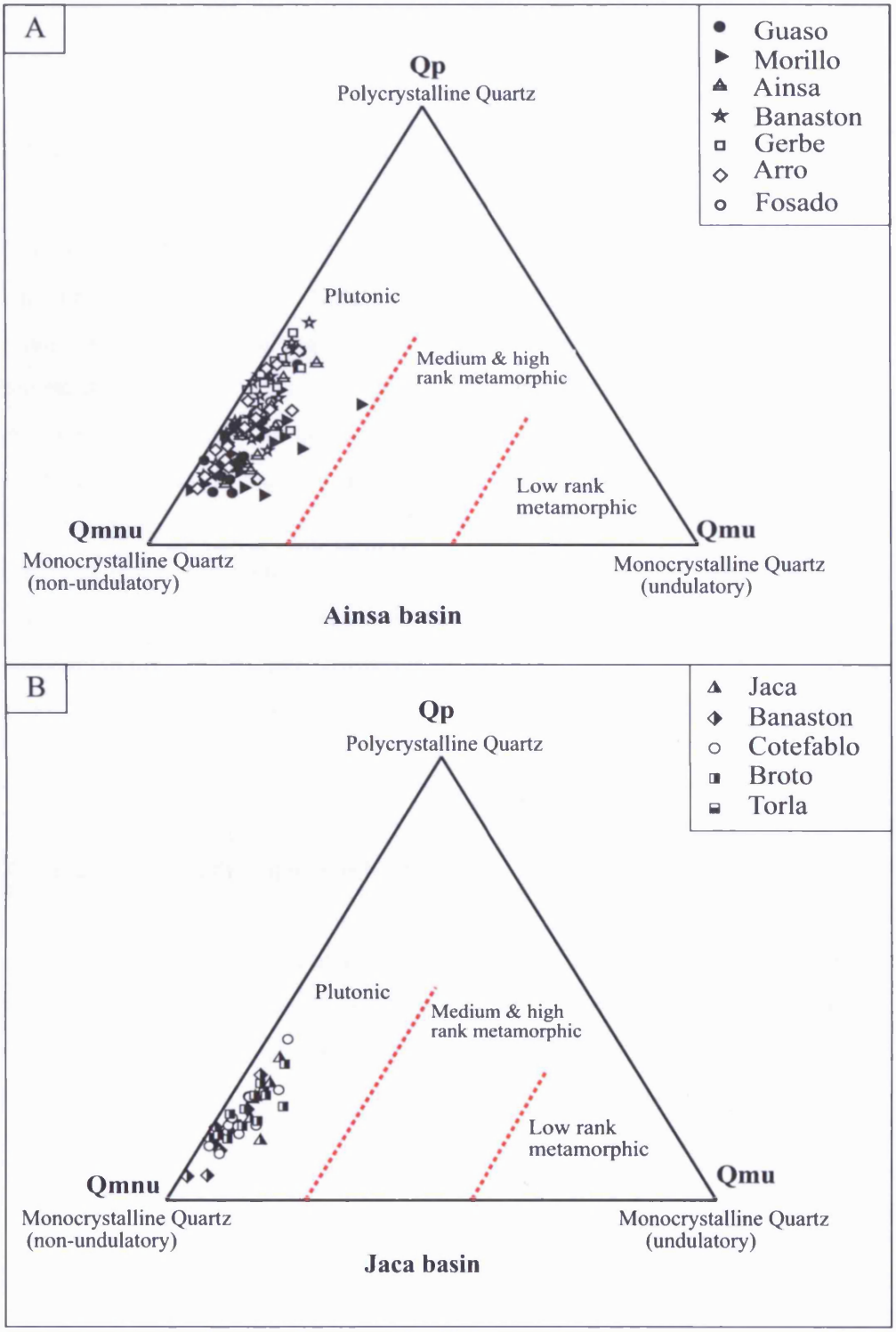

Figure 4.10: Ternary plot of detrital quartz varieties from the Ainsa and Jaca basins (after Basu et al., 1975).

have incipient silica overgrowths. These overgrowths might be the result of pressure solution at the grain contacts, indicated by the occurrence of concavo-convex and sutured grain to grain contacts (Pettijohn et al., 1987), due to burial pressure of the overlying rocks.

All the system in the Ainsa basin shows that the plagioclase to K-feldspar (P/K) ratio is <1, however, in the Jaca basin only two systems have a similar ratio, and the other three (i.e., Broto, Cotefablo and Banaston) have a P/K ratio >1. A low P/K ratio has long been assumed to indicate a polycyclic origin for the clastic sediments (Blatt 1967), because of the lower chemical stability of calcium-bearing plagioclase with respect to potassium feldspar (Nesbitt et al. 1997). Plausible explanations for the elevated P/K ratios is that the sediments in those sandy systems, which tend to be the thickest sandbodies in the Ainsa and Jaca basins, were accumulated and buried more rapidly and, therefore, are the least weathered. There are although other possible explanations for these P/K ratios, e.g., changing feldspar components in the source area. However, it is noteworthy that in this study P/K ratios were not used to constrain the nature of the sediment source.

4.8 Corrections for indistinguishable limeclasts

As discussed in earlier section of this chapter, the siliciclastic fraction of the Ainsa and Jaca basins was insufficient to identify any compositional trend or petrofacies. It was only when the carbonate fractions were included, along with the siliciclastic fraction and differentiated as non-coeval extrabasinal (CE) or coeval intrabasinal (CI) grains in the petrographic modal analysis, the compositional trend and petrofacies were revealed which were then used to constrain the evolution of the basinal sediments.

It was not always possible, however, to discriminate between the non-coeval extrabasinal and coeval intrabasinal grains. These carbonate framework grains, which could not be identified either as CE or CI due to the lack of diagnostic characteristics, were counted as a separate group (limeclasts) while performing modal analyses. In order to test the validity of the compositional trend discussed above, the limeclasts

were reapportioned in two different ways: (i) as if they are all extrabasinal, and (ii) as if they are all intrabasinal. Figure 4.11A shows that despite making these modifications to the petrographic data from the arenites of the Ainsa basin, the three main petrofacies field and the overall evolution patterns do not show any significant change. This is also true in the case for the Jaca basin arenites (Fig. 4.11B). Hence by introducing these corrections the main pattern in the ternary plots do not change significantly and the discussed results remain valid.

Although similar petrofacies to those described by Fontana et al. (1989) were identified, some of the results acquired in this study differ significantly from their work. The Banaston and the Ainsa systems were previously classified as calcilithite petrofacies but this study has shown that they belong to the hybrid arenite petrofacies. Similarly, the Gerbe system now belongs to the sandstone petrofacies instead of the hybrid arenites petrofacies as described by Fontana et al. (1989). The major reason for these disagreements is a better understanding of the stratigraphy of the Ainsa and Jaca basins resulted from recent studies (e.g., Pickering and Corregidor, 2000, 2005; Remacha and Fernandez, 2003; Fernandez et al., 2004; Remacha et al., 2005). This improved understanding has led to the availability of more detailed geological maps and stratigraphic sections, thereby, permitting more reliable and better-constrained sampling from the various sandbodies within the basin.

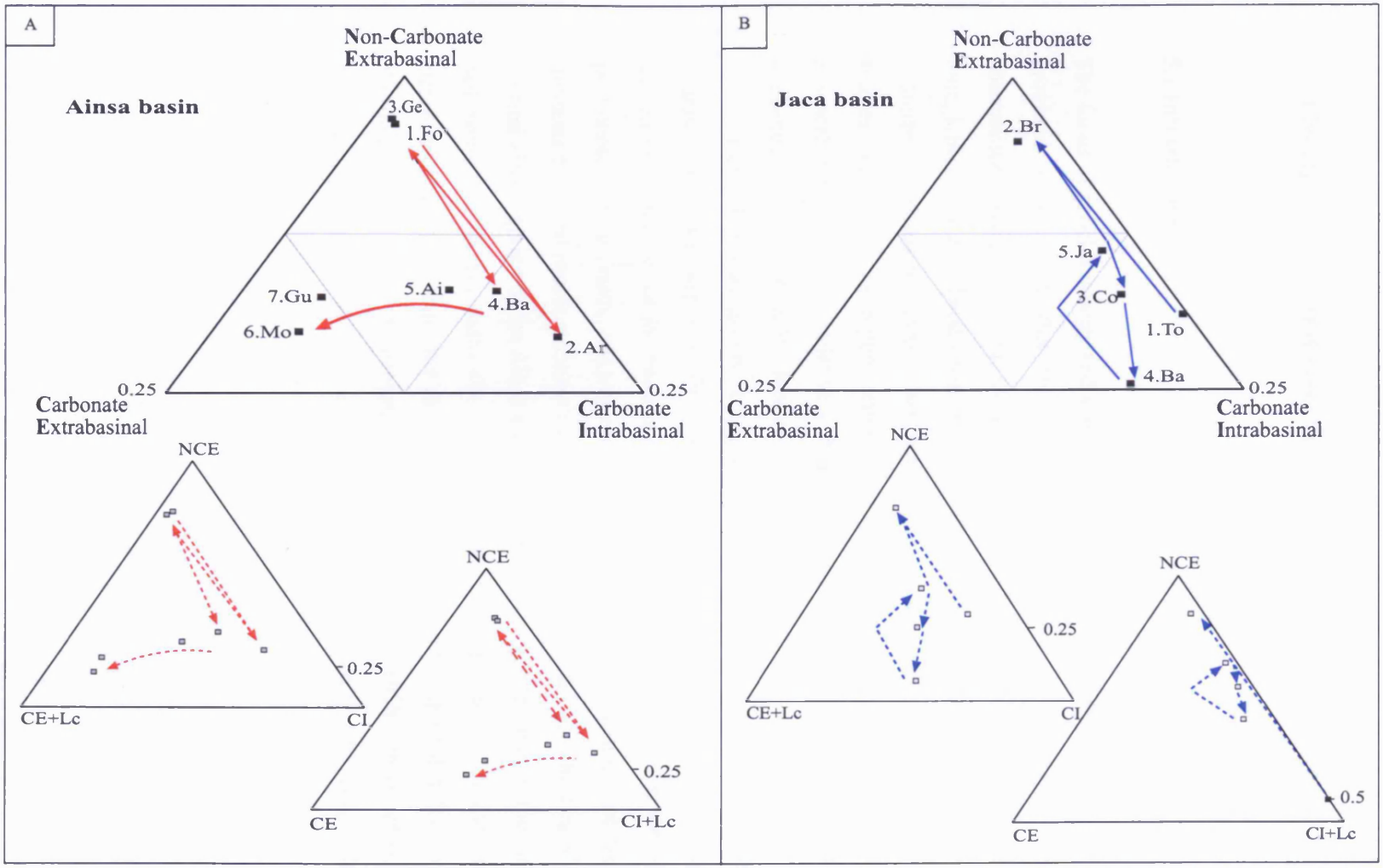

Figure 4.11: Compositional changes observed in (A) Ainsa basin systems and (B) Jaca basin systems. Incorporating limeclasts (Lc) either in carbonate extrabasinal (CE) corner or in carbonate intrabasinal (CI) corner does not change the compositional trend significantly. Numbers refer to chronological order of the sandy systems. [Ainsa basin: Fo: Fosado; Ar: Arro; Ge: Gerbe; Ba: Banaston; Ai: Ainsa; Mo: Morillo; Gu: Guaso. Jaca basin: To: Torla; Br: Broto; Co: Cotefablo; Ba: Banaston; Ja: Jaca.]

CHAPTER 5

Geochronology and Geochemistry of the proximal Ainsa basin

5.1 Introduction

The focus of geochronology and geochemistry study in this thesis is principally on the proximal Ainsa basin, that represent essentially slope and proximal basin-floor channelised environments, rather than the Jaca basin which are essentially outer-fan lobe, lobe-fringe and distal basin floor deposits, in order to achieve constraints on the sediment provenance. Zircon has been more widely used in provenance-related studies because of its higher temperature stability, generally robust resistance to physical transport and relatively high concentrations of U and Th and low concentration of common Pb (Reiners et al., 2005).

Detrital zircon grains, being a heavy mineral, are relatively abundant in coarser siliciclastic deposits. The deep-marine systems of the Ainsa basin represent the coarsest fraction of the basinal deposits and also the sediments in the proximal part contain more clastic components than the distal units. In contrast, the Jaca basin contains finer sediments enriched in carbonate. Therefore, the possibilities of finding detrital zircon grains in the Ainsa basin sediments is far greater than in the Jaca basin sediments. The Ainsa basin also represents the 'transfer zone' from shelf to slope depositional environment through which sediments were transported to the Jaca basin throughout most of the depositional history (Marzo et al., 1998; Dreyer et al., 1999). Considering these factors, along with scope of the research and funding constraints, sediments from the Ainsa basin siliciclastic systems were mainly targeted for detrital zircon geochronology.

Within the wider framework of sedimentary provenance studies, geochronology data are best used alongside other geological methods like petrography, geochemistry and sedimentology, to develop the most complete picture of the sediment provenance of a basin and its source region discrimination, characterisation and thermotectonic aspects of hinterland evolution. Various researchers (e.g., McLennan et al. 1993; Carter, 1999) have remarked that studies

which fail to integrate data from a variety of disciplines are open to the effects of distortion and bias arising from diagenesis, climate, sediment recycling, and changing geology associated with increased levels of erosion. Hence, major and trace elements were analysed from the Ainsa basin principally to *complement* the geochronology data. In the following sections, results from the major and trace element geochemistry and detrital zircon geochronology of the Ainsa basin are reported.

5.2 Geochemistry

5.2.1 Major element composition

Table 5.1 lists major element concentrations from each system of the Ainsa basin obtained from the XRF analyses and also the errors on major element determinations (2σ). It is noteworthy that the major element data are corrected for the effect of high amount of carbonates in the samples using a synthetic $CaO\text{-}SiO_2$ standard (Chapter 3). It is very common to estimate the degree of chemical alteration of the rocks (sandstones) involved in any geochemical studies before deciphering any ideas utilising the major element data. The extent of chemical weathering of the source rock and/or weathering of the sediment during transport can be assessed by calculating the chemical index of alteration (CIA = $Al_2O_3/ [Al_2O_3+Na_2O+K_2O + CaO^*] \times 100$) whereby CaO* being the amount of CaO in the silicate fraction only (Nesbitt and Young, 1982). A low CIA indicates that alteration is absent or only incipient, whereas a moderate or high CIA is correlated with the removal of mobile cations (e.g. Ca^{2+}, Na^+ and K^+) relative to the less mobile residual constituents (Al^{3+} and Ti^+) (Nesbitt and Young, 1982). On such a scale, the CIA values vary from about 50 for unweathered upper crust igneous rock to about 100 for highly weathered residual clays, and typical shales average about 70 to 75 (McLennan et al., 1993; Taylor and McLennan, 1985). Although CIA has been established as a general guide to the degree of weathering, chemical changes resulting from other processes, such as diagenesis and metamorphism, have not been fully evaluated.

Table 5.1: Major element chemical composition (in wt %) of the Ainsa basin sandstones. Note that totals do not include the LOI column, and the major oxides are calculated on an anhydrous basis and sum to 100%.

	LOI	SiO_2	Al_2O_3	Fe_2O_3	MgO	CaO	Na_2O	K_2O	TiO_2	MnO	P_2O_5	Total
Error (2σ)		± 0.15	± 0.1	± 0	± 0.07	± 0.5	± 0.1	± 0.2	± 0.006	± 0.006	± 0.005	
Fosado System												
F/1	16.44	59.07	10.04	3.95	1.86	22.19	1.41	1.68	0.420	0.068	0.095	100.78
F/2	11.5	66.07	10.76	3.38	1.95	12.84	1.71	1.75	0.408	0.048	0.108	99.02
F/3	14.75	62.25	10.22	3.64	2.16	17.49	1.24	1.85	0.485	0.063	0.117	99.51
Arro System												
Ar/B	25.44	48.36	5.05	2.27	1.46	40.37	0.79	0.65	0.180	0.060	0.061	99.24
Ar/M	21.44	54.48	5.02	2.10	1.21	32.77	1.14	1.10	0.072	0.043	0.063	98.00
Ar3/L	27.14	44.85	5.40	2.49	1.92	44.46	0.52	0.74	0.324	0.070	0.077	100.86
Ar2/B	21.75	48.01	5.04	2.25	1.41	40.91	0.89	0.66	0.175	0.066	0.066	99.47
Ar2/M	27.4	54.08	5.02	2.08	1.11	33.38	1.13	1.11	0.068	0.046	0.053	98.07
Ar2/T	24.6	36.60	3.70	2.22	1.03	53.45	0.71	0.70	0.089	0.056	0.075	98.63
Ar4/1	13.18	62.89	11.45	4.82	2.32	14.25	1.03	2.11	0.607	0.060	0.140	99.66
Ar4/2	16.7	58.47	9.20	3.55	1.93	21.82	1.28	1.51	0.419	0.065	0.099	98.34
Ar5/1	19.23	49.84	13.20	5.39	4.27	21.31	0.68	2.51	0.705	0.085	0.148	98.14
Ar6/1	21.77	54.10	6.93	2.04	1.01	33.43	1.43	0.66	0.185	0.054	0.059	99.90
Ar7/1	23.95	50.61	4.63	2.03	0.99	38.70	1.17	0.82	0.079	0.052	0.042	99.13
Ar7/2	26.63	45.61	4.65	2.02	1.01	43.89	0.98	0.90	0.073	0.050	0.059	99.24
Ar7/3	28.42	41.35	3.51	2.46	1.26	49.11	0.94	0.64	0.059	0.073	0.053	99.45
Ar8/1	22.63	51.55	6.41	2.89	1.72	34.02	1.15	1.20	0.175	0.061	0.071	99.25
Ar8/2	27.5	41.56	5.88	2.52	1.86	45.43	0.88	1.03	0.232	0.062	0.084	99.54
Ar8/3	22.95	52.40	6.34	2.65	2.14	33.92	1.13	1.40	0.160	0.055	0.056	100.23
Ar8/4	24.41	47.60	6.52	2.15	1.32	39.07	1.41	0.89	0.192	0.053	0.059	99.25
Gerbe System												
G/B	16.12	64.80	7.14	2.49	1.40	21.22	1.02	1.54	0.225	0.059	0.080	99.97
G/T	18.99	59.59	6.87	2.22	1.32	27.06	0.90	1.82	0.238	0.064	0.083	100.17
G/1	16.67	58.77	8.46	3.54	2.30	22.32	1.13	1.49	0.391	0.080	0.131	98.61
G/2	16.34	59.64	8.23	4.27	2.55	21.11	1.22	1.40	0.348	0.083	0.103	98.94
Banaston System												
B/1	25.60	44.84	4.92	1.86	1.25	42.45	0.74	1.35	0.170	0.068	0.076	97.72
B/2	18.82	59.35	5.76	1.80	1.08	28.38	0.67	1.60	0.194	0.044	0.053	98.94
B/3	18.93	60.12	6.16	1.49	1.51	27.41	0.83	1.90	0.173	0.036	0.056	99.68
B*/I	29.47	46.23	4.82	2.00	1.70	42.27	0.69	1.14	0.189	0.063	0.060	99.16
B*/II	32.84	51.35	5.82	2.68	1.94	35.76	0.64	1.15	0.362	0.057	0.073	99.82
B*/1	25.93	39.93	4.45	2.34	1.44	48.34	0.54	1.21	0.134	0.048	0.064	98.50
B*/2	23.43	51.70	5.94	2.70	2.06	35.16	0.56	1.14	0.370	0.054	0.071	99.76
B*/3	28.12	40.33	4.66	2.35	1.51	47.20	0.50	1.21	0.141	0.049	0.066	98.02
Ainsa System												
Ail/1	17.65	61.33	8.19	2.21	0.79	25.35	1.60	0.94	0.175	0.053	0.051	100.68
Ail/2	23.13	53.42	6.03	1.92	2.09	34.86	1.25	0.79	0.199	0.059	0.056	100.65
Ail/3	22.3	52.74	6.54	2.73	1.46	33.49	1.06	0.91	0.250	0.052	0.062	99.30
AiIII/1	22.97	50.35	6.64	2.73	1.69	35.44	0.90	1.64	0.307	0.059	0.064	99.81
AiIII/2	28.04	40.73	5.09	2.15	1.86	47.29	0.75	1.29	0.217	0.071	0.055	99.49
AiIII/3	30.23	35.93	4.62	2.81	1.65	52.40	0.36	1.07	0.249	0.065	0.061	99.21
Ai I	18.8	58.76	6.21	1.77	1.05	28.02	0.97	1.61	0.175	0.039	0.062	98.66
Morillo System												
Mo/1	28.55	40.09	5.68	1.67	2.03	47.40	0.81	1.32	0.200	0.054	0.063	99.31
Mo/2	31.72	31.67	5.18	2.19	2.20	55.81	0.63	1.21	0.182	0.093	0.061	99.22
Mo/3	27.17	43.16	5.82	1.54	2.12	44.61	0.85	1.46	0.181	0.046	0.064	99.85
Mo1/1	24.94	46.27	6.88	1.31	2.17	39.71	1.19	1.91	0.136	0.045	0.050	99.68
Mo1/2	34.02	26.31	5.08	1.69	3.58	60.23	0.69	1.17	0.186	0.061	0.053	99.05
Mo1/3	27.43	40.74	6.96	1.94	2.93	44.17	1.00	1.66	0.261	0.045	0.064	99.76
Mo3/1	30.79	34.88	5.45	1.54	3.04	52.47	0.75	1.40	0.219	0.056	0.063	99.86
Mo3/2	34.95	25.22	4.12	2.22	4.60	61.95	0.41	0.88	0.224	0.061	0.064	99.76
Mo3/3	29.25	37.91	5.82	1.63	2.97	48.71	0.75	1.42	0.243	0.051	0.062	99.56
Mo-Gu/1	31.76	31.66	5.07	2.52	3.71	54.64	0.51	0.98	0.295	0.066	0.071	99.51
Mo-Gu/2	25.7	44.44	5.95	1.44	2.73	40.96	1.06	1.49	0.178	0.035	0.054	98.34
Mo-Gu/3	30.82	33.59	5.56	1.97	3.66	52.19	0.91	1.49	0.198	0.058	0.066	99.68
Guaso System												
Gu1/1	22.31	32.82	6.02	2.43	3.60	51.93	0.38	1.18	0.327	0.071	0.082	98.83
Gu1/2	26.44	43.77	7.06	2.73	4.06	38.86	0.56	1.56	0.361	0.079	0.092	99.13
Gu1/3	27.47	41.83	6.41	2.58	3.87	42.46	0.67	1.42	0.353	0.082	0.090	99.77
Gu2/1	31.94	32.84	4.75	1.97	3.68	53.94	0.45	1.05	0.285	0.075	0.079	99.11
Gu2/2	31.43	32.92	4.82	1.87	3.47	54.05	0.57	1.13	0.231	0.073	0.070	99.20
Gu3/1	26.82	41.72	5.87	1.50	2.31	44.02	1.07	1.92	0.125	0.047	0.053	98.64
Gu3/2	29.83	36.15	5.19	2.33	3.27	49.95	0.71	1.16	0.264	0.055	0.062	99.13
Gu3/3	30.65	34.54	5.83	1.50	4.26	50.87	0.89	1.66	0.195	0.041	0.067	99.85

Evaluating CIA for the Ainsa basin sandstones requires estimating the amount of CaO present in the silicate fraction. It is already mentioned that the Ainsa basin sandstones contain variable amounts of carbonate minerals in different phases as revealed by microscopic examination of the thin-sections (Chapter 4). Calcite and dolomite coexist in these rocks, and there are no microprobe data available on these minerals. In this scenario, an indirect way of estimating CaO in the silicate fraction, excluding the carbonate fraction, is attempted here.

It is stated that for XRF analysis sample powders were pre-ignited at 1100^0C for 20 minutes (Section 3.4.1). If it is assumed that there is a negligible H_2O component in loss on ignition (LOI) and no Ca in silicate minerals, there should be an excellent correlation between CaO and LOI. In the Ainsa basin sandstones this is true for most of the samples (Fig.5.1) suggesting most of the CaO has a carbonate origin and there is very little Ca in the silicate phases. All samples, except for a few outliers, fall on a straight line (Fig.5.1) which would suggest that the line represents a mixing relationship between a carbonate and a clastic end member. The outliers above the mixing line can be explained by dolomite contamination. The outliers below the main trend come from the Arro, Banaston and Guaso systems. Sandstones in the first two systems are subarkose arenites while sandstones from the Guaso system are feldspathic litharenites (see Table 4.4), and so it is reasonable to assume that these few samples have a relatively high percentage of Ca-rich feldspar (e.g., albite). These samples are used in the calculation of CIA and the value calculated ranges between 50 and 74 reflecting a moderately weathered source. For comparison, the CIA of average upper continental crust (UCC) is 50 (Taylor and McLennan, 1985).

The SiO_2 content of the samples (sandstones) from the Ainsa basin ranges from 25.22 to 66.07 wt %. The mean SiO_2 content of the Morillo and the Guaso system are the least among the Ainsa basin samples, the highest being that of the Fosado and the Gerbe system (Table 5.2). Two samples, Mo1/2 and Mo 3/2, have less than 30 wt % of SiO_2 (Table 5.1) and these two samples are also marked by relatively higher concentrations of CaO, MgO and CO_2 (assuming loss on ignition equals CO_2). The Arro, Banaston and Ainsa system have intermediate values of SiO_2. A similar pattern can also be observed when comparing the mean Al_2O_3 values of each system. The mean CaO value ranges between 17.51% and 47.56%. The Fosado and the Gerbe system are on the lower end of the range, the highest value being noted in the Morillo system. In case of the MgO content all the systems have $\leq$2% MgO (mean), except for

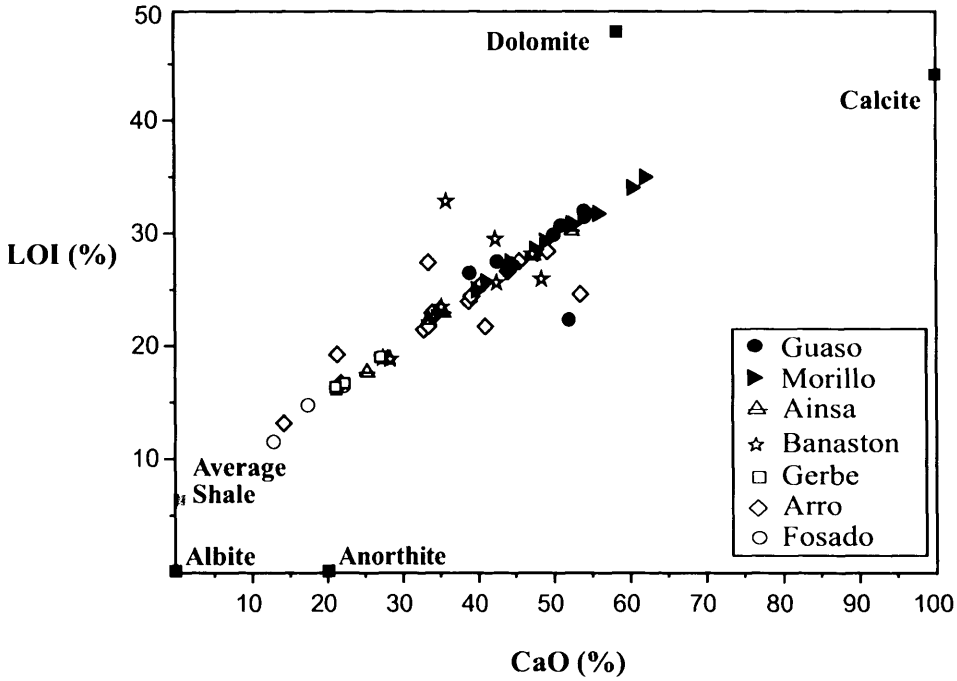

Figure 5.1: Cross-plot illustrating the relation between CaO and LOI (loss on ignition) in the Ainsa basin samples. A good correlation exists between the two parameters, suggesting most of the CaO is present in calcite.

Table 5.2: Mean concentration of major oxides (in wt %) and K_2O/Na_2O values of the seven depositional systems from the Ainsa basin.

System	*N*	SiO_2	Al_2O_3	CaO	MgO	Fe_2O_3	K_2O/Na_2O
Guaso	8	37.07	5.74	48.26	3.57	2.11	2.09
Morillo	12	33.59	5.63	50.24	2.98	1.81	1.64
Ainsa	7	50.47	6.19	36.69	1.51	2.33	1.47
Banaston	8	49.23	5.32	38.37	1.56	2.15	2.08
Gerbe	4	60.70	7.68	22.93	1.89	3.13	1.46
Arro	17	49.55	6.35	36.49	1.65	2.70	1.08
Fosado	3	62.46	10.34	17.51	1.99	3.66	1.23

the Morillo and the Guaso system where it is ≥3%. The remaining major oxides, except Fe_2O_3, show similar pattern of concentration among all the seven sandstone systems. In contrast, the mean Fe_2O_3 concentration in the Fosado and the Gerbe system is >3% while in all the other systems it is <3%

The major oxide composition outlined above can be correlated with the petrofacies of each system e.g., the Fosado and the Gerbe system both belong to siliciclastic rich 'sandstone' (non-carbonate extrarenites) petrofacies and have higher amount of SiO_2 and lower CaO. Similarly, theses two systems are also enriched in Al_2O_3 that can be linked to feldspar modal abundance in these systems. The Fe_2O_3 content correlates well with the concentration of lithic fragments (siliciclastic sedimentary, low-grade metamorphic and volcanic rock fragments), at least as long as Fe does not occur dominantly in carbonates and it shows relative enrichment in the Fosado and the Gerbe system (sandstone petrofacies). In all other systems, which belong to either carbonate enriched 'hybrid arenite' or 'calcilithite' (carbonate extrarenites) petrofacies, SiO_2 and Al_2O_3 content is relatively lower along with higher CaO content than the 'sandstone' petrofacies. The carbonate enriched petrofacies can be distinguished on the basis of MgO content. The Morillo and the Guaso system both belong to 'calcilithite' petrofacies, have higher MgO amount than the systems belonging to 'hybrid arenite' petrofacies (i.e., Arro, Ainsa and Banaston). This relatively high MgO content is most likely due to the abundance of dolostones in the Morillo and the Guaso system.

There is a weak positive correlation between SiO_2 - Al_2O_3, SiO_2 – Na_2O and SiO_2 – K_2O (Fig. 5.2). These weak correlations are most likely due to the occurrence of plagioclase [albite ($NaAlSi_3O_8$)-anorthite ($CaAl_2Si_2O_8$)] and K-feldspar [microcline ($KAlSi_3O_8$)] in the framework grains of the sandstone systems. In contrast there is a very strong negative correlation between SiO_2 and CaO (Fig. 5.2). This is simply a consequence of mixing limestone debris with siliciclastic material. The average K_2O/Al_2O_3 ratios of the Ainsa basin sediments is 0.21, which is very close to K_2O/Al_2O_3 ratios in the upper continental crust (UCC) average composition (0.22). The FeO + MgO value ranges between 2.8 and 9.7, which is close to the FeO + MgO range of modern deep-sea sands (Taylor and McLennan, 1985).

The effect of grain size on the major oxide concentrations are verified using a scatter plot between the two parameters (Fig. 5.3). Most of the samples analysed ranges between very-fine (lower) sand and medium (lower) sand size, i.e., between 65

and 350μm. However, a few samples reach up to coarse sand size (~700μm). Majority of the major oxides show various degree of dispersion of the weight% values in the size range between 65 and 350μm. Apparently there are very weak or no correlations between the concentration and the grain-size for most of the major oxides, e.g, SiO_2, Al_2O_3, K_2O, Na_2O, MnO and P_2O_5. Among the other major oxides, the CaO concentration shows weak positive correlation with increasing grain-size. In contrast, the Fe_2O_3, MgO and TiO_2 values show a slight decrease (replacement decrement) in concentration with increase in grain-size. The pattern displayed by CaO implies that the finer-grained sandstones are relatively depleted in calcite than the coarser-grained sandstones (assuming CaO originating mainly from calcite, as SiO_2 and Al_2O_3 should have some effects if it would have come from feldspars). Similarly depletion of MgO indicates coarser sandstones have lower dolomite component. The Fe_2O_3 values also show negative correlation with increasing grain size which might be due to the fact that carbonates show mutual substitution of Mg^{+2} and Fe^{+2}. Interestingly, the TiO_2 concentration seems replicating the negative correlation pattern of Fe_2O_3 concentration suggesting a possible relationship between the two oxides. This might be due to the occurrence of opaque minerals such as ilmenite in the sandstones (e.g., Ryu, 2003) and in this study particularly in the finer-grained sandstones (Fig.5.3).

Crook (1974) subdivided flysch arenites (graywackes) on the basis of SiO_2 content and the relative K_2O/Na_2O ratio into three distinct groups: quartz-poor (average 58% SiO_2; K_2O/Na_2O <<1), quartz-intermediate (average 68-74% SiO_2; K_2O/Na_2O <1) and quartz-rich (average 89% SiO_2; K_2O/Na_2O >1). All samples from the Ainsa basin may be classified as quartz-poor (mean 47%) as per the SiO_2 content; however, according to the K_2O/Na_2O ratio the same samples may be classified as quartz-rich (K_2O/Na_2O >1). The Ainsa basin sandstones contain a significant carbonate component, as framework grains and cements, in addition to the other siliciclastic minerals and therefore classification scheme is not relevant for these rocks. The presence of carbonates is unlikely to affect the K_2O/Na_2O ratio, whereas the abundance of carbonate grains is more likely to reduce the amount of quartz as reflected in the abundance of quartz.

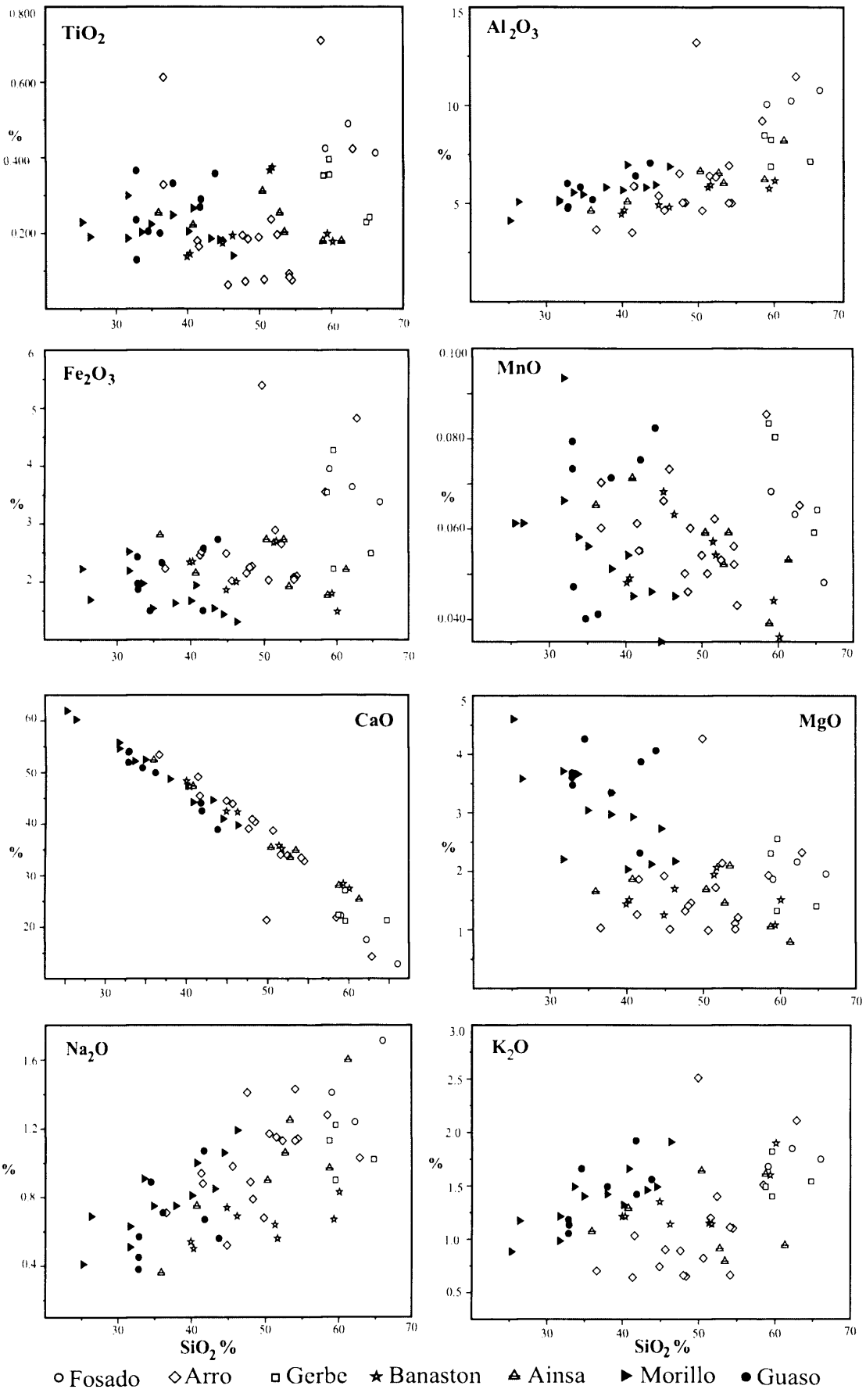

Figure 5.2: Harker variation diagram of major elements for sandstones of the Ainsa basin.

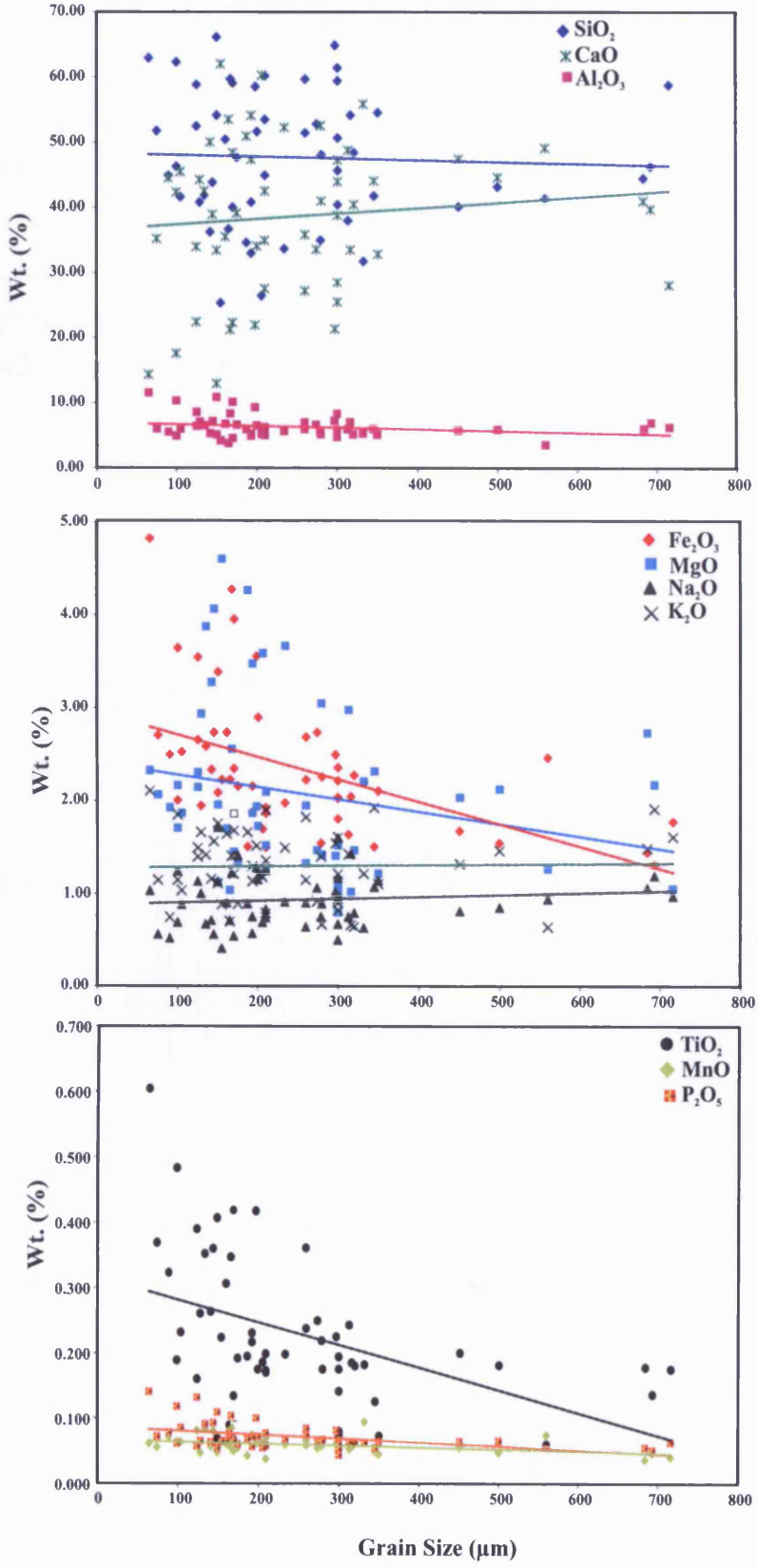

Figure 5.3: Plots displaying the effect of grain size on major element distributions in the Ainsa basin sandstones. Note the relative increment or decrement of each oxide relative to increasing grain size (see text for details). Dashed lines represent the linear trend line for each major oxide.

Pettijohn et al. (1987) used a widely employed diagram to classify terrigenous sands on the basis of log (Na_2/K_2O) versus log (SiO_2/Al_2O_3). The same geochemical classification for sandstone is also used in this study (Fig. 5.3), although most of the sandstones in this study are not typical 'sandstone'. In the cross-plot, all of the samples are seen to cluster at the border of the three sandstone types – arkose, lithic arenite and subarkose. However, the plot reveals that the Ainsa basin sandstones are principally arkose arenites along with some lithic arenites which correlates well with the result obtained from the petrographic classification (see Table 4.4).

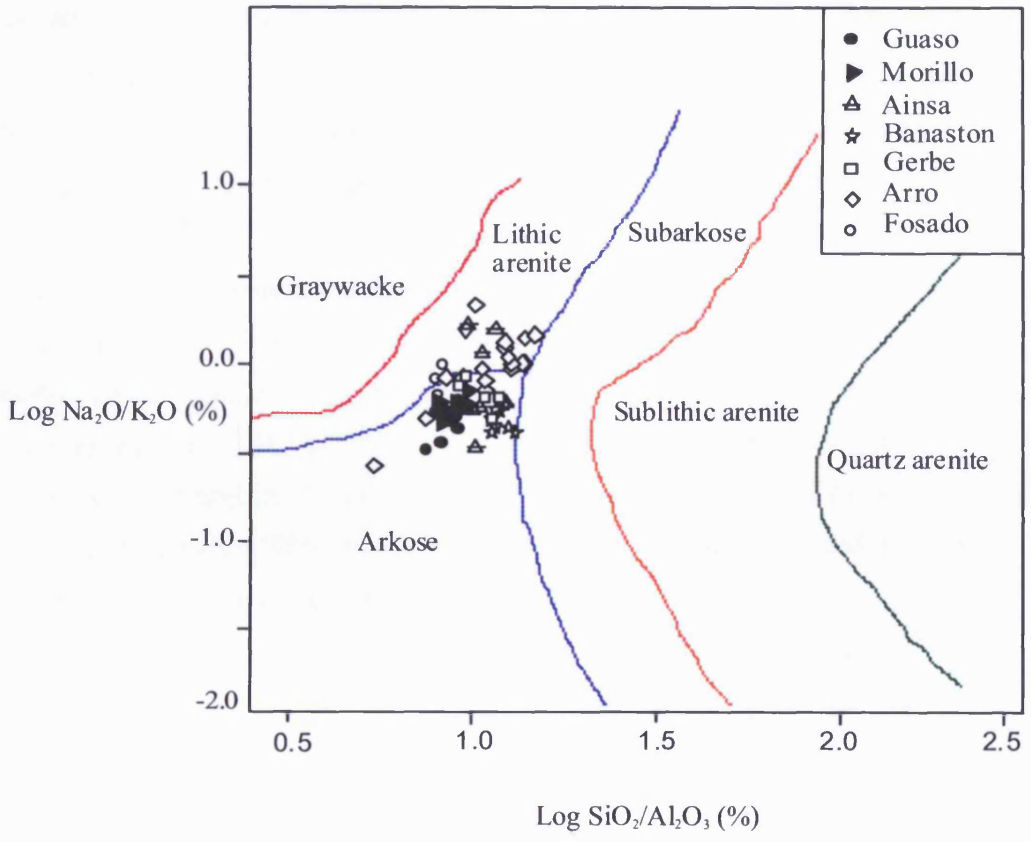

Figure 5.4: Geochemical classification of Ainsa basin sandstones using log (Na_2O/K_2O) vs. log (SiO_2/Al_2O_3) (after Pettijohn et al., 1987). The sandstones fall mostly into the arkose field, although some plot in lithic arenite range.

As the goal for major (and trace element) analysis was set to complement geochronology data, different discrimination diagrams to characterise the tectonic setting (and the source rock composition) are presented in the following sections. In this study the widely adopted discrimination diagrams proposed by Bhatia (1983) and Roser and Korsch (1986) are used for characterising the tectonic setting. Although the major element concentrations were adjusted using a synthetic CaO-SiO_2 standard to minimise the effect of higher carbonate content, it is stressed here that the attempt to characterise the tectonic settings of the Ainsa basin using those widely used discrimination diagram is more of a test to see whether these diagrams are applicable for sandstones with higher carbonate content.

In the SiO_2 vs. K_2O/Na_2O discrimination diagram of Roser and Korsch (1986) (Fig. 5.5a) majority of the samples fall in the ACM (active continental margin) field, with a few sample plotting outside the ACM field. In contrast, data are more dispersed in the Fe_2O_3+MgO-TiO_2 (Fig. 5.5b) and the Fe_2O_3+MgO – Al_2O_3/SiO_2 (Fig. 5.5c) discrimination diagrams proposed by Bhatia (1983). Majority of the samples lie outside but the ACM field. However, data in the latter diagram cluster more in and around the ACM field. Nevertheless, taking all the three diagrams into account, these discrimination diagrams broadly suggest an active continental margin setting for the Ainsa basin sandstones. Therefore, the discrimination diagrams of Bhatia (1983) and, Roser and Korsch (1986) for determining tectonic settings of sandstones with a significant carbonate component are only applicable to a certain extent.

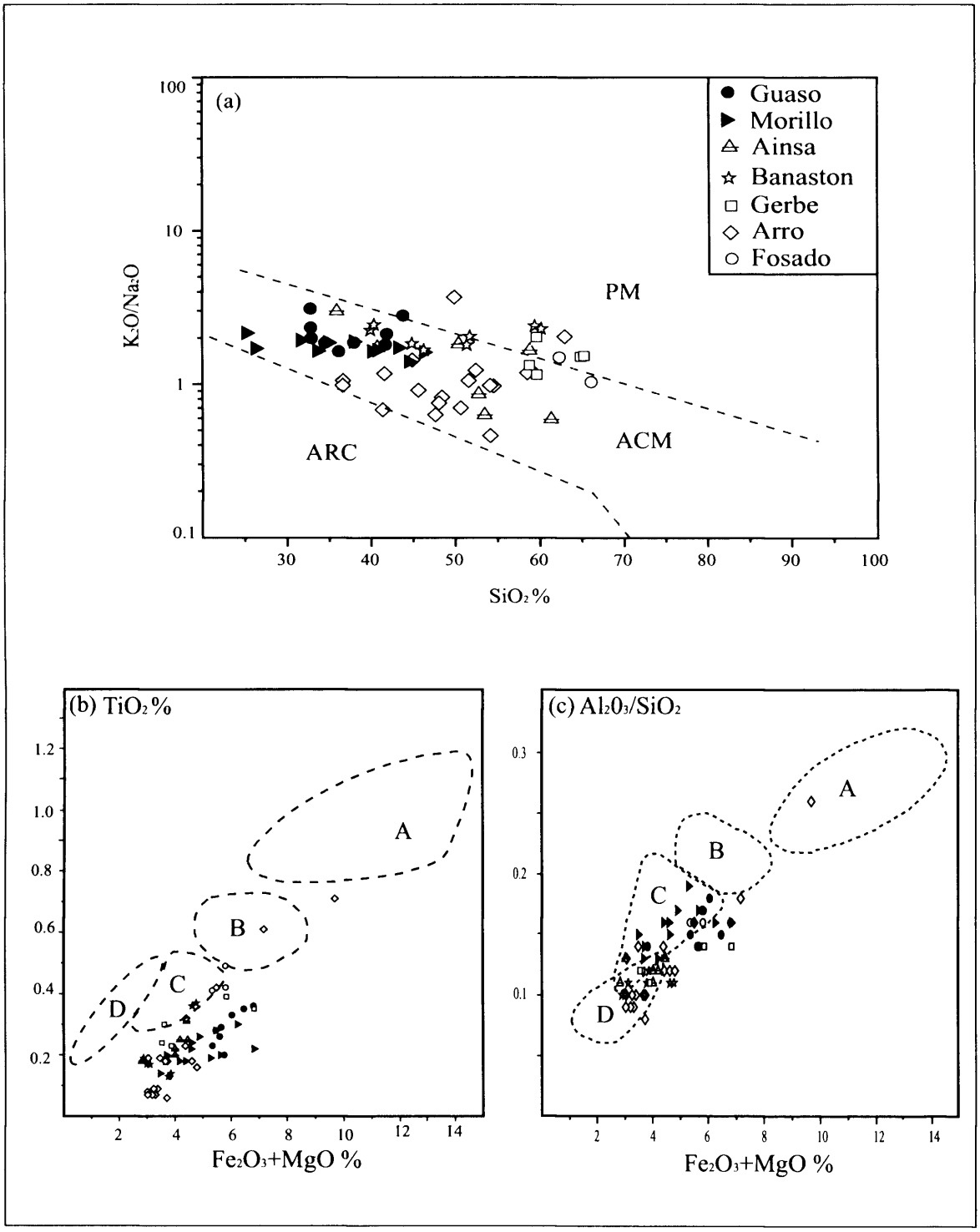

Figure 5.5: Tectonic discrimination diagram of (a) Roser and Korsch (1986). PM= passive margin; ACM = active continental margin; ARC= oceanic island arc margin; (b) and (c) Bhatia (1983). A: Oceanic island arc; B: Continental island arc; C: Active continental margin; D: Passive margin. These discrimination diagrams suggest that the Ainsa basin clastic sediments were deposited in an active continental margin tectonic setting.

5.2.2 Trace element composition

The following set of trace elements were analysed using the XRF technique (Chapter 3) from the clastic systems of the Ainsa basin: Ni, Cr,V, Sc, Cu, Zn, Cl, Ga, Pb, Sr, Rb, Ba, Zr, Nb, Th, Y, La, Ce and Nd. Concentrations of each of these element are presented, along with the errors on trace element determinations (2σ), in Table 5.3. No such systematic trends of trace element concentration among the systems of the Ainsa basin were observed. Figure 5.6 shows distribution of some of the trace elements against major elements.

Chlorine concentration was below detection limit of XRF in most of the samples. Among the transition metals (i.e. Ni, Cr and V), in general, V has relatively higher concentration in all the systems (Table 5.3). However, all of them have a positive correlation with TiO_2 (Fig. 5.6), titanium being one of the most refractory products of crustal weathering (Taylor and McLennan, 1985). Nickel, Cr, and V concentration proved to be very important for discrimination of source rock lithologies and tectonic setting. Vanadium, Cr, Co and Ni are compatible elements during igneous fractionation processes and are generally 'depleted' in felsic minerals and 'enriched' in mafic minerals. Common felsic minerals include quartz, muscovite, orthoclase, and the sodium-rich plagioclase feldspars, whereas common rock-forming mafic minerals include olivine, pyroxene, amphibole, biotite, augite and the calcium-rich plagioclase feldspars. Strontium has the highest concentration in the Ainsa basin sediments among all the measured trace elements, with a maximum value of ~900 ppm, followed by Ba and Zr. It (Sr) has a weakly negative correlation with K_2O, in contrast, a strong positive correlation exist between Rb and K_2O (Fig. 5.5). Rubidium and Ba substitute for K that mainly exists in the mineral phases like K-feldspar and biotite .The chemical similarity of Sr to Ca allows it to substitute into calcium bearing minerals such as feldspar, muscovite, biotite, and calcite.

Table 5.3: Trace element content of the Ainsa basin sandstones (in ppm).

	Ni	Cr	V	Sc	Cu	Zn	Cl	Ga	Pb	Sr	Rb	Ba	Zr	Nb	Th	Y	La	Ce	Nd
Error (2σ)	± 0.6	± 1.5	± 1.4	± 1.3	± 0.7	± 0.9	± 9.5	± 1.2	±1.1	± 1.8	± 0.6	± 3.8	± 0.8	± 0.3	± 0.9	± 0.5	± 1.2	± 2.8	± 1.4
Fosado System																			
F/1	27.7	49.5	83.5	12.0	12.5	77.6	36.9	13.5	12.0	491.1	75.9	318.5	137.7	9.3	7.5	27.5	22.2	44.5	22.8
F/2	24.0	48.7	80.9	11.7	8.2	70.0	-	13.5	11.1	217.0	81.8	290.7	148.5	8.5	7.8	20.1	28.1	51.5	23.1
F/3	25.8	47.9	79.7	11.7	9.6	72.1	-	11.6	7.6	325.0	81.0	327.6	190.3	10.2	9.0	25.1	27.0	50.2	25.5
Arro System																			
Ar/B	25.2	32.1	29.4	13.5	3.0	54.5	-	6.7	11.4	810.2	30.5	198.8	58.6	3.7	2.7	23.0	16.7	30.5	19.6
Ar/M	13.2	12.4	13.4	7.4	1.1	25.2	-	4.4	14.6	1059.4	40.5	103.8	37.2	1.3	0.8	13.2	9.7	17.8	10.9
Ar3/L	16.5	37.8	36.0	11.4	4.3	44.6	-	4.2	8.3	931.4	31.2	108.0	182.8	6.6	5.9	21.5	17.9	37.3	19.4
Ar2/B	16.7	34.3	37.5	8.0	2.9	25.9	-	5.0	12.4	636.8	35.1	79.2	51.2	3.1	3.4	18.0	16.6	33.1	16.7
Ar2/M	26.0	54.0	48.4	12.5	4.6	57.5	-	6.0	10.9	757.0	41.9	155.4	118.5	6.5	5.0	24.3	19.9	43.6	23.0
Ar2/T	19.0	40.8	37.5	12.4	3.9	45.1	-	5.9	11.1	791.0	34.5	115.0	80.1	4.8	3.6	20.0	20.7	36.9	21.1
Ar4/1	35.7	67.3	111.5	14.2	22.9	84.5	-	15.9	20.4	245.1	90.0	411.1	213.2	12.1	9.9	29.6	33.0	68.0	31.1
Ar4/2	25.8	46.5	72.3	10.3	8.8	58.5	-	10.7	13.7	380.3	67.2	378.6	176.2	8.5	8.4	22.7	24.5	49.0	23.1
Ar5/1	40.4	84.2	138.6	16.8	22.7	91.7	-	17.2	20.1	348.7	112.4	342.1	200.0	15.0	11.3	31.3	37.6	74.2	33.9
Ar6/1	14.4	33.7	36.3	9.1	1.7	33.0	-	5.9	9.6	702.3	31.2	220.6	67.5	4.1	3.4	15.6	15.1	30.3	15.4
Ar7/1	21.1	13.9	15.7	6.6	3.2	30.7	-	4.3	18.1	1304.0	32.5	77.8	33.6	1.6	2.3	15.3	9.6	18.5	12.9
Ar7/2	10.3	13.7	15.5	11.5	3.2	22.5	-	3.9	11.7	951.6	33.8	75.9	28.8	1.4	2.0	11.2	8.9	15.8	10.0
Ar7/3	14.7	12.3	13.3	9.8	2.3	14.6	-	2.4	13.8	1513.0	25.4	84.0	26.9	1.2	1.7	10.0	10.8	18.9	12.2
Ar8/1	18.2	27.6	28.1	10.4	2.9	37.8	-	8.0	14.0	876.2	47.0	271.8	67.1	3.9	4.0	16.7	15.9	31.5	16.9
Ar8/2	16.9	30.4	34.8	14.8	3.8	46.6	-	5.6	8.4	1142.4	42.5	114.8	61.1	5.4	4.0	17.8	15.8	26.6	17.7
Ar8/3	14.4	26.8	29.7	8.4	1.9	25.7	-	6.4	10.5	653.8	51.8	224.4	55.1	3.6	2.5	13.7	14.8	25.2	16.1
Ar8/4	21.8	45.9	57.8	9.4	4.0	40.8	-	6.8	16.5	718.7	40.3	153.6	56.2	4.4	4.9	17.9	17.8	34.7	18.0
Gerbe System																			
G/B	15.4	28.2	45.8	7.1	3.1	32.6	-	8.8	10.0	476.0	62.6	745.1	73.4	4.8	4.4	15.2	21.0	34.3	15.9
G/T	15.1	22.7	33.8	9.0	3.5	31.1	-	7.7	8.8	666.4	69.4	223.8	94.6	4.6	4.6	14.5	17.2	28.0	15.5
G/1	24.9	43.0	65.7	11.1	6.4	54.0	-	9.9	8.4	585.9	61.0	265.5	130.4	7.4	5.9	17.5	21.2	42.5	19.9
G/2	21.0	41.0	66.8	10.1	7.1	49.4	-	10.2	9.4	686.8	62.4	394.5	109.8	7.2	6.4	19.9	25.4	47.9	23.7
Banaston System																			
B/1	11.4	24.0	28.6	10.7	2.3	22.8	-	5.2	9.8	1132.3	48.7	144.0	61.6	3.3	3.1	9.8	9.5	21.5	12.0
B/2	16.8	27.0	35.7	10.6	3.7	24.7	-	5.2	12.8	483.1	60.8	195.4	67.5	4.0	4.2	12.1	13.3	24.2	12.8
B/3	11.5	25.7	28.0	6.7	1.3	22.2	-	6.6	10.5	459.9	64.4	205.5	67.3	3.5	2.6	11.0	21.2	23.7	13.4
B*/I	23.3	34.3	44.9	12.9	5.6	39.2	-	5.2	12.7	1188.5	42.5	156.6	93.6	5.5	3.7	16.5	16.6	35.5	18.1
B*/II	13.5	23.2	31.3	19.0	3.6	18.4	-	3.5	7.9	1252.1	28.2	100.2	41.2	2.9	3.7	10.8	12.1	20.7	13.1

Table 5.3. *(Continued)*

	Ni	Cr	V	Sc	Cu	Zn	Cl	Ga	Pb	Sr	Rb	Ba	Zr	Nb	Th	Y	La	Ce	Nd
B*/1	13.9	27.2	26.0	9.2	3.7	21.6	-	6.2	9.2	825.0	43.2	120.7	90.8	3.9	3.9	13.9	15.4	30.4	16.0
B*/2	22.5	39.6	52.1	11.4	5.5	39.6	-	7.1	12.2	739.6	49.1	151.0	161.9	7.8	5.2	17.9	18.5	39.9	18.4
B*/3	21.5	21.8	27.9	12.4	3.2	34.3	-	5.8	17.0	1286.4	45.0	123.9	51.8	2.7	1.7	12.1	9.6	22.1	14.7
Ainsa System																			
AiI/1	12.9	25.9	31.3	5.7	2.4	23.2	-	7.1	11.6	530.6	40.0	412.6	62.0	3.4	2.8	11.1	13.5	21.6	12.4
AiI/2	14.4	27.4	30.8	10.3	3.4	28.2	2.2	6.1	8.6	755.6	32.6	112.7	69.7	3.6	2.9	16.1	12.3	29.0	16.9
AiI/3	19.7	30.8	40.1	10.6	4.4	37.0	-	5.7	12.3	782.0	39.3	121.5	90.1	5.4	4.6	16.4	13.7	29.2	16.5
AiIII/1	22.5	37.7	48.5	9.5	6.0	41.8	37.2	7.2	15.5	786.8	61.0	160.3	132.6	6.3	5.1	17.5	17.1	31.1	17.6
AiIII/2	14.4	25.6	32.1	15.2	6.5	26.3	35.5	5.1	9.2	1229.4	46.4	117.5	89.3	4.1	3.2	15.1	14.4	25.5	14.8
AiIII/3	28.4	39.1	43.3	17.5	6.9	33.0	4.4	4.9	21.8	867.3	41.0	94.4	77.7	5.0	3.6	15.4	16.1	31.7	18.3
Ai I	15.5	27.4	38.4	7.2	4.0	39.6	-	7.7	14.5	670.5	60.5	215.2	71.3	4.0	3.7	13.4	13.3	24.5	13.7
Morillo System																			
Mo/1	18.0	46.0	37.0	15.6	3.9	27.5	38.8	5.0	11.3	575.1	47.3	151.5	55.5	3.5	2.5	13.0	12.8	26.5	15.2
Mo/2	17.2	36.1	34.1	18.6	4.1	22.5	45.2	5.4	7.4	867.6	44.2	120.9	45.1	3.6	2.8	11.9	10.0	26.4	14.5
Mo/3	16.0	36.1	38.2	13.2	4.0	21.6	9.0	4.6	9.7	575.5	51.6	148.0	57.5	3.6	3.4	10.9	12.8	23.9	13.6
Mo1/1	15.3	27.8	28.1	12.2	3.1	21.9	50.6	6.7	10.4	560.4	68.2	433.2	49.9	3.1	2.2	9.9	11.3	27.8	13.9
Mo1/2	17.6	42.0	39.9	20.4	3.9	23.2	-	5.2	7.4	1216.9	42.1	112.0	61.4	3.5	2.1	12.7	15.5	31.1	17.9
Mo1/3	17.7	38.4	50.3	11.3	5.9	33.9	-	9.0	10.7	597.0	63.3	158.3	92.3	6.0	4.7	14.1	17.2	33.1	17.6
Mo3/1	18.1	44.5	41.5	16.8	9.5	28.9	39.7	5.1	10.7	531.9	52.3	129.0	93.3	3.6	4.6	14.2	15.1	35.9	18.6
Mo3/2	15.2	28.1	34.5	22.1	4.8	34.6	59.2	4.5	9.8	1259.6	32.1	87.2	71.3	4.3	3.3	12.1	25.1	26.9	15.0
Mo3/3	18.9	44.3	49.4	14.1	5.1	32.9	186.4	5.5	10.4	805.8	52.6	140.9	70.5	4.6	3.4	14.1	18.7	34.6	17.6
Mo-Gu/1	19.5	39.4	46.7	18.9	5.7	27.3	-	6.2	6.7	960.9	38.0	86.5	113.9	5.3	3.1	16.0	15.9	28.2	18.0
Mo-Gu/2	16.4	33.3	42.1	10.8	3.9	21.6	15.0	6.2	11.0	532.0	54.4	314.8	54.3	2.9	3.3	10.8	13.7	28.2	15.3
Mo-Gu/3	15.0	25.6	30.6	17.4	3.7	19.8	166.5	4.4	10.5	794.4	52.0	135.7	104.4	3.8	4.3	15.0	19.3	35.6	17.9
Guaso System																			
Gu1/1	22.7	44.0	55.9	18.0	10.0	33.0	70.0	8.4	6.5	708.2	46.5	142.6	87.7	6.3	4.3	18.6	21.9	43.0	22.8
Gu1/2	22.2	46.1	76.2	14.7	11.5	38.9	82.7	7.8	6.9	505.2	62.0	176.8	93.6	7.2	5.6	18.5	20.0	35.3	19.6
Gu1/3	20.8	45.6	64.2	16.3	12.3	32.7	66.2	8.2	6.4	546.7	55.0	152.9	136.2	6.7	6.0	19.8	20.2	40.1	21.9
Gu2/1	18.0	38.4	42.6	17.9	5.8	32.6	19.6	5.2	10.4	796.4	39.6	130.2	123.7	5.1	4.4	16.9	16.8	34.6	19.0
Gu2/2	18.4	35.6	40.8	19.5	5.6	24.7	177.8	5.5	9.8	744.3	40.6	136.0	74.6	4.1	3.9	13.7	12.6	26.1	17.4
Gu3/1	13.5	25.6	24.9	10.7	2.4	18.7	455.7	4.7	15.0	890.4	61.6	178.2	35.7	2.4	1.5	8.6	9.1	17.7	11.1
Gu3/2	24.0	43.8	48.3	14.7	3.6	25.7	-	5.3	5.6	1059.2	39.5	116.4	60.4	4.5	2.0	13.7	12.8	23.0	14.5
Gu3/3	15.8	35.5	32.3	16.6	2.9	21.8	80.9	5.7	11.6	781.9	51.1	160.5	72.3	3.5	3.2	13.3	11.9	21.6	14.4

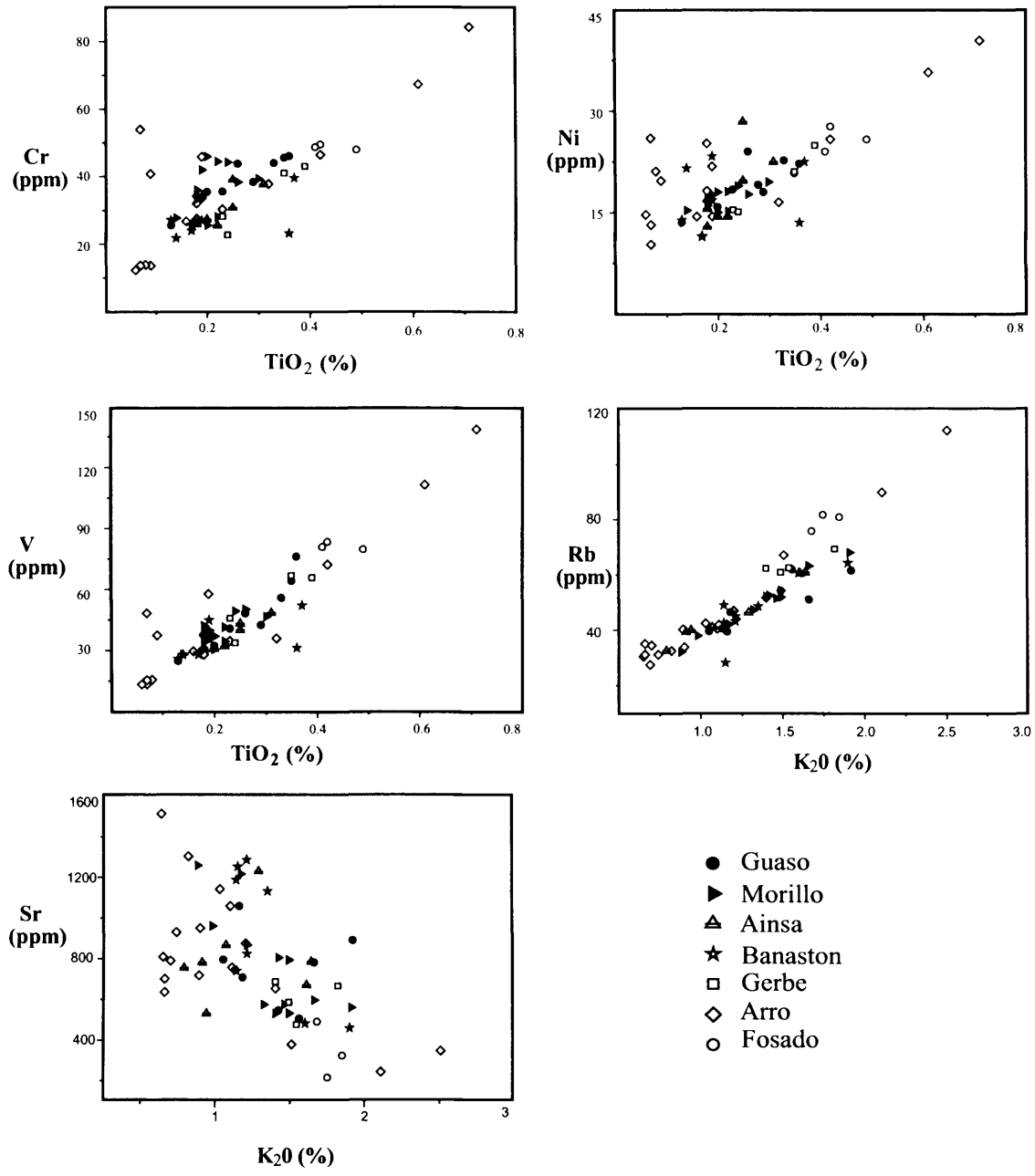

Figure 5.6: Trace element characteristics of sandstones from the Ainsa basin.

The average Cr/Ni ratio of the Ainsa basin sandstone corresponds well to the average Cr/Ni ratio of the UCC (Table 5.4). The average Th/Cr ratio of the sediments is 0.12 which is very close to the average Th/Cr ratio of sediments derived from a felsic source (i.e. 0.13). However, the mean Th/Sc and La/Sc ratios from the Ainsa basin sediments lies in between the reported average values of sediments derived from mafic and felsic rocks(Table 5.4). Average Zr concentration in the Ainsa basin clastic sediments is 87 ppm, whereas fine-grained clastic sedimentary rocks are characterised by an average Zr concentration of 200±100 ppm (Taylor and McLennan, 1985).

Table 5.4: Mean element concentrations and ratios in the Ainsa basin clastic systems compared to Upper Continental Crust (UCC), sands derived from mafic and felsic rocks.

	Ainsa basin sediments		UCC[1]	Sands derived from mafic rocks[2]	Sands derived from felsic rocks[2]
	Range	Mean			
K_2O/Al_2O_3	0.10-0.33	0.21	0.22		
Al_2O_3/SiO_2	0.08-0.26	0.14	0.23		
Cr/Ni	0.7-2.6	1.9	1.8		
Cr/V	0.6-1.2	0.8	0.6		
V/Ni	0.7-3.4	2.3	3		
Th/Cr	0.05-0.2	0.12	0.31	0.018-0.046	0.13-2.7
Th/Sc	0.10-0.82	0.35		0.05-0.22	0.84-20.5
La/Sc	0.54-3.16	1.44		0.43-0.86	2.5-16.3

[1]Taylor and McLennan (1995); [2]Cullers (2000)

Similar to the major element data, the trace element concentrations were also used to determine constraints on tectonic setting. In this study the widely used discriminate plots proposed by Bhatia and Crook (1986) utilising Sc, Cr, La, Y, Zr and Th concentrations were applied. All the data in the three plots (Fig. 5.7) are found to be dispersed among different tectonic fields and which in turn, unlike the major element plots, did not lead to any conclusion regarding the tectonic setting.

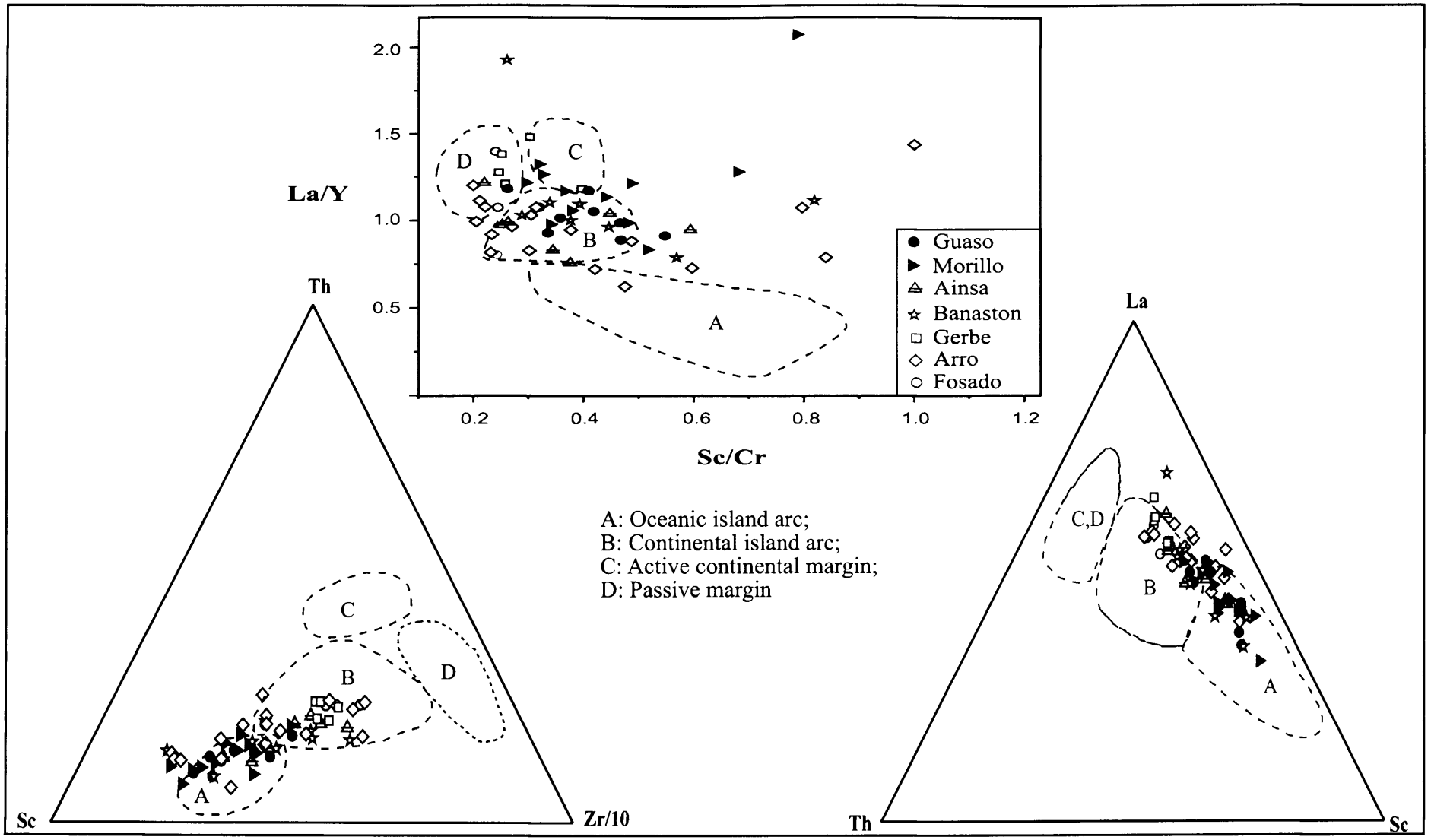

Figure 5.7: Tectonic discrimination diagram of Bhatia and Crook (1986) utilising trace element data. These diagrams remain inconclusive regarding tectonic setting discrimination for the Ainsa basin sediments

However, trace element plots using ratios of compatible elements enriched in mafic rocks (Ti, Cr, Sc, Co) to incompatible elements enriched in felsic rocks (Zr, La, Y, Th) are more reliable indicators of source composition because of their low residence times in seawater and immobility during weathering and alteration (Roser 2000). Elemental ratios like La/Sc, La/Co, are usually good discriminators between mafic and felsic source rocks as La, Th and Zr are more concentrated in felsic igneous rocks whereas Co, Sc and Cr have higher concentrations in mafic rocks (e.g., Wronkiewicz and Condie, 1987). Vanadium, Cr, Co and Ni are compatible elements during igneous fractionation processes and are generally "depleted" in felsic rocks and "enriched" in mafic–ultramafic rocks.

Enrichment of Ba, Rb and Sr in sandstones relative to other trace elements generally reflects feldspar enrichment (Winter, 2001), however, in the Ainsa basin the enrichment (Table 5.3) could also indicate the significant carbonate component of the sandstones, as suggested by the petrography data. Most of the analysed samples from the Ainsa basin have La/Sc, Sc/Th and Cr/Th ratios that are comparable with sand derived from felsic to intermediate rocks of upper continental crustal provenance (Table 5.4). Although the Cr/Th ratio is sensitive to oxidation state, this is believed to be of minor significance because of the relative consistency of these ratios throughout the sample sets. A further chemical check on the original lithological composition can be achieved by using relatively immobile elements, such as Ti and Ni. In the Ni-TiO_2 cross plot (Fig. 5.8, after Floyd et al., 1989) for source rock discrimination, the Ainsa basin samples plot in and around the field of acidic igneous rock. All these features are indicative of a felsic rather than mafic source for the Ainsa basin siliciclastic sediments.

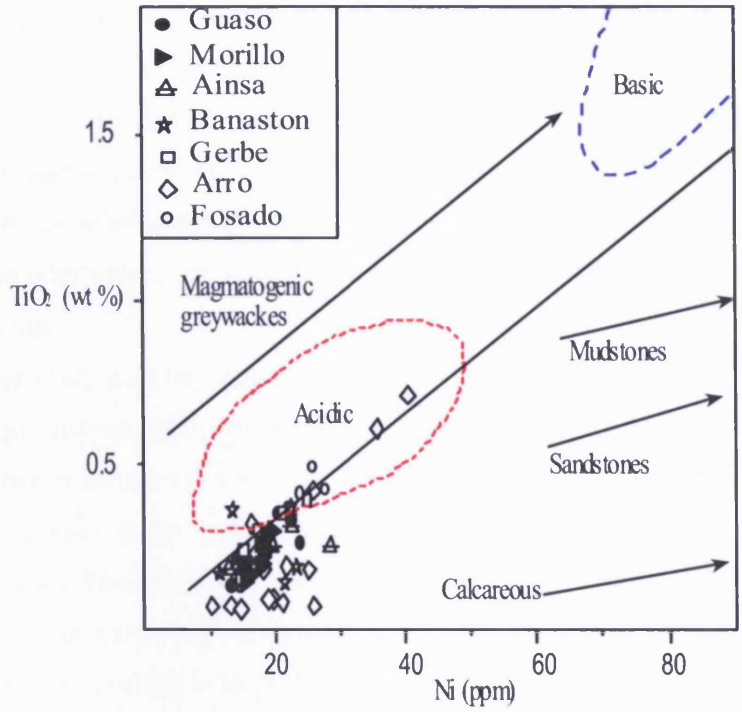

Figure 5.8: Nickel versus TiO_2 plot for the discrimination of source rocks of the Ainsa basin sandstones. Acidic and basic fields and trends are from Floyd et al. (1989) and Joo et al. (2007). The studied samples plot in and around the field of acidic source.

5.3 Geochronology

5.3.1 Fission Track (FT) data

The samples selected for geochronology are medium-sand to coarse-sand sized as the presence and/or abundance of zircon, being a heavy mineral, will be higher in such samples. Samples which generated abundant zircon for FT and U-Pb chronometry, along with their locations, are shown in Table 3.1 and Fig. 3. 1. All the systems in the Ainsa basin contain abundant detrital zircon grains for FT analyses, however, only some zircon grains could be analysed because of high track densities and/or small counting areas. In case of the Guaso system it was impossible to analyse any zircon crystals due to very high track densities which resulted in total lack of FT data from this system. Overall, the number of grains analysed was low (< 40 grain ages per

sample) which can restrict interpretation as decomposition of pooled mixed age data relies on an adequate number of grains within each data set (e.g. Vermeesch, 2004). Whilst the number of zircon FT grain ages determined in each sample for this study is clearly not adequate to obtain a full measure of the range of possible provenance types, the data are suitable though for detecting the most dominant sources. Before the results can be interpreted, the mixed grain ages are de-convoluted into their principal age components.

The primary aim for principal component analysis was to detect any major shift in source between the deep-marine siliciclastic systems, rather than to detect any variation between samples from within the same system. In this study the principal detrital source age modes are extracted by using the approach of Sambridge & Compston (1994). The distribution of individual grain ages is presented as radial plots in Fig. 5.9 and the results are presented in Table 5.5. The effects of partial annealing on the FT ages are negligible as the bedrocks occurring in the regional context of the study area are very poorly metamorphosed (maximum up to 'low grade metamorphism'), given that the partial annealing for zircon FT age occurs at ~200 – 310^{0}C depending on levels of alpha radiation damage (Carter, 1999; Rahn et al., 2004). The maximum palaeotemperature for the sample localities were around or below the temperature required for low grade metamorphism (i.e., ~200 – 320 ^{0}C).

The results show that each system contains a dominant age mode between 227±13 Ma (Banaston) and 349±27 Ma (Gerbe) and a secondary minor source between 109±9 Ma (Arro) and 174±9 Ma (Morillo). There is no systematic trend between the dominant source age components and sample depositional age indicating no major change in source between the siliciclastic systems. In contrast the younger minor age components appear to show a trend of increasing age up section. The significance of this trend and the zircon FT ages in general, in terms of whether the ages relate to zircon formation (e.g. granite emplacement) or regional exhumation, can be understood by using the zircon U-Pb data. When a zircon FT age is identical within error to a corresponding U-Pb age mode, these results show a similar thermal history and a volcanic origin is indicated. To obtain a statistically robust U-Pb dataset zircon grain mounts were made for each sample and dated by LA-ICPMS. These data were then compared against U-Pb ages measured on the same grains used for zircon FT analysis (Fig. 5.9). This dual method approach (Carter and Moss, 1999) has the advantage of using each method to constrain provenance interpretation of the other

and provides a means of detecting any technique-based bias (Carter & Bristow, 2000). It is noteworthy that the samples containing zircons with dominant FT ages that are younger than ~300 Ma are from the relatively older stratigraphic units (Arro, Banaston and Ainsa), implying that the older sandstones were initially eroding younger cover rocks which were later completely removed.

Table 5.5: Fission track (FT) analytical data for the Ainsa basin systems.

Strat. Age	*System* Sample No.	No. of grains	Dosimeter ρd (Nd)	Sponta-neous ρs (Ns)	Induced ρi (Ni)	Age dispersion $P\chi^2$	Age dispersion RE %	Central Age ±1σ (Ma)	Age Components [Ma] (no. of grains)	
Ypresian - Lutetian	*Morillo* Mo/3	28	0.562 (3093)	23.86 (10496)	3.149 (1474)	0.0	52.7	239±25	174±9 (9)	317±17 (17)
	Ainsa Ai I	38	0.561 (3093)	27.87 (13639)	3.354 (1664)	0.0	33.6	278±18	132±13 (4)	236±16 (13) 323±21 (21)
	Banaston B/2	22	0.418 (2589)	20.69 (6051)	2.663 (786)	0.0	33.2	200±17	130±9 (7)	227±13 (15)
	Gerbe G/T	10	0.4.18 (2589)	24.86 (3489)	2.686 (392)	0.0	60.8	227±46	110±0 (3)	349±27 (7)
	Arro Ar/B	31	0.409 (2271)	21.11 (9607)	2.230 (1052)	0.0	36.9	235±18	109±9 (4)	245±11 (27)

Notes:

(i) Track densities are ($\times 10^6$ tr cm^{-2}) numbers of tracks counted (N) shown in brackets; (ii) Analyses by external detector method using 0.5 for the $4\pi/2\ \pi$ geometry correction factor; (iii) Ages calculated using dosimeter glass CN-2 (zircon); analyst Carter ζ_{CN2} = 127±4; calibrated by multiple analyses of IUGS apatite and zircon age standards (see Hurford 1990b); (iv) $P\chi^2$ is probability for obtaining χ^2 value for *n* degrees of freedom, where *n* = number of crystals - 1; (v) Central age is a modal age, weighted for different precisions of individual crystals; (vi) Age modes calculated using the approach of Sambridge and Compston (1994).

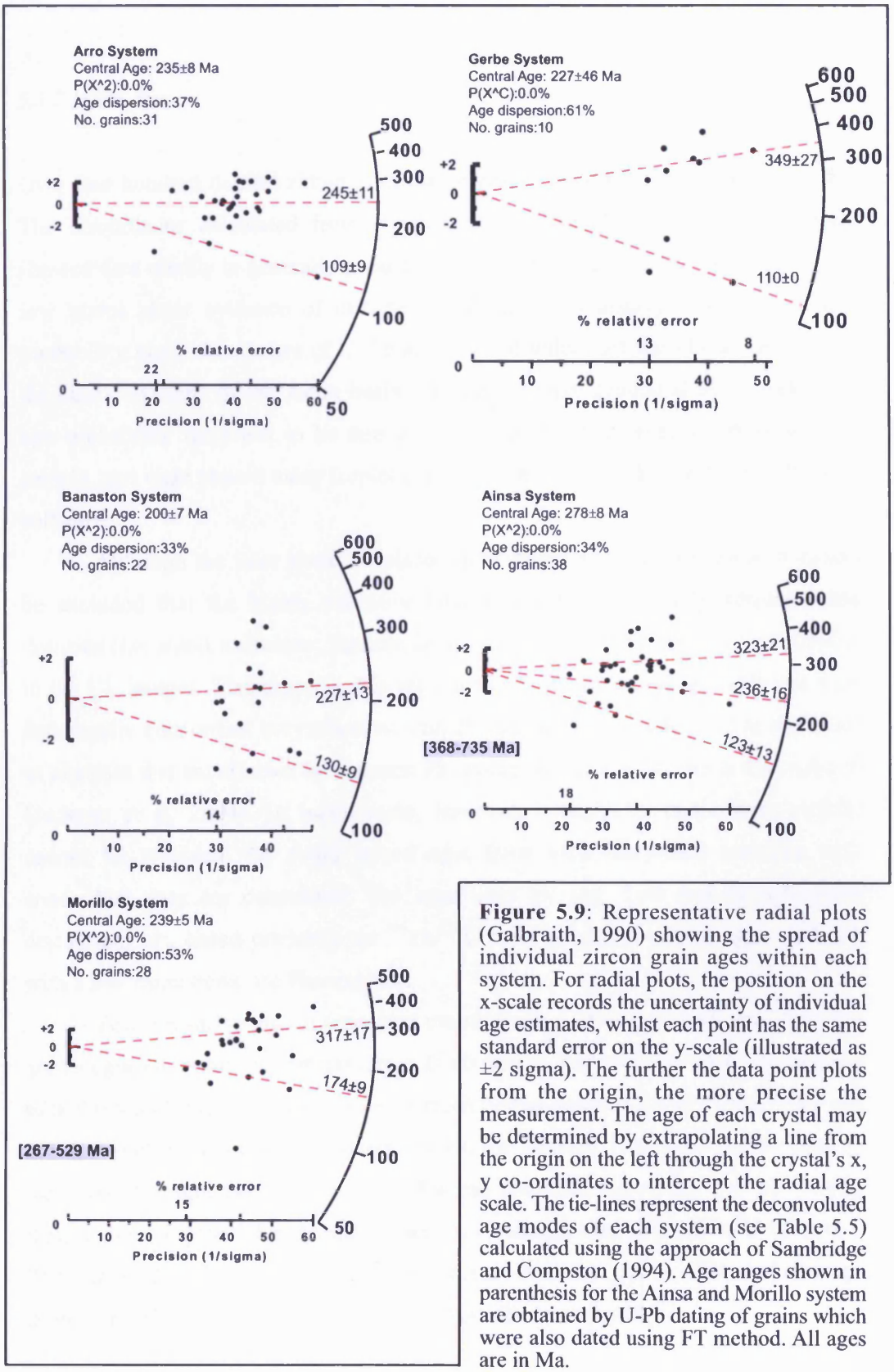

Figure 5.9: Representative radial plots (Galbraith, 1990) showing the spread of individual zircon grain ages within each system. For radial plots, the position on the x-scale records the uncertainty of individual age estimates, whilst each point has the same standard error on the y-scale (illustrated as ±2 sigma). The further the data point plots from the origin, the more precise the measurement. The age of each crystal may be determined by extrapolating a line from the origin on the left through the crystal's x, y co-ordinates to intercept the radial age scale. The tie-lines represent the deconvoluted age modes of each system (see Table 5.5) calculated using the approach of Sambridge and Compston (1994). Age ranges shown in parenthesis for the Ainsa and Morillo system are obtained by U-Pb dating of grains which were also dated using FT method. All ages are in Ma.

5.3.2 U-Pb data

Over four hundred detrital zircon grains were analysed for U-Pb ages (Appendix II). The discordance calculated from comparison of $^{206}Pb/^{238}U$ and $^{207}Pb/^{235}U$ ages, showed data quality is generally good for each system in the Ainsa basin, although a few grains show evidence of disturbance. Figure 5.10 displays, as relative age–probability plots, the spectra of U–Pb ages for individual detrital zircon grains from the clastic systems of the Ainsa basin. The curves were generated by summing the age–probability (assumed to be normally distributed) of all analyses from a given sample, and were plotted using Isoplot (Ludwig, 2000) – a toolkit for Microsoft Excel software.

Although the laser spots are placed in homogeneous CL structures, it cannot be excluded that the highly pervasive laser penetrates isotopically heterogeneous domains (i.e. small inclusions, fissures, or different crystal portions) not recognizable in the CL images. Therefore, signals are selectively integrated so that only the most isotopically concordant intervals of at least 25 seconds are considered. The incidence of analyses that are affected by common Pb contamination and Pb loss is thus reduced (Jackson et al. 2004). In many cases, however, isotopically concordant portions cannot be resolved. To avoid mixed ages from such discordant portions, only concordant data are considered. The ages used for Fig. 5.10 and in subsequent discussions are based primarily on $^{206}Pb/^{238}U$ ratio as almost all the ages obtained, with a few exceptions, are Phanerozoic.

Four pervasive zircon formation events (each comprising more than 5 grains) are recognised within the detrital zircon U-Pb data at 300-360, 440-490, 500-600 and 620-770 Ma (Table 5.6). Another lesser mode occurs between 250-300 Ma. Other age clusters (with $\leq$5 grains) are also observed in the samples, few of which are younger than 200 Ma, some between 800-2000 Ma and few older than 2 Ga. It is noteworthy that, unlike with the FT age modes, there is an almost total absence of U-Pb ages < 250 Ma (Table 5.6). Figure 5.11 summarises both the radial plots and the age probability plots for each system analysed from the Ainsa basin.

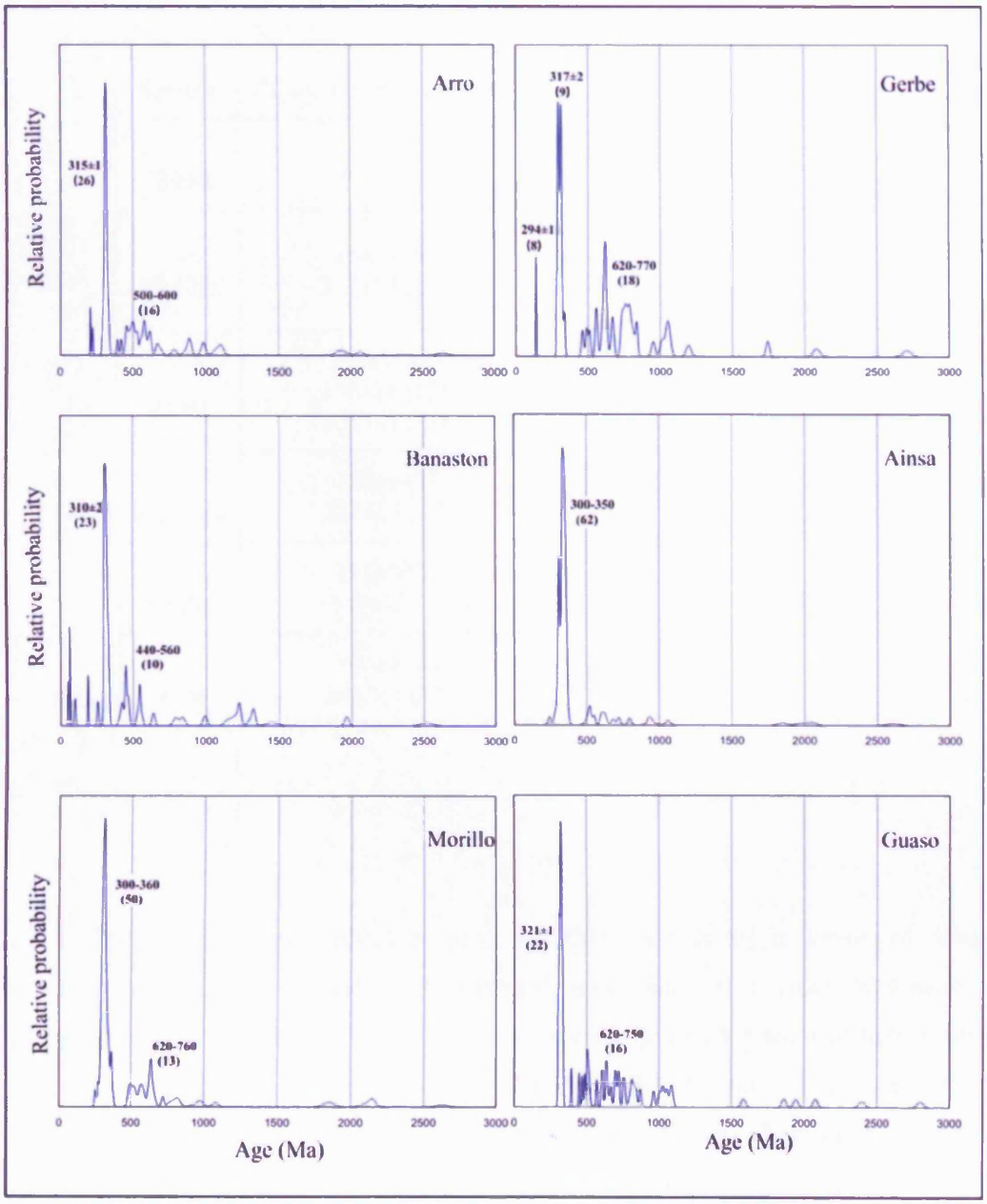

Figure 5.10: Age – probability plots of U-Pb ages of detrital zircons in systems of the Ainsa basin. Also see Table 5.6.

Table 5.6: Principal zircon fission track (FT) and U-Pb ages (±1σ) for the Ainsa basin systems. Number of grains is given in parenthesis; for U-Pb data age modes with ≥5 grains are considered. Note the oldest Fosado system is not included here, see text for explanation.

System	FT component ages (Ma)	U-Pb component age modes (Ma)	
		Phanerozoic	Precambrian
Guaso	No data	321±1 (22) 481±2(7)	620±2 (7) 747±3 (9)
Morillo	174±9 (9) 317±17 (17)	308±1 (41) 353±3 (9) 523±4 (8)	627±4 (9)
Ainsa	132±13 (4) 236±16 (13) 323±21 (21)	308±1 (14) 331±1 (18) 350±2 (30)	559±4 (7)
Banaston	130±9 (7) 227±13 (15)	310±2 (23) 448±3 (6)	n/a
Gerbe	110±0 (3) 349±27 (7)	294± 1(8) 317±2 (9)	627±3 (9) 768±4 (9)
Arro	109±9 (4) 245±11 (27)	315±1 (26) 508±3 (8)	584±2 (8)

McLennan et al. (2001) pointed out that absence of a zircon of some hypothesized source terrane does not necessarily mean that such a terrane was not part of the provenance. It might be possible that such a source terrane did not contain zircon bearing lithologies (e.g., mafic or carbonate rocks) or contained zircons that are too small to be sampled by standard separation methods (e.g., shale or slate source rocks). Even in a study with a relatively large number of zircon analyses, there is a statistical probability that a zircon population will be missed. Vermeesch (2004) showed that if it is desired that no fraction of the population comprising more than 0.05 of the total is missed at the 95% confidence level, then at least 117 grains should be dated. However, studies reporting fewer than the optimal number of 117 single-grain measurements do not mean they are scientifically wrong. For example, if only

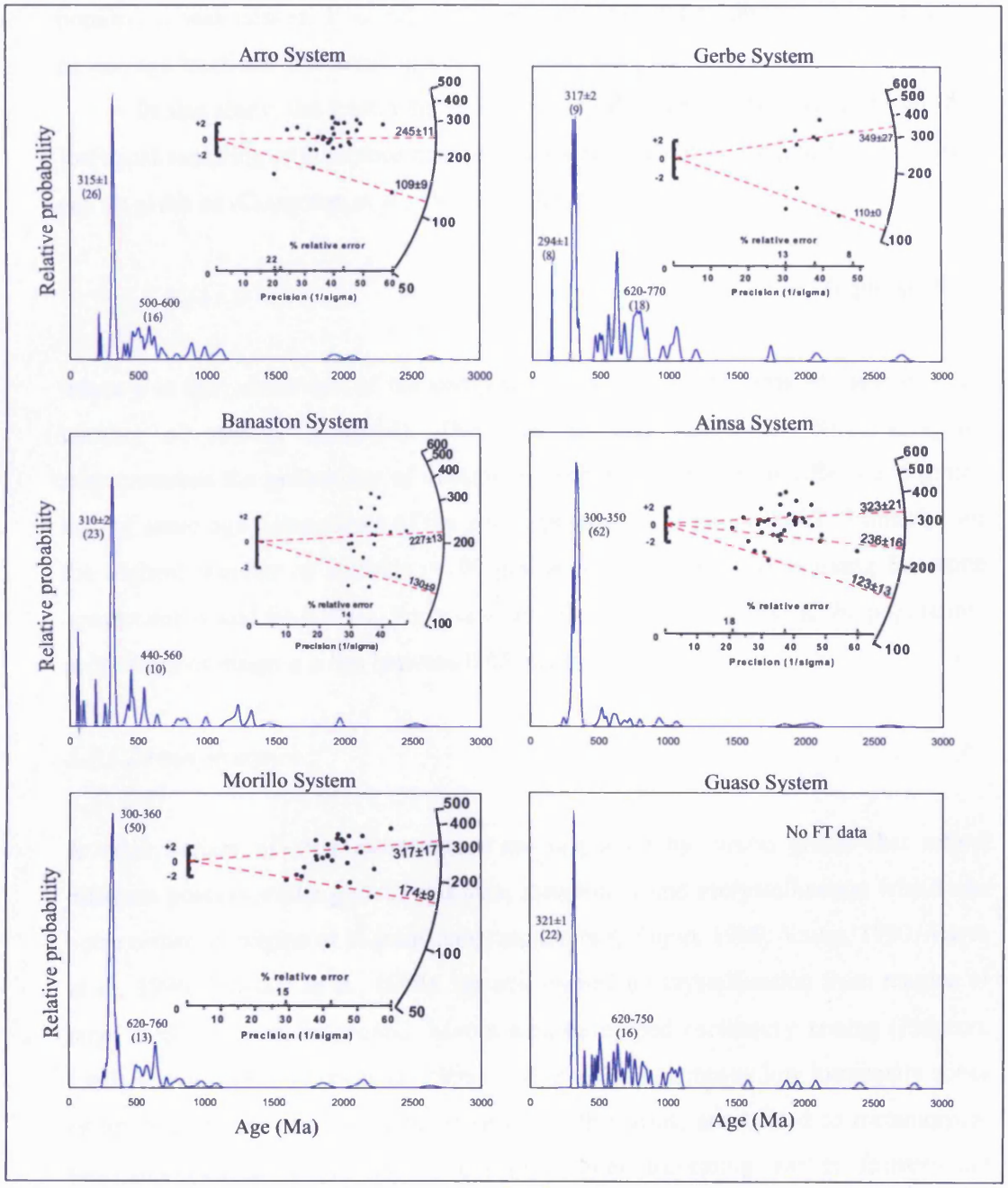

Figure 5.11: Diagram illustrating the radial plots and the age-probability plots for each system analysed from the Ainsa basin. Note that U-Pb dating of grains previously dated by FT shows that the majority of the grains from the Ainsa basin have FT ages that are within error or slightly younger than their U-Pb ages.

60 grains were dated there is 95% confidence that no fraction ≥ 0.085 of the total population was missed. It is only when provenance studies discuss the absence of certain age fractions that counting statistics come into play.

In this study, the least number of grains analysed for each system is ~60. For statistical sampling with replacement, the probability (P) of missing some component can be given as (Compston et al., 1985; Dodson et al., 1988):

$$P = (1 - f)^n \qquad \text{[equation 5.1]}$$

where f is the proportion of the component and n is the number of samples (i.e., number of zircons analyzed). Therefore, in this case with 60 single-grain measurements the probability of missing a component making up 10% (i.e. 6 grains having same age component) of the zircon population is about 0.002. Similarly, for the highest number of analysis (~ 90 grains) the probability of missing the same component would be 0.0001. For a component that makes up 5% of the population, probability of missing it lies between 0.05 and 0.01.

5.3.3 Zircon structure

A wide variety of internal structures are displayed by zircon grains that reflect different processes like growth episodes, dissolution and recrystallisation which can occur either in magma or in solid-state reaction (e.g. Pupin, 1980; Vavra, 1990; Vavra et al., 1996; Pidgeon et al., 1998). Zircons formed by crystallisation from magma or large melt reservoir, in general, have a well-developed oscillatory zoning (Pidgeon, 1992; Vavra, 1994; Vavra et al., 1996). Whereas homogeneous low luminosity zones or bright zones in zircons, often occurring as thin rims, are related to metamorphic processes (Vavra et al., 1999). Irregular zones truncating earlier features are considered to form during grain recrystallisation (Pidgeon, 1992).

The zircon grains from the Ainsa basin are predominantly translucent and colourless, as observed under reflected light microscope, with a variety of external morphologies. Cathodoluminescence (CL) imaging of the zircons reveals a variety of internal morphologies (Fig. 5.12). The majority of grains show oscillatory zoning with thin bands, suggesting magmatic origin of the grain. Zoning within grains are generally conformable with grain margins. Metamorphic overgrowths, as in grain

Ar05 (Fig. 5.12), are quite rare and could not be dated due to their thin width. Several grains (e.g. grains Ar08, A1, G2 in Fig. 5.12) show a relatively homogeneous, muted CL response, suggesting formation during high-grade metamorphism. Evidence of recrystallisation is found in very few grains. It is noteworthy that in one such recrystallised grain both the core (Ar06) and rim (Ar07) age was found to be exactly the same (Fig. 5.12), suggesting equilibrium between melt and crystal during its formation.

An interesting pattern is noted regarding the U-Pb age distribution. Ages older than 542 Ma or Precambrian ages are obtained exclusively from the grain core, as in the cases of the following grains (Fig. 5.12): G1 (623±7 Ma), G5 (1744±13 Ma), MO2 (2148±19 Ma), MO5 (720±9 Ma), Mo3 (637±7 Ma), Gu7 (872±7 Ma), Gu35 (813±7 Ma) and Gu33 (1584±15 Ma). However, the younger ages are found to be derived from both inner core (e.g., Ar03, Ar05, A1, A2 and A8) and outer rim of grains (as in G2, A15, MO6, G9, Gu37, etc). Another pattern is observed while comparing grain shape with U-Pb age distribution. In general, rounded grains are found to contain older U-Pb ages like in grains MO2 (2148±19 Ma) and Gu35 (813±7 Ma). This is simply because rounded grains are more likely to be polycyclic and are derived from a source that retains a record of several cycles of burial and erosion. By contrast, the majority of euhedral and subhedral zircon grains (Ar01, Ar05, A11, MO6, etc) have younger U-Pb ages suggesting they are first-cycle zircons derived directly from crystalline basement sources.

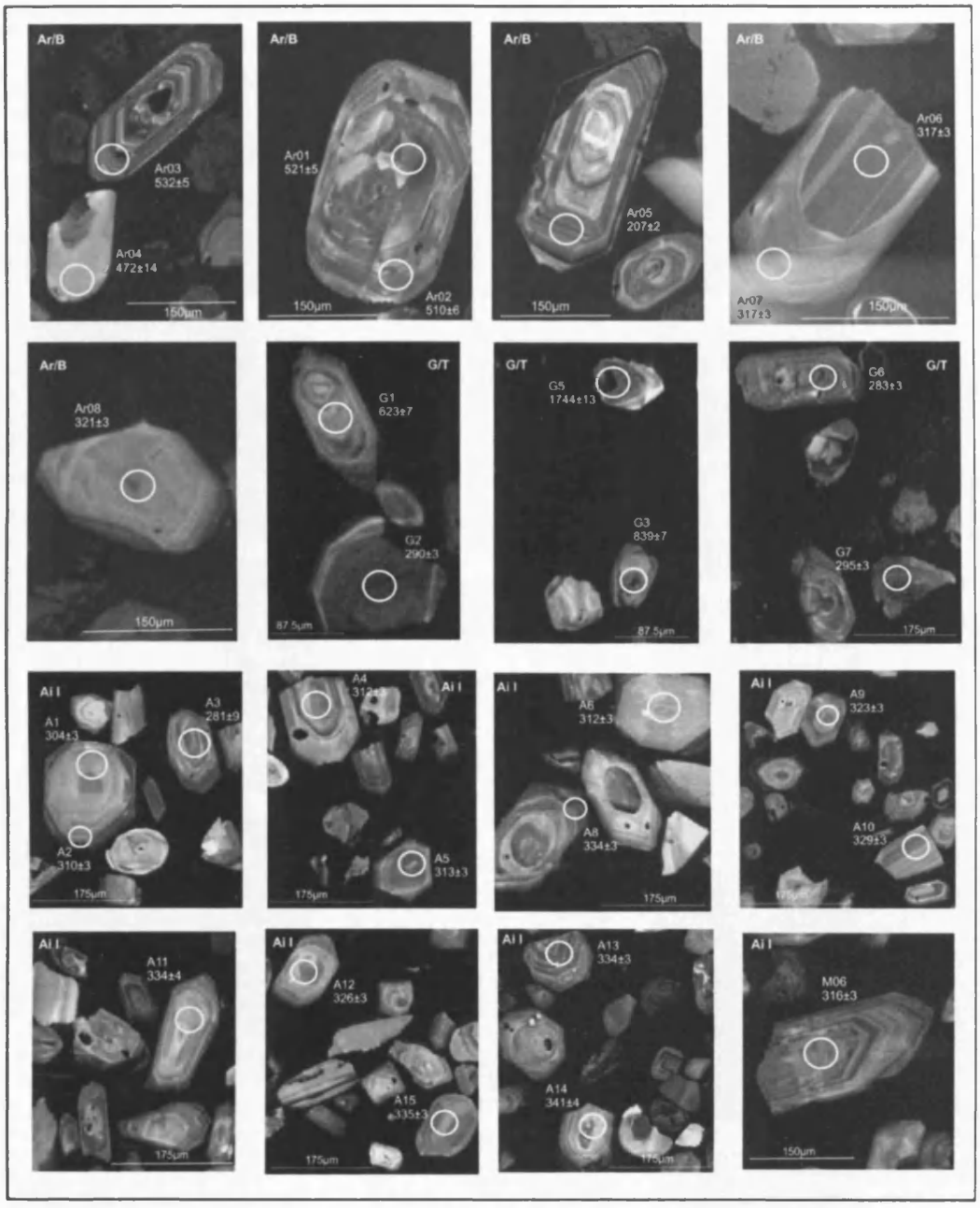

Figure 5.12: Internal structure of selected zircon grains from different systems of the Ainsa basin as revealed by cathodoluminescence (see text for details). Ages (Ma) and the location of analysed spots are also shown.

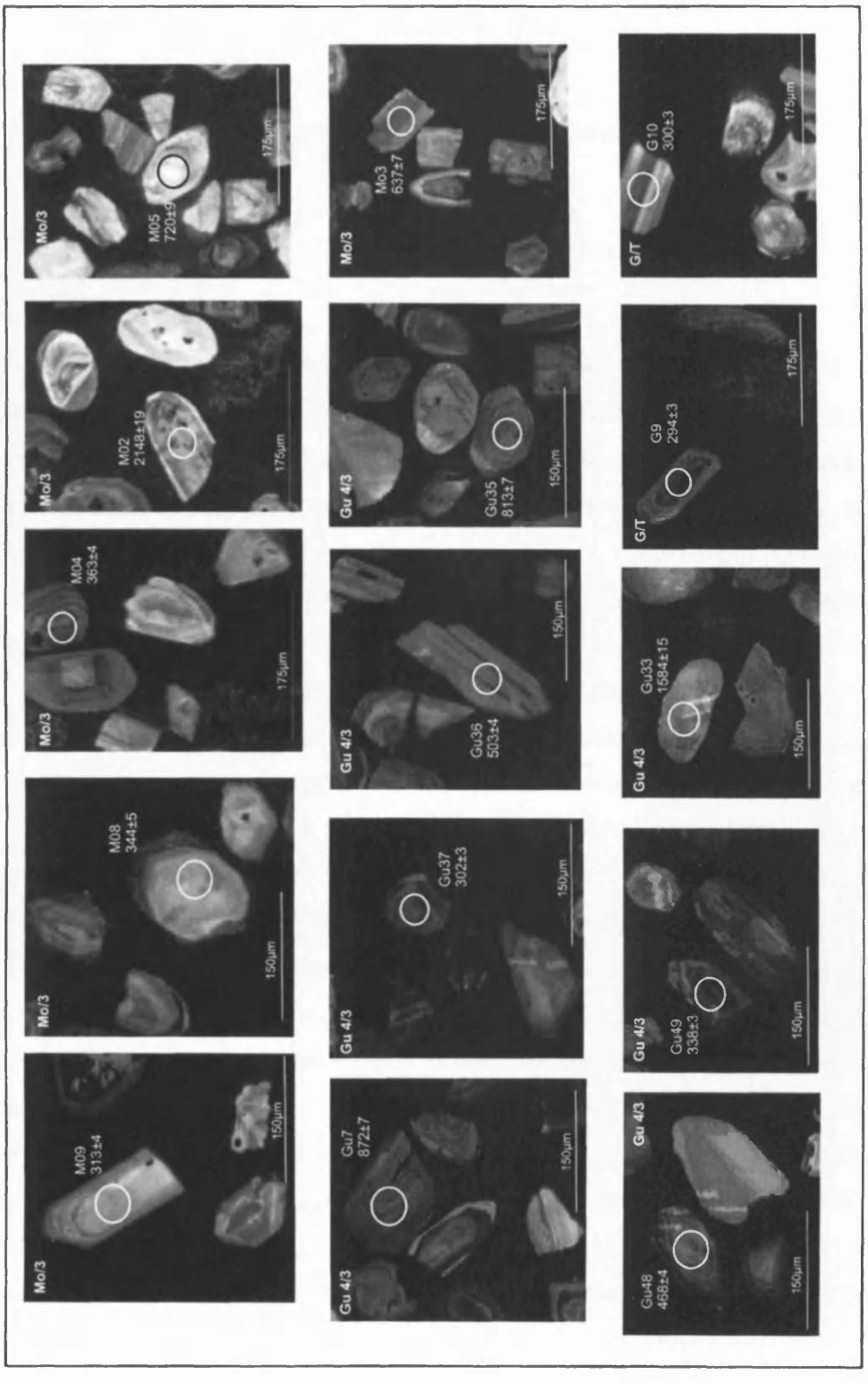

Figure 5.9 (*Continued*).

CHAPTER 6

Isotopic Signatures of Foraminifera

6.1 Introduction

As discussed in Chapter 1 and 3, a pilot study on isotopic signatures of foraminifera from the Ainsa basin was undertaken as part of this research. This pilot study, using stable isotopes, was undertaken in an attempt to deconvolve any global eustatic sea-level signal from tectonic and other regional events, i.e., Pyrenean tectono-environmental change. It was hoped that such a study might provide some fundamental understanding not only of the evolution of the deep-marine Ainsa basin, but might also contribute to a generic model for distinguishing global from tectonic controls in other modern and ancient foreland basins throughout the world.

Foraminifera and their stable isotope compositions are commonly used to help in the reconstruction of Recent and ancient bottom-water environments, to identify different deep-water masses, for the reconstruction of past sea levels and palaeo-climate, and as stratigraphic tools (e.g., Sarnthein et al., 1994; Mackensen et al., 2001; Huber et al., 2002; Waelbroeck et al., 2002; Bohaty and Zachos, 2003). The $\delta^{13}C$ values of foraminifera also provide information on the carbon cycling of the oceans and changes in the organic matter fluxes (e.g., Woodruff and Savin, 1985, Mackensen et al., 1994). In general, most of these applications have been found to be restricted to the Cenozoic period as the availability of pristine foraminiferal tests and knowledge of the ecological requirements of different species are generally limited for older time periods. It is assumed, since early studies on the isotopic composition of fossil carbonates (Urey et al., 1951), that carbonate growth out of thermodynamic isotope equilibrium is a common phenomenon which is more expressed in carbon than in oxygen generally (e.g., Wefer and Berger, 1991).

In the Ainsa basin each of the seven depositional system (Fig. 2.10) contains 2-6 individual sandbodies (30-100 m thick), separated by tens of metres of mainly thin-bedded and very thin-bedded sandstones with subordinate marls. The successive depositional systems are separated vertically by several hundred metres of mainly

marl deposits with thin-bedded and very thin-bedded sandstone turbidites. Most of these marls, and in some cases the sandstone units, contain larger (benthic) foraminifera which were loosely embedded within sediments. Their abundance and apparent lack of substantial physical alteration make them ideal for stable isotopic analysis of oxygen and carbon. Both the sediment and larger foraminifera were collected (Fig. 3.1 and Table 3.1) throughout the Ainsa basin. In addition to stable isotope analyses of the foraminifera samples, carbon analyses were made on some of the marl samples associated with the foraminifera (see Chapter 3).

6.2 Results

Four different species of foraminifera were recovered from the Ainsa basin outcrops: *Nummulites lyelli*, *Nummulites gizehensis*, *Discocyclina* sp., and *Assilina* sp. (Fig. 6.1), *Nummulites* sp. being the most abundant in the basin. Most of the foraminifera show surficial weathering which is rather normal for samples collected from outcrops. Carbon and oxygen stable isotope data from the above mentioned foraminifera assemblage are presented in Table 6.1 and Fig. 6.2. The values are reported in terms of δ- notation and in this context, $\delta^{13}C$ and $\delta^{18}O$ are defined as below:

$$\delta^{13}C = \left[\frac{\left({}^{13}C/{}^{12}C\right)_{Sample}}{\left({}^{13}C/{}^{12}C\right)_{S\,tan\,dard}} - 1 \right] \times 1000\ ‰ \qquad \text{[equation 6.1]}$$

$$\delta^{18}O = \left[\frac{\left({}^{18}O/{}^{16}O\right)_{Sample}}{\left({}^{18}O/{}^{16}O\right)_{S\,tan\,dard}} - 1 \right] \times 1000\ ‰ \qquad \text{[equation 6.2]}$$

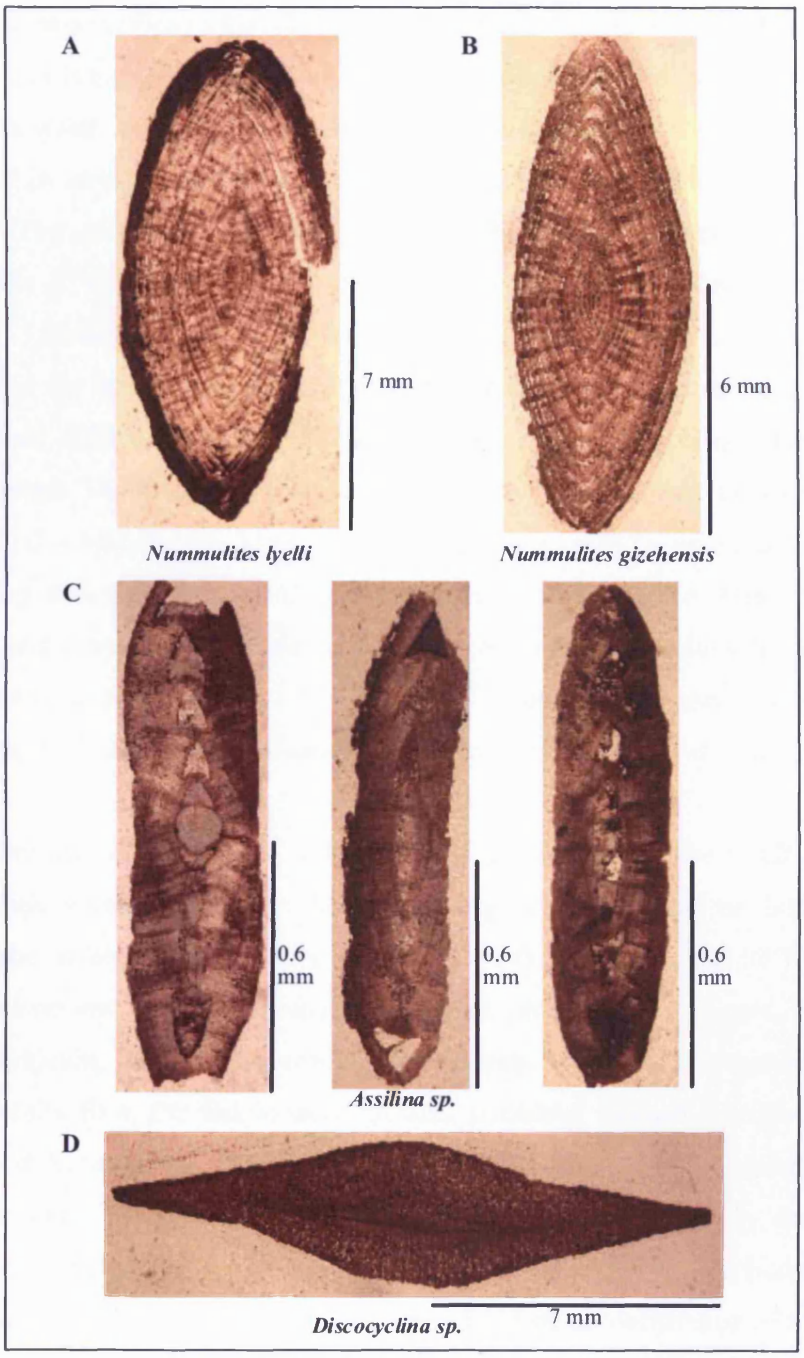

Figure 6.1: Photomicrograph of the four larger (benthic) foraminifera species recovered from the Ainsa basin.

A positive value indicates that the sample has higher $^{13}C/^{12}C$ or $^{18}O/^{16}O$ ratio than the standard and is expressed by stating that the sample is enriched in ^{13}C or ^{18}O relative to the sea water. In other words, the isotopic composition in the sample is always expressed in terms of enrichment or depletion of the heavy isotope relative to the standard. The standard analysed for this study is the Pee Dee Belemnite (PDB).

The $\delta^{13}C$ values of the Ainsa basin foraminifera samples (N = 44) vary between -3.96 ‰ and 2.51 ‰ PDB, the most negative and most positive values are recorded in the Banaston and Guaso system respectively. In contrast, the $\delta^{18}O$ value ranges from -9.20 ‰ to -1.29 ‰ PDB and both of the extreme values come from the Guaso system. The oxygen isotope data show more dispersion than the carbon isotope data ($\Delta\delta^{13}C$ = 6.47 ‰; $\Delta\delta^{18}O$ = 7.92 ‰). Travé et al. (1997), who studied sediment dewatering and pore fluid migration along thrust faults in the Ainsa basin using isotopic and elemental geochemical analyses, reported $\delta^{13}C$ values from the Ainsa basin ranging between -3.3 and -0.3 ‰ and $\delta^{18}O$ between -9.6 and -5.8 ‰, although samples in their study were different calcite cements in shear-veins and marly host-rock.

The final $\delta^{18}O$ and $\delta^{13}C$ value of a foraminifera test is the result of multiple calcification events during the life of an organism, and can be influenced by ontogenetic or ecological changes in habitat depth, secondary calcite formation in deeper waters and post-depositional preservation processes (e.g., Spero, 1998; Pfuhl and Schackleton, 2003). The isotopic composition of benthic foraminifera deviates systematically from the fractionation of total dissolved inorganic carbon and water (Pfuhl and Schackleton, 2003), however, the deviations for the most frequently analysed benthic species are well established and apparently fairly constant (see Shackleton and Hall, 1997 for a list). Purton and Brasier (1999), in a study of Eocene *Nummulites* sp. from Hampshire basin, UK, observed no occurrence of foraminifera physiology effects or 'vital effects' on $\delta^{18}O$ data, however, the $\delta^{13}C$ values were slightly offset ($\delta^{13}C$ ~1‰ more positive). Influence of 'vital effects' on stable isotope data, although, are more significant in palaeoceanographic and palaeoclimatic research (e.g., Spero, 1998).

Table 6.1: Carbon and oxygen isotopic analyses of larger foraminifera recovered from the Ainsa basin. Values, arranged chronostratigraphically, are reported as ‰ PDB (Pee Dee Belemnites).Total organic carbon (TOC) and total carbon (TC) analyses were carried out on associated marls in some cases.

System	Sample No.	$\delta^{13}C$	$\delta^{18}O$	TOC%	TC%
Guaso	GUIII/1	-0.09	-6.55	-	-
	LOC 26/A	-1.93	-4.75	0.85	7.23
	GU/3	0.80	-9.20	-	-
	GU/2	2.51	-1.29	-	-
	GU/1	0.12	-6.00	-	-
	Gu/4	-0.09	-6.66	-	-
	LOC 25/B	-0.83	-4.74	0.32	6.26
Inter-	Mo/Gu	1.05	-2.15	-	-
Morillo	LOC 10/C	0.21	-2.73	0.12	6.20
	LOC 1/D	0.38	-1.74	0.12	6.57
	Mo/6	0.78	-4.80	-	-
	LOC 2/E	-0.08	-2.71	0.15	5.95
	LOC 18/F	0.74	-2.68	0.44	6.73
Inter-	Ai/Mo	0.12	-5.81	-	-
Ainsa	LOC 12/G	-0.25	-5.69	1.29	4.93
	LOC 13/H	-0.53	-5.31	0.42	5.40
	LOC 17/I	0.17	-4.45	0.30	5.84
	LOC 16/J	0.40	-6.88	0.42	5.11
	LOC 15/K	0.16	-6.56	1.09	5.54
	LOC 14/L	-2.28	-6.92	0.50	5.21
	LOC 9/M	0.09	-6.75	1.01	0.44
	LOC 8/N	-2.13	-3.92	0.79	4.12
Inter-	LOC 19/O	-1.94	-7.12	0.40	4.63
	B/Ai	-2.22	-6.20	-	-
Banaston	B/1	0.57	-2.31	-	-
	LOC 20/P	-3.96	-6.27	0.23	5.83
	LOC 21/Q	-0.43	-5.17	0.28	4.98
	LOC 22/R	0.23	-5.38	0.20	4.68
	LOC 23/S	-2.53	-6.29	0.31	6.24
Gerbe	G/1	-0.78	-6.86	-	-
	G/2	1.37	-3.27	-	-
Inter-	AR/G	1.60	-4.37	-	-
Arro	AR/1	-1.79	-5.96	-	-
	AR/2	-0.07	-6.80	-	-
	LOC 27/T	-1.05	-6.92	2.48	4.80
	LOC 11/V	-2.92	-7.45	0.81	5.20
	F/AR	-1.12	-7.78	-	-
	F/1	-0.84	-7.54	-	-
	LOC 7/W	-1.04	-7.94	0.64	4.45
	LOC 6/X	-2.25	-7.49	0.31	5.23
	LOC 5/Y	-1.00	-7.45	0.29	4.50
	LOC 3/Z	-1.94	-8.18	0.27	3.05
	LOC 4/Z1	-1.27	-7.78	0.67	4.86
Fosado	F/2	-0.70	-8.09	-	-

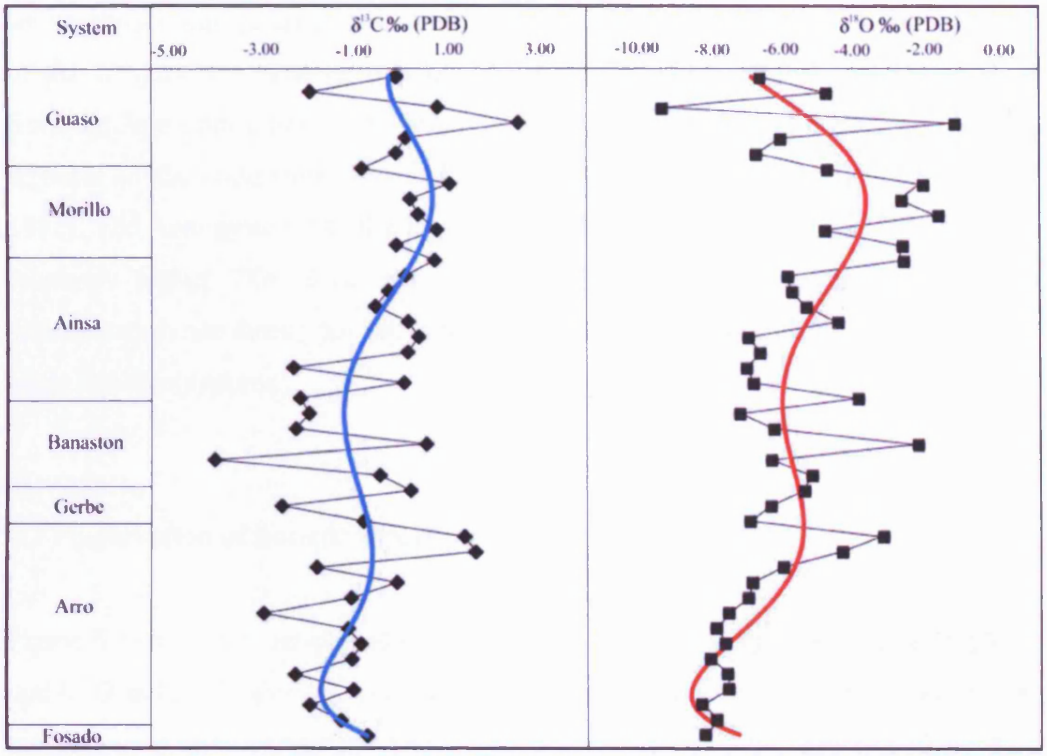

Figure 6.2: Carbon and oxygen isotope record of the clastic systems of the Ainsa basin, derived from larger foraminifera. A sixth-order polynomial curve is fitted with the data to show isotopic trend in the basin. Analytical precision ranges between 0.03 – 0.1‰ (1σ) for both $\delta^{13}C$ and $\delta^{18}O$ ratios. PDB is Pee Dee Belemnite.

The isotopic trend of the Ainsa basin systems is revealed by plotting the isotope values relative to stratigraphic position (Fig. 6.2). Both $\delta^{13}C$ and $\delta^{18}O$ show a negative excursion at the lower part of the stratigraphy. In the Arro system $\delta^{13}C$ is quite erratic, however $\delta^{18}O$ show a positive up section excursion in this system. Similar erratic nature for $\delta^{13}C$ can also be observed in the Gerbe and the Banaston system. However, a positive excursion can be noticed in the Ainsa system, which continued through the overlying Morillo system. Finally in the Guaso system a negative shift can be seen. In general $\delta^{18}O$ show positive excursions throughout the stratigraphy as well as within each system, except in the youngest Guaso system where it is more erratic.

Total organic carbon (TOC) and total carbon (TC) analyses were carried out on twenty-six marl samples associated with the foraminifera (Table 6.1). TOC content of the samples lies between 0.12% and 2.48%. However, majority of the samples from the Ainsa basin have TOC less than 0.5%. For comparison, deep-sea sediments adjacent to the continents tend to have TOC values above 0.5% (Premuzic et al., 1982). The Arro system has the highest TOC from a single sample, at 2.48 %. This relatively higher TOC level may be related to low oxygenation level or high sedimentation rate during the deposition of sediments in Arro system, compared to the other turbidite systems.

6.3 Preservation of isotopic signal

Figure 6.3 shows a cross-plot of $\delta^{18}O$ and $\delta^{13}C$. A point to note from the cross-plot is that $\delta^{18}O$ and $\delta^{13}C$ values from the foraminifera samples, in most cases, are lower than the Eocene marine carbonates values. Eocene carbonates are characterised by $\delta^{18}O$ values ranging from -4 to +2 ‰ PDB and $\delta^{13}C$ from -0.3 to +2.8 ‰ PDB (Shackleton and Kennett, 1975; Veizer and Hoefs, 1976; Hudson and Anderson, 1989). The depletion in ^{18}O in those samples which fall outside the Eocene carbonate range might be due to an increase of temperature during burial diagenesis. Similarly, an input of organogenic carbon to the system might be responsible for the depletion in ^{13}C (Irwin et al., 1977).

Another noteworthy point from the cross-plot (Fig. 6.3) is the insignificant correlation between the two parameters. The correlation co-efficient (R) between $\delta^{18}O$ and $\delta^{13}C$ is computed at 0.507, which indicates that $\delta^{13}C$ and $\delta^{18}O$ are partially independent of each other. Corfield et al. (1991) suggested that sample-by sample covariance of $\delta^{18}O$ and $\delta^{13}C$ may reflect a meteoric isotopic signature induced at a later stage, during post-burial cementation. The absence of a clear correlation between $\delta^{18}O$ and $\delta^{13}C$ values in the Ainsa basin (Fig. 6.3) supports the assertion that the $\delta^{13}C$ values primarily preserve at least some "memory" of the original isotopic signals.

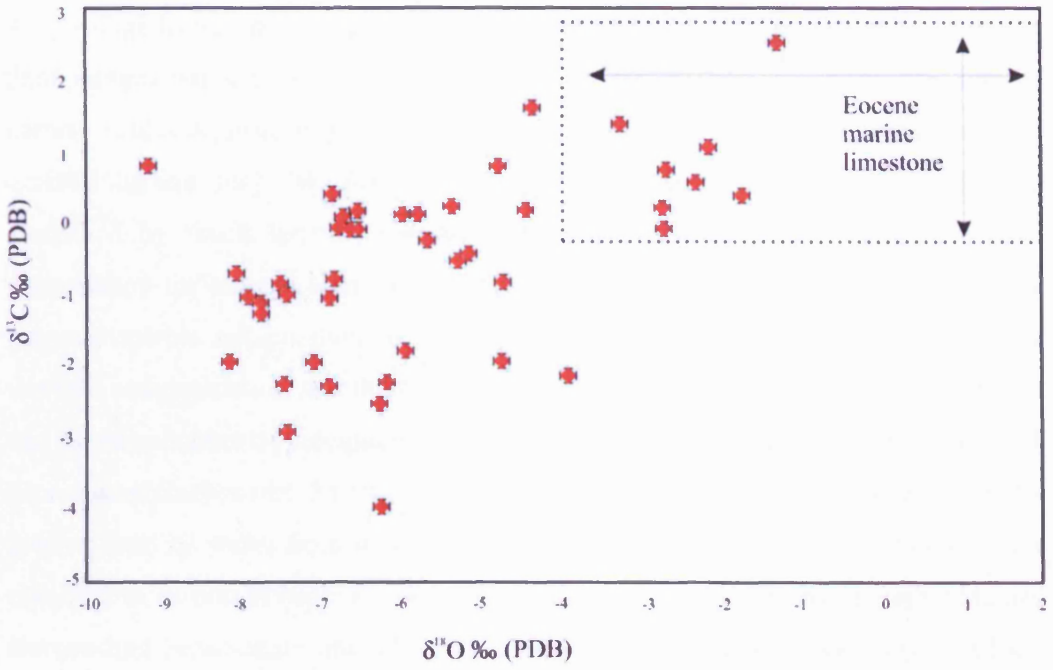

Figure 6.3: Cross-plot of the oxygen and carbon isotopic data of larger foraminifera from the Ainsa basin outcrops. The stippled box shows isotopic range of the Eocene carbonates.

There are a variety of different post-depositional processes like meteoric diagenesis, burial diagenesis and marine diagenesis (oxic and anoxic) that may affect either oxygen or carbon or both stable isotopic records. Diagenetic processes imprint different effects on the bulk sediment (rock) and components of the sediment (rock), e.g., fossil, cement, micrite. The most common processes involved in changing the isotopic composition are replacement including recrystallisation and cementation. Both may involve the precipitation of new carbonate minerals with isotopic composition different from that formed in the depositional environment originally. The chemical composition of pore-fluids is determined among others by the water-rock ratio ("openness") of the diagenetic system (Brand and Veizer, 1981; Marshall, 1992). Carbonate minerals reach equilibrium with pore fluid $\delta^{13}C$ values at three orders of magnitude (10^3) higher water-rock ratios than water-rock ratios at which $\delta^{18}O$ values of the rock approaches equilibrium with the fluid, based on the stoichiometry of the fluid as well as the rock (Banner and Hanson, 1990).

Carbon isotopic compositions tend to be less affected by diagenetic alteration than oxygen values, however, cementation or replacement reactions can change carbon values significantly in several diagenetic environments where organically-derived carbon may be incorporated (Marshall, 1992). The difference can be explained by much larger temperature dependent fractionation during diagenetic cementation for oxygen than for carbon isotopes (Friedman and O'Neil, 1977). The oxygen isotopic composition of a carbonate mineral is determined by the oxygen isotopic composition of the fluid from which the mineral precipitated in equilibrium and the temperature of precipitation. The fractionation effects are relatively large with precipitated carbonates having isotopic compositions typically around 25-30 ‰ greater than the water from which they formed. In case of carbon in carbonates, the equilibrium carbon isotopic fractionation effects between precipitating carbonate and surrounding bicarbonate are relatively small and temperature effects are relatively minor. For example, the relationships determined by Emrich et al. (1970) imply an enrichment in the solid of 1.85 ‰ at 25^0C and that $\delta^{13}C_{calcite}$ increases by approximately 1 ‰ for every 27 ^{0}C increase in temperature.

In the Ainsa basin, $\delta^{18}O$ values from the foraminifera are consistently low throughout the stratigraphy (Fig.6.3). This suggests partial recrystallisation at slightly elevated temperatures (Friedman and O'Neil, 1977) and/or equilibration with ^{18}O depleted meteoric waters (e.g. Brand and Veizer, 1981). An earlier study from the Ainsa basin (Travé et al., 1997), showed how the very early stages of fluid history in an ancient thrust belt can be inferred through geochemical analyses of fluid products, and this study concluded that $\delta^{18}O$ and $\delta^{13}C$ values of the calcite cements in veins were controlled by the isotopic composition of the marly host sediment. The depletion of both $\delta^{18}O$ and $\delta^{13}C$ with respect to Eocene seawater composition, together with elemental geochemistry of calcite cements in the veins, however, points to burial transformations of a seawater-derived fluid to a formation water composition. Travé et al. (1997) also concluded that the distribution of $\delta^{18}O$ and $\delta^{13}C$ values of the marly host-rock and calcite cements in veins from different outcrops probably resulted from differences in the meteoric water influences.

By comparison, the $\delta^{13}C$ record from the Ainsa basin seems to be only little affected by diagenetic processes as suggested by similarities with the global record (Fig. 6.4). In this case, carbon isotopic ratios mainly remain similar to the original $^{13}C/^{12}C$ seawater ratios as registered in the biogenic calcite. The meteoric diagenesis

did not affect the carbon isotopic values meaningfully, as these are less prone to alteration during diagenesis than oxygen values (Scholle and Arthur, 1980; Marshall, 1992). Oxidation of organic matter after burial in the sediment provides ^{12}C enriched dissolved carbon which may contribute to lighter $\delta^{13}C$ cements. Marine organic matter typically has a $\delta^{13}C$ which is 25‰ more negative than that of contemporaneous inorganic bicarbonate (Marshall, 1992); therefore, any cement incorporating a component of organic-derived carbon will have a very different isotopic composition from an open marine precipitate. The bulk of the sediments associated with the foraminifera samples from the Ainsa basin, however, yield low total organic carbon content (Table 6.1) on carbon analysis. In general, in such sediments, the carbonate content is many orders of magnitude lower in the pore-waters than in the initial solid carbonate phases (Scholle and Arthur, 1980) and therefore cements precipitated from such pore-waters are less effective in altering carbon isotopic content of the original material.

A detailed study of the possible conditions caused by local meteoric diagenesis in the Ainsa basin is beyond the scope of this pilot study. However, possible explanations for $\delta^{13}C$ preservation are likely to be : (1) meteoric diagenesis at some distance from recharge may be a closed system for carbon isotope values whilst oxygen values change considerably (Lohmann, 1988); (2) low water-rock ratios favour partial or even total retention of the original composition (Marshall, 1992); (3) recrystallisation in the meteoric environment is much more likely to result in the preservation of carbon isotopic signatures than those of oxygen (Marshall, 1992).

6.4 Ainsa basin *versus* global isotopic signal

Both $\delta^{13}C$ and $\delta^{18}O$ curve (sixth-order polynomial fit) from the Ainsa basin were compared with the Eocene global open-ocean curve (Fig. 6.4) of Zachos et al. (2001), which was derived from global deep-sea oxygen and carbon isotope records based on data compiled from more than 40 Deep Sea Drilling Project (DSDP) and Ocean Drilling Program (ODP) sites. By making such a comparison, and with reliable data, it

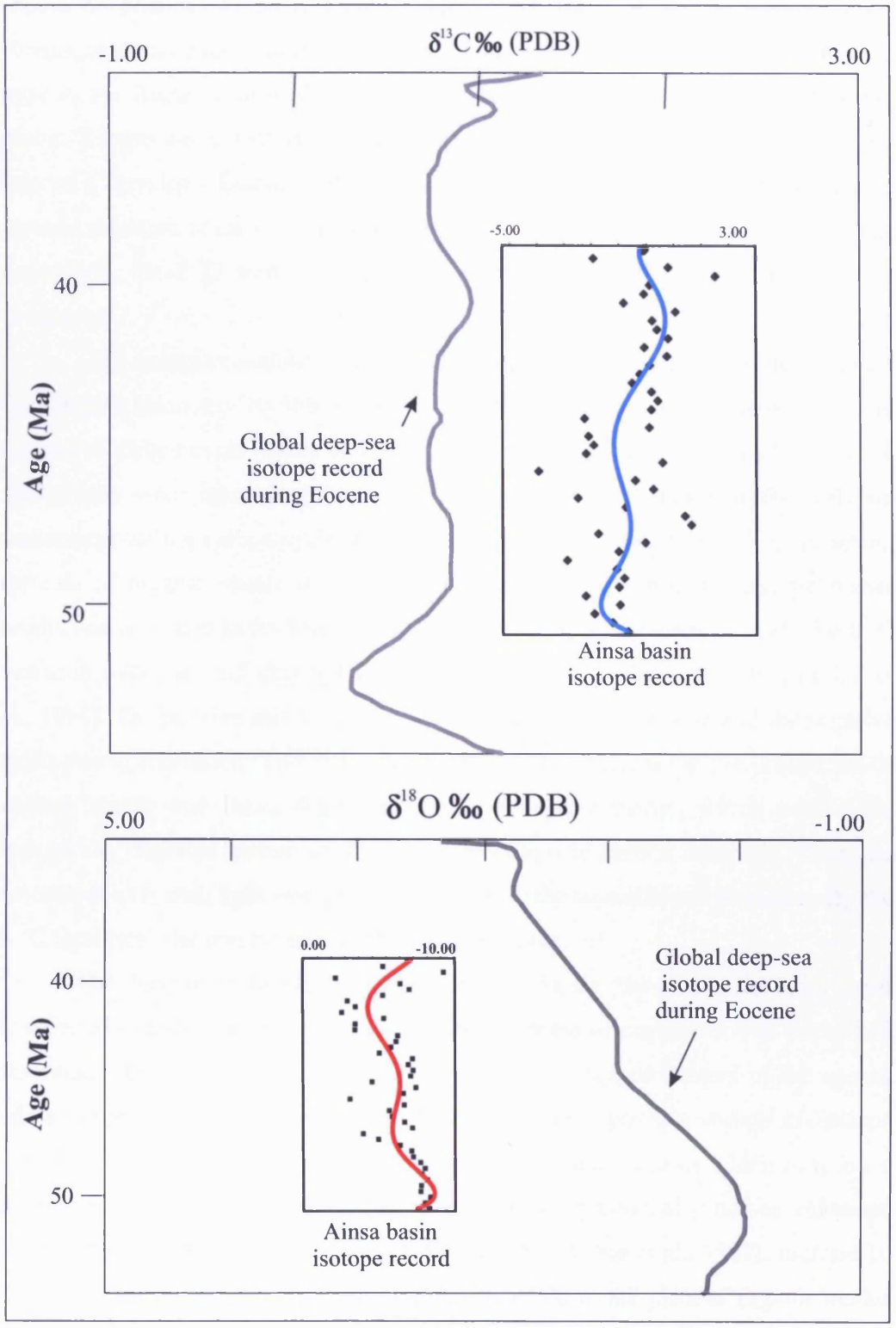

Figure 6.4: Carbon and oxygen isotope record of the Ainsa basin clastic systems in comparison with the global deep-sea isotope record (Zachos et al., 2001). PDB is Pee Dee Belemnite. Note the scale on Y-axis is same for the Ainsa basin and the global deep-sea isotope record.

should be possible to unravel any global signal, for example, eustatic sea-level change, from more regional processes, i.e., Pyrenean tectono-environmental change. It appears the Ainsa basin $\delta^{13}C$ curve show a better correlation with that part of the global Eocene curve that is interpreted to be equivalent to the Ainsa basin time interval (Ypresian - Lutetian), than the $\delta^{18}O$ curve. As discussed above, the carbon isotope signature tends to be less altered than the oxygen isotopic signature. Thus, henceforth, the $\delta^{18}O$ trend of the Ainsa basin is not considered further in this discussion.

The isotopic composition of carbon in the hydrosphere and biosphere reflects the complex balance of equilibrium and kinetic fractionation reactions associated with the global carbon cycle (Faure and Mensing, 2005). Variations in the carbon isotope stratigraphy were interpreted in terms of changes in the balance of the different components of the carbon cycle. Among various factors contributing $\delta^{13}C$ variation, the role of organic matter is well known (Craig, 1953). Since the organic matter production is related to sea level variation, attempts are being made to relate the $\delta^{13}C$ variation with sea level change (Schackleton et al., 1983; Weissert, 1989; Follmi et al., 1994). The positive shifts are seen to occur during transgression and the negative shifts during regression. The rise in sea levels leads to decrease in the production of organic matter and slows down the decay of organic matter, which returns the isotopically depleted carbon to the dissolved inorganic carbon reservoir. Thus, the amount of CO_2 with light isotopic ratio reduces in the seawater and consequently the $\delta^{13}C$ increases. The reverse is true when sea level falls.

The long-term trends in carbon values during the Cenozoic have been interpreted in terms of changes in the relative amounts of organic carbon burial and oxidation which are thought to reflect changes in the oxygen content of the oceans and atmosphere (Schackleton, 1986). In the Mesozoic, positive carbon excursions have been encountered at several important stratigraphic horizons which have been interpreted to reflect the times of increased organic productivity and/or enhanced organic deposition within the oceans (Jenkyns, 1980; Arthur et al., 1987). Increase in the rate of withdrawal of isotopically negative carbon in the form of organic matter leaves the residual dissolved inorganic carbon isotopically 'heavy'. In some instances carbon isotope excursions have been correlated with black shale depositional episodes or evidence for expanded oxygen minimum zones (Shlanger et al., 1987).

The $\delta^{13}C$ curve of the Ainsa basin shows correlatable evolutionary pattern with that of the global deep-sea carbon isotope records shown by Zachos et al. (2001). This similarity suggests that, as a "first-order control", eustatic changes in sea-level have exerted more influence in the Ainsa basin than any regional, tectono-environmental changes. The data also suggest that during the evolution of the deep-water Ainsa basin, it remained connected to the global open ocean, also supported by the abundance of *Nummulites* throughout the Ainsa basin sediments. During Ypresian the Pyrenean foreland was fringed by large carbonate platforms and by Late Lutetian the marine corridor connecting Atlantic to the Tethys was closed, to be replaced by a foreland basin, i.e., the Ainsa and Jaca basins (see Chapter 2). On either side of the foreland basin, marine carbonate platforms became more restricted, but a connection to the Bay of Biscay remained open (Meulenkamp and Sissingh, 2000).

6.5 Summary

A pilot study on stable isotopic signature (carbon and oxygen) of larger foraminifera from the Ainsa basin was undertaken in an attempt to recognise any eustatic sea-level change from more regional tectono-environmental changes. The carbon isotope curve from the Ainsa basin appears to correlate well with the global Eocene deep-sea carbon isotope curve. The Ainsa basin remained connected with the open ocean throughout its history of infill. Interpreting the carbon isotope curve excursions in terms of sea-level changes, however, has proved to be difficult and somewhat inconclusive, due to the limited number of samples. This, in turn, restricted the possibility of deconvolving any regional or Pyrenean tectono-environmental effects from eustatic sea-level control.

CHAPTER 7

Discussion

7.1 Tectonic setting

Sandstones originating from different tectonic settings have characteristic detrital minerals (Crook, 1974; Dickinson and Suczek, 1979; Dickinson, 1985) and also characteristic major and trace elements chemistry (Bhatia, 1983; Roser and Korsch, 1986; Kroonenberg, 1994). Sandstone geochemistry depends on the dominant mineralogy, hence also varies systematically with provenance, source-area weathering, and tectonic setting (Johnsson and Basu 1993; Roser 2000). Whole-rock chemistry can also detect variations in elements that are not picked up in modal analysis, for example Cr, Sc, Zr, La, and Th. In the following account the detrital and chemical compositions of the Ainsa basin sandstones (arenites) are discussed to determine their tectonic setting.

Crook (1974) first proposed the determination of tectonic setting of sandstones using framework mineral composition (detrital modes), and this model has since undergone considerable refinement (e.g. Dickinson and Suczek, 1979; Dickinson et al., 1983). Inferring sandstone provenance utilising Q-F-L plot of Dickinson and Suczek (1979) is well established and a common routine in provenance studies for sandstones. However, such provenance determination needs to be considered with caution as post-depositional modifications and/or diagenesis might cause changes in the original composition, leading to modification in the Q-F-L plot (McBride, 1985). In this study the petrographic modal analysis data were also plotted on the standard Q-F-L ternary diagram which reveals that the Ainsa basin sandstones cluster entirely in the recycled orogen field (Fig. 4.5A). This is also the case for majority of the Jaca basin arenites (Fig. 4.5A), with a very few exceptions which plot outside the recycled orogen field. In this context, recycled orogen includes the deformed and uplifted supracrustal strata, dominantly sedimentary but also volcanic in part, exposed in varied fold-thrust belts of orogenic regions (Dickinson, 1985). It is noteworthy that L

pole of the Q-F-L plots does not include the carbonate lithic fragments commonly present among the sandstones of the Ainsa and Jaca basins.

The geochemical analysis of sedimentary rocks is also a valuable tool for determining the tectonic settings, as the chemical composition of source rocks exerts a major influence on the chemistry of sedimentary rocks which can be greatly modified by subsequent processes (Rollinson 1993). Ratios of relatively immobile major and trace elements have been widely used to provenance sandstones (e.g., Bhatia 1983; Bhatia and Crook 1986) although such studies were developed using small, geographically restricted datasets. Nevertheless, they are useful as indicators of likely source-rock compositions. Since the pioneering studies by Schwab (1975), Bhatia (1983) and Roser and Korsch (1986), major element chemistry has been used to discriminate the tectonic settings of sandstones, and has been commonly applied in more recent publications, e.g., Shao et al. (2001) reconstructed the evolution of the Turpan basin (NW China) from the Permian to the Tertiary using geochemistry and sandstone petrology; Zimmermann and Bahlburg (2003) commented on provenance analysis and tectonic setting of the Ordovician clastic deposits of the southern Puna basin (NW Argentina) using petrography and various geochemical techniques; Armstrong-Altrin et al. (2004) investigated petrographic, major, trace and rare earth element compositions of sandstones from the upper Miocene Kudankulam Formation, South India to determine their provenance, tectonic setting and weathering condition.

Roser and Korsch (1986) examined the significance of K_2O/Na_2O ratios and SiO_2 contents of sandstones from contrasting tectonic settings and extended their application to the finer-grained members of turbidite suites (New Zealand greywackes). Their compilation of published data defined three first-order tectonic setting field - passive margin (PM), active continental margin (ACM) and oceanic island arc (ARC) - on a simple bivariate SiO_2-K_2O/Na_2O plot. These categories are broadly similar to those of Crook (1974) (see Section 5.2.1) and within these divisions several depositional settings are possible. In case of the Ainsa basin sandstones majority of the samples plot in the ACM field of the SiO_2 vs. K_2O/Na_2O diagram (Fig. 5.5a), with a few sample plotting outside the ACM field. In contrast, plots are more dispersed in the Fe_2O_3+MgO-TiO_2 (Fig. 5.5b) and the Fe_2O_3+MgO – Al_2O_3/SiO_2 (Fig. 5.5c) discrimination diagram proposed by Bhatia (1983) who analysed 69 sandstone samples that represents five Paleozoic sandstone suites of eastern Australia. In both these plots majority of the samples lie in and around the

active continental margin field. The discrimination diagrams of Bhatia (1983) are not definitely conclusive in this study which might be due to the presence of higher amount of carbonates in the Ainsa basin samples (~18-50% CaO) than of those analysed by Bhatia (1983). However, Roser and Krosch (1986) classification scheme found to be more applicable for the Ainsa basin sandstones as examination of individual oxide data from their study shows that some samples in their dataset also contain considerable CaO (up to 19%).

Nevertheless, all these discrimination diagrams mentioned above at least suggest that the Ainsa basin clastic sediments were deposited in an active continental margin tectonic setting. The types of sedimentary basins related to this particular tectonic settings are subduction-related basins, continental collision basins and pull-apart basins associated with strike-slip fault zones (Reading, 1982), which developed on or adjacent to a thick continental crust composed of rocks of older fold belts. Sediments in such basins are dominantly derived from granite-gneisses and siliceous volcanics of the uplifted basement (Bhatia, 1983). The petrography data, especially the suggestions about source rocks utilising different quartz varieties (Section 4.7), also points to a similar kind of provenance.

Trace elements (e.g. Ti, Nb, Ta, Cs, Ce, Ni, V, Co, Y, La, Th, Sc and Zr) in clastic sedimentary rocks are considered to be immobile under conditions of weathering, diagenesis and moderate levels of metamorphism, and are commonly preserved in sedimentary rocks (Bhatia and Crook, 1986; McLennan et al., 1993). Their geochemical composition in siliciclastic sedimentary rocks is a sensitive indicator of provenance and weathering at the source of sediments (Taylor and McLennan, 1985; Roser and Korsch, 1986; Hassan et al., 1999; Cullers, 2000). Therefore, the trace elements represent well-established provenance and tectonic setting indicator and this fact has led to several studies using trace element composition of sedimentary rocks in order to determine their provenance and tectonic setting (e.g. McLennan et al., 1993; Eriksson et al., 1994; Bahlburg, 1998; Burnett and Quirk, 2001; Zimmermann and Bahlburg, 2003). However, there is a widespread agreement that the finer-grained clastics like shale are more likely to preserve trace elements than coarser-grained clastics like sand (McLennan, 2001). Modern studies have used shale compositions to estimate upper crustal trace element abundances (Taylor and McLennan, 1985) because most trace elements are enriched in shales compared to most other sediment types. In addition, shales dominate the sedimentary

records constituting almost up to 70% of the stratigraphic record depending on the method of estimation.

In this study discriminate plots proposed by Bhatia and Crook (1986) utilising trace element ratios were used to determine constraints on tectonic setting. Bhatia and Crook (1986) noted a large variation of trace element characteristics in the greywackes of Paleozoic turbidite sequences of eastern Australia which reflected distinct provenance types and tectonic settings for various suites. Surprisingly all of the three discriminate plots (Fig. 5.7) from the Ainsa basin failed to reveal any conclusive tectonic setting. However, it is noteworthy to mention that the samples used by Bhatia and Crook (1986) are similar to those of Bhatia (1983) given that the discrimination diagrams of Bhatia (1983) utilising major oxides found to be inapplicable for the Ainsa basin samples. The apparent inconclusiveness of trace element discrimination diagrams used in this study might be a cumulative effect of different interrelated factors. The samples collected for this study, in general, are all above 'very-fine sand' size, majority being medium-grained clastics with carbonate components occurring in different phases. Chemical weathering at the source and/or during sediment transport might also be a factor for this discrepancy in trace element data. In summary, the mixed siliciclastic-carbonate nature of the Ainsa basin samples restricts the application of standard geochemical (major and trace element) discrimination diagrams to these samples. However, a detailed investigation on this particular aspect is beyond the scope of the study

7.2 Provenance

Heavy mineral assemblages have been used as provenance indicators for many years. The ability to date some of these detrital minerals using isotopic techniques provides chronological information that relates to the sediment source and pathways. This may include an actual age of sedimentation if the dated crystals come from syndepositional volcanic eruptions, or alternatively, the measured isotopic ages may reflect a variety of factors including the age of the hinterland lithologies, weathering, transport, and post-depositional heating, which can reset the earlier isotopic signature (Köppen and Carter, 2000). The ages of detrital zircon grains in quartzose sandstones provide direct evidence for the ages of bedrock from which the sand grains were derived (Gehrels et

al., 1995) as the generally distinct thermotectonic signatures of source regions are retained clearly in the erosional detritus.

Detrital zircon fission-track analysis has a long tradition in provenance analysis (e.g. see review in Hurford and Carter 1991; Carter 1999), in fact, its earliest use was for simple provenance analysis as the technique allows identification of major cooling ages in the source terrain. This approach to provenance analysis, i.e., the analysis of a single mineral phase to address sediment provenance, is referred to as varietal study (Haughton et al., 1991). However, varietal studies have limitations because the unique source terrain indicated by the data only pertains to the specific mineral studied, and there may be a host of other lithologies in the source terrain that are essentially unidentified. Therefore, varietal studies are most effective when combined with other sediment provenance techniques like petrography and geochemistry aimed at identifying the full provenance spectrum (Bernet and Garver, 2005).

Previous detrital zircon studies include: identifying sediment provenance and source thermal history (Hurford et al., 1984; Hurford and Carter, 1991; Dickinson and Gehrels, 2003), an age or constraint on the time of sedimentation (Carter et al., 1995), the time/rate of basement exhumation and its evolution (Garver and Brandon, 1994; Lonergan and Johnson, 1998; Spiegel et al., 2000; Helbing and Tiepolo, 2005) and cooling/exhumation history of convergent mountain belts (Bernet et al., 2006).

Commonly the young populations of grain FT ages have received the most attention as they can be ascribed to active processes in the source terrain. For example, if a young population of euhedral zircon FT ages is close or identical to the depositional age, then they are likely derived from a volcanic source. Otherwise, young age peaks in sediment derived from convergent mountain belts without active volcanism reflect rapid exhumation of deep-seated rocks. Zircons from such rocks have been fully reset during regional metamorphism and their cooling ages represent the recent thermal history of the source area. Zircons with older cooling ages are usually derived from partially or non-reset cover units and are therefore recycled and re-introduced into the rock cycle (Bernet and Garver, 2005).

In this study combined FT and U-Pb age data from detrital zircons were used to monitor the provenance of the Ainsa basin sediments and thermo-tectonic evolution of its hinterland. From the detrital zircon FT data (Section 5.3.1) two major cooling age modes are obtained: (i) Hercynian and/or post-Hercynian, which are similar to the

U-Pb ages and (ii) Mesozoic (Lower Triassic-Lower Cretaceous). The consistent occurrence of these two age modes in majority of samples requires a continuous supply of zircons from sources that have similar kind of age structure. Shoemaker and Garver (2000) reported similar age patterns in their study of detrital zircons from modern river sediments to characterise cooling ages of either side of the Pyrenean orogen as well as from syn-orogenic strata from the north side of the orogen. It showed that sediments shed off the north, draining the older section of the orogen (Ariege River, France), are dominated by mid-Cretaceous (~110 Ma) and Late Cretaceous (~67 Ma) cooling ages, where as sediments shed off the south (Segre River, Spain) are dominated by Eocene (~ 47 Ma), mid-Cretaceous (~ 91 Ma) and lower Mesozoic (~240 Ma) cooling ages. However, the zircon population from the north side of the Pyrenees is dominated by post-Hercynian cooling ages with a lesser fraction related to Late Cretaceous initiation of the Pyrenean orogeny (~ 75-65 Ma).

In addition to the Hercynian age mode, there is evidence of other U-Pb age modes in the present study that range between ~ 448-481 Ma and ~ 620-768 Ma (Table 5.6). Recent U-Pb dating on zircons provided a ca. 474 Ma, early Ordovician (Arenigian) age for the meta-granites in the Pyrenees, along with a wide range of significant concordant inherited ages spanning from early Archean (3.5 Ga) to Pan-African / Cadomian (600–800 Ma) from orthogneisses (Cocherie et al., 2005). The petrography and geochemistry data (to some extent) also points to a granitic a source of the siliciclastic materials in the Ainsa basin sediments.

U-Pb dating of grains also dated by FT shows that the majority of the grains from the Ainsa basin have FT ages that are within error or slightly younger than their U-Pb ages (Fig. 5.9). This indicates that the bulk of the FT data is recording rapid exhumation following granite emplacement events. The most likely sources for such histories are the Hercynian granites located in parts of the Pyrenean Axial Zone and thrust belts. The North and South Pyrenean thrust belts comprise thrusted Mesozoic and/or basement rocks derived from the European and Iberian plates, respectively. By contrast the Axial Zone is an imbricate stack of crystalline Hercynian basement thrust sheets. The North Pyrenean thrust belt involves Hercynian basement massifs overlain in part by an Upper Cretaceous flysch deposits (Fiescher, 1984; Déramond et al., 1993). The South Pyrenean thrust belt consists of southward - imbricated thrust sheets comprising mainly Mesozoic platform series and Palaeogene siliciclastics (Morris et al., 1998). Accordingly, the majority of zircons from the Ainsa basin deep-marine

clastic deposits are likely to have been eroded from granites within the Axial Zone and the South Pyrenean Thrust belt. This is further supported by the petrography and geochemical data which defined the tectonic setting and sediment source in a regional context.

Combined zircon FT and U-Pb dating has shown that the young age components reflect Cretaceous exhumation of much older sources dated to between 258±1 and 735±3 Ma. Since the geochronology and petrography data indicate that the main sediment source region for the siliciclastics does not change significantly throughout the evolution of the Ainsa basin, the change in exhumation age must reflect source behaviour rather than any major changes in sediment routing. A systematic trend of increasing exhumation ages as seen in this study does not fit with a single source region experiencing progressively deeper levels of erosion. Instead such a trend can only be explained by erosion of a sediment sequence that contains a conventional exhumation trend (Fig. 7.1). Accordingly the first sedimentary units to be eroded and re-deposited would contain the youngest exhumation ages (e.g. Arro, 109±9 Ma) and the oldest units would contain the oldest exhumation ages (Morillo, 174±9 Ma). The youngest zircon FT exhumation age places a maximum age constraint on the depositional age of the recycled sediment, i.e. the youngest eroded sediments must be Lower Cretaceous or younger in age. This is consistent with the presence of reworked carbonate clasts with Cretaceous pelagic calcispheres (Chapter 4).

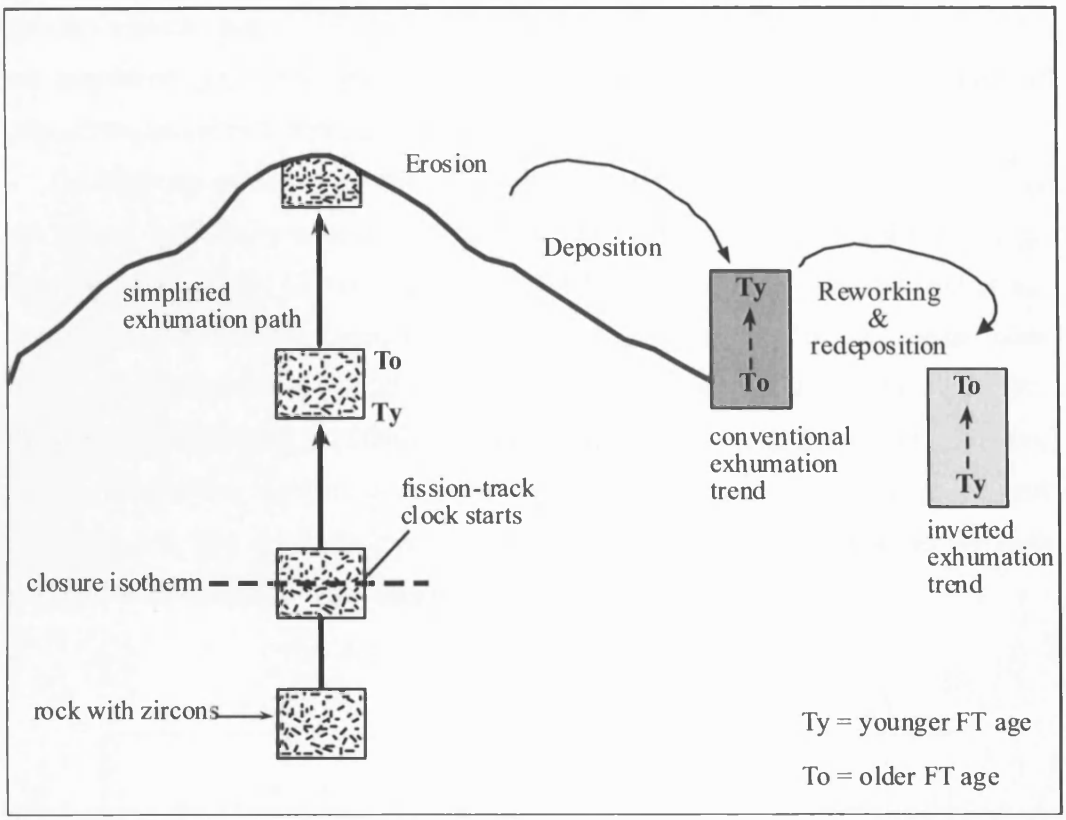

Figure 7.1: A simplified sketch showing development of an 'inverted exhumation trend' in fission-track (FT) ages. Conventionally zircon FT ages decreases towards the top (younger part) of the stratigraphy, in the first cycle of erosion and deposition of sediments. In case of reworked sediments (second or more cycles of erosion-deposition), FT ages show a reverse pattern of the conventional trend.

7.3 Hinterland evolution and sediment dispersal

Central to most detrital FT thermochronology study is the concept of 'lag time', which is defined as the thermochronological age minus the depositional age (e.g. Garver et al., 1999; Bernet et al., 2001). In other words, lag-time of a sample is the time required for the sample to cool, get exhumed to the surface, and then get deposited in a nearby basin (Fig. 7.2). As a rock is exhumed to the surface, the rock cools below the closure temperatures of the different thermochronometers. When this happens, various isotopic clocks start. Eventually the rock reaches the surface where it is subject to erosion. Zircon grains are then released into sediment and transported

into the adjacent basins through different medium like rivers or glaciers, where they are deposited. Lag time integrates the time between closure and the time of deposition, and mainly represents the time needed to exhume the rock to the surface.

Studying cooling ages of detrital grains from synorogenic sediments provides the unique opportunity to obtain information about exhumation rates in the past (e.g., Cerveny et al., 1988; Garver & Brandon, 1994; Garver et al., 1999; Spiegel et al., 2000; Bernet et al., 2001; Carter and Bristow, 2003). The concept of lag time has been used for determination of past exhumation events in a convergent mountain belts like the Himalaya (Bernet et al., 2006). An attempt has been made to use a similar kind of approach involving lag time concept in this study, the Pyrenees being a convergent mountain belt like the Himalaya. However, there is certain limitation in the data obtained from the Ainsa basin clastic sediments

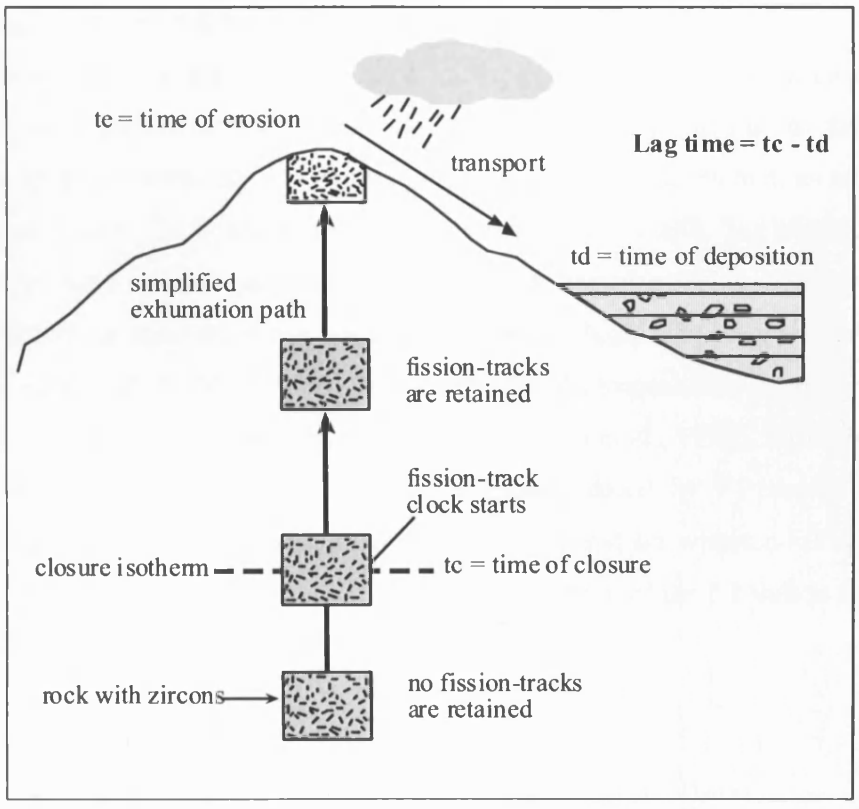

Figure 7.2: The lag time integrates the time between closure and the time of deposition, and mainly represents the time needed to exhume the rock to the surface (after Bernet and Garver, 2005).

As pointed out by Bernet et al., (2006), it is very important that the depositional age of the studied strata is reasonably well known (±1Myr) to be able to apply the lag-time concept. Pickering and Corregidor (2005) reported the age of the deep-marine parts of the Ainsa - Jaca basin spans the early to middle Eocene (Ypresian and Lutetian Stage), using the planktonic foraminifera zonation of Berggren et al. (1995) and the geological time scale of Gradstein et al. (2004). However the age of individual clastic systems from the Ainsa basin is not known, except the fact that deep-marine sandbodies in the Ainsa basin (~25) were accumulated in a period of ~10 myr based on biostratigraphy (Pickering and Corregidor, 2005). This time-frame has been corroborated by Payros et al. (1999) (see Section 2.3.1). In the absence of any alternative and ultra-high-resolution chronostratigraphic framework of the Ainsa basin, it is assumed that each individual depositional system spanned linearly within the 10 myr period for constructing the lag plot (Fig. 7.3). It would be more realistic to have a non-linear distribution of the systems, but the trend of up-section evolution of the FT age modes would, however, remain the same in such a case.

The other vital aspects for lag plots are (a) post-depositional burial and heating that can cause partial or full resetting of FT ages and (b) the ability to distinguish between ages that record cooling and those that record zircon formation, as in the case of volcanic grains (Carter and Bistrow, 2003; Bernet et al., 2006). The resetting of FT ages are of little concern only for the most deeply buried samples, because the FT partial annealing zone of zircon occurs at relatively high temperatures and ranges between ~200– 320 °C (for 10^6–10^8 years), although the upper value is poorly defined due to a lack of suitable geological constraints (Tagami et al., 1998). Furthermore, as discussed earlier, U-Pb dating of grains previously dated by FT shows that the majority of grains from the Ainsa basin have FT ages that are within error or slightly younger than their U-Pb ages. This indicates that the bulk of the FT data is recording cooling due to exhumation, not zircon formation ages.

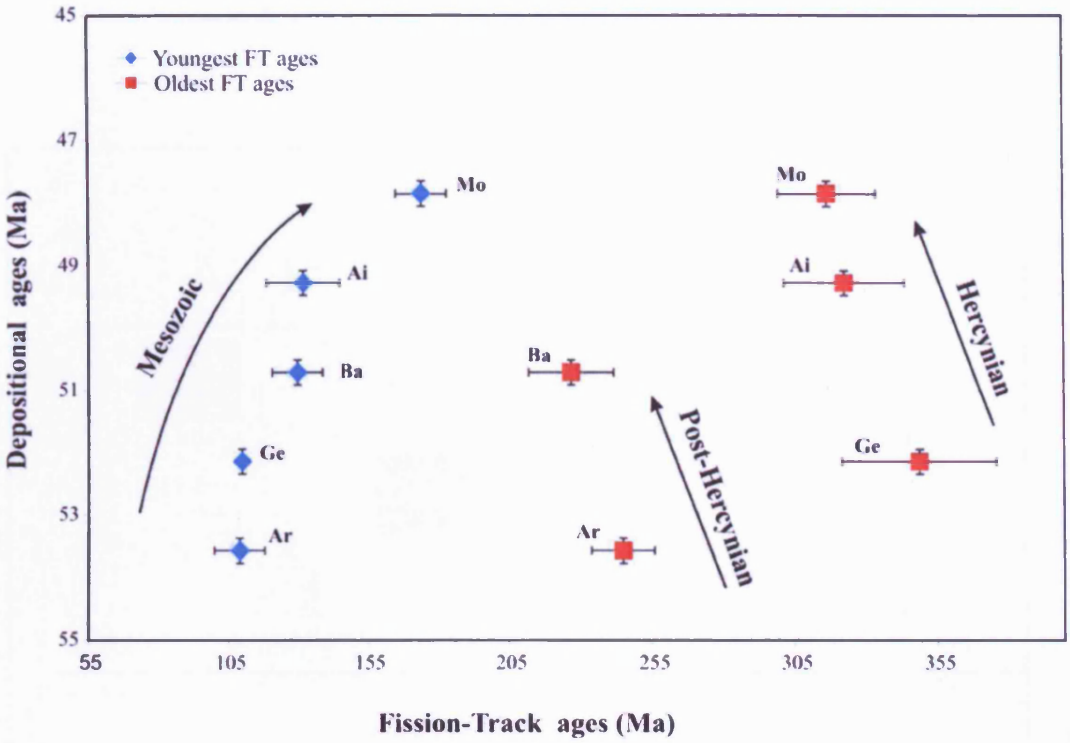

Figure 7.3: Lag plot of detrital zircon fission track (FT) ages of the Ainsa basin. The youngest (Mesozoic) FT ages exhibits inverted exhumation trend, however, the oldest FT ages (Hercynian and post-Hercynian) show a conventional exhumation trend. See text for explanation. Note only the youngest and oldest age components are plotted. Ar: Arro; Ge: Gerbe; Ba: Banaston; Ai: Ainsa; Mo: Morillo.

The lag plot (Fig. 7.3) shows that the youngest zircon FT ages which are all Mesozoic, are getting older up the stratigraphy (inverted exhumation trend); however, the oldest FT ages, both Hercynian and post-Hercynian, show a conventional exhumation trend i.e. ages young up-section. Although the principal provenance for the siliciclastic sediments of the Ainsa basin is the Axial Zone and South Pyrenean Thrust belt, these two zircon exhumation trends require different granitic sources which experienced different exhumation histories (Fig. 7.4).

The conventional exhumation trend requires granite samples to reach shallow crustal levels soon after granite emplacement. The zircons present within the inverted exhumation trend originally came from a part of the granite belt where emplacement depths were most likely greater, and which therefore subsequently experienced much deeper levels of erosion with final exhumation taking place in the Cretaceous. This later exhumation probably occurred during the extensional/transtensional Mesozoic stage of the evolving Pyrenean belt. To explain the inverted trend the Cretaceous

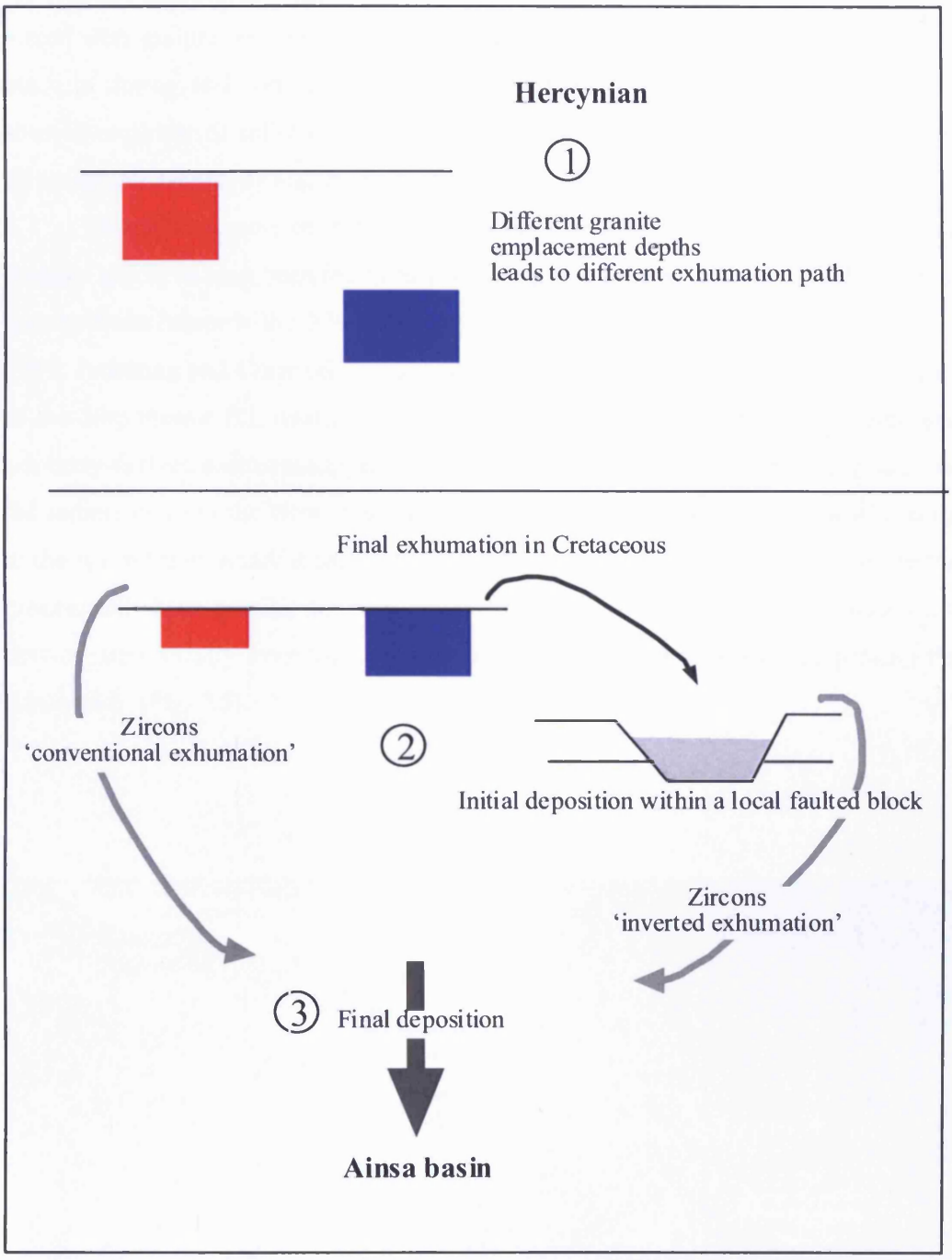

Figure 7.4: Schematic illustration explaining the two different zircon exhumation trends observed in Ainsa basin. See text for details. Red and blue boxes signify granitic bodies containing zircons with Hercynian and Mesozoic principal FT age components respectively.

phase of exhumation must be linked to initial deposition within a local basin, probably within a faulted block that was subsequently inverted and progressively eroded during the Palaeocene feeding into the fluvial systems supplying the Ainsa basin where it mixed with granite detritus sourced directly from an area where cooling had taken place in during and soon after granite emplacement. Fitzgerald et al. (1999) also showed presence of relict extensional features in the Pyrenees that accommodated thrusting and eventually leading to relatively slow exhumation in the Eocene.

Throughout most of the history of the Ainsa basin the deep-marine clastic systems appear to have been fed from a south-eastern point source with axial sediment gravity flows towards the NW (~320°) in the proximal Ainsa basin (Dreyer et al., 1999; Pickering and Corregidor 2005) (Fig. 2.9). In the younger, upper Lutetian part of the deep-marine fill, west of the Boltaña anticline in the Jaca basin, an additional northerly-derived sediment supply is recognized (Remacha et al. 2003). It appears that the sediments from the Hercynian basement from the North were not routed directly to the Ainsa basin, rather it came via the south-eastern entry point to the basin. In the process, all these granitic material got mixed with the other sediments which are derived more locally from the anticlines and associated structures encompassing the Ainsa basin (Fig. 7.5).

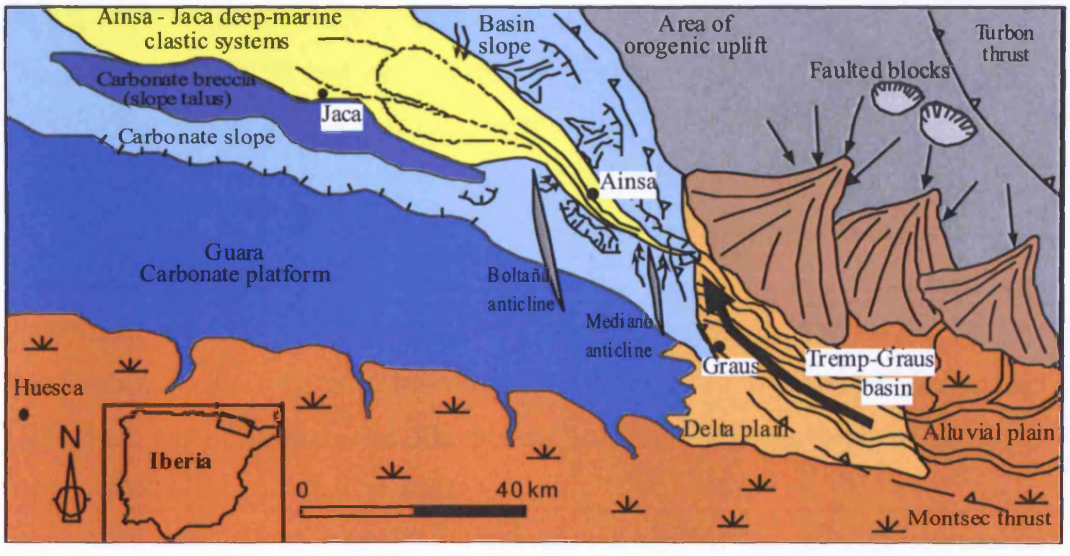

Figure 7.5: Palaeogeographic reconstruction of the Ainsa and Jaca basins, modified after Dreyer et al. (1999). Arrow indicates sediment dispersal. See text for details.

7.4 Evolution of basinal sediments

7.4.1 Ainsa basin

Evolution of the basinal sediments is discussed in the following paragraphs in terms of their petrographic composition reported in Chapter 4 with inputs from the geochronology and geochemistry data (Chapter 5). Prior to deep-marine conditions (created by the flexural response to loading of the lithosphere by thrust-sheet stacking), the Ainsa and Jaca basins would have had a relatively low seafloor gradient from non-marine to shallow-marine environments. The shallow-marine shelf would have been covered by unconsolidated siliciclastic sediments, which were supplied by fluvial, fluvio-deltaic and coastal systems. During the initial stages of the rapid deepening of the Ainsa and Jaca basins, it is reasonable to assume that these unconsolidated siliciclastic-rich sediments, including those stored in the terrestrial and coastal environments (NCE grains), were reworked to accumulate as arenites of the Fosado system in the Ainsa basin.

There must have been a time lag between the development of the deep-marine Ainsa basin, the thrust-related uplift, exhumation and erosion of underlying consolidated (mainly carbonate) stratigraphy, and the deep erosion of any submarine canyons, as seen in the Arro system (Fig. 2.10). The first significant uplift and erosion of the underlying and surrounding early Eocene carbonate stratigraphy could explain well the first influx of reworked shallow-marine carbonate grains in the Arro system. The relative paucity in reworked carbonate grains in the overlying Gerbe system (compared with the Arro system) might be due to the entire non-marine to marine sediment-delivery system trying to reach some kind of equilibrium profile, with a time lag for volumetrically significant siliciclastic recharge to near-shore, coastal and shelf environments.

The presence of angular-unconformity-bound stratigraphic intervals in the Ainsa basin (Fig. 2.10), and the likely time intervals of 2-3 myr (Pickering and Corregidor, 2005), suggests that the erosion and reworking of substantial carbonate material took place at such time scales.

At the start of the Banaston system, there is a substantial and significant influx of reworked intrabasinal carbonate clasts, including large carbonate olistoliths up to metres in maximum dimension. By the time of the accumulation of the Ainsa system,

the large shift between carbonate-rich and carbonate-poor clastics appears to have ceased, with the petrography of the Ainsa system suggesting the development of an important sediment source that supplied extrabasinal carbonates. Although this source existed prior to the Ainsa system times, it appears to have become progressively more important. This trend is also mirrored in the petrography of the youngest two deep-marine systems (the Morillo and Guaso systems). Unlike in the Ainsa system, within the Morillo and Guaso systems, the importance of intrabasinal carbonate grains, as represented by bioclasts, was reduced. However, the supply of extrabasinal carbonate material increased. These extrabasinal carbonate clasts commonly contain Pithonellids that suggest a reworked Cretaceous source. The Guaso system is relatively enriched in siliciclastic material (NCE grains), compared with the Morillo system, a signature that would be expected during the final stages of infill of the deep-marine Ainsa basin, as it shallowed up, with progradation of the overlying fluvio-deltaic systems (Fig. 2.10).

The main source area for the deep-marine siliciclastic sediments was in the subaerial rising Pyrenean orogen, as discussed in Section 7.2, that funnelled sediments through the Tremp-Graus basin (e.g., Mutti et al., 1985, Marzo et al., 1988, Vincent, 1999, Clevis et al., 2004). The intrabasinal carbonate grains, however, were derived both from the resedimentation of virtually coeval sediments of shelf marginal in which carbonate factories were already active (Fontana et al., 1989), and from slightly older eroded carbonates associated with the intrabasinal seafloor growth structures of, for example, the early stages of the Mediano and Boltaña anticlines (Mutti, 1977; Poblet et al., 1998; Pickering and Corregidor, 2005). Another source provided the extrabasinal carbonate grains to the deep-marine deposits. The majority of those extrabasinal carbonate grains show a Cretaceous dolomitic source as evident from composition. The growth and associated erosion of the Mediano and Boltaña anticlines, at the eastern and western margins of the Ainsa basin, respectively, could be a possible source, particularly as they have a close proximity to the basin. In the case of the Mediano anticline, the actual sediment source may have been a similar but buried stratigraphic sequence further east.

The rocks exposed in the core of the Boltaña anticline comprise carbonates and terrigenous sediments of Palaeocene to Middle Eocene age, and they are partly time equivalent of the Hecho Group turbidites (Mutti, 1977). However, the Mediano anticline contains two stratigraphic units, separated by an angular unconformity: (1) an older unit of Triassic shale, evaporite, limestone and dolomite horizons, and (2) a

younger unit of Cenomanian to Ypresian (Cuisian) limestone, dolomite, calcareous sandstone and marls (Poblet et al., 1998). The syndepositional uplift and erosion of the Mediano anticline is, therefore, a more attractive source to provide the majority of the (CE grains) to the basin during Morillo-Guaso time. Palaeocurrent data suggest that erosional submarine channels cut through the Mediano anticline while travelling towards the deeper parts of the Ainsa basin. In particular, palaeocurrent data from the southern outcrops of the Ainsa system (south of Ainsa), and in the southeaster parts of the older Banaston system, around the villages of Banaston and Usana, suggest a more easterly sediment source (Pickering and Corregidor, 2005; Bayliss and Pickering, *pers. comm.*, 2007).

In summary, this petrographic study shows that all three sediment sources were active throughout the depositional history of the Ainsa basin, but the relative importance of each source shows temporal changes. In the older parts of the Ainsa and Jaca basins, the siliciclastic and the intrabasinal carbonate sources predominated, although not simultaneously. During sediment deposition of the Ainsa system, the extrabasinal carbonate source gained in importance, and by Morillo-Guaso times it became very significant.

7.4.2 Jaca basin

In the past few decades, there has been less published research from the Jaca basin compared to the Ainsa basin. Although this study has attempted to redress the balance, nevertheless, much of this work still has remained focused on the more proximal Ainsa basin considering the analytical techniques and scope of the project. Furthermore, detailed mapping and bed correlation data for each system in the Ainsa basin is available whereas, generating such data from the Jaca basin was beyond the scope of this project.

The petrographic characteristics and evolutionary pattern of the Jaca basin systems are shown in Fig. 4.9B. The Jaca basin systems are the more distal basinal equivalents of the Ainsa basin systems (Figs. 2.9 and 2.11), and, therefore, it seems intuitively reasonable to expect that the petrographic trends should be directly comparable between the Ainsa and Jaca basins. In general the grain sizes of the distal Jaca basin sediments are finer than their proximal counterparts in the Ainsa basin. This lateral grain-size variation could be ascribed to sorting during transportation.

However, possible down-current compositional variations due to a hydrodynamic sorting effect appear negligible as all the various framework grain types observed in the Ainsa basin sediments also exist in the Jaca basin sediments.

During the Broto and Banaston periods of development, the basin was narrow, elongated and relatively small and for both periods there was a strong structural control (Remacha and Fernández, 2003). The bounding limits of the basin are illustrated in Fig. 7. 6. The northern boundary was formed of a poorly developed submarine orogen constituted by the Lakora thrust systems during sediment deposition of the Broto system. In the east, the basin was bound by the Central South-Pyrenean Unit, on which the shallow-water Ager-Tremp-Graus piggyback basin hosted flood-related fluvio-deltaic sedimentation (Mutti et al., 1996). The southern boundary was formed of a flexed foreland margin as the onlap of the turbidite systems onto a carbonate ramp reveals. Finally, the western boundary of the basin was represented by a structural rise of the basin floor (Remacha et al., 1998) that prevented any connection between the Hecho Group turbidites and the deep-marine systems of the Bay of Biscay.

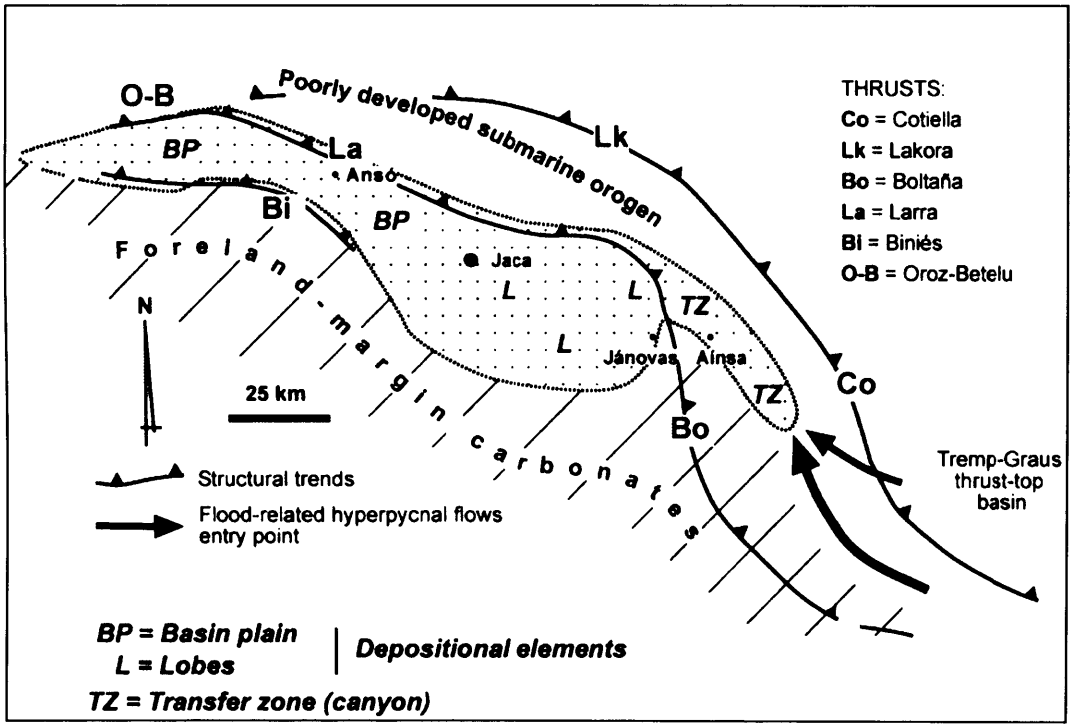

Figure 7.6: Palaeogeographic sketch map showing the bounding limits and structural features of the Jaca basin (Remacha and Fernández, 2003).

The structural framework during Banaston time can be related to three thrust systems (Teixell 1996), named Lakora–Cotiella, Larra–Boltaña, and Gavarnie–Biniés (Figs. 7.6). Once the Lakora–Cotiella unit had been emplaced, the onset of thrusting of the Larra–Boltaña cover system and, to a lesser extent, the initial thrusting of the Biniés cover thrust (an extension of the basement involved Gavarnie thrust; Teixell 1996) led to a reorganization of the foredeep. Synsedimentary thrusting of the Larra–Boltaña and Biniés thrusts is demonstrated by the progressive unconformities locally exposed in the Boltaña and Biniés ramp anticlines (Remacha et al. 1998). At the western end of the Banaston turbidites outcrop belt, the Oroz–Betelu massif constituted a submarine high forming the western closure of the deep-water basin during the Banaston time. The Oroz–Betelu basement-involved thrust represents the western prolongation of the Larra–Boltaña system (Remacha et al., 2005), connecting the poorly developed submarine orogen in the north (the Lakora and Larra–Boltaña thrusts) with the southern foreland margin (Fig. 7.6). Therefore, the basin was a structurally confined and relatively small, extending longitudinally for some 150 km. The basin width (north–south) is more difficult to calculate because of generalized erosion in the north but can be estimated to be about 25–45 km west of the Boltaña anticline (Remacha et al., 2005).

Except for the latest stages of turbidite sedimentation, recorded in the Jaca system, the deep-marine basin sediments were sourced from the same provenance like in the Ainsa basin and was fed from single entry points located in the southeast, which were partly controlled by the western oblique (NW-SE to N-S trending) lateral ramps of the Central South-Pyrenean Unit (Boltaña and Cotiella lateral ramps). These structurally controlled funnels, interpreted as submarine canyons (Mutti et al., 1985, 1988), transferred the clastic sediments from the shallow water Ager-Tremp-Graus piggyback basin into the deep-marine environments of the Jaca basin through the Ainsa basin. Sediment dispersal within the foredeep followed the structural directions, first of the oblique lateral ramps in the east, trending roughly N-S, and then, bending to the west, of the frontal ramps trending WNW-ESE (Fig. 7.6). Finally, as reported above, flows were completely blocked by the western limit of the basin.

The arenite composition in the Ainsa and Jaca basins was mainly controlled by synsedimentary tectonic processes which led to changes in sediment sources during the basin evolution, however, it is suspected that climate have determined the actual

timing of sand delivery to the deep-marine basin. The number of deep-marine sandbodies in the Ainsa basin (~25) that accumulated in ~10 million years, suggests the operation of a faster, non-tectonic driver, possibly related to the long-period eccentricity of frequency 400 kyr, in contrast to the longer-term 4-5 million-year tectonic driver that controlled the two angular-unconformity-bound units. Recently, using a discrete element model approach to analyse the behaviour of individual thrust units in the context of asymmetric doubly-vergent thrust wedges (such as the Pyrenees), Naylor and Sinclair (2007) proposed that the rates of surface uplift, frontal accretion, and exhumation should be punctuated on a time scale linked to thrust-sheet geometry and convergence rates. The central southern Pyrenees accreted the Montsec and Sierras Marginales thrust sheets during Eocene time with a regional convergence rate of ~6 km/myr (Vergés et al., 1995). They have a high aspect-ratio associated with strong, competent limestones detached on a weak Triassic evaporate layer, each with a length of ~24 km. This results in a minimum limit on the time scale of internal (tectonic) variability of ~4 million years, a result that is consistent with the recognition of a 4-5 million-year tectonic driver, with the time-averaged driver for the sandbodies being an order of magnitude too fast and, therefore, better explained by climatic processes.

7.5 Revised correlation of sandy systems of the Ainsa and Jaca basins

To date, any published correlations of sandbodies from the more proximal Ainsa to the more distal Jaca basin are essentially based on non-peer-reviewed fieldtrip guidebooks (Mutti et al., 1985; Remacha et al., 2003), or magnetostratigraphy only from the Jaca basin that has been extrapolated to the Ainsa basin (Oms et al., 2003; Remacha et al., 2003). Biostratigraphic data from the Ainsa and Jaca basins is scarce (but see Kapellos and Schaub, 1973; Schaub, 1981; Labaume et al., 1985; Payros et al., 1999; Pickering and Corregidor, 2005), and much of this information is not readily available (grey literature) and, in addition, different biostratigraphic zonation schemes have been used over the decades that further exacerbate any correlation. Thus, published correlations of the sandbodies between the Ainsa and Jaca basins must be treated with caution and, in the absence of more robust and reliable, high-resolution, age dating of the basin sediments, compositional finger-prints of

sandbodies should be regarded as a better candidate tool in any correlations. In the following paragraphs a revised correlation is proposed (Fig. 7.7) based principally on the petrographic data.

Despite the difficulties in using biostratigraphic data for correlation purposes within the Ainsa and Jaca basins (discussed above), some data exists. Labaume et al. (1985) placed two megaturbidites, MT-3 and MT-4, in the Jaca basin within Biozones NP-14 and NP-15 (uppermost Ypresian and lower Lutetian; Berggren and Pearson, 2005; Payros et al., 2007b), corresponding with the *Subbotina frontosa*, *Truncorotaloides praetopilensis* and *Globigerinatheka subconglobata* Biozones of the planktonic foraminifera zonation. The lower part of the Torla system contains the MT-3 megaturbidite; whereas, the uppermost part of Broto system contains the MT-4 (Remacha et al., 2003). However, a more recent study (Payros et al., 1999) placed those two megaturbidites, MT-3 and MT-4, around the boundary of Biozones *Morozovella aragonensis* and *Morozovella caucasica,* and in Biozone *Subbotina frontosa* respectively. These planktonic foraminifera Biozones correspond to NP-13 and part of NP-14, making both of the megaturbidites relatively younger, but still broadly corresponding to the uppermost Ypresian and lower Lutetian.

Canudo and Molina (1988) studied the planktonic foraminifers of the Jaca basin in several sections and placed the Jaca system, which is the youngest system in the Jaca basin within the upper Lutetian (*Morozovella lehneri* Zone or P12). Using planktonic foraminifera, Payros et al. (1999) came to a similar conclusion about the age range of the Jaca basin sediments. Age dating of foraminifera from the Ainsa system (middle part of the deep-marine Ainsa basin stratigraphy) suggests deposition within the Mid-Lutetian Stage around the boundary of planktonic foraminifera Zones P11–P12 (calcareous nannofossil zones NP14 and NP15) (Pickering and Corregidor, 2005). Additional micropalaeontological data from the youngest deep-marine system in the Ainsa basin (Guaso system) yield a Lutetian P12 Zone age (Pickering and Corregidor, 2005). Thus, within the limits of biostratigraphic resolution and the available evidence, it appears that the Ainsa and Jaca basin deep-marine deposits are broadly age-equivalent. As the individual sandy systems within the Ainsa and Jaca basins are likely to represent time intervals in the order of 1-1.5 million years (at most), it is very unlikely that a more refined biostratigraphic resolution is possible and, therefore, petrographic and geochemical studies, such as those carried out here, are likely to prove more fruitful in establishing correlations.

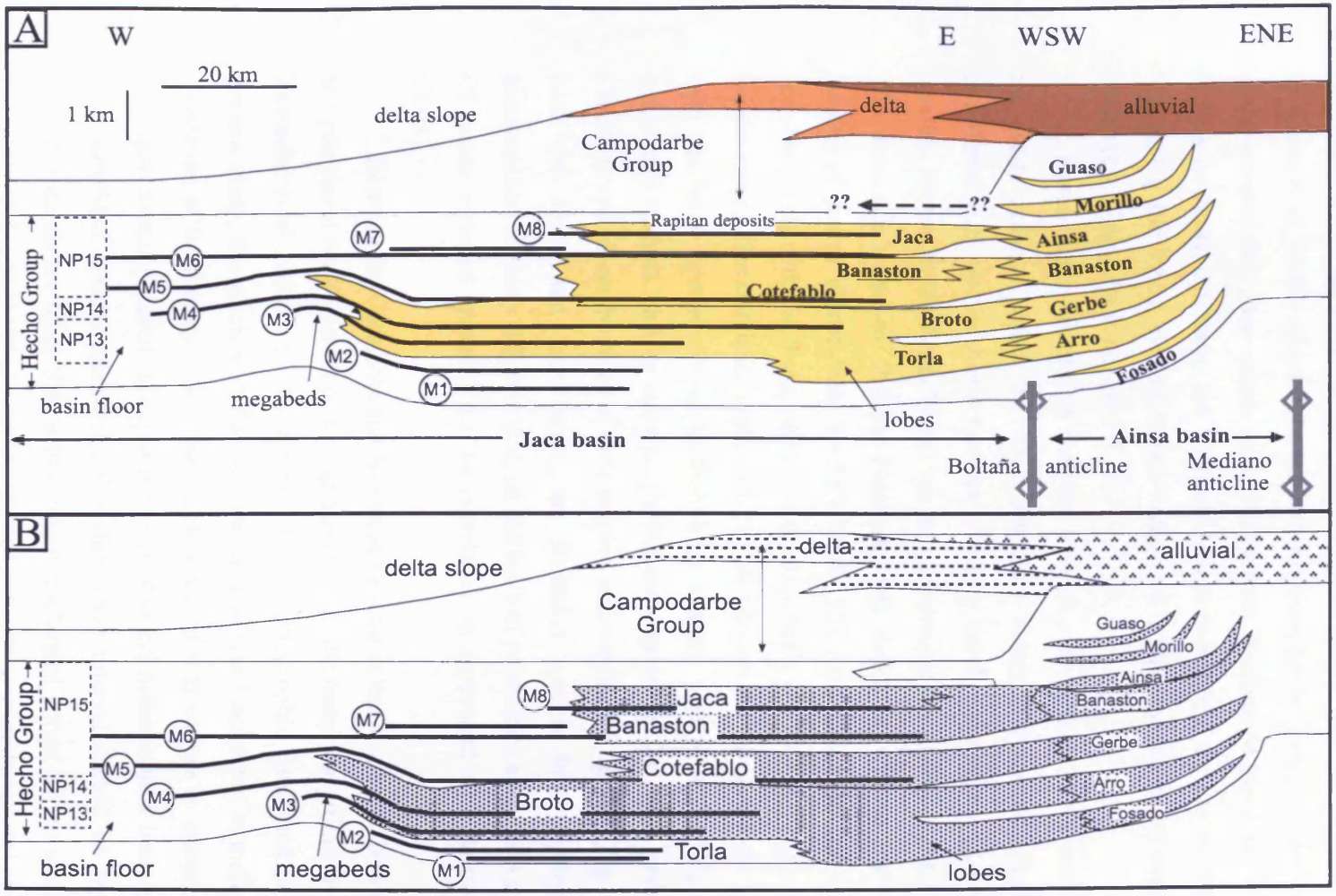

Figure 7.7: (A) Revised correlation of the sandy systems in the Ainsa and Jaca basins on the basis of observed petrofacies. (B) Previous correlation framework of the Ainsa and Jaca basins sandy systems. Compare the two figures and note the difference in correlation, especially in the lower part of the stratigraphy (See text for details). Note that the Rapitan deposits (*sensu* Remacha et al., 1996) are the youngest part of the Jaca system but shown by Remacha et al. (1998) as essentially time-equivalent to the Guaso system in the Ainsa basin. M: megaturbidites; NP: calcareous nannofossil zones.

Mutti et al. (1985) tentatively correlated the Fosado system, in the Ainsa basin, with the Torla system, in the Jaca basin (Fig. 7.7B). They also correlated the Arro system with the Broto system, and the Gerbe system with the Cotefablo system. Remacha et al. (1998) adopted the same correlations for the Lower Hecho Group, but also correlated the Ainsa system to the Jaca system. It should be noted that Mutti et al. (1988), however, correlated the Banaston (Ainsa basin) with the Fiscal system (Jaca basin), but the Fiscal system is now subsumed within the Banaston system (Jaca basin) (e.g., Remacha et al., 2003).

Based on the petrofacies analysis, a revision of the most likely correlations of the sandy systems within the Ainsa and Jaca basins is proposed (Fig.7.7). The petrofacies analysis has shown that the relatively thin Fosado system (the oldest and smallest system in the Ainsa basin) has no petrographic correlative in the Jaca basin. Therefore, it is suspected that the Fosado system shaled out without any significant feeding of coarse clastics into the Jaca basin. The Arro system in the Ainsa basin correlates well with the Torla system of the Jaca basin (Fig. 7.8 A), because of their hybrid arenite characteristic. Figure 7.8 (B) also shows the Gerbe system correlating with the Broto system owing to their high average content of NCE grains. The petrofacies analysis leads to correlate the Banaston system in the Ainsa basin with the Cotefablo system on the basis of their relative enrichment in CI grains (Fig. 7.9 A). In both the Ainsa and Jaca basin, the Banaston system form relatively thick accumulation of sandy deposits that, on the basis of petrofacies analysis (i.e., both are CI grains enriched systems) can be correlated, in agreement with Remacha et al. (2003).

Between the Cotefablo and Banaston systems in the Jaca basin, however, there is a prominent thick interval of fine-grained sediments; many tens of metres thick (cf. Remacha et al., 2003). In the absence of the petrographic data resulted from the present study, this prominent fine-grained interval was interpreted to mark a natural separation of both sandy lobe systems. However, if it is correct to interpret that the principal control on sand supply was the ca. 400-kyr Milankovitch frequency, then, and somewhat counter-intuitively, this distinctive interval should be regarded as arising from causes other than a particularly prolonged period of fan abandonment, but rather as due to locally increased rates of sediment accumulation and preservation of fine-grained sediments. In the Ainsa basin, the Banaston system comprises several sandbodies (Remacha et al., 1998; seven according to Bayliss and Pickering, *pers.*

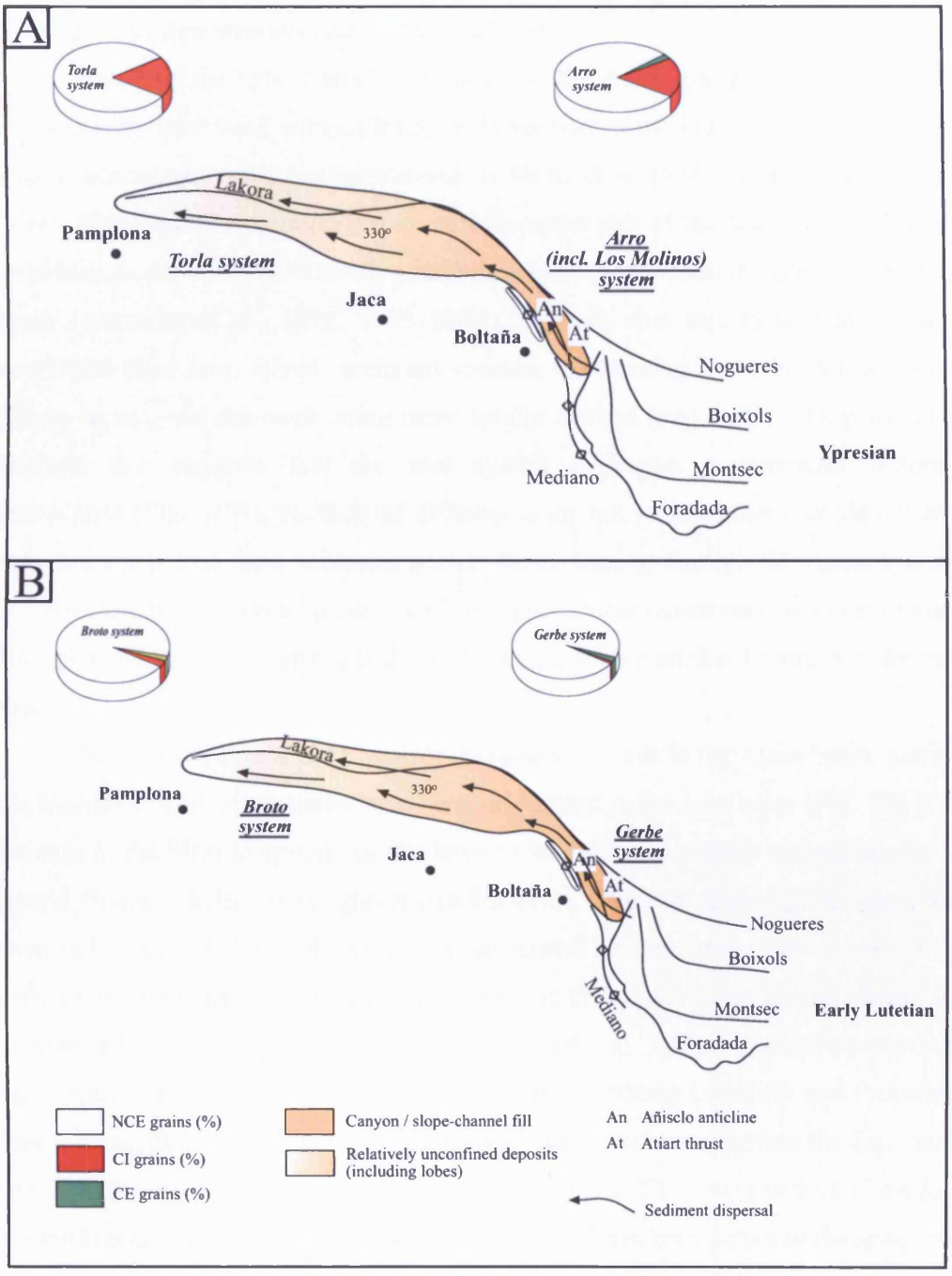

Figure 7.8: Palaeogeographic sketches showing sediment dispersal patterns in the Ainsa and Jaca basins. Principal petrographic components for each system are shown as pie charts. Schematic structural elements are redrawn and modified after Remacha et al. (2003).

comm., 2007) any two of which could sandwich this fine-grained interval between the Cotefablo and Banaston systems in the Jaca basin.

Based on the hybrid arenite composition, the Ainsa system (Ainsa basin) can be tentatively correlated with, at least, the lower part of the Jaca system (Jaca basin), also in accordance with the correlations of Mutti et al. (1985) and Remacha et al. (1998, 2003). The recognition that at least the upper part of the Jaca system (Rapitan turbidites) is derived from a newly-established (northerly) sediment source in the Jaca basin (Remacha et al., 1991, 1995, 2003), suggests that this system might have developed from two, mixed, sediment sources, one coming from the Ainsa system (Ainsa basin), and the other being more locally derived (Fig. 7.9C). The petrofacies analysis also suggests that the Jaca system represents a somewhat different provenance (Fig. 4.9B), but that the differences are not so great that it could not also have been supplied from sediment gravity-flows routing through the Ainsa system, i.e., the Jaca system has a "mixed" sediment provenance containing sediments routed through the Ainsa basin mixed with those coming from a northern route into the Jaca basin.

No counterparts of the youngest two sandy systems in the Ainsa basin, namely the Morillo and Guaso systems have been recognised in the Jaca basin (Fig. 7.9C). In the case of the Morillo system, on the basis of its high sand content and abundance of typical "bypass facies" (e.g., gravel-rich barforms, abundant coarse grain sizes, and erosional scours), there might have been associated lobe deposits in the region of the Boltaña anticline and in the Jaca basin, but that these have been eroded during the most recent phases of uplift of the Boltaña anticline (Fig. 7.10). For the Guaso system, the overall fine grain sizes and interpreted ramp-like setting (Sutcliffe and Pickering, *pers. comm.*, 2007) suggest that it might easily have shaled out before the Jaca basin and, therefore, have no more distal sandy lobe deposits. The youngest part of the Jaca system is sourced from the north, and therefore may have been active *at the same time* as the Morillo and Guaso systems, although there is no clear evidence to suggest that they were physically connected. The abundance of typical bypass facies, together with the abundance of cobble-pebble deposits, in the Morillo system (not present in the Guaso system) suggest that a sizeable accumulation of sands probably accumulated, but has subsequently been eroded. The most likely site of such sediment accumulation is postulated as in the region of the Boltaña anticline and immediately basinwards of

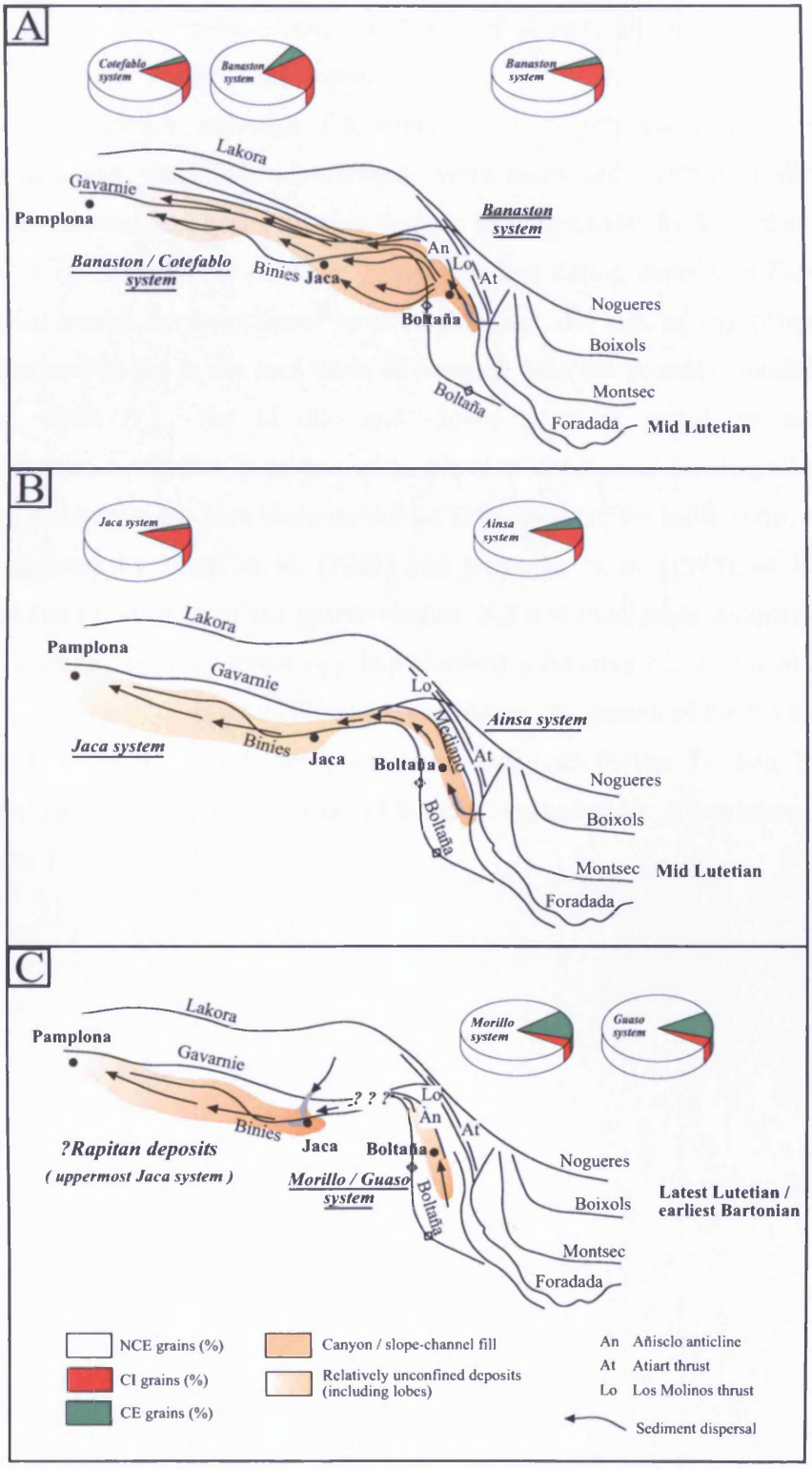

Figure 7.9: Palaeogeographic sketches showing sediment dispersal patterns in the Ainsa and Jaca basins. Principal petrographic components for each system are shown as pie charts. Schematic structural elements are redrawn and modified after Remacha et al. (2003). Note that the Rapitan deposits (*sensu* Remacha et al., 1995) are the youngest part of the Jaca system but shown by Remacha et al. (1998) as essentially time-equivalent to the Guaso system in the Ainsa basin.

this, i.e., over a down-basin length in the order of 10 to 20 km. Present-day erosion levels have removed any such deposits.

In summary, although it is convenient to loosely define a coarser grained, more proximal, essentially channelised, Ainsa basin, and a relatively distal, mainly non-channelised Jaca basin, because they are separated today by the Boltaña anticline, there is no unequivocal evidence to suggest that during deposition there was any physical barrier between these "basins". However, the lack of any petrographically similar sandbodies in the Jaca basin to correlate with the youngest sandbodies in the Ainsa basin (i.e., the Morillo and Guaso systems), could be construed as circumstantial evidence in favour of the physical isolation of the deepest parts of the Ainsa basin from the Jaca basin during the final stages of the infill of the Ainsa basin, as suggested by Mutti et al. (1985) and Remacha et al. (1998), at least for the accumulation of most of the coarse clastics. Silt and mud-grade sediment could still have been transported across any hypothesised submarine sill, to accumulate in the Jaca basin. Thus, during Morillo and Guaso times, the growth of the Boltaña anticline might have created a submarine sill to separate both basins. To date, however, no palaeocurrent evidence for flow reflections against such a postulated barrier is observed.

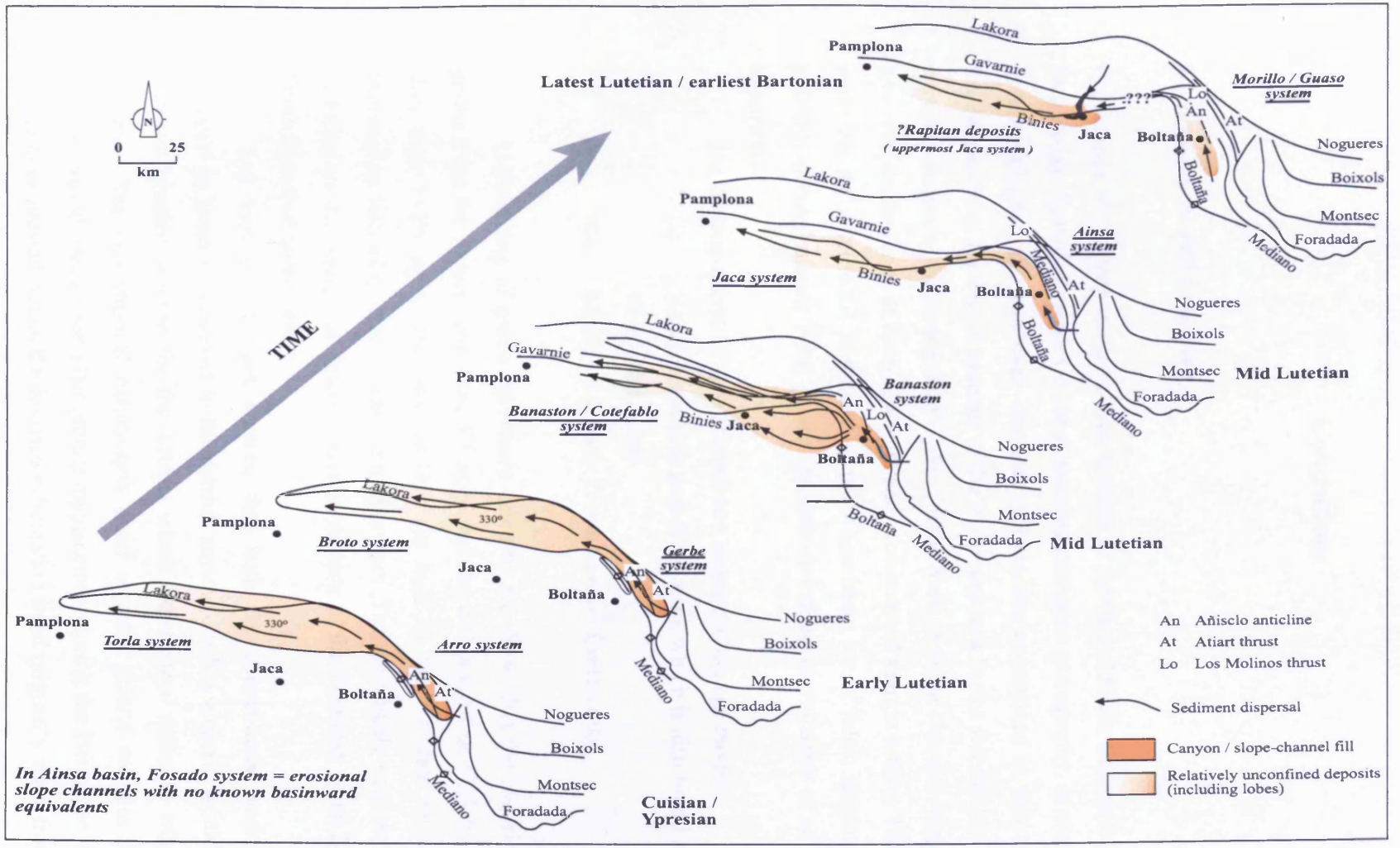

Figure 7.10: Summary evolution of the deep-marine sandy systems in the Ainsa and Jaca basins, including main sediment dispersal pattern. Principal structural features (thrusts and anticlines) are shown. Schematic structural elements are redrawn and modified after Remacha et al. (2003).

CHAPTER 8

Conclusions

8.1 Provenance and Evolution

Provenance of the deep-marine clastic systems of the Early-Middle Eocene Ainsa and Jaca basins, Spanish Pyrenees is constrained by sandstone petrography, detrital zircon geochronology and major/trace elements composition as outlined in this research. Sandstones from the clastic systems of the Ainsa and Jaca basins fall into the field of recycled orogen in the standard QFL plot. On the basis of major element composition, however, the majority of them represent active continental margin setting. The source rocks for the siliciclastic sediments in the Ainsa basin are of felsic igneous origin, probably derived mainly from granite-gneisses and siliceous volcanics of an uplifted basement.

The detrital zircon FT data showed two major cooling age modes:

(i) Hercynian and/or post-Hercynian, which is also found in the U-Pb age data , and

(ii) Mesozoic (Lower Triassic-Lower Cretaceous).

U-Pb dating of grains previously dated by FT shows that the majority of the grains from the Ainsa basin have FT ages that are within error or slightly younger than their U-Pb ages. This implies that the bulk of the FT data record rapid exhumation following granite emplacement events. The most likely sources for such histories are the Hercynian granites located in parts of the Pyrenean Axial Zone and South Pyrenean thrust belts.

Lag plot of FT ages showed that both the conventional and inverted exhumation trend is preserved in the detrital zircons. Such a scenario would require different granitic sources for the zircons which experienced different exhumation histories. The conventional exhumation trend requires granite samples to reach shallow crustal levels soon after granite emplacement during the Hercynian orogeny. The zircons present within the inverted exhumation trend originally came from a part

of the granite belt where emplacement depths were likely greater and which therefore subsequently experienced much deeper levels of erosion with final exhumation taking place in the Cretaceous during the extensional/ transtensional stage of the evolving Pyrenean belt. To explain the inverted trend the Cretaceous phase of exhumation must be linked to an initial deposition within a local basin, probably within a faulted block that was subsequently inverted and progressively eroded during the Palaeocene. Afterwards this deposit went into the fluvial systems supplying the Ainsa basin where it was mixed with granite detritus sourced directly from an area where cooling had taken place during and soon after granite emplacement, thereby preserving conventional exhumation trend. All this granitic detritus from the Axial Zone and South Pyrenean thrust belt was routed to the Ainsa basin via the south-eastern entry points into the deep-marine environment along with carbonate materials derived from relatively local source, e.g. Mediano/Boltaña anticline and associated structures.

Petrographic data has provided details of the sedimentary provenances for the deep-marine sandbodies in the Ainsa and Jaca basins. Three discrete sediment sources are recognised on the basis of the three petrofacies identified in the clastic systems:

(i) Subaerial rising Pyrenean orogen that funnelled siliciclastic sediments (NCE grains) through the Tremp-Graus basin, except for the youngest part of the Jaca system (e.g., Rapitan turbidites);

(ii) Intrabasinal carbonate grains being derived both from the resedimentation of virtually coeval marginal shelfal sediments in which carbonate factories were already active, and from slightly older carbonates eroded from the intrabasinal seafloor growth structures like, for example, the early stages of the Mediano and Boltaña anticlines; and

(iii) Erosion of Cretaceous limestone from the Mediano anticline provided the majority of the extrabasinal carbonate grains towards the later stage of the basin infill.

The different compositional (petrographic) trends in the arenites of the Ainsa and Jaca basins were differentiated only when the carbonate clasts of extrabasinal and

intrabasinal origin were considered separately in the modal analyses. Arenite composition was found to be mainly controlled by the unroofing and erosion of carbonate and siliciclastic deposits during basin evolution (e.g., from the core of the Mediano anticline, and associated sediment sources), a process that could have been controlled by synsedimentary tectonics as recorded by the angular unconformities that exist between various stratigraphic units in the Ainsa basin. These synsedimentary tectonic processes led to changes in sediment sources during basin evolution. However, global climatic changes may have determined the actual timing of sand delivery to the deep-marine basin. The carbon isotope curve measured on the foraminifera from the Ainsa basin suggested that the Ainsa basin remained connected with the open ocean throughout its history of sediment infill.

8.2 Correlation and Palaeogeography

Petrofacies analysis of the Ainsa and Jaca basins sediments has led to a revision in the correlation of the sandy systems between the proximal (Ainsa) and distal (Jaca) basin, now separated by the Boltaña anticline, and across which it is impossible to actually trace out individual beds or sandstone packages between basins. This revised correlation, in turn, has changed the current (published) understanding of the Ainsa and Jaca basins palaeogeography. Three distinct petrofacies were identified from the arenites of the Ainsa and Jaca basins on the basis of their average content of non-carbonate (siliciclastic) and carbonate framework grains – sandstone or non-carbonate extrarenite, hybrid arenite and calcilithite. Each clastic system was assigned with a petrofacies which were also corroborated by the major element data. Siliciclastic rich 'sandstone' (non-carbonate extrarenites) petrofacies have higher amount of SiO_2, and Al_2O_3 but lower CaO percentage. In contrast carbonate enriched 'hybrid arenite' or 'calcilithite' (carbonate extrarenites) petrofacies have lower SiO_2 and Al_2O_3 but higher CaO content. The two carbonate enriched petrofacies were distinguished by their MgO proportion - calcilithite petrofacies having relatively higher MgO proportion than the hybrid arenite petrofacies owing to the relative abundance of dolomite.

According to the revised correlation scheme from this research, the Fosado system has no correlatives in the Jaca basin, the Arro system correlates with the Torla system and the Gerbe system with the Broto system. The Banaston system in the

Ainsa basin correlates with both the Banaston and Cotefablo system of the Jaca basin. The Ainsa system correlates with the Jaca system. There are no sandy systems in the Jaca basin that can be interpreted as petrographically equivalent to those in the Morillo and Guaso systems in the Ainsa basin. Thus, during Morillo and Guaso times, the growth of the Boltaña anticline might have created a submarine sill to separate both basins. No palaeocurrent evidence, however, for flow reflections against such a postulated barrier had been observed.

The deep-marine clastic systems have been fed, throughout most of the history of the Ainsa and Jaca basins, from a south-eastern point source, with axial sediment gravity flows towards the NW in the proximal Ainsa basin (~320°), and more westerly across the Boltaña anticline in the relatively distal Jaca basin (~270°). The youngest part of the Jaca system (i.e., Rapitan deposits) is sourced from the north, and therefore may have been active at the same time as the Morillo and Guaso systems. Although there is no clear evidence to suggest that they were physically connected, it is possible that finer grained, more distal deposits of the Morillo - Guaso systems reached the Jaca basin. Indeed, the abundance of typical bypass facies, together with the abundance of cobble-pebble deposits, in the Morillo system suggest that a sizeable accumulation of sands probably accumulated, but has subsequently been eroded.

8.3 Recommendation for future work

Inevitably there is always more that could be done in any research programme. This section is intended to record possible future research activities in the Ainsa and Jaca basins that could enhance the understanding of the evolution of this basin. Below are some ideas of possible future projects:

- Higher resolution petrography with a sequence stratigraphic approach. This can help to quantify any significantly variable or systematic change within *each* clastic system. The ideal system to study would be the Ainsa system as cores are available from the system which will help to resolve any changes in a stratigraphic order. Outcrop samples are more difficult to arrange in accurate stratigraphic order, especially for contemporaneous deposits occurring at different outcrops.

- Multivariate statistical analyses are recommended for the quantitative petrographic data generated in this study which can characterise each clastic system statistically and further strengthen the correlation of the clastic systems between the proximal (Ainsa basin) and distal (Jaca basin) part. Unfortunately, such studies could not be included within the scope of this work. All the compositional plots used in this study are actually a comparison with previously established compositional plots, e.g., the QFL plot of Dickinson and Suczek (1979) for tectonic settings. In order to undertake multivariate analyses on the petrographic data generated from this study and to compare them with previously established compositional plots, the original data also needs to be analysed by the same rigorous statistical methods.

- A revision of the stratigraphic nomenclature for the Ainsa and Jaca basins. While drawing the correlation framework for the Ainsa and Jaca basins, the necessity of a revision in stratigraphic nomenclature was realised strongly. In the Ainsa and Jaca basins there are discrete thick sandbodies which has not been formally defined as 'system, e.g., Los Molinos sandbody in the Ainsa basin and Rapitan channel-levee-overbank deposits in the Jaca basin.

- Higher resolution geochemical studies including stable isotope of the fine-grained intervals between each clastic systems in order to decipher the principal control (climate or tectonism) on sand supply to the Ainsa and Jaca basins.

- Low-temperature thermochronometry of sediments from Sabiñánigo delta complex that forms part of the southern Pyrenean foreland basin fill in the Jaca basin to establish the thermal, uplift and denudation history of this region and to distinguish from the resulting age populations between different source areas.

References

Abdel-Wahab, A. A., 1992, Provenance of Gebel El-Zeit sandstones, Gulf of Suez, Egypt: Sedimentary Geology, v. 75, p. 241-255.

Anadon, P., Cabrera, L., Colombo, F., Marzo, M., and Riba, O., 1986, Syntectonic intraformational unconformities in alluvial fan deposits, eastern Ebro Basin margins (NE Spain), *in* Allen, P.A. and Homewood, P., eds., Foreland Basins: International Association of Sedimentologists Special Publications, v. 8, p. 259-271.

Anderson, A., 2002, Correction of common lead in U–Pb analyses that do not report ^{204}Pb: Chemical Geology, v. 192, p. 59-79.

Armstrong-Altrin, J. S., Lee, Y. I., Verma, S. P., and Ramasamy, S., 2004, Geochemistry of sandstones from the Upper Miocene Kudankulam Formation, southern India: Implications for provenance, weathering, and tectonic setting: Journal of Sedimentary Research, v. 74, p. 285-297.

Asiedu, D. K., Suzui, S., and Shibata, T., 2000, Provenance of sandstones from the Lower Cretaceous Sasayama Group, inner zone of southwest Japan: Sedimentary Geology, v. 131, p. 9-24.

Arthur, M.A., Schlanger, S.O., and Jenkyns, H.C., 1987, The Cenomanian-Turonian anoxic event II: Palaeoceanographic controls on organic matter production and preservation *in* Brooks, J. and Fleet, A.J., eds., Marine Petroleum Source Rocks: Geological Society of London Special Publication, v. 26, p. 401-420.

Bahlburg, H., 1998, The geochemistry and provenance of Ordovician turbidites in the Argentine Puna, *in* Pankhurst, R. J., Rapela, C. W., eds., The Proto-Andean Margin of Gondwana: Geological Society of London Special Publication, v. 142, p. 127-142.

Banner, J.L. and Hanson, G.N., 1990, Calculation of simultaneous isotopic and trace element variations during water-rock interaction with applications to carbonate diagenesis: Geochimica et Cosmochimica Acta, v. 54, p. 3123-3137.

Basu, A., Young, S. W., Suttner, L. J., James, W. C., and Mack, G. H., 1975, Re-evaluation of the use of undulatory extinction and polycrystallinity in detrital quartz for provenance interpretation: Journal of Sedimentary Petrology, v. 45, p. 873-882.

Bentham, P. A., Burbank, D. W., and Puigdefabregas, C., 1992, Temporal and spatial controls on the alluvial architecture of an axial drainage system: Late Eocene Escanilla Formation, southern Pyrenean foreland basin, Spain: Basin Research, v. 4, p. 335-352.

Berggren, W.A., Kent, D.V., Swisher, C.C., and Aubry, M.-P., 1995, A revised Cenozoic geochronology and chronostratigraphy, *in* Berggren, W.A., Kent, D.V., Aubrey, M.-P., and Hardenbol, J., eds., Geochronology, Time Scales and Global Stratigraphic Correlation: SEPM Special Publication, v. 54, p. 129-212.

Berggren, W. A. and Pearson, P. N., 2005, A revised tropical to subtropical Palaeogene planktonic foraminiferal zonation: Journal of Foraminiferal Research, v. 35, p. 279-298.

Bernet, M., Zattin, M., Garver, J. I., Brandon, M. T., and Vance, J. A., 2001, Steady- state exhumation of the European Alps: Geology, v. 29, p. 35-38.

Bernet, M. and Garver, J. I., 2005, Fission-track analysis of detrital zircon: Reviews in Mineralogy and Geochemistry, v. 58, p. 205-238.

Bernet, M., van der Beek, P., Pik, R., Huyghe, P., Mugnier, J. -L., Labrin, E., and Szulc, A., 2006, Miocene to Recent exhumation of the central Himalaya determined from combined detrital zircon fission-track and U/Pb analysis of Siwalik sediments, western Nepal: Basin Research, v. 18, p. 393-412.

Bhatia, M. R., 1983, Plate tectonics and geochemical composition of sandstones: Journal of Geology, v. 91, p. 611-627.

Bhatia, M.R. and Crook, K.A.W., 1986, Trace element characteristics of greywackes and tectonic setting discrimination of sedimentary basins: Contributions to Mineralogy and Petrology, v. 92, p. 181-193.

Blatt, H., 1967, Provenance determinations and recycling of sediments: Journal of Sedimentary Petrology, v. 37, p. 1031-1044.

Blatt, H., Middleton, G., and Murray, R., 1980, Origin of Sedimentary Rocks: Englewood Cliffs, N.J., Prentice-Hall, p. -782.

Bohaty, S. M. and Zachos, J. C., 2003, Significant Southern Ocean warming event in the late middle Eocene: Geology, v. 31, p. 1017-1020.

Brand, U. and Veizer, J., 1981, Chemical diagenesis of a multicomponent carbonate system. 2. Stable isotopes: Journal of Sedimentary Petrology, v. 50, p. 987-997.

Broecker, W.S., 1982, Ocean chemistry during glacial time: Geochimica et Cosmochimica Acta, v. 46, p. 1689-1705.

Brunet, M. F., 1986, The influence of the Pyrenees on the evolution of adjacent basins, *in* Banda, E., Wickham, S. M., eds., The Geological Evolution of the Pyrenees: Tectonophysics, v. 129, p. 343-354.

Burgess, P.M. and Hovius, N., 1998, Rates of delta progradation during highstands: consequences for timing of deposition in deep-marine systems: Journal of the Geological Society London, v. 155, p. 217-222.

Burnett, D. J. and Quirk, D. G., 2001, Turbidite provenance in the Lower Paleozoic Manx Group, Isle of Man: implications for the tectonic setting of Eastern Avalonia: Journal of the Geological Society of London, v. 158, p. 913-924.

Canudo, J. I. and Molina, E., 1988, Biocronología de foraminíferos planctónicos de la secuencia deposicional de Jaca (Pirineo Aragonés): Eoceno medio y superior, *in* II Congreso Geológicode España, Granada, Comunicaciones, v. 1, p. 273-276.

Carter, A., Bristow, C., and Hurford, A. J., 1995, The application of FT analysis to the dating of barren sequences: examples from red beds in Scotland and Thailand, *in* Dunay, R. E., and Hailwood,E. A., eds., Non-biostratigraphical methods of dating and correlation: Geological Society of London Special Publication, v. 89, p. 57-68.

Carter, A., 1999, Present status and future avenues of source region discrimination and characterization using fission track analysis: Sedimentary Geology, v. 124, p. 31-45.

Carter, A. and Moss, S. J., 1999, Combined detrital-zircon fission-track and U-Pb dating: A new approach to understanding hinterland evolution: Geology, v. 27, p. 235.

Carter, A. and Bristow, C. S., 2000, Detrital zircon geochronology: enhancing the quality of sedimentary source information through improved methodology and combined U-Pb and fission-track techniques: Basin Research, v. 12, p. 47-57.

Carter, A. and Bristow, C. S., 2003, Linking hinterland evolution and continental basin sedimentation by using detrital zircon thermochronology: a study of the Khorat Plateau Basin, eastern Thailand: Basin Research, v. 15, p. 271-285.

Cerveny, P. F., Naeser, N. D., Zeitler, P. K., Naeser, C. W., and Johnson, C., 1988, History of uplift and relief of the Himalayas during the past 18 million years: evidence from fission-track ages of detrital zircons from sandstones of the Siwalik Group, *in* Kleinspehn, K. L. and Paola, C., eds., New Perspectives in Basin Analysis: New York, Springer-Verlag, p. 43-61.

Choukroune, P. and ECORS TEAM, 1989, The ECORS Pyrenean deep seismic profile reflection data and the overall structure of an orogenic belt: Tectonics, v. 8, p. 23-39.

Clark, J. D. and Pickering, K. T., 1996, Architectural elements and growth patterns of submarine channels: application to hydrocarbon exploration: American Association of Petroleum Geologists Bulletin, v. 80, p. 194-221.

Clevis, Q., de Jager, G., Nijman, W., and de Boer, P. L., 2004, Stratigraphic signatures of translation of thrust-sheet top basins over low-angle detachment faults: Basin Research, v. 16, p. 145-163.

Cocherie, A., Baudin, T., Autran, A., Guerrot, C., Fanning, C.M., and Laumonier, B., 2005, U-Pb zircon (ID-TIMS and SHRIMP) evidence for the early Ordovician intrusion of metagranites in the late Proterozoic Canaveilles Group of the Pyrenees and the Montagne Noire (France): Bulletin de la Société Géologique de France, v. 176, p. 269-282.

Compston, W., Froude, D. O., Ireland, T.R., Kinny, P. D., Williams, I. R., and Myers, J. S., 1985, The age of (a tiny part of) the Australian continent: Nature, v. 317, p. 559-560.

Corfield, R.M., Cartlidge, J.E., Premoli-Silvia, I., and Housley, R.A., 1991, Oxygen and carbon isotope stratigraphy of the Paleogene and Cretaceous limestones in the Bottacione Gorge and the Contessa Highway sections, Umbria, Italy: Terra Nova, v. 3, p. 414-422.

Coxall, H.K., Wilson, P.A., Pälike, H., Lear, C.H., and Backman, J., 2005, Rapid stepwise onset of Antarctic glaciation and deeper calcite compensation in the Pacific Ocean: Nature, v. 433, p. 53-57.

Craig, H., 1953, The geochemistry of the stable carbon isotopes: Geochimica et Cosmochimica Acta, v. 3, p. 53-92.

Crook, K. A. W., 1974, Lithogenesis and geotectonics: the significance of compositional variation in flysch arenites (greywackes): Society of Economic Paleontologists and Mineralogists Special Publication, v. 19, p. 304-310.

Cullers, R.L., 2000, The geochemistry of shales, siltstones and sandstones of Pennsylvanian–Permian age, Colorado, USA: implications for provenance and metamorphic studies: Lithos, v. 51, p. 181-203.

Daignieres, M., Seguret, M., Specht, M., and ECORS TEAM, 1994, The Arzacq-Western Pyrenees ECORS deep seismic profile: Publication of the European Association of Petroleum Geologists, Memoir 4, p. 199-208.

Déramond, J., Souquet, P., Fondecave-Wallez, M. J., and Spetch, M., 1993, Relationships between thrust tectonics and sequence stratigraphy surfaces in foredeeps: model and examples from the Pyrenees (Cretaceous-Eocene, France, Spain), *in* Williams, G. D., Dobb, A., eds., Tectonics and Seismic Sequence Stratigraphy: Geological Society of London Special Publication, v. 71, p. 193-219.

Dercourt, J., Ricou, L.E., and Vrielynck, B., 1993, Atlas Tethys palaeoenvironmental maps: Paris, Gauthier-Villars, 307p.

Dias-Brito, D., 2000, Global stratigraphy, palaeobiogeography and palaeoecology of Albian–Maastrichtian pithonellid calcispheres: impact on Tethys configuration: Cretaceous Research, v. 21, p. 315-349.

Dickinson, W. R., 1970, Interpreting detrital modes of graywacke and arkose: Journal of Sedimentary Petrology, v. 40, p. 695-707.

Dickinson, W. R. and Suczek, C. A., 1979, Plate tectonics and sandstone compositions: The American Association of Petroleum Geologists Bulletin, v. 63, p. 2164-2182.

Dickinson, W.R., Beard, L.S., Brakenridge, G.R., Erjavec, J.L., Ferguson, R.C., Inman, K.F., Knepp, R.A., Lindberg, F.A., and Ryberg, P.T., 1983, Provenance of North American Phanerozoic sandstones in relation to tectonic setting: Geological Society of America Bulletin, v. 94, p. 222-235.

Dickinson, W. R., 1985, Interpreting provenance relations from detrital modes of sandstones, *in* Zuffa, G. G., ed., Provenance of Arenites: NATO-ASI Series, v. 148, p. 3-61.

Dickinson, W.R. and Gehrels, G.E., 2003, U–Pb ages of detrital zircons from Permian and Jurassic eolian sandstones of the Colorado Plateau, USA: paleogeographic implications: Sedimentary Geology, v. 163, p. 29-66.

Dodson, M. H., Compston, W., Williams, I. S., and Wilson, J. F., 1988, A search for ancient detrital zircons in Zimbabwean sediments: Journal of the Geological Society of London, v. 145, p. 977-983.

Dreyer, T., Corregidor, J., Arbues, P., and Puigdefabregas, C., 1999, Architecture of the tectonically influenced Sobrarbe deltaic complex in the Ainsa Basin, northern Spain: Sedimentary Geology, v. 127, p. 127-169.

Dryden, A. L., 1931, Accuracy in Percentage Representation of Heavy Mineral Frequencies: Proceedings of the National Academy of Sciences of the United States of America, v. 17, p. 233-238.

Dupont-Nivet, G., Krijgsman, W., Langereis, C.G., Abels, H.A., Dai, S., and Fang, X., 2007, Tibetan plateau aridification linked to global cooling at the Eocene–Oligocene transition: Nature, v. 445, p. 635-638.

ECORS Pyrenees Team, 1988, The ECORS deep reflection survey across the Pyrenees: Nature, v. 331, p. 508-511.

Emery, D. and Myers, K.J., 1996, Sequence stratigraphy: Oxford, Blackwell Science, 297p.

Emrich, K., Ehhalt, D., and Vogel, J.C., 1970, Carbonate isotope fractionation during the precipitation of calcium carbonate: Earth and Planetary Science Letters, v. 8, p. 363-371.

Eriksson, P. G., Schreiber, U. M., Reczko, B. F., and Snyman, C. P., 1994, Petrography and geochemistry of sandstones interbedded with the Rooiberg Felsite Group (Transvaal

sequence, South Africa): implication for provenance and tectonic setting: Journal of Sedimentary Research, v. A64, p. 836-846.

Faure, G. and Mensing, T. M., 2005, Isotopes: principles and applications: New Jersey, John Wiley and Sons, 897p.

Fernandez, O., Munoz, J. A., Arbues, P., Falivene, O., and Marzo, M., 2004, Three dimensional reconstruction of geological surfaces: An example of growth strata and turbidite systems from the Ainsa basin (Pyrenees, Spain): American Association of Petroleum Geologists Bulletin, v. 88, p. 1049-1068.

Fiescher, M. W., 1984, Thrust tectonics in the Northern Pyrenees: Journal of Structural Geology, v. 6, p. 721-726.

Fitzgerald, P.G., Muñoz, J. A., Coney, P.J., and Baldwin, S.L., 1999, Asymmetric exhumation across the Pyrenean orogen: implications for the tectonic evolution of a collisional orogen: Earth and Planetary Science Letters, v. 173, p. 157-170.

Fleet, A.J. and Boldy, S.A.R., 1999, Petroleum Geology of Northwest Europe - Proceedings of the 5th Conference: London, Geological Society, 1398p.

Flood, R.D., Piper, D.J.W., and Shipboard Scientific Party, 1995, Proceedings of the Ocean Drilling Program, initial Reports, *in* Flood, R.D., Piper, D.J.W. and Klaus, A., eds., Ocean Drilling Program: College Station, A &M University Texas 155, p. 5-16.

Floyd, P. A., Winchester, J. A., and Park, R. G., 1989, Geochemistry and tectonic setting of Lewisian clastic metasediments from the early Proterozoic Loch Maree Group of Gairloch, N.W. Scotland: Precambrian Research, v. 45, p. 203-214.

Folk, R. L., Andrews, P. B., and Lewis, D. W., 1970, Detrital sedimentary rock classification and nomenclature for use in New Zealand : New Zealand Journal of Geology and Geophysics, v. 13, p. 937-968.

Follmi, K., Weissert, H., Bisping, M., and Funk, H., 1994, Phospogenesis, carbon isotope stratigraphy, and carbonate-platform evolution along the Lower Cretaceous northern Tethyan margin: Geological Society of America Bulletin, v. 106, p. 729-746.

Fontana, D., Zuffa, G. G., and Garzani, E., 1989, The interaction of eustacy and tectonism from provenance studies of the Eocene Hecho Group turbidite complex (South-Central Pyrenees, Spain): Basin Research, v. 2, p. 223-237.

Friedman, I. and O'Neil, J.R., 1977, Compilation of stable isotope fractionation factors of geochemical interest, *in* Fleicher, M., ed., Data of Geochemistry: Geological Survey Professional paper 440-KK, p. KK1-KK12.

Frimmel, H. E., Tack, L., Basei, M. S., Nutman, A. P., and Boven, A., 2006, Provenance and chemostratigraphy of the Neoproterozoic West Congolian Group in the Democratic Republic of Congo: Journal of African Earth Sciences, v. 46, p. 221-239.

Galbraith, R.F., 1990, The radial plot: Graphical assessment of spread in ages: Nuclear Tracks and Radiation Measurement, v. 17, p. 207-214.

Galbraith, R. F. and Green, P. F., 1990, Estimating the component ages in a finite mixture: Nuclear Tracks and Radiation Measurement, v. 17, p. 197-206.

Gallagher, K., Brown, R., and Johnson, C., 1998, Fission track analysis and its applications to geological problems: Annual Review of Earth and Planetary Sciences, v. 26, p. 519-572.

Garver, J. I. and Brandon, M. T., 1994, Erosional Denudation of the British Columbia Coast Ranges as Determined from Fission-Track Ages of Detrital Zircon from the Tofino Basin, Olympic Peninsula: Geological Society of America Bulletin, v. 106, p. 1398-1412.

Garver, J.I., Brandon, M.T., Roden-Tice, M.K., and Kamp, P.J.J., 1999, Exhumation history of orogenic highlands determined by detrital fission track thermochronology, *in* Ring, U., Brandon, M.T., Lister, G.S., and Willett, S.D., eds., Exhumation processes: normal faulting, ductile flow, and erosion: Geological Society London Special Publication, v. 154, p. 283-304.

Gazzi, P., 1966, Le arenarie del flysch sopracretaceo dell'Appennino modenese: correlazioni con il flysch di Monghidoro: Mineralogica et Petrographica Acta, v. 12, p. 69-97.

Gehrels, G. E., Dickinson, W. R., Ross, M. G., Stewart, J. H., and Howell, D. G., 1995, Detrital zircon reference from Cambrian to Triassic miogeoclinal strata of western North America: Geology, v. 23, p. 831-834.

Gingerich, P.D., 2006, Environment and evolution through the Paleocene–Eocene thermal maximum: Trends in Ecology and Evolution, v. 21, p. 246-253.

Gleadow, A. J. W., Hurford, A. J., and Quaife, R. D., 1976, Fission track dating of zircon; improved etching techniques: Earth and Planetary Science Letters, v. 33, p. 273-276.

Gleadow, A. J. W., 1981, Fission track dating methods: what are the real alternatives?: Nuclear Tracks, v. 5, p. 3-14.

Govindaraju, K., 1989, 1989 compilation of working values and sample descriptions for 272 geostandards: Geostandards Newsletter XIII (special issue).

Gradstein, F. M., Ogg, J. G., Smith, A. G., Agterberg, F. P., Bleeker, W., Cooper, R. A., Davydov, V., Gibbard, P., Hinnov, L., House, M. R., Lourens, L., Luterbacher, H. -P., McArthur, J., Melchin, M. J., Robb, L. J., Shergold, J., Villenueve, M., Wardlaw, B. R., Ali, J., Brinkhuis, H., Hilgen, F. J., Hooker, J., Howarth, R. J., Knoll, A. H., Laskar, J., Monechi, S., Powell, J., Plumb, K.A., Raffi, I., Röhl, U., Sanfilipo, A., Schmitz, B., Schakleton, N. J., Shields, G. A., Strauss, H., van Dam, J., Veizer, J., van Kolfschoten, T., and Wilson, D., 2004, A Geologic Time Scale 2004: Cambridge, UK, University Press, 384p.

Gray, M. B. and Zeitler, P. K., 1997, Comparison of clastic wedge provenance in the Appalachian foreland using U/Pb ages of detrital zircons: Tectonics, v. 16, p. 151-160.

Hall, M., 1997, Sequence stratigraphy and early diagenesis: the Sobrarbe Formation, Ainsa Basin, Spain [PhD thesis]: Manchester, University of Manchester, 388p.

Hardenbol, J., Thierry, J., Farley, M.B., Jacquin, Th., de Graciansky, P.C., and Vail, P.R., 1998, Mesozoic and Cenozoic sequence chronostratigraphic framework of European basins: Society of Economic Paleontologists and Mineralogists Special Publication, v. 60, 8 charts.

Hassan, S., Ishiga, H., Roser, B.P., Dozen, K., and Naka, T., 1999, Geochemistry of Permian–Triassic shales in the Salt Range, Pakistan: implications for provenance and tectonism at the Gondwana margin: Chemical Geology, v. 158, p. 293-314.

Haughton, P.D.W., Todd, S.P., and Morton, A.C., 1991, Sedimentary provenance studies, *in* Morton, A. C., Todd, S. P. and Haughton, P. D. W., Developments in sedimentary provenance studies: Geological Society of London Special Publication, v. 57, p. 1-11.

Hay, W.W., DeConto, R., Wold, C.N., Wilson, K.M., Voigt, S., Schulz, M., Wold-Rossby, A., Dullo, W.-C., Ronov, A.B., Balukhovsky, A.N. and Soeding, E., 1999, Alternative global Cretaceous paleogeography, *in* Barrera, E. and Johnson, C., eds., The Evolution of Cretaceous Ocean/Climate Systems: Geological Society of America Special Paper 332, pp. 1-47.

Helbing, H. and Tiepolo, M., 2005, Age determination of Ordovician magmatism in NE Sardinia and its bearing on Variscan basement evolution: Journal of the Geological Society of London, v. 162, p. 689-700.

Helmold, K. P., 1985, Provenance of feldspathic sandstones—the effects of diagenesis on provenance interpretations: a review, *in* Zuffa, G. G., ed., Provenance of Arenites, NATO-ASI Series, v. 148, p. 139-163.

Hiscott, R. N., 1978, Provenance of Ordovician deep-water sandstones, Tourelle Formation, Quebec and implications for initiation of the Taconic Orogeny: Canadian Journal of Earth Sciences, v. 15, p. 1579-1597.

Hogan, P. J. and Burbank, D. W., 1996, Evolution of the Jaca piggyback basin and emergence of the External Sierra, southern Pyrenees, *in* Friend, P. F., Dabrio, C. J., eds., Tertiary Basins of Spain: the Stratigraphic Record of Crustal Kinematics: Cambridge, University of Cambridge Press, p. 153-160.

Holl, J. E. and Anastasio, D. J., 1993, Paleomagnetically derived folding rates, Southern Pyrenees, Spain: Geology, v. 13, p. 271-274.

Huber, B.T., Norris, R.D., and MacLeod, K.G., 2002, Deep-sea paleotemperature record of extreme warmth during the Cretaceous: Geology, v. 30, p. 123-126.

Hudson, J. D. and Anderson, T. F., 1989, Ocean temperatures and isotopic compositions through time: Transactions of the Royal Society of Edinburgh: Earth Sciences, v. 80, p. 183-192.

Hurford, A. J. and Green, P. F., 1983, The zeta age calibration of fission-track dating: Chemical Geology (Isotope Geoscience), v. 1, p. 285-317.

Hurford, A. J., Fitch, F. J., and Clarke, A., 1984, Resolution of the age structure of detrital zircon populations of two Lower Cretaceous sandstones from the Weald of England by fission track dating: Geological Magazine, v. 121, p. 269-277.

Hurford, A. J., 1986, Application of the fission track dating method to young sediments: principles, methodology and examples, *in* Hurford, A. J., Jäger, E. and ten Cate, J. A. M., eds., Dating Young Sediments: Proceedings of the Workshop, Beijing, China, September 1985, v. 16, p. 199-233.

Hurford, A. J., 1990a, International Union of Geological Sciences Subcommission on Geochronology recommendation for the standardization of fission track dating calibration and data reporting: Nuclear Tracks, v. 17, p. 233-236.

Hurford, A. J., 1990b, Standardization of fission track dating calibration: recommendation by the Fission Track Working Group of the I.U.G.S. Subcommission on Geochronology: Chemical Geology, v. 80, p. 171-178.

Hurford, A. J. and Carter, A., 1991, The role of fission track dating in discrimination of provenance, *in* Morton, A. C., Todd, S. P. and Haughton, P. D. W., Developments in sedimentary provenance studies: Geological Society of London Special Publication, v. 57, p. 67-78.

Ingersoll, R. V., 1978, Petrofacies and petrologic evolution of the late Cretaceous fore-arc basin, northern and central California: Journal of Geology, v. 86, p. 335-353.

Ingersoll, R. V., Bullard, T. F., Ford, R. L., Grimm, J. P., Pickle, J. D., and Sares, S. W., 1984, The effect of grain size on detrital modes: A test of the Gazzi-Dickinson point-counting method: Journal of Sedimentary Petrology, v. 54, p. 103-116.

Ingersoll, R. V., 1990, Actualistic sandstone petrofacies: Discriminating modern and ancient source rocks: Geology, v. 18, p. 733-736.

Irwin, H., Curtis, C., and Coleman, M., 1977, Isotopic evidence for source of diagenetic carbonates formed during burial of organic-rich sediments: Nature, v. 269, p. 209-213.

Jackson, S. E., Pearson, N. J., Griffin, W. L., and Belousova, E. A., 2004, The application of laser ablation-inductively coupled plasma-mass spectrometry to in situ U-Pb zircon geochronology: Chemical Geology, v. 211, p. 47-69.

Jenkyns, H.C., 1980, Cretaceous anoxic events: from continents to oceans: Journal of the Geological Society London, v. 137, p. 171-188.

Johnsson, M.J. and Basu, A., 1993, Processes controlling the composition of clastic sediments: Special paper - Geological Society of America, Colorado, Boulder, v. 284, 342p.

Jones, R.W., Pickering, K.T,. Boudagher-Fadel, M. and Matthews, S., 2005, Preliminary observations on the micropalaeontological characterization of submarine fan /channel sub-environments, Ainsa System, south-central Pyrenees, Spain, *in* Powell, A. J. and Riding, J. B., eds., Recent developments in applied biostratigraphy: The Micropalaeontological Society Special Publications, p. 55–68.

Joo, Y. J., Lee, Y., and Hisada, K. -I., 2007, Provenance of Jurassic accretionary complex: Mino terrane, inner zone of south-west Japan - implications for palaeogeography of eastern Asia: Sedimentology, v. 54, p. 515-543.

Juez-Larré, J. and Andriessen, P. A. M., 2006, Tectonothermal evolution of the northeastern margin of Iberia since the break-up of Pangea to present, revealed by low-temperature fission-track and (U–Th)/He thermochronology: A case history of the Catalan Coastal Ranges: Earth and Planetary Science Letters, v. 243, p. 159-180.

Kapellos, V. C. and Schaub, H., 1973, Zur Korrelation von Biozonierungen mit Grossforaminiferen und Nannoplankton im Paläogen der Pyrenäen: Eclogae Geologicae Helvetiae, v. 66, p. 687-737.

Kelley, S. and Bluck, B. J., 1989, Detrital mineral ages from the Southern Uplands using 40Ar–39Ar laser probe: Journal of the Geological Society of London, v. 146, p. 401-403.

Köppen, A. and Carter, A., 2000, Constraints on provenance of the central European Triassic using detrital zircon fission track data: Palaeogeography, Palaeoclimatology, Palaeoecology, v. 161, p. 193-204.

Krogh, T. E., 1973, A low contamination method for hydrothermal decomposition of zircon and extraction of U and Pb for isotope age determinations: Geochimica et Cosmochimica Acta, v. 37, p. 485-494.

Kroonenberg, S.B., 1994, Effects of provenance, sorting and weathering on the geochemistry of fluvial sands from different tectonic and climatic environments: Proceedings of the 29th International Geological Congress, v. Part A, p. 69-81.

Labaume, P., Mutti, E., Séguret, M., and Rosell, J., 1983, Mégaturbidites carbonatées du basin turbiditique de l'Eocene inférieur et moyen sud-pyrénéen: Bulletin de la Société Géologique de France, v. 7 (XXV-6), p. 927-941.

Labaume, P., Séguret, M., and Seyve, C., 1985, Evolution of a turbiditic foreland basin and analogy with an accretionary prism: Example of the Eocene South-Pyrenean basin: Tectonics, v. 4, p. 661-685.

Labaume, P., Mutti, E., and Séguret, M., 1987, Megaturbidites: a depositional model from the Eocene of the SW-Pyrenean Foreland Basin, Spain: Geo-Marine Letters, v. 7, p. 91-101.

Li, R., Li, S., Jin, F., Wanc, Y., and Zhang, S., 2004, Provenance of Carboniferous sedimentary rocks in the northern margin of Dabie Mountains, central China and the tectonic significance: constraints from trace elements, mineral chemistry and SHRIMP dating of zircons: Sedimentary Geology, v. 166, p. 245-264.

Lohmann, K.C., 1988, Geochemical patterns of meteoric diagenetic systems and their application to studies of palaeokarst, *in* James, N.P. and Choquette, P.W., eds., Palaeokarst, p. 58-80.

Lonergan, L. and Johnson, C., 1998, Reconstructing orogenic exhumation histories using synorogenic detrital zircons and apatites: an example from the Betic Cordillera, SE Spain: Basin Research, v. 10, p. 353-364.

Ludwig, K.R., 2000, Isoplot—a Geochronological Toolkit for Microsoft Excel: Berkeley Geochronology Center, Special Publications, v. 1a, p. 1-53.

Mackensen, A., Grobe, H., Hubberten, H.-W., and Kuhn, G., 1994, Benthic foraminiferal assemblages and the δ13C-signal in the Atlantic sector of the Southern Ocean: glacial-to-interglacial contrasts, *in* Zahn, R., Pedersen, T.F., Kaminski, M.A., and Labeyrie, L., eds., Carbon Cycling in the Glacial Ocean: Constrains on the Ocean's Role in Global Change, NATO ASI Series I, v. 17, p. 105-144.

Mackensen, A., Rudolph, M., and Kuhn, G., 2001, Late Pleistocene deep-water circulation in the subantarctic eastern Atlantic: Global and Planetary Change, v. 30, p. 197-229.

Marchesini, L., Amorosi, A., Cibin, U., Spadafora, E., Zuffa, G. G., and Preti, D., 2000, Detrital supply versus facies architecture in the Late Quaternary deposits of the south-eastern Po plain (Italy): Journal of Sedimentary Research, v. 70, p. 829-838.

Marshall, J.D., 1992, Climatic and oceanographic isotopic signals from the carbonate rock record and their preservation: Geological Magazine, v. 129, p. 143-160.

Marzo, M., Nijman, W., and Puigdefabregas, C., 1988, Architecture of the Castissent fluvial sheet sandstones, Eocene, South Pyrenees, Spain: Sedimentology, v. 35, p. 719-738.

McBride, E. F., 1985, Diagenetic processes that affect provenance determinations in sandstone, *in* Zuffa, G. G., ed., Provenance of Arenites, NATO-ASI Series, v. 148, p. 95-113.

McLennan, S. M., Hemming, S. R., McDaniel, D. K., and Hanson, G. N., 1993, Geochemical approaches to sedimentation, provenance, and tectonics, *in* Johnsson, M. J., and Basu, A., eds., Processes Controlling the Composition of Clastic Sediments: Geological Society of America Special Paper, v. 284, p. 21-40.

McLennan, S. M., Bock, B., Compston, W., Hemming, S. R., and McDaniel, D. K., 2001, Detrital zircon geochronology of Taconian and Acadian foreland sedimentary rocks in New England: Journal of Sedimentary Research, v. 71, p. 305-317.

McLennan, S. M., 2001, Relationships between the trace element composition of sedimentary rocks and upper continental crust: Geochemistry Geophysics Geosystems, v. 2, doi: 10.1029/2000GC000109.

Meigs, A. J., Vergés, J., and Burbank, D. W., 1996, Ten-million-year history of a thrust sheet: Geological Society of America Bulletin, v. 108, p. 1608-1625.

Meulenkamp, J.E. and Sissingh, W., 2000, Maps 17 to 23 – Tertiary, *in* Crasquin, S., ed., Atlas Peri-Tethys, Palaeogeographical Maps - Explanatory Notes, CCGM/ CGMW, Paris, p. 153-208.

Meulenkamp, J.E., Sissingh, W., and Beniamovskii, V.N., 2000a, Early / Middle Ypresian, *in* Dercourt, J., Gaetani, M., et al., eds., Atlas Peri-Tethys, Palaeogeographical Maps, CCGM/ CGMW, Paris, map 17, scale 1:10 000 000, 1sheet.

Meulenkamp, J.E., Sissingh, W., Beniamovskii, V.N., and Barrier, E., 2000b, Late Lutetian, *in* Dercourt, J., Gaetani, M., et al., eds., Atlas Peri-Tethys, Palaeogeographical Maps, CCGM/ CGMW, Paris, map 18, scale 1:10 000 000, 1sheet.

Meulenkamp, J.E., Sissingh, W., Popov, S.V., Kovac, M., and Bergerat, F., 2000c, Late Rupellian, *in* Dercourt, J., Gaetani, M., et al., eds., Atlas Peri-Tethys, Palaeogeographical Maps, CCGM/ CGMW, Paris, map 19, scale 1:10 000 000, 1sheet.

Mezger, K. and Krogstad, E. J., 1997, Interpretation of discordant U-Pb ages: an evaluation: Journal of Metamorphic Petrology, v. 15, p. 127-140.

Miller, K.G., Kominz, M.A., Browning, J.V., Wright, J.D., Mountain, G.S., Katz, M.E., Sugarman, P.J., Cramer, B.S., Christie-Blick, S., and Pekar, S.F., 2005, The Phanerozoic record of global sea-level change: Science, v. 310, p. 1293-1298.

Millington, J. J. and Clark, J. D., 1995, The Charo/Arro canyon-mouth sheet system, south-central Pyrenees, Spain: a structurally influenced zone of sediment dispersal: Journal of Sedimentary Research, v. 65, p. 443-454.

Morris, R. G., Sinclair, H. D., and Yelland, A. J., 1998, Exhumation of the Pyrenean orogen: implications for sediment discharge: Basin Research, v. 10, p. 69-85.

Morton, A. C., Jonathan, C., Claoue-Long, A., and Berge, C., 1996, SHRIMP constraints on sediment provenance and transport history in the Mesozoic Stratfjord Formation, North Sea: Journal of the Geological Society of London, v. 153, p. 915-929.

Muñoz, J. A., 1992, Evolution of a continental collision belt: ECORS-Pyrenean crustal balanced section, *in* McClay, K. R., ed., Thrust Tectonics: London, Chapman & Hall, p. 235-246.

Muñoz, J. A., McClay, K. R., and Poblet, J., 1994, Synchronous extension and contraction in frontal thrust sheets of the Spanish Pyrenees: Geology, v. 22, p. 921-924.

Muñoz, J. A., Arbues, P., and Serra-Kiel, J., 1998, The Ainsa basin and the Sobrarbe oblique thrust system: Sedimentological and tectonic processes controlling slope and platform sequences deposited synchronously with a submarine emergent thrust system, *in* International Association of Sedimentologists, 15th International Sedimentological Congress, Alicante, Spain, Field Trip Guidebook, p. 213-223.

Mutti, E., Luterbacher, H. P., Ferrer, J., and Rosell, J., 1972, Schema estratigrafico e lineamenti di facies del Paleogene marino della zona centrale sudpirenaica tra Tremp (Catalogna) e Pamplona (Navarra): Società Geologica Italiana, Memorie, v. 11, p. 391-416.

Mutti, E., 1977, Distinctive thin-bedded turbidite facies and related depositional environments in the Eocene Hecho Group (south-central Pyrenees, Spain): Sedimentology, v. 24, p. 107-131.

Mutti, E., Remacha, E., Gavetti, M., Rosell, J., Valloni, R., and Zamorano, M., 1985, Stratigraphy and facies characteristics of the Eocene Hecho Group turbidite systems, south-central Pyrenees, *in* Mila, M.D., and Rosell, J., eds., Excursion Guidebook of the 6th European Regional Meeting: International Association of Sedimentologists, 6th European Regional Meeting, Lleida, Spain, p. 519-576.

Mutti, E., 1985, Turbidite systems and their relations to depositional sequences, *in* Zuffa, G. G., ed., Provenance of Arenites, NATO-ASI Series, v. 148, p. 65-93.

Mutti, E., Seguret, M., and Sgavetti, M., 1988, Sedimentation and deformation in the Tertiary sequences of the Southern Pyrenees: Field Trip 7 Guidebook: American Association of Petroleum Geologists, Mediterranean Basins Conference, Nice, France, Special Publication of the Institute of Geology of the University of Parma, 169p.

Mutti, E., Davoli, G., Tinterri, R., and Zavala, C., 1996, The importance of fluvio-deltaic systems dominated by catastrophic flooding in tectonically active basins: Memorie Science Geology, v. 48, p. 233-291.

Naylor, M. and Sinclair, H. D., 2007, Punctuated thrust deformation in the context of doubly vergent thrust wedges: Implications for the localization of uplift and exhumation: Geology, v. 35, p. 559-562.

Nesbitt, H.W. and Young, Y.M., 1982, Early Paleozoic climates and plate motions inferred from major element chemistry of lutites: Nature, v. 299, p. 715-717.

Nesbitt, H. W., Fedo, C. M., and Young, G. M., 1997, Quartz and feldspar stability, steady and non-steady-state weathering, and petrogenesis of siliciclastic sands and muds: Journal of Geology, v. 105, p. 173-191.

Normark, W. R. and Piper, D. J., 1991, Initiation processes and flow evolution of turbidity currents: implications for the depositional record, *in* Osborne, R.H., ed., Shoreline to Abyss, Contributions in Marine Geology in honour of Francis Parker Shepard: Society of Economic Paleontologists and Mineralogists, v. 46, p. 207-230.

Oms, O., Dinares-Turell, J., and Remacha, E., 2003, Magnetic stratigraphy from deep clastic turbidites: An example from the Eocene Hecho Group (Southern Pyrenees): Studia Geophysica et Geodaetica, v. 47, p. 275-288.

Pawlowsky-Glahn, V. and Egozcue, J. J., 2006, Compositional data and their analysis: an introduction, *in* Buccianti, A., Mateu-Figueras, G. and Pawlowsky-Glahn, V., eds., Compositional Data Analysis in the Geosciences: From Theory to Practice: Geological Society of London Special Publications, v. 264, p. 1-10.

Payros, A., Pujalte, V., Orue-Etxebarria, X., and Baceta, J. I., 1997, A Bartonian channel-levee turbiditic system in the Pamplona Basin: tectonic and paleogeographic implications: Geogaceta, v. 22, p. 145-148.

Payros, A., Pujalte, V., and Orue-Etxebarria, X., 1999, The South Pyrenean Eocene carbonate megabreccias revisited: new interpretation based on evidence from the Pamplona Basin: Sedimentary Geology, v. 125, p. 165-194.

Payros, A., Orue-Etxebarria, X., and Pujalte, V., 2006, Covarying sedimentary and biotic fluctuations in Lower–Middle Eocene Pyrenean deep-sea deposits: Palaeoenvironmental implications: Palaeogeography, Palaeoclimatology, Palaeoecology, v. 234, p. 258-276.

Payros, A., Bernaola, G., Orue-Etxebarria, X., Dinarès-Turell, J., Tosquella, J., and Apellaniz, E., 2007a, Reassessment of the Early–Middle Eocene biomagnetochronology based on evidence from the Gorrondatxe section (Basque Country, western Pyrenees): Lethaia, v. 40, p. 183-195.

Payros, A., Pujalte, V., and Orue-Etxebarria, X., 2007b, A point-sourced calciclastic submarine fan complex (Eocene Anotz Formation, western Pyrenees): facies architecture, evolution and controlling factors: Sedimentology, v. 54, p. 137-168.

Pettijohn, F. J., Potter, P. E., and Siever, R., 1987, Sand and Sandstone: New York, Springer, 553p.

Pekar, S.F., Hucks, A., Fuller, M., and Li, S., 2005, Glacio-eustatic changes in the early and middle Eocene (51-42 Ma): Shallow-water stratigraphy from ODP Leg 189 Site 1171 (South Tasman Rise) and deep-sea $\delta^{18}O$ records: Geological Society of America Bulletin, v. 117, p. 1081-1093.

Pfuhl, H.A. and Schakleton, N.J., 2003, Changes in coiling direction, habitat depth and abundance in two menardellid species: Marine Micropaleontology, v. 50, p. 3-20.

Pickering, K.T., 1982, The shape of deep-water siliciclastic systems: A discussion: Geo-Marine Letters, v.2, p. 41-46.

Pickering, K.T., Clark, J.D., Smith, R.D.A., Hiscott, R.N., Ricci Lucci, F., and Kenyon, N.H., 1995, Architectural element analyses of turbidite systems, and selected topical problems of sandprone deep water systems, *in* Pickering, K.T., Hiscott, R.N., Kenyon, N.H., Ricci Lucci, F., Smith, R.D.A., eds., Atlas of deep water environments: architectural style in turbidite systems: London, Chapman and Hall, p. 1-11.

Pickering, K. T. and Corregidor, J., 2000, 3D Reservoir scale study of Eocene confined submarine fans, south central Spanish Pyrenees, *in* Weimer, P., Slatt, R. M., Coleman, J., Rosen, N. C., Nelson, H., Bouma, A. H., Styzen, M. J., and Lawrence, D. T., eds., Deep Water Reservoirs of the World: SEPM, Gulf Coast Section, 20th Annual Bob F. Perkins Research Conference, p. 776-781.

Pickering, K. T. and Corregidor, J., 2005, Mass-transport complexes (MTCs) and tectonic control on basin-floor submarine fans, Middle Eocene, south Spanish Pyrenees: Journal of Sedimentary Research, v. 75, p. 761-783.

Pidgeon, R. T., 1992, Recrystallization of oscillatory-zoned zircon: some geochemical and petrological implications: Contributions to Mineralogy and Petrology, v. 110, p. 463-472.

Pidgeon, R. T., Nemchin, A. A., and Hitchen, G. J., 1998, Internal structures of zircons from Archaean granites from the Darling Range batholith: implications for zircon stability and the interpretation of zircon ages: Contributions to Mineralogy and Petrology, v. 132, p. 288-299.

Piper, D.J.W. and Normark, W.R., 1983, Turbidite depositional patterns and flow characteristics, Navy submarine fan, California Borderland: Sedimentology, v. 30, p. 681-694.

Poblet, J., Muñoz, J. A., Travé, A., and Serra-Kiel, J., 1998, Quantifying the kinematics of detachment folds using three-dimensional geometry: Application to the Mediano anticline (Pyrenees, Spain): Geological Society of America Bulletin, v. 110, p. 111-125.

Posamentier, H.W. and Vail, P.R., 1988, Eustatic controls on clastic deposition II – sequence and system tract models, *in* Wilgus, C.K., Hastings, B.S., Kendall, C.G., Posamentier, H.W., Ross, C.A. and Van Wagoner, J.C., eds., Sea-level change - an integrated approach: SEPM Special Publication, v. 42, p. 125-154.

Premuzic, E. T., Benkovitz, C. M., Gaffney, J. S., and Walsh, J. J., 1982, The nature and distribution of organic matter in the surface sediments of world oceans and seas: Organic Geochemistry, v. 4, p. 63-77.

Prothero, D. R., Ivany, L. C., and Nesbitt, E. A., 2003, From greenhouse to icehouse: the marine Eocene–Oligocene transition: New York, Columbia University Press, 541p.

Puigdefabregas, C. and Souquet, P., 1986, Tectono-sedimentary cycles and depositional sequences of the Mesozoic and Tertiary from the Pyrenees, *in* Banda, E., Wickham, S. M., eds., The Geological Evolution of the Pyrenees: Tectonophysics, v. 129, p. 173-203.

Pupin, J. P., 1980, Zircon and granite petrology: Contributions to Mineralogy and Petrology, v. 73, p. 207-220.

Purton, L.M.A. and Brasier, M.D., 1999, Giant protist Nummulites and its Eocene environment: Life span and habitat insights from $\delta^{18}O$ and $\delta^{13}C$ data from *Nummulites* and *Venericardia*, Hampshire basin, UK: Geology, v. 27, p. 711-714.

Rahn, M. K., Brandon, M. T., Batt, G. E., and Garver, J., 2004, A zero-damage model for fission-track annealing in zircon: American Mineralogist, v. 89, p. 473-484.

Reading, H. G., 1982, Sedimentary basins and global tectonics: Proceedings of the Geologists Association, v. 93, p. 321-350.

Reading, H.G. and Richards, M., 1994, Turbidite systems in deepwater basin margins classified by grain-size and feeder system: American Association of Petroleum Geologists Bulletin, v. 78, p. 792-822.

Reiners, P. W., Campbell, I. H., Nicolescu, S., Allen, C. M., Hourigan, J. K., Garver, J. I., Mattinson, J. M., and Cowan, D. S., 2005, (U-Th)/(He-Pb) double dating of detrital zircons: American Journal of Science, v. 305, p. 259-311.

Remacha, E., Pickart, J., and Oms, O., 1991, The Rapitan turbidite channel, *in* Colombo, F., Ramos-Guerrero, E. and Riera, S., eds., 1st congress of the Spanish Group on the Tertiary, p. 280-282.

Remacha, E., Oms, O., and Coello, J., 1995, The Rapitán turbidite channel and it's related eastern levee-ovebank deposits, Eocene Hecho group, south-central Pyrenees, Spain, *in* Pickering, K. T., Hiscott, R. N., Kenyon, N. H., Ricci Lucchi F., and Smith, R. D. A., eds., Atlas of Deep Water Environments: Architectural Style in Turbidite Systems: London, Chapman & Hall, p. 145-149.

Remacha, E., Fernandez, L.P., Maestro, E., Oms, O., and Estrada, R., 1998, The Upper Hecho Group turbidites and their vertical evolution to deltas (Eocene, South-central Pyrenees), *in* International Association of Sedimentologists, 15th International Sedimentological Congress, Alicante, Spain, Field Trip Guidebook p. 1-25.

Remacha, E. and Fernandez, L. P., 2003, High-resolution correlation patterns in the turbidite systems of the Hecho Group (South-Central Pyrenees, Spain): Marine and petroleum geology, v. 20, p. 711-726.

Remacha, E., Oms, O., Gual, G., Bolano, F., Climent, F., Fernandez, L. P., Crumeyrollle, P., Pettingill, H., Vicente, J. C., and Suarez, J., 2003, Sand-rich turbidite systems of the Hecho Group from slope to basin plain; facies, stacking patterns, controlling factors and diagnostic features: American Association of Petroleum Geologists International Conference and Exhibition, Barcelona, Spain, Geological Field Trip 12.

Remacha, E., Fernandez, L. P., and Maestro, E., 2005, The transition between sheet-like lobe and basin-plain turbidites in the Hecho basin (South-central Pyrenees, Spain): Journal of Sedimentary Research, v. 75, p. 798-819.

Rollinson, H. R., 1993, Using geochemical data: evaluation, presentation, interpretation: New York, Longman Scientific and Technical, 352p.

Roser, B. P. and Korsch, R. J., 1986, Determination of tectonic setting of sandstone-mudstone suites using SiO_2 content and K_2O/Na_2O ratio: Journal of Geology, v. 94, p. 635-650.

Roser, B. P., 2000, Whole rock geochemical studies of clastic sedimentary suites: Geological Society of Japan Memoirs, v. 57, p. 73-89.

Ryu, I. C., 2003, Petrography, diagenesis and provenance of Eocene Tyee Basin sandstones, southern Oregon Coast Range: New view from sequence stratigraphy: Island Arc, v. 12, p. 398-410.

Sambridge, M. S., and Compston, W., 1994, Mixture modelling of multi-component data sets with application to ion probe zircon ages: Earth and Planetary Science Letters, v. 128, p. 373–390.

Sarnthein, M., Winn, K., Jung, S.J.A., Duplessey, J.-C., Labeyrie, L., Erlenkeuser, H., and Ganssen, G., 1994, Changes in east Atlantic deep water circulation over the last 30, 000 years: eight time slice reconstructions: Paleoceanography, v. 9, p. 209-267.

Schaub, H., 1981, Nummulites et Assilines de la Tethys Paléogène. Taxanomie, phylogénèse et biostratigraphie: Mémoires Suisses de Paléontologie, v. 104-106, p. 1-236.

Scholle, P.A. and Arthur, M.A., 1980, Carbonate isotope fluctuations in Cretaceous pelagic limestones: potential stratigraphic and petroleum exploration tool: American Association of Petroleum Geologists Bulletin, v. 64, p. 67-87.

Serra-Kiel, J., Travé, A., Mató, E., Saula, E., Fernàndez-Cañadell, C., Busquets, P., Tosquella, J., and Vergés, J., 2003, Marine and Transitional Middle/Upper Eocene Units of the Southeastern Pyrenean Foreland Basin (NE Spain): Geologica Acta, v. 1, p. 177-200.

Shackleton, N. J. and Kennett, J. P., 1975, Paleo-temperature history of the Cenozoic and the initiation of Antarctic glaciation: oxygen and carbon isotope analyses in DSDP Sites 277, 279 and 281: Initial Reports of the Deep Sea Drilling Project, v. 29, p. 743-755.

Shackleton, N.J., Imbrie, J., and Hall, M.A., 1983, Oxygen and carbon isotopic record of East Pacific core V19-30: implications for formation of deep water in the Pleistocene North Atlantic: Earth and Planetary Science Letters, v. 65, p. 233-244.

Shackleton, N.J., 1987, The carbon isotope record of the Cenozoic: history of organic carbon burial and of oxygen in the ocean and atmosphere, *in* Brooks, J. and Fleet, A.J., eds., Marine Petroleum Source Rocks: Geological Society of London Special Publication, v. 26, p. 423-434.

Schakleton, N.J. and Hall, M.A., 1997, The late Miocene stable isotope record, Site 926, *in* Shackleton, N.J., Curry, W.B., Richter, C., and Bralower, T.J., eds., Proceedings of the Ocean Drilling Program Scientific Results: College Station, TX (Ocean Drilling Program), v. 154, p. 367-374.

Shanmugam, G., 2000, 50 years of the turbidite paradigm (1950s-1990s): deep-water processes and facies models – a critical perspective: Marine and petroleum geology, v. 17, p. 285-342.

Shao, L., Stattegger, K., and Garbe-Schoenberg, C. -D., 2001, Sandstone petrology and geochemistry of the Turpan Basin (NW China): Implications for the tectonic evolution of a continental basin: Journal of Sedimentary Research, v. 71, p. 37-49.

Shoemaker, S.J. and Garver, J., 2000, Exhumation history of the Pyrenees using detrital zircon thermochronology: Geological Society of America Abstracts with Program, v. 32, p. 74.

Schlanger, S.O., Arthur, M.A., Jenkyns, H.C., and Scholle, P.A., 1987, The Cenomanian-Turonian anoxic event I: Stratigraphy and distribution of organic-rich beds and the marine $\delta^{13}C$ excursion *in* Brooks, J. and Fleet, A.J., eds., Marine Petroleum Source Rocks: Geological Society of London Special Publication, v. 26, p. 371-379.

Schwab, F.L., 1975, Framework mineralogy and chemical composition of continental margin-type sandstone: Geology, v. 3, p. 487-490.

Spero, H.J., 1998, Life history and stable isotope geochemistry of planktonic foraminifera, *in* Norris, R. D. and Corfield, R. M., eds., Isotope Paleobiology and Paleoecology: Paleontological Society Papers Special Publication, v. 4, p. 7-36.

Spiegel, C., Kuhlemann, J., Dunkl, I., Frisch, W., von Eynatten, H., and Balogh, K., 2000, The erosion history of the Central Alps: evidence from the zircon fission-track data of the foreland basin sediments: Terra Nova, v. 12, p. 163-170.

Stock, J. D. and Montgomery, D. R., 1996, Estimating palaeorelief from detrital mineral age ranges: Basin Research, v. 8, p. 317-327.

Stow, D.A.V. and Mayall, M., 2000, Deep-water sedimentary systems: new models for the 21st century: Marine and petroleum geology, v. 17, p. 125-135.

Svojtka, M., Košler, J., and Venera, Z., 2001, Dating granulite-facies structures and the exhumation of lower crust in the Moldanubian Zone of the Bohemian Massif: International Journal of Earth Sciences, v. 91, p. 373-385.

Tagami, T., Galbraith, R. F., Yamada, G. M., and Laslett, G. M., 1998, Revised annealing kinetics of fission tracks in zircon and geological implications, *in* Van den Haute, P., and De Corte, F., eds., Advances in Fission-Track Geochronology, p. 99-112.

Taylor, S. R. and McLennan, S. M., 1985, The continental crust: Its composition and evolution: Oxford, Blackwell Scientific, 312p.

Taylor, S.R. and McLennan, S.M., 1995, The geochemical evolution of the continental crust: Reviews of Geophysics, v. 33, p. 241-265.

Teixell, A., 1996, The Ansó transect of the southern Pyrenees: basement and cover thrust geometries: Journal of the Geological Society of London, v. 153, p. 301-310.

Teixell, A., 1998, Crustal structure and orogenic material budget in the west central Pyrenees: Tectonics, v. 17, p. 395-406.

Travé, A., Labaume, P., Calvet, F., and Soler, A., 1997, Sediment dewatering and pore fluid migration along thrust faults in a foreland basin inferred from isotopic and elemental geochemical analyses (Eocene southern Pyrenees, Spain): Tectonophysics, v. 282, p. 375-398.

Uddin, A. and Lundberg, N., 1998, Unroofing history of the eastern Himalaya and the Indo-Burman Ranges: Heavy-mineral study of Cenozoic sediments from the Bengal basin, Bangladesh: Journal of Sedimentary Research, v. 68, p. 465-472.

Underwood, M. B., Orr, R., Pickering, K. T., and Taira, A., 1993, Provenance and dispersal patterns of sediments in the turbidite wedge of Nankai Trough, *in* Taira, A., Hill, I. A. H., Firth, J., Vrolijk, P.J., eds., Proceedings of the Ocean Drilling Program, Scientific Results, v. 131, p. 15-33.

Underwood, M. B., Ballance, P. F., Clift, P., Hiscott, R. N., Marsaglia, K. M., Pickering, K. T., and Reid, R.P., 1995, Sedimentation in Forearc Basins, Trenches, and Collision Zones of the Western Pacific: A summary of Results from the Ocean Drilling Program, *in* Taylor, B., and Natland, J., eds., Active Margins and Marginal Basins of the Western Pacific: American Geophysical Monograph, v. 88, p. 315-353.

Underwood, M.B. and Hoke, K.D., 2000, Composition and provenance of turbidite sand and hemipelagic mud in northwestern Cascadia Basin, Leg 168 of the Ocean Drilling Program: Proceedings of the Ocean Drilling Program, Scientific Results, v. 168, p. 51-65.

Urey, H.C., Lowenstam, H.A., Epstein, S., and McKinney, C.R., 1951, Measurements of paleotemperatures and temperatures of the Upper Cretaceous of England, Denmark and the Southeastern United States: Geological Society of America Bulletin, v. 62, p. 399-416.

Valloni, R., 1985, Reading provenance from modern marine sands *in* Zuffa, G. G., ed., Provenance of Arenites, NATO-ASI Series, v. 148, p. 309-332.

Van Der Plas, L. and Tobi, A.C., 1965, A chart for judging the reliability of point counting results: American Journal of Science, v. 263, p. 87-90.

Vavra, G., 1990, On the kinematics of zircon growth and its petrogenetic significance: a cathodoluminescence study: Contributions to Mineralogy and Petrology, v. 106, p. 90-99.

Vavra, G., 1994, Systematics of internal zircon morphology in major Variscan granitoid types: Contributions to Mineralogy and Petrology, v. 117, p. 331-344.

Vavra, G., Gebauer, D., Schmid, R., and Compston, W., 1996, Multiple zircon growth and recystallization during polyphase Late Carboniferous to Triassic metamorphism in granulites of the Ivrea Zone (Southern Alps): an ion microprobe (SHRIMP) study: Contributions to Mineralogy and Petrology, v. 122, p. 337-358.

Vavra, G., Schmid, R., and Gebauer, D., 1999, Internal morphology, habit and U-Th-Pb microanalysis of amphibole-to-granulite facies zircons: geochronology of the Ivrea Zone (Southern Alps): Contributions to Mineralogy and Petrology, v. 134, p. 380-404.

Vegas, R., Vazquez, J.T., Surinach, E., and Marcos, A., 1990, Model of distributed deformation, block rotations and crustal thickening for the formation of the Spanish Central system: Tectonophysics, v. 184, p. 367-378.

Veizer, J. and Hoefs, J., 1976, The nature of O^{18}/O^{16} and C^{13}/C^{12} secular trends in sedimentary carbonate rocks: Geochimica et Cosmochimica Acta, v. 40, p. 1387-1395.

Vergés, J. and Muñoz, J. A., 1990, Thrust sequences in the Southern Central Pyrenees: Bulletin de la Société Géologique de France, v. 8, p. 265-271.

Vergés, J., Millán, H., Roca, E., Muñoz, J.A., Marzo, M., Cirés, J., Den Bezemer, T., Zoetemeijer, R., and Cloetingh, S., 1995, Eastern Pyrenees and related foreland basins: pre-, syn- and post-collisional crustal-scale cross-sections: Marine and petroleum geology, v. 12, p. 803-915.

Vergés, J. and Burbank, D. W., 1996, Eocene-Oligocene thrusting and basin configuration in the eastern and central Pyrenees (Spain), *in* Friend, P. F., Dabrio, C. J., eds., Tertiary Basins of Spain: the Stratigraphic Record of Crustal Kinematics, p. 120-133.

Vergés, J., Marzo, M., Santaeuleria, T., Serra-Kiel, J., Burbank, D. W., Munoz, J. A., and Gimenez-Montsant, J., 1998, Quantified vertical motions and tectonic evolution of the SE Pyrenean foreland basin *in* Mascle, A., Puigdefabregas, C., Luterbacher, H. P. and Fernandez, M., eds., Cenozoic Foreland Basins of Western Europe: Geological Society of London Special Publications, v. 134, p. 107-134.

Vermeesch, P., 2004, How many grains are needed for a provenance study?: Earth and Planetary Science Letters, v. 224, p. 441-451.

Vielzeuf, D. and Kornprobst, J., 1984, Crustal splitting and the emplacement of the Pyrenean lherzolites and granulites: Earth and Planetary Science Letters, v. 67, p. 87-96.

Vincent, S. J., 1999, The role of sediment supply in controlling alluvial architecture: an example from the Spanish Pyrenees: Journal of the Geological Society of London, v. 156, p. 749-759.

von Eynatten, H., Gaup, R., and Wijbrans, J. R., 1996, $^{40}Ar/^{39}Ar$ laser-probe dating of detrital white micas from Cretaceous sedimentary rocks of Eastern Alps: evidence for Variscan high pressure metamorphism and implications for Alpine Orogeny: Geology, v. 24, p. 691-694.

Waelbroeck, C., Labeyrie, L., Michel, E., Duplessey, J.-C., McManus, J.F., Lambeck, K., Balbon, E., and Labracherie, M., 2002, Sea-level and deep water temperature changes derived from benthic foraminifera isotopic records: Quaternary Science Reviews, v. 21, p. 295-305.

Wefer, G. and Berger, W.H., 1991, Isotope paleontology: growth and composition of extant calcareous species: Marine Geology, v.100, p. 207-248.

Weissert, H., 1989, C-isotope stratigraphy, a monitor of paleoenvironmental change: a case study from the early Cretaceous: Surveys in Geophysics, v. 10, p. 1-61.

Weltje, G. J., 2002, Quantitative analysis of detrital modes: statistically rigorous confidence regions in ternary diagrams and their use in sedimentary petrology: Earth-Science Reviews, v. 57, p. 211-253.

Weltje, G. J. and von Eynatten, H., 2004, Quantitative provenance analysis of sediments: review and outlook: Sedimentary Geology, v. 171, p. 1-11.

Weltje, G. J., 2006, Ternary sandstone composition and provenance: an evaluation of the 'Dickinson model', *in* Buccianti, A., Mateu-Figueras, G. and Pawlowsky-Glahn, V., eds., Compositional Data Analysis in the Geosciences: From Theory to Practice: Geological Society of London Special Publications, v. 264, p. 79-99.

Wing, S.L., Gingerich, P. D., and Schmitz, B., 2003, Causes and consequences of globally warm climates in the Early Paleogene: Geological Society of America Special Papers 369, 614p.

Winter, J. D., 2001, An introduction to igneous and metamorphic petrology: NJ, Prentice Hall, Englewood Cliffs, 697p.

Woodruff, F. and Savin, S.M., 1985, $\delta^{13}C$ values of Miocene Pacific benthic foraminifera: correlations with sea level and biological productivity: Geology, v. 13, p. 119-122.

Wronkiewicz, D. J. and Condie, K. C., 1987, Geochemistry of Archean shales from the Witwatersrand Supergroup, South Africa: source-area weathering and provenance: Geochimica et Cosmochimica Acta, v. 51, p. 2401-2416.

Yuste, A., Luzon, A., and Bauluz, B., 2004, Provenance of Oligocene–Miocene alluvial and fluvial fans of the northern Ebro Basin (NE Spain): an XRD, petrographic and SEM study: Sedimentary Geology, v. 172, p. 251-268.

Zachos, J., Pagani, M., Sloan, L., Thomas, E. and Billups, K., 2001, Trends, rhythms, and aberrations in global climate 65 Ma to Present: Science, v. 292, p. 686-693.

Zachos, J.C., Röhl, U., Schellenberg, S.A., Sluijs, A., Hodell, D.A., Kelly, D.C., Thomas, E., Nicolo, M., Raffi, I., Lourens, L.J., McCarren, H., and Kroon, D., 2005, Rapid acidification of the ocean during the Paleocene-Eocene Thermal Maximum: Science, v. 308, p. 1611-1615.

Zattin, M., Stefani, C., and Martin, S., 2003, Detrital fission-track analysis and sedimentary petrofacies as keys of Alpine exhumation: the example of the Venetian foreland (European southern Alps, Italy): Journal of Sedimentary Research, v. 73, p. 1051-1061.

Zimmermann, U. and Bahlburg, H., 2003, Provenance analysis and tectonic setting of the Ordovician clastic deposits in the southern Puna Basin, NW Argentina: Sedimentology, v. 50, p. 1079-1104.

Zuffa, G. G., 1980, Hybrid arenites: their composition and classification: Journal of Sedimentary Petrology, v. 50, p. 21-29.

Zuffa, G. G., 1985, Optical analyses of arenites: Influence of methodology on compositional results, *in* Zuffa, G. G., ed., Provenance of Arenites, NATO-ASI Series, v. 148, p. 165-189.

Zuffa, G. G., 1987, Unravelling hinterland and offshore palaeogeography from deep-water arenites, *in* Legget, J. K. and Zuffa, G. G., eds., Marine Clastic Sedimentology: London, Graham and Trotman, p. 39-61.

Zuffa, G. G., 1991, On the use of turbidite arenites in provenance studies: critical remarks, *in* Morton, A. C., Todd, S. P. and Haughton, P. D. W., Developments in sedimentary provenance studies: Geological Society of London Special Publication, v. 57, p. 23-29.

Zuffa, G. G., Cibin, U., and Di Giulio, A., 1995, Arenite Petrography in Sequence Stratigraphy: The Journal of Geology, v. 103, p. 451-459.

Zwart, H. J., 1979, The geology of the Central Pyrenees: Leidse Geologische Mededelingen, v. 50, p. 1-44.

APPENDIX – I

U–Pb geochronologic analyses of the Ainsa basin detrital zircons

	Isotope ratios						Estimated ages (Ma)							
Grain	$^{206}Pb/^{238}U$	1 σ	$^{207}Pb/^{235}U$	1 σ	$^{207}Pb/^{206}Pb$	1 σ	$^{206}Pb/^{238}U$	1σ	$^{207}Pb/^{235}U$	1σ	$^{207}Pb/^{206}Pb$	1σ	Discordant%	Use raw age?
Arro system														
AR1	0.14798	0.00221	1.4712	0.02116	0.07207	0.00111	889.6	12.4	918.6	8.69	987.8	31.02	3.16	YES
AR2	0.05071	0.00099	0.38876	0.01189	0.05558	0.00186	318.9	6.1	333.5	8.69	435.3	72.82	4.38	YES
AR3	0.05009	0.00098	0.36792	0.01147	0.05325	0.00181	315.1	6.01	318.1	8.52	339.3	75.22	0.94	YES
AR4	0.04863	0.00089	0.36199	0.00991	0.05396	0.00161	306.1	5.49	313.7	7.38	369.4	65.68	2.42	YES
AR5	0.04909	0.00099	0.48076	0.01406	0.071	0.00231	308.9	6.08	398.6	9.64	957.4	65.25	22.50	YES
AR6	0.05209	0.00116	0.3813	0.01493	0.05306	0.00227	327.4	7.12	328	10.97	331.4	93.99	0.18	YES
AR7	0.14779	0.00252	1.53757	0.03083	0.07542	0.00167	888.5	14.14	945.5	12.33	1079.8	43.79	6.03	YES
AR8	0.08109	0.00117	0.67819	0.00886	0.06063	0.00082	502.6	6.96	525.7	5.36	626.2	29.06	4.39	YES
AR9	0.04974	0.00095	0.3751	0.01101	0.05467	0.00175	312.9	5.84	323.4	8.13	398.7	69.55	3.25	YES
AR10	0.0505	0.00122	0.37123	0.01647	0.05329	0.00258	317.6	7.48	320.6	12.19	341.1	105.73	0.94	YES
AR11	0.11274	0.00268	1.10381	0.03954	0.07098	0.00286	688.6	15.51	755.2	19.08	957	80.26	8.82	YES
AR12	0.07294	0.00131	0.57875	0.01467	0.05753	0.00159	453.8	7.87	463.7	9.43	511.5	60.01	2.14	YES
AR13	0.06733	0.00099	0.53887	0.00777	0.05802	0.00088	420.1	5.98	437.7	5.13	530.3	33.26	4.02	YES
AR14	0.37777	0.00541	7.02963	0.08018	0.13491	0.00158	2065.9	25.32	2115.2	10.14	2162.9	20.32	2.33	YES
AR15	0.09237	0.00235	0.81794	0.0366	0.0642	0.00316	569.6	13.86	606.9	20.44	748.2	100.72	6.15	YES
AR16	0.16449	0.00303	1.70435	0.03977	0.07512	0.00195	981.7	16.76	1010.2	14.93	1071.8	51.2	2.82	YES
AR17	0.06312	0.001	0.49452	0.00929	0.0568	0.00115	394.6	6.07	408	6.31	483.3	44.27	3.28	YES
AR18	0.07381	0.00121	0.59107	0.01207	0.05806	0.00128	459.1	7.27	471.6	7.71	531.5	48.08	2.65	YES
AR19	0.04918	0.00093	0.35718	0.01036	0.05265	0.00166	309.5	5.69	310.1	7.75	313.9	70.12	0.19	YES
AR20	0.09383	0.0019	0.82016	0.02492	0.06338	0.00212	578.1	11.21	608.1	13.9	721	69.56	4.93	YES
AR21	0.05308	0.0012	0.36303	0.01452	0.04959	0.00216	333.4	7.36	314.5	10.82	175.8	98.73	-6.01	YES
AR22	0.09997	0.00193	0.81924	0.02318	0.05942	0.00184	614.2	11.28	607.6	12.94	582.6	65.95	-1.09	YES
AR23	0.05144	0.0014	0.36624	0.01894	0.05162	0.00292	323.4	8.6	316.9	14.07	268.8	124.78	-2.05	YES
AR24	0.00761	0.00075	0.09994	0.02287	0.09526	0.02367	48.9	4.78	96.7	21.11	1533.3	407.02	49.43	NO
AR25	0.1649	0.00239	1.66556	0.02153	0.07324	0.00098	983.9	13.25	995.5	8.2	1020.6	26.79	1.17	YES
AR26	0.05014	0.0009	0.36746	0.00971	0.05314	0.00152	315.4	5.54	317.8	7.21	334.7	63.63	0.76	YES
AR27	0.04944	0.00092	0.39831	0.01079	0.05842	0.00173	311.1	5.67	340.4	7.83	545.4	63.46	8.61	YES
AR28	0.04977	0.00096	0.34666	0.01067	0.05051	0.00169	313.1	5.91	302.2	8.05	218.4	75.56	-3.61	YES
AR29	0.09897	0.00221	0.85129	0.03133	0.06237	0.00252	608.4	12.94	625.4	17.18	686.8	83.9	2.72	YES
AR30	0.04754	0.00112	0.36735	0.01519	0.05603	0.00254	299.4	6.9	317.7	11.28	453.1	97.9	5.76	YES
AR31	0.10095	0.00166	0.8632	0.01709	0.06201	0.00132	619.9	9.71	631.9	9.31	674.3	45.01	1.90	YES

	Isotope ratios						Estimated ages (Ma)							
Grain	$^{206}Pb/^{238}U$	1 σ	$^{207}Pb/^{235}U$	1 σ	$^{207}Pb/^{206}Pb$	1 σ	$^{206}Pb/^{238}U$	1σ	$^{207}Pb/^{235}U$	1σ	$^{207}Pb/^{206}Pb$	1σ	Discordant%	Use raw age?
AR32	0.07962	0.00151	0.62241	0.01772	0.05668	0.00176	493.9	9.02	491.4	11.09	478.5	67.78	-0.51	YES
AR33	0.07902	0.00131	0.61401	0.01278	0.05634	0.00126	490.3	7.81	486.1	8.04	465.2	49.29	-0.86	YES
AR34	0.17928	0.00378	1.93868	0.05607	0.07841	0.00254	1063.1	20.67	1094.5	19.37	1157.3	62.93	2.87	YES
AR35	0.50612	0.0076	13.47004	0.17159	0.19299	0.00257	2640	32.53	2713.2	12.04	2767.8	21.69	2.70	YES
AR36	0.10884	0.00173	0.92476	0.01676	0.06161	0.00119	666	10.06	664.9	8.84	660.8	40.97	-0.17	YES
AR37	0.04945	0.00091	0.36117	0.01004	0.05296	0.00159	311.2	5.61	313.1	7.49	327	66.92	0.61	YES
AR38	0.08931	0.00136	0.71445	0.0114	0.05801	0.00097	551.5	8.03	547.4	6.75	529.6	36.69	-0.75	YES
AR39	0.14366	0.00352	1.36127	0.05408	0.06871	0.00302	865.3	19.85	872.4	23.25	890.1	88.31	0.81	YES
AR40	0.04773	0.00105	0.39739	0.01406	0.06037	0.00235	300.6	6.43	339.8	10.21	617	81.93	11.54	NO
AR41	0.04935	0.00111	0.34483	0.01368	0.05067	0.00219	310.5	6.8	300.8	10.33	225.7	96.74	-3.22	YES
AR42	0.04647	0.00091	0.35356	0.0108	0.05517	0.00184	292.8	5.63	307.4	8.11	419	72.23	4.75	YES
AR43	0.34572	0.00586	5.73933	0.09887	0.12039	0.00228	1914.1	28.07	1937.3	14.9	1962	33.42	1.20	YES
AR44	0.1815	0.00291	2.27626	0.03777	0.09095	0.00163	1075.1	15.88	1205	11.71	1445.4	33.68	10.78	NO
AR45	0.04914	0.00089	0.37924	0.00981	0.05597	0.00157	309.2	5.49	326.5	7.23	450.8	61.18	5.30	YES
AR46	0.05273	0.001	0.3701	0.011	0.0509	0.00163	331.2	6.11	319.7	8.15	236.4	72.38	-3.60	YES
AR48	0.05037	0.00132	0.36662	0.0177	0.05279	0.00279	316.8	8.1	317.1	13.15	319.6	115.6	0.09	YES
AR49	0.09362	0.00164	0.74046	0.01731	0.05736	0.00145	576.9	9.65	562.7	10.1	504.8	55.06	-2.52	YES
AR50	0.35481	0.00628	5.80788	0.10876	0.11871	0.00246	1957.5	29.9	1947.6	16.22	1936.9	36.66	-0.51	YES
AR51	0.09439	0.00163	0.77783	0.01746	0.05976	0.00145	581.4	9.62	584.2	9.97	594.7	51.98	0.48	YES
AR52	0.18807	0.00342	1.95885	0.04489	0.07553	0.0019	1110.9	18.58	1101.5	15.4	1082.7	49.55	-0.85	YES
AR53	0.0498	0.00103	0.3841	0.01274	0.05593	0.00202	313.3	6.33	330	9.35	449.3	78.45	5.06	YES
AR54	0.04984	0.00111	0.36571	0.01411	0.05321	0.00223	313.5	6.82	316.5	10.49	337.9	92.17	0.95	YES
AR55	0.03496	0.00056	0.2648	0.0051	0.05493	0.00112	221.5	3.51	238.5	4.1	409.4	44.78	7.13	YES
AR56	0.04771	0.00091	0.38435	0.01077	0.05842	0.00178	300.5	5.58	330.2	7.9	545.4	65.28	8.99	YES
AR57	0.07647	0.0012	0.60597	0.01073	0.05747	0.00107	475	7.21	481	6.78	509	40.82	1.25	YES
AR58	0.01562	0.00078	0.12909	0.01411	0.05994	0.00715	99.9	4.96	123.3	12.69	601.4	239.1	18.98	NO
AR59	0.12907	0.00294	1.22839	0.04197	0.06902	0.00262	782.5	16.78	813.6	19.12	899.4	76.48	3.82	YES
AR60	0.18556	0.0032	1.86987	0.03894	0.07308	0.00165	1097.3	17.42	1070.5	13.78	1016.2	44.96	-2.50	YES
AR01	0.08432	0.00093	0.67471	0.02121	0.05806	0.00147	521.9	5.52	523.6	12.86	531.7	54.83	0.32	YES
AR02	0.08237	0.0011	0.66126	0.03413	0.05608	0.00227	510.2	6.54	515.4	20.86	455	87.83	1.01	YES
AR03	0.08605	0.00089	0.67716	0.01665	0.05563	0.00112	532.2	5.31	525.1	10.08	437.1	43.96	-1.35	YES
AR04	0.07602	0.00242	0.56	0.09131	0.05458	0.00725	472.3	14.49	451.5	59.43	394.9	273.14	-4.61	YES
AR05	0.03272	0.00033	0.22552	0.00399	0.0499	0.00079	207.6	2.04	206.5	3.31	190.6	36.52	-0.53	YES
AR06	0.05042	0.00053	0.34479	0.00857	0.05315	0.00116	317.1	3.28	300.8	6.47	335	48.75	-5.42	YES

	Isotope ratios						Estimated ages (Ma)							
Grain	$^{206}Pb/^{238}U$	1 σ	$^{207}Pb/^{235}U$	1 σ	$^{207}Pb/^{206}Pb$	1 σ	$^{206}Pb/^{238}U$	1σ	$^{207}Pb/^{235}U$	1σ	$^{207}Pb/^{206}Pb$	1σ	Discordant%	Use raw age?
AR07	0.05045	0.00055	0.35447	0.00945	0.05401	0.00126	317.3	3.35	308.1	7.08	371.4	51.64	-2.99	YES
AR08	0.05108	0.00056	0.34596	0.00984	0.05209	0.0013	321.2	3.44	301.7	7.43	289.2	55.91	-6.46	YES
Gerbe system														
G2-1	0.09086	0.00141	0.66856	0.01351	0.05339	0.00117	560.6	8.34	519.8	8.22	345.3	48.88	-7.85	YES
G2-2	0.20413	0.00324	2.08028	0.03824	0.07395	0.0015	1197.5	17.34	1142.3	12.61	1040	40.46	-4.83	YES
G2-3	0.17914	0.00268	1.87193	0.02971	0.07582	0.00132	1062.3	14.67	1071.2	10.5	1090.4	34.54	0.83	YES
G2-4	0.16994	0.00239	1.69275	0.02268	0.07228	0.00104	1011.8	13.15	1005.8	8.55	993.8	29.07	-0.60	YES
G2-5	0.09945	0.0017	0.87606	0.02017	0.06392	0.00163	611.2	9.98	638.9	10.92	739.1	52.99	4.34	YES
G2-6	0.08984	0.00124	0.7666	0.01006	0.06192	0.00087	554.6	7.32	577.8	5.78	671.2	29.66	4.02	YES
G2-7	0.04983	0.00082	0.37895	0.00883	0.05519	0.0014	313.4	5.06	326.3	6.5	419.7	55.27	3.95	YES
G2-8	0.04805	0.0007	0.34393	0.00576	0.05194	0.00093	302.5	4.28	300.1	4.35	282.7	40.59	-0.80	YES
G2-9	0.04861	0.00074	0.3797	0.00702	0.05668	0.00114	306	4.52	326.8	5.17	478.5	44.3	6.36	YES
G2-11	0.10559	0.00197	1.26017	0.02972	0.0866	0.00233	647.1	11.49	828	13.35	1351.6	51.01	21.85	NO
G2-12	0.52189	0.00729	12.58602	0.13961	0.17499	0.00208	2707.2	30.86	2649.2	10.43	2605.9	19.71	-2.19	YES
G2-13	0.04697	0.00073	0.35822	0.00711	0.05534	0.00119	295.9	4.48	310.9	5.32	425.7	46.88	4.82	YES
G2-14	0.10208	0.0018	0.885	0.02181	0.06291	0.00171	626.6	10.55	643.7	11.75	705.2	56.88	2.66	YES
G2-15	0.05381	0.00083	0.4189	0.00808	0.05649	0.00118	337.9	5.06	355.3	5.78	470.8	46.14	4.90	YES
G2-16	0.12961	0.00177	1.15951	0.01456	0.06491	0.00086	785.6	10.13	781.7	6.85	771.5	27.69	-0.50	YES
G2-17	0.12547	0.00195	1.07726	0.02062	0.0623	0.0013	762	11.18	742.3	10.08	684.3	43.87	-2.65	YES
G2-18	0.381	0.00521	6.9007	0.07716	0.13141	0.00155	2081	24.31	2098.7	9.92	2116.9	20.55	0.84	YES
G2-19	0.05149	0.00112	0.36839	0.01436	0.05191	0.00221	323.7	6.85	318.5	10.65	281.5	94.38	-1.63	YES
G2-20	0.10015	0.00143	0.85328	0.01276	0.06182	0.00099	615.3	8.39	626.4	6.99	667.8	33.92	1.77	YES
G2-21	0.17811	0.00281	1.89311	0.03437	0.07712	0.00154	1056.6	15.39	1078.7	12.06	1124.2	39.33	2.05	YES
G2-22	0.10906	0.00173	0.97773	0.01913	0.06504	0.00139	667.3	10.07	692.4	9.82	775.6	44.42	3.63	YES
G2-23	0.12575	0.00198	1.16348	0.02236	0.06713	0.00141	763.6	11.36	783.6	10.5	841.7	43.13	2.55	YES
G2-24	0.02215	0.00032	0.16032	0.00262	0.05251	0.00092	141.2	2.02	151	2.29	307.5	39.26	6.49	YES
G2-25	0.15933	0.00239	1.46553	0.02512	0.06673	0.00123	953.1	13.29	916.3	10.35	829.3	38.13	-4.02	YES
G2-26	0.07425	0.00128	0.593	0.01445	0.05794	0.00155	461.7	7.67	472.8	9.21	527.2	57.77	2.35	YES
G2-27	0.28324	0.00399	4.87919	0.06113	0.12497	0.00168	1607.6	20.07	1798.7	10.56	2028.4	23.56	10.62	NO
G2-28	0.07901	0.00123	0.64253	0.01253	0.059	0.00125	490.2	7.34	503.9	7.75	567	45.37	2.72	YES
G2-29	0.12502	0.00309	1.13563	0.04694	0.0659	0.00302	759.4	17.7	770.4	22.32	803.1	93.27	1.43	YES
G2-30	0.09722	0.00168	0.8048	0.01957	0.06005	0.0016	598.1	9.89	599.5	11.01	605.4	56.59	0.23	YES
G2-31	0.12188	0.0018	1.04899	0.01727	0.06243	0.0011	741.4	10.34	728.4	8.56	688.9	37.26	-1.78	YES
G2-32	0.01119	0.00039	0.10254	0.00682	0.06647	0.0049	71.7	2.46	99.1	6.28	821.4	146.83	27.65	NO

	Isotope ratios						Estimated ages (Ma)							
Grain	$^{206}Pb/^{238}U$	1 σ	$^{207}Pb/^{235}U$	1 σ	$^{207}Pb/^{206}Pb$	1 σ	$^{206}Pb/^{238}U$	1σ	$^{207}Pb/^{235}U$	1σ	$^{207}Pb/^{206}Pb$	1σ	Discordant%	Use raw age?
G2-33	0.05018	0.00077	0.38713	0.0075	0.05597	0.00117	315.6	4.75	332.3	5.49	450.6	45.59	5.03	YES
G2-34	0.1303	0.00193	1.18492	0.01942	0.06596	0.00116	789.6	11.01	793.6	9.03	805.1	36.46	0.50	YES
G2-35	0.05002	0.0008	0.36816	0.00792	0.05339	0.00124	314.6	4.9	318.3	5.88	345.3	51.83	1.16	YES
G2-36	0.0189	0.00089	0.19541	0.02073	0.07498	0.00863	120.7	5.62	181.2	17.61	1067.9	215.42	33.39	NO
G2-37	0.13446	0.00251	1.22711	0.03299	0.06619	0.00196	813.3	14.28	813	15.04	812.4	60.83	-0.04	YES
G2-38	0.10135	0.00156	0.86302	0.01611	0.06176	0.00125	622.3	9.16	631.8	8.78	665.7	42.62	1.50	YES
G2-39	0.04046	0.00121	0.35655	0.0198	0.06392	0.00393	255.7	7.51	309.6	14.82	738.8	125.04	17.41	NO
G2-40	0.1456	0.00273	1.64864	0.04091	0.08212	0.00228	876.2	15.36	989	15.68	1248.3	53.35	11.41	NO
G2-41	0.08244	0.00132	0.65464	0.0138	0.05758	0.00131	510.7	7.89	511.3	8.47	513.6	49.69	0.12	YES
G2-42	0.05028	0.00105	0.34461	0.01274	0.04971	0.002	316.2	6.47	300.7	9.62	181.2	91.15	-5.15	YES
G2-43	0.04618	0.0007	0.347	0.00634	0.05448	0.00106	291	4.29	302.5	4.78	391.1	43	3.80	YES
G2-44	0.1341	0.00346	1.38224	0.05655	0.07474	0.00343	811.2	19.65	881.4	24.1	1061.5	89.79	7.96	YES
G2-45	0.09973	0.00168	0.85061	0.01948	0.06184	0.00154	612.9	9.85	625	10.69	668.7	52.5	1.94	YES
G2-46	0.11006	0.00165	0.93751	0.01628	0.06176	0.00115	673.1	9.59	671.6	8.53	665.8	39.25	-0.22	YES
G2-47	0.12051	0.00178	1.06527	0.01739	0.06409	0.00111	733.5	10.21	736.4	8.55	744.7	36.26	0.39	YES
G2-48	0.04953	0.00075	0.3666	0.00685	0.05367	0.00107	311.6	4.62	317.1	5.09	357	44.51	1.73	YES
G2-49	0.04967	0.00079	0.36844	0.00769	0.05378	0.00121	312.5	4.83	318.5	5.7	361.8	49.88	1.88	YES
G2-50	0.17572	0.00258	1.84796	0.02903	0.07624	0.00127	1043.6	14.14	1062.7	10.35	1101.4	32.89	1.80	YES
G1	0.10158	0.00114	0.91968	0.04067	0.06588	0.00211	623.7	6.66	662.2	21.51	802.5	65.56	5.81	YES
G2	0.04603	0.00041	0.35025	0.00769	0.05664	0.00114	290.1	2.55	304.9	5.78	476.9	44.36	4.85	YES
G3	0.13901	0.00128	1.31238	0.03539	0.06982	0.00134	839.1	7.22	851.2	15.54	923.2	38.92	1.42	YES
G4	0.06889	0.00071	2.59177	0.0657	0.28303	0.00472	429.5	4.25	1298.3	18.57	3379.7	25.77	66.92	NO
G5	0.3106	0.00255	5.09003	0.06201	0.12471	0.00139	1743.7	12.56	1834.4	10.34	2024.7	19.63	4.94	YES
G6	0.04483	0.00047	0.33294	0.01104	0.05517	0.00162	282.7	2.87	291.8	8.41	419.1	63.85	3.12	YES
G7	0.04683	0.00047	0.33238	0.01041	0.05241	0.00146	295	2.91	291.4	7.93	303.5	62.21	-1.24	YES
G8	0.05388	0.00053	0.45176	0.01275	0.06114	0.00149	338.3	3.26	378.5	8.92	644.2	51.52	10.62	NO
G9	0.04675	0.00046	0.32793	0.00931	0.05244	0.00134	294.5	2.83	288	7.12	304.7	56.97	-2.26	YES
G10	0.04769	0.00048	0.32056	0.00985	0.05092	0.0014	300.3	2.97	282.3	7.57	237.4	62.31	-6.38	YES
Banaston system														
B3-1	0.06638	0.00228	0.57571	0.03426	0.0628	0.00421	414.3	13.79	461.7	22.07	701.3	136.53	10.27	YES
B3-2	0.05186	0.00107	0.38861	0.01211	0.05427	0.00188	325.9	6.55	333.4	8.85	382.2	75.83	2.25	YES
B3-3	0.08588	0.00159	0.70332	0.01738	0.05933	0.00163	531.1	9.47	540.8	10.36	579.3	58.72	1.79	YES
B3-4	0.05141	0.00108	0.45818	0.01354	0.0646	0.00216	323.1	6.61	383	9.43	761.2	68.82	15.64	NO
B3-5	0.05293	0.00176	0.49559	0.02651	0.06788	0.00415	332.5	10.79	408.7	18	864.8	122.37	18.64	NO

	Isotope ratios						Estimated ages (Ma)							
Grain	$^{206}Pb/^{238}U$	1 σ	$^{207}Pb/^{235}U$	1 σ	$^{207}Pb/^{206}Pb$	1 σ	$^{206}Pb/^{238}U$	1σ	$^{207}Pb/^{235}U$	1σ	$^{207}Pb/^{206}Pb$	1σ	Discordant%	Use raw age?
B3-6	0.19451	0.0043	2.22014	0.0631	0.08277	0.0027	1145.8	23.2	1187.4	19.9	1263.7	62.36	3.50	YES
B3-7	0.16608	0.00248	1.71289	0.02251	0.07481	0.00105	990.5	13.72	1013.4	8.43	1063.3	28.1	2.26	YES
B3-8	0.08965	0.00197	0.73764	0.02447	0.05969	0.00221	553.5	11.66	561	14.3	593	77.77	1.34	YES
B3-9	0.04902	0.00093	0.35981	0.00973	0.05327	0.00159	308.5	5.73	312.1	7.27	340.1	66.14	1.15	YES
B3-10	0.05198	0.00118	0.35301	0.01329	0.04932	0.00204	326.6	7.21	307	9.98	163	94.04	-6.38	YES
B3-11	0.05063	0.00108	0.34491	0.0119	0.04947	0.00187	318.4	6.65	300.9	8.99	170.3	86.11	-5.82	YES
B3-12	0.04878	0.00141	0.34799	0.01828	0.05182	0.00301	307	8.69	303.2	13.77	277.6	127.7	-1.25	YES
B3-13	0.04905	0.00095	0.36476	0.01012	0.05403	0.00165	308.7	5.86	315.8	7.53	372.1	67.18	2.25	YES
B3-14	0.01645	0.00026	0.12731	0.00192	0.05625	0.0009	105.2	1.62	121.7	1.73	461.3	35.23	13.56	NO
B3-15	0.00787	0.00024	0.06693	0.00362	0.06178	0.00374	50.6	1.57	65.8	3.44	666.4	124.67	23.10	NO
B3-16	0.13038	0.00304	1.18616	0.04041	0.06613	0.00252	790	17.32	794.2	18.77	810.6	77.87	0.53	YES
B3-17	0.20805	0.00333	2.33319	0.03583	0.08153	0.00133	1218.4	17.76	1222.5	10.92	1234.2	31.75	0.34	YES
B3-18	0.2521	0.00758	3.56574	0.13793	0.10283	0.00468	1449.3	39.04	1541.9	30.68	1675.9	81.73	6.01	YES
B3-19	0.04863	0.00101	0.33986	0.01083	0.05082	0.00177	306.1	6.22	297.1	8.2	232.6	78.53	-3.03	YES
B3-20	0.10598	0.00199	1.14414	0.02529	0.07851	0.00192	649.4	11.57	774.5	11.98	1159.9	47.72	16.15	NO
B3-21	0.04755	0.00122	0.39439	0.01607	0.06033	0.00274	299.4	7.48	337.6	11.7	615.4	95.16	11.32	NO
B3-22	0.22423	0.00369	2.54588	0.04195	0.08258	0.00143	1304.2	19.44	1285.3	12.01	1259.4	33.31	-1.47	YES
B3-23	0.06818	0.00147	0.52231	0.01697	0.05572	0.00198	425.2	8.89	426.7	11.32	441.1	77.38	0.35	YES
B3-24	0.04974	0.00105	0.34765	0.01129	0.05083	0.0018	313	6.47	303	8.5	233.2	79.56	-3.30	YES
B3-25	0.07414	0.00139	0.54271	0.01353	0.05324	0.00143	461.1	8.35	440.2	8.91	338.9	59.62	-4.75	YES
B3-26	0.04825	0.0012	0.33597	0.0141	0.05064	0.00233	303.8	7.36	294.1	10.72	224.6	102.83	-3.30	YES
B3-27	0.00822	0.00049	0.05175	0.00835	0.04581	0.00784	52.8	3.15	51.2	8.06	0.1	356.18	-3.12	YES
B3-28	0.04812	0.00105	0.33147	0.01134	0.05009	0.00186	303	6.43	290.7	8.65	199.1	83.88	-4.23	YES
B3-29	0.05014	0.00115	0.34248	0.01296	0.04967	0.00204	315.4	7.07	299.1	9.8	179.4	92.9	-5.45	YES
B3-30	0.05041	0.00109	0.35126	0.01188	0.05065	0.00184	317.1	6.7	305.7	8.93	224.9	82.05	-3.73	YES
B3-31	0.05151	0.00131	0.3505	0.01564	0.04946	0.00239	323.8	8.01	305.1	11.76	169.6	109.08	-6.13	YES
B3-32	0.05145	0.0015	0.37194	0.01973	0.05253	0.00304	323.4	9.21	321.1	14.6	308.6	126.49	-0.72	YES
B3-33	0.04789	0.00097	0.34854	0.01012	0.05288	0.00163	301.5	5.98	303.6	7.62	323.8	68.67	0.69	YES
B3-34	0.04943	0.00136	0.37123	0.01771	0.05455	0.00284	311	8.36	320.6	13.11	393.9	112.41	2.99	YES
B3-35	0.08483	0.00251	0.91511	0.0415	0.07834	0.00399	524.9	14.91	659.8	22	1155.6	97.78	20.45	NO
B3-36	0.02443	0.00043	0.24697	0.00496	0.0734	0.00147	155.6	2.72	224.1	4.04	1025.1	39.88	30.57	NO
B3-37	0.04844	0.00103	0.37388	0.01162	0.05603	0.00185	304.9	6.35	322.5	8.59	453.3	71.8	5.46	YES
B3-39	0.07485	0.00156	0.56056	0.01683	0.05435	0.00172	465.3	9.36	451.9	10.95	385.5	69.22	-2.97	YES
B3-38	0.10403	0.00188	0.81778	0.01746	0.05703	0.0012	638	10.97	606.8	9.75	492.1	45.7	-5.14	YES

	Isotope ratios						Estimated ages (Ma)							
Grain	$^{206}Pb/^{238}U$	1 σ	$^{207}Pb/^{235}U$	1 σ	$^{207}Pb/^{206}Pb$	1 σ	$^{206}Pb/^{238}U$	1σ	$^{207}Pb/^{235}U$	1σ	$^{207}Pb/^{206}Pb$	1σ	Discordant%	Use raw age?
B3-40	0.62543	0.01184	24.18173	0.5393	0.28022	0.00616	3131.5	46.95	3275.7	21.75	3364.2	33.9	4.40	YES
B3-41	0.20287	0.00389	2.30132	0.05499	0.08218	0.00195	1190.7	20.84	1212.7	16.91	1249.9	45.6	1.81	YES
B3-42	0.05083	0.00127	0.37504	0.01548	0.05344	0.00235	319.6	7.8	323.4	11.43	347.3	96.35	1.18	YES
B3-43	0.01534	0.00079	0.11056	0.01216	0.05218	0.00625	98.1	5.03	106.5	11.12	293.1	252.74	7.89	YES
B3-44	0.05208	0.00135	0.37184	0.0166	0.05166	0.00245	327.3	8.27	321	12.28	270.6	105.1	-1.96	YES
B3-45	0.07837	0.00165	0.79317	0.02271	0.07319	0.00213	486.4	9.84	593	12.86	1019.3	57.7	17.98	NO
B3-46	0.47792	0.00928	10.95388	0.27058	0.16568	0.00392	2518.2	40.46	2519.2	22.98	2514.5	39.19	0.04	YES
B3-47	0.0508	0.00109	0.37109	0.01169	0.05278	0.00168	319.4	6.68	320.5	8.66	319.4	70.73	0.34	YES
B3-48	0.04946	0.00111	0.35139	0.01227	0.0513	0.00183	311.2	6.85	305.8	9.22	254.4	79.99	-1.77	YES
B3-49	0.13857	0.00292	1.38577	0.04046	0.07217	0.00208	836.6	16.54	882.9	17.22	990.8	57.49	5.24	YES
B3-50	0.05038	0.00127	0.37892	0.01587	0.05424	0.00237	316.9	7.77	326.2	11.68	381.1	94.57	2.85	YES
B3-51	0.0406	0.00091	0.32543	0.011	0.05777	0.00196	256.6	5.65	286.1	8.43	520.9	73.06	10.31	YES
B2	0.0034	0.00004	0.03179	0.00119	0.06698	0.00256	21.9	0.27	31.8	1.17	837.3	77.77	31.13	NO
B1	0.20956	0.0018	2.53824	0.02738	0.08536	0.00096	1226.4	9.59	1283.1	7.86	1323.6	21.78	4.42	YES
B3	0.2279	0.00205	2.60272	0.04961	0.08832	0.00122	1323.5	10.77	1301.4	13.98	1389.5	26.24	-1.70	YES
B4	0.07232	0.00064	0.58357	0.00768	0.05708	0.00074	450.1	3.83	466.8	4.92	494.1	28.65	3.58	YES
B5	0.35613	0.00315	7.32219	0.10662	0.15749	0.00186	1963.8	14.98	2151.5	13.01	2428.9	19.87	8.72	YES
B6	0.00995	0.0001	0.06717	0.00154	0.04793	0.0011	63.8	0.62	66	1.46	94.9	54.66	3.33	YES
B7	0.0773	0.00074	0.70851	0.01487	0.06979	0.00124	480	4.42	543.9	8.84	922.1	36.23	11.75	NO
B8	0.02959	0.00043	0.22169	0.0126	0.05773	0.00305	188	2.68	203.3	10.47	519.3	112.03	7.53	YES
B9	0.07127	0.00078	0.51705	0.01813	0.0565	0.00165	443.8	4.72	423.2	12.13	471.2	63.68	-4.87	YES
B10	0.08814	0.00086	0.74883	0.01674	0.06583	0.00123	544.5	5.09	567.5	9.72	800.9	38.51	4.05	YES
Ainsa system														
AINSA1	0.05481	0.00135	0.41576	0.02368	0.05494	0.00312	344	8.26	353	16.99	409.9	121.9	2.55	YES
AINSA2	0.49951	0.01065	11.3863	0.49544	0.16499	0.00672	2611.7	45.77	2555.3	40.61	2507.4	66.89	-2.21	YES
AINSA3	0.35958	0.00786	5.38004	0.2463	0.1082	0.00462	1980.2	37.27	1881.7	39.2	1769.3	76.02	-5.23	YES
AINSA4	0.05117	0.00147	0.36946	0.0261	0.05217	0.00368	321.7	9.02	319.3	19.35	292.8	153.35	-0.75	YES
AINSA5	0.04792	0.00154	0.34377	0.02816	0.05178	0.00428	301.7	9.48	300	21.28	275.8	178.58	-0.57	YES
AINSA6	0.04909	0.00172	0.35554	0.03193	0.05222	0.00475	308.9	10.57	308.9	23.91	294.8	194.65	0.00	YES
AINSA7	0.05724	0.00182	0.42176	0.03345	0.05306	0.00417	358.8	11.07	357.3	23.89	331.3	168.74	-0.42	YES
AINSA8	0.04962	0.00176	0.36057	0.03313	0.05226	0.00481	312.2	10.82	312.6	24.72	297	196.94	0.13	YES
AINSA9	0.04863	0.00139	0.35696	0.02525	0.05272	0.00354	306.1	8.57	309.9	18.89	316.9	145.23	1.23	YES
AINSA10	0.05138	0.00163	0.37579	0.03017	0.05245	0.00406	323	10.01	323.9	22.27	305.2	166.8	0.28	YES
AINSA11	0.05102	0.00228	0.36982	0.04401	0.0519	0.00625	320.8	13.96	319.5	32.62	281	253.84	-0.41	YES

	Isotope ratios						Estimated ages (Ma)							
Grain	$^{206}Pb/^{238}U$	1 σ	$^{207}Pb/^{235}U$	1 σ	$^{207}Pb/^{206}Pb$	1 σ	$^{206}Pb/^{238}U$	1σ	$^{207}Pb/^{235}U$	1σ	$^{207}Pb/^{206}Pb$	1σ	Discordant%	Use raw age?
AINSA12	0.05258	0.00155	0.38073	0.02817	0.05176	0.00351	330.3	9.5	327.6	20.71	274.9	148.34	-0.82	YES
AINSA13	0.08142	0.00334	0.64589	0.06815	0.0566	0.00589	504.6	19.89	505.9	42.05	475.3	215.62	0.26	YES
AINSA14	0.05432	0.00169	0.39302	0.03113	0.05153	0.0037	341	10.31	336.6	22.69	264.4	156.63	-1.31	YES
AINSA15	0.04729	0.00183	0.33192	0.03455	0.04988	0.00499	297.9	11.27	291	26.34	189.4	217.54	-2.37	YES
AINSA16	0.10073	0.00321	0.78281	0.06375	0.05511	0.00394	618.7	18.81	587.1	36.31	416.5	152.54	-5.38	YES
AINSA17	0.15845	0.00538	1.75738	0.14666	0.07847	0.00572	948.1	29.93	1029.9	54.01	1158.8	138.1	7.94	YES
AINSA18	0.05033	0.00211	0.36517	0.04169	0.05121	0.00555	316.5	12.97	316.1	31.01	250.3	231.17	-0.13	YES
AINSA19	0.05731	0.00219	0.42273	0.04345	0.05192	0.00484	359.2	13.37	358	31.01	281.9	199.72	-0.34	YES
AINSA20	0.05672	0.00239	0.4458	0.05052	0.05517	0.00577	355.6	14.57	374.3	35.48	419.1	218.3	5.00	YES
AINSA21	0.05758	0.00138	0.41893	0.01746	0.05279	0.0024	360.9	8.44	355.3	12.49	319.8	100	-1.58	YES
AINSA22	0.04792	0.00079	0.34642	0.0064	0.05246	0.00102	301.7	4.84	302	4.83	305.5	43.46	0.10	YES
AINSA23	0.05455	0.0009	0.39236	0.00743	0.05219	0.00104	342.4	5.53	336.1	5.42	293.9	44.74	-1.87	YES
AINSA24	0.05326	0.00162	0.38118	0.02217	0.05193	0.0033	334.5	9.93	327.9	16.3	282.3	139.23	-2.01	YES
AINSA25	0.0558	0.00109	0.39954	0.0118	0.05196	0.00165	350	6.68	341.3	8.56	283.7	71.11	-2.55	YES
AINSA26	0.05386	0.00089	0.39545	0.00746	0.05328	0.00105	338.2	5.46	338.3	5.43	340.7	44.09	0.03	YES
AINSA27	0.05459	0.00105	0.40481	0.01123	0.05381	0.00161	342.7	6.41	345.1	8.11	362.9	65.92	0.70	YES
AINSA28	0.09764	0.0017	0.79258	0.01653	0.05891	0.00131	600.6	10.01	592.6	9.36	563.6	47.71	-1.35	YES
AINSA29	0.05407	0.00099	0.37765	0.00966	0.05069	0.00139	339.5	6.07	325.3	7.12	226.6	61.96	-4.37	YES
AINSA40	0.05182	0.00123	0.37146	0.01518	0.05202	0.00232	325.7	7.57	320.7	11.24	286.4	98.62	-1.56	YES
AINSA41	0.08923	0.00151	0.68972	0.01326	0.0561	0.00113	551	8.92	532.6	7.97	456	44.05	-3.45	YES
AINSA42	0.08325	0.00219	0.70417	0.03089	0.06139	0.00297	515.5	13.01	541.3	18.41	653	100.63	4.77	YES
AINSA43	0.05568	0.00097	0.42729	0.00901	0.0557	0.00124	349.3	5.91	361.2	6.41	440.2	48.61	3.29	YES
AINSA44	0.05349	0.00097	0.37477	0.00927	0.05085	0.00133	335.9	5.91	323.2	6.85	234.2	59.47	-3.93	YES
AINSA45	0.05579	0.00096	0.40809	0.00854	0.0531	0.00117	349.9	5.89	347.5	6.16	333	49.18	-0.69	YES
AINSA46	0.05685	0.00102	0.40909	0.00961	0.05223	0.0013	356.4	6.22	348.2	6.92	295.6	55.89	-2.35	YES
AINSA47	0.0545	0.00088	0.40159	0.00659	0.05348	0.0009	342.1	5.41	342.8	4.77	349.3	37.61	0.20	YES
AINSA48	0.03849	0.00159	0.26604	0.03365	0.05017	0.00662	243.5	9.9	239.5	26.99	202.9	279.99	-1.67	YES
AINSA49	0.05522	0.00134	0.41732	0.01716	0.05486	0.00246	346.5	8.17	354.1	12.29	406.4	96.96	2.15	YES
AINSA30	0.05642	0.00111	0.40445	0.01198	0.05204	0.00165	353.8	6.79	344.9	8.66	287.3	70.86	-2.58	YES
AINSA31	0.05518	0.00096	0.41002	0.00847	0.05395	0.00117	346.3	5.86	348.9	6.1	368.7	48.24	0.75	YES
AINSA32	0.0547	0.00098	0.40239	0.00916	0.05341	0.00129	343.3	5.99	343.4	6.63	346.1	54.01	0.03	YES
AINSA33	0.08449	0.0014	0.64399	0.01103	0.05534	0.00098	522.8	8.33	504.8	6.81	425.9	38.31	-3.57	YES
AINSA34	0.1186	0.00191	1.02885	0.01484	0.06299	0.00091	722.5	11.01	718.4	7.43	707.8	30.5	-0.57	YES
AINSA35	0.05462	0.00098	0.40535	0.00909	0.05388	0.00128	342.9	5.99	345.5	6.57	365.9	52.66	0.75	YES

	Isotope ratios						Estimated ages (Ma)							
Grain	$^{206}Pb/^{238}U$	1 σ	$^{207}Pb/^{235}U$	1 σ	$^{207}Pb/^{206}Pb$	1 σ	$^{206}Pb/^{238}U$	1σ	$^{207}Pb/^{235}U$	1σ	$^{207}Pb/^{206}Pb$	1σ	Discordant%	Use raw age?
AINSA36	0.11172	0.00244	0.99023	0.03275	0.06436	0.00232	682.7	14.18	698.8	16.71	753.4	74.25	2.30	YES
AINSA37	0.05329	0.00112	0.39087	0.01276	0.05326	0.00188	334.7	6.86	335	9.32	339.9	77.81	0.09	YES
AINSA38	0.15577	0.00251	1.39894	0.01981	0.06521	0.00092	933.2	14.02	888.5	8.38	781.2	29.36	-5.03	YES
AINSA39	0.05182	0.00152	0.36724	0.0205	0.05146	0.00313	325.7	9.34	317.6	15.22	261.6	133.93	-2.55	YES
AINSA50	0.05704	0.00112	0.40745	0.01159	0.05188	0.00158	357.6	6.81	347	8.36	280	68.04	-3.05	YES
AINSA51	0.3319	0.00612	4.59637	0.08398	0.10058	0.00198	1847.6	29.6	1748.6	15.24	1634.7	36.18	-5.66	YES
AINSA52	0.13131	0.0021	1.16759	0.01559	0.06458	0.00084	795.3	11.99	785.5	7.3	760.6	27.13	-1.25	YES
AINSA53	0.05808	0.00103	0.40884	0.00908	0.05112	0.00119	364	6.3	348	6.55	246.4	52.75	-4.60	YES
AINSA54	0.37444	0.00606	5.60712	0.07028	0.10876	0.00132	2050.3	28.42	1917.2	10.8	1778.7	21.98	-6.94	YES
AINSA55	0.05591	0.00105	0.40238	0.01024	0.05227	0.00141	350.7	6.39	343.4	7.41	297.4	60.21	-2.13	YES
AINSA56	0.05783	0.0013	0.41855	0.01536	0.05257	0.00208	362.4	7.91	355	11	310.3	87.85	-2.08	YES
AINSA57	0.05589	0.00104	0.41521	0.01022	0.05397	0.00141	350.6	6.37	352.6	7.33	369.5	57.61	0.57	YES
AINSA58	0.05648	0.00105	0.42764	0.01021	0.055	0.00139	354.2	6.39	361.5	7.26	412.2	54.85	2.02	YES
AINSA59	0.05389	0.00139	0.3803	0.01752	0.05126	0.00256	338.4	8.48	327.3	12.89	252.5	110.94	-3.39	YES
AINSA60	0.0568	0.001	0.42249	0.00855	0.05404	0.00114	356.1	6.1	357.8	6.1	372.4	46.64	0.48	YES
AINSA61	0.05696	0.00102	0.41101	0.0088	0.05243	0.00117	357.1	6.22	349.6	6.33	304	50.07	-2.15	YES
AINSA62	0.17896	0.00311	1.75086	0.03022	0.07108	0.00126	1061.3	16.99	1027.5	11.15	959.8	35.92	-3.29	YES
AINSA63	0.05563	0.00133	0.41057	0.01638	0.05362	0.00232	349	8.13	349.3	11.79	355	94.69	0.09	YES
AINSA64	0.10181	0.002	0.80926	0.02189	0.05775	0.00166	625	11.71	602	12.28	520.1	62.24	-3.82	YES
AINSA65	0.05721	0.001	0.4165	0.00809	0.0529	0.00106	358.6	6.09	353.5	5.8	324.5	44.66	-1.44	YES
A1	0.04826	0.00049	0.33074	0.00774	0.05213	0.00111	303.9	2.98	290.1	5.91	291.2	47.86	-4.76	YES
A2	0.04927	0.00055	0.34335	0.01183	0.05224	0.0016	310.1	3.38	299.7	8.94	296	68.48	-3.47	YES
A3	0.04453	0.00145	0.32544	0.04928	0.05773	0.00768	280.8	8.98	286.1	37.76	519.3	268.13	1.85	YES
A4	0.04958	0.00051	0.34323	0.00858	0.05421	0.00122	312	3.16	299.6	6.48	379.8	49.73	-4.14	YES
A5	0.04974	0.00051	0.34372	0.0077	0.05287	0.00107	312.9	3.11	300	5.82	323.4	45.36	-4.30	YES
A6	0.04961	0.00053	0.33044	0.00935	0.05124	0.0013	312.1	3.27	289.9	7.14	251.7	57.36	-7.66	YES
A7	0.05054	0.00054	0.32469	0.00861	0.05081	0.00121	317.8	3.29	285.5	6.6	232.1	54.19	-11.31	NO
A8	0.05316	0.00055	0.36221	0.00801	0.05282	0.00105	333.9	3.35	313.9	5.97	320.9	44.42	-6.37	YES
A9	0.05141	0.00056	0.35942	0.0099	0.05378	0.00132	323.2	3.42	311.8	7.39	361.7	54.25	-3.66	YES
A10	0.05241	0.00057	0.34854	0.00952	0.05234	0.00127	329.3	3.49	303.6	7.17	300.1	54.42	-8.47	YES
A11	0.05319	0.00058	0.35453	0.00973	0.05225	0.00127	334.1	3.56	308.1	7.29	296.5	54.42	-8.44	YES
A12	0.05189	0.00054	0.3662	0.0073	0.05533	0.00099	326.1	3.3	316.8	5.42	425.5	38.84	-2.94	YES
A13	0.0532	0.00057	0.37093	0.00856	0.0547	0.00112	334.1	3.48	320.3	6.34	400.1	44.59	-4.31	YES
A14	0.05441	0.0006	0.37811	0.01036	0.05379	0.00129	341.5	3.69	325.6	7.63	362.1	53.42	-4.88	YES

	Isotope ratios						Estimated ages (Ma)							
Grain	$^{206}Pb/^{238}U$	1 σ	$^{207}Pb/^{235}U$	1 σ	$^{207}Pb/^{206}Pb$	1 σ	$^{206}Pb/^{238}U$	1σ	$^{207}Pb/^{235}U$	1σ	$^{207}Pb/^{206}Pb$	1σ	Discordant%	Use raw age?
A15	0.05336	0.00058	0.36025	0.00833	0.05372	0.0011	335.1	3.52	312.4	6.22	359.4	45.6	-7.27	YES
Morillo system														
MO1	0.13474	0.00414	0.96254	0.05253	0.05171	0.00305	814.9	23.55	684.6	27.18	272.6	129.81	-19.03	NO
MO2	0.05436	0.00165	0.4045	0.02058	0.05388	0.003	341.2	10.06	344.9	14.88	365.7	120.46	1.07	YES
MO3	0.05944	0.00138	0.44677	0.01412	0.05442	0.00186	372.2	8.42	375	9.91	388.5	74.05	0.75	YES
MO4	0.0507	0.00107	0.37504	0.00906	0.05356	0.00137	318.8	6.56	323.4	6.69	352.6	56.88	1.42	YES
MO5	0.09155	0.00191	0.72409	0.0163	0.05729	0.00136	564.7	11.26	553.1	9.6	502	51.87	-2.10	YES
MO6	0.08436	0.00172	0.71555	0.01451	0.06144	0.0013	522.1	10.21	548	8.59	654.6	44.85	4.73	YES
MO7	0.03891	0.00089	0.31315	0.00904	0.0583	0.00182	246.1	5.5	276.6	6.99	540.5	67.48	11.03	NO
MO8	0.05646	0.0012	0.42278	0.01035	0.05425	0.00141	354	7.33	358	7.38	381.5	57.08	1.12	YES
MO9	0.10501	0.00238	0.89721	0.02452	0.06191	0.00182	643.7	13.86	650.2	13.12	671	61.74	1.00	YES
MO10	0.07889	0.00165	0.61664	0.01393	0.05665	0.00134	489.5	9.87	487.7	8.75	477.4	51.88	-0.37	YES
MO11	0.07092	0.00178	0.65585	0.02175	0.06704	0.00244	441.7	10.7	512.1	13.34	838.9	74.04	13.75	NO
MO12	0.10617	0.00265	0.94195	0.03127	0.06432	0.00233	650.5	15.47	673.9	16.35	752.2	74.73	3.47	YES
MO13	0.04299	0.00085	0.31215	0.0055	0.05264	0.00093	271.4	5.23	275.8	4.26	313.5	39.66	1.60	YES
MO14	0.0954	0.00199	0.78251	0.01693	0.05948	0.00134	587.4	11.72	586.9	9.65	584.6	48.27	-0.09	YES
MO15	0.04828	0.00112	0.33885	0.01071	0.05089	0.00172	304	6.9	296.3	8.13	236	76.17	-2.60	YES
MO16	0.09205	0.00204	0.78331	0.02009	0.06172	0.00169	567.7	12.05	587.4	11.44	664.3	57.49	3.35	YES
MO17	0.04772	0.00115	0.34834	0.01166	0.05295	0.00191	300.5	7.08	303.5	8.78	326.7	79.83	0.99	YES
MO18	0.04739	0.0013	0.34511	0.01509	0.05283	0.0025	298.5	7.99	301	11.39	321.3	104.13	0.83	YES
MO19	0.04833	0.00105	0.33542	0.00871	0.05035	0.00137	304.2	6.45	293.7	6.62	211.3	62.07	-3.58	YES
MO21	0.18245	0.00387	1.87568	0.03917	0.0746	0.00161	1080.4	21.08	1072.5	13.83	1057.5	43.26	-0.74	YES
MO22	0.39239	0.01045	6.75103	0.18799	0.12486	0.00387	2133.9	48.4	2079.3	24.63	2026.9	53.93	-2.63	YES
MO23	0.04866	0.00144	0.34788	0.01738	0.05189	0.00281	306.3	8.86	303.1	13.09	280.5	119.59	-1.06	YES
MO24	0.50287	0.00988	12.79722	0.19069	0.18471	0.00258	2626.1	42.38	2664.8	14.03	2695.6	22.87	1.45	YES
MO25	0.04837	0.00126	0.34724	0.01395	0.05211	0.00225	304.5	7.77	302.6	10.52	290.4	95.82	-0.63	YES
MO26	0.04631	0.00128	0.33853	0.01538	0.05306	0.0026	291.8	7.87	296.1	11.67	331.4	107.04	1.45	YES
MO27	0.07866	0.0022	0.61781	0.0265	0.05702	0.00266	488.1	13.16	488.5	16.63	491.6	100.25	0.08	YES
MO28	0.05094	0.00133	0.36554	0.01431	0.0521	0.0022	320.3	8.14	316.3	10.64	289.8	93.44	-1.26	YES
MO29	0.04966	0.00125	0.33742	0.01257	0.04933	0.00196	312.4	7.65	295.2	9.54	163.6	90.46	-5.83	YES
MO30	0.13744	0.00302	1.39395	0.03181	0.07365	0.00175	830.2	17.12	886.4	13.49	1031.8	47.24	6.34	YES
MO31	0.04802	0.0013	0.40993	0.01601	0.06199	0.00264	302.3	8.01	348.8	11.53	673.9	88.53	13.33	NO
MO32	0.17145	0.00367	2.48528	0.04905	0.10526	0.00212	1020.1	20.2	1267.8	14.29	1718.9	36.53	19.54	NO
MO33D	0.10261	0.00259	0.85186	0.029	0.06029	0.0022	629.7	15.13	625.7	15.9	614	77	-0.64	YES

	Isotope ratios						Estimated ages (Ma)							
Grain	$^{206}Pb/^{238}U$	1 σ	$^{207}Pb/^{235}U$	1 σ	$^{207}Pb/^{206}Pb$	1 σ	$^{206}Pb/^{238}U$	1σ	$^{207}Pb/^{235}U$	1σ	$^{207}Pb/^{206}Pb$	1σ	Discordant%	Use raw age?
MO34	0.0474	0.00111	0.36339	0.0109	0.05567	0.00176	298.6	6.85	314.7	8.12	439	68.9	5.12	YES
MO35	0.05013	0.00124	0.36567	0.01267	0.05297	0.00195	315.3	7.61	316.4	9.42	327.4	81.57	0.35	YES
MO36	0.04663	0.00181	0.3322	0.02421	0.05174	0.00412	293.8	11.17	291.2	18.45	273.9	172.37	-0.89	YES
MO37	0.05149	0.00137	0.41247	0.01614	0.05818	0.00245	323.7	8.42	350.7	11.6	535.9	90.3	7.70	YES
MO38	0.04001	0.00092	0.30505	0.00867	0.05537	0.00165	252.9	5.73	270.3	6.75	426.8	64.7	6.44	YES
MO39	0.04539	0.00199	0.35416	0.02871	0.05667	0.00506	286.2	12.29	307.8	21.52	477.9	186.79	7.02	YES
MO40	0.04819	0.00139	0.35272	0.0163	0.05316	0.00265	303.4	8.52	306.8	12.24	335.6	108.82	1.11	YES
MO41	0.38679	0.00918	7.19492	0.1703	0.1351	0.00334	2107.9	42.68	2135.9	21.1	2165.3	42.49	1.31	YES
MO42	0.08417	0.00339	0.67139	0.0489	0.05793	0.00462	521	20.16	521.6	29.71	526.7	166.15	0.12	YES
MO43	0.04988	0.00129	0.35355	0.01349	0.05148	0.00209	313.8	7.93	307.4	10.12	262.2	90.37	-2.08	YES
MO44	0.03777	0.00089	0.31776	0.00907	0.06109	0.00182	239	5.52	280.2	6.99	642.4	62.74	14.70	NO
MO45	0.05124	0.00143	0.41338	0.01736	0.05858	0.00265	322.2	8.74	351.3	12.47	551.6	95.64	8.28	YES
MO46	0.05149	0.00125	0.35507	0.01164	0.05007	0.00171	323.7	7.66	308.5	8.72	198.4	77.57	-4.93	YES
MO47	0.05003	0.00145	0.38072	0.01815	0.05526	0.00282	314.7	8.92	327.6	13.35	422.6	109.83	3.94	YES
MO48	0.08128	0.00189	0.63941	0.01784	0.05712	0.00163	503.8	11.27	501.9	11.05	495.7	62.39	-0.38	YES
MO49	0.32905	0.00725	5.10467	0.1114	0.11264	0.0024	1833.8	35.18	1836.9	18.53	1842.5	38.12	0.17	YES
MO50	0.05104	0.00123	0.36862	0.01145	0.05244	0.00168	320.9	7.52	318.6	8.5	304.5	71.26	-0.72	YES
MO51	0.04803	0.00143	0.34827	0.01708	0.05264	0.00277	302.4	8.82	303.4	12.86	313.1	115.12	0.33	YES
MO52	0.04953	0.00208	0.37476	0.02998	0.05492	0.00478	311.7	12.81	323.2	22.14	409	184.27	3.56	YES
MO53	0.05014	0.00167	0.36589	0.02134	0.05297	0.00333	315.4	10.27	316.6	15.87	327.3	136.11	0.38	YES
MO54	0.05065	0.00117	0.37665	0.01031	0.05397	0.00148	318.5	7.19	324.6	7.61	369.7	60.52	1.88	YES
MO55	0.04032	0.001	0.33617	0.01078	0.06051	0.00201	254.8	6.19	294.3	8.19	621.8	70.03	13.42	NO
MO56	0.05284	0.00135	0.38347	0.01381	0.05267	0.00197	331.9	8.28	329.6	10.14	314.6	83.11	-0.70	YES
MO57	0.0526	0.00144	0.39163	0.0161	0.05403	0.00234	330.5	8.82	335.6	11.74	372	94.19	1.52	YES
MO58	0.05074	0.00144	0.3529	0.01608	0.05046	0.00243	319.1	8.86	306.9	12.07	216.3	107.81	-3.98	YES
MO59	0.05264	0.00197	0.36783	0.0256	0.0507	0.00381	330.7	12.06	318	19.01	227.1	164.88	-3.99	YES
MO60	0.12692	0.00353	1.19598	0.04651	0.06835	0.0028	770.3	20.22	798.7	21.5	879.2	82.63	3.56	YES
MO61	0.053	0.00135	0.39324	0.0139	0.05381	0.00195	332.9	8.29	336.7	10.13	362.9	79.6	1.13	YES
MO62	0.05621	0.00154	0.41936	0.01733	0.0541	0.00234	352.5	9.42	355.6	12.4	375.1	93.72	0.87	YES
MO63	0.05268	0.00161	0.38431	0.01932	0.0529	0.00282	330.9	9.85	330.2	14.17	324.4	116.51	-0.21	YES
MO64	0.08668	0.00254	0.79983	0.0344	0.06689	0.00305	535.9	15.06	596.7	19.41	834.5	92.29	10.19	YES
MO65	0.05224	0.00166	0.39101	0.02093	0.05426	0.00309	328.2	10.2	335.1	15.27	381.7	122.96	2.06	YES
MO66	0.04961	0.00118	0.40118	0.01625	0.05861	0.00259	312.1	7.22	342.5	11.78	552.6	93.53	8.88	YES
MO67	0.05828	0.00142	0.45047	0.01927	0.05602	0.00261	365.1	8.63	377.6	13.49	452.8	100.48	3.31	YES

	Isotope ratios						Estimated ages (Ma)							
Grain	$^{206}Pb/^{238}U$	1 σ	$^{207}Pb/^{235}U$	1 σ	$^{207}Pb/^{206}Pb$	1 σ	$^{206}Pb/^{238}U$	1σ	$^{207}Pb/^{235}U$	1σ	$^{207}Pb/^{206}Pb$	1σ	Discordant%	Use raw age?
MO68	0.04861	0.0012	0.3422	0.01649	0.05102	0.00264	306	7.39	298.8	12.48	241.9	115.09	-2.41	YES
MO69	0.04883	0.0011	0.34218	0.01377	0.05079	0.0022	307.3	6.76	298.8	10.42	231.2	97.14	-2.84	YES
MO70	0.33618	0.00728	5.04523	0.13846	0.10878	0.00335	1868.3	35.12	1826.9	23.26	1779	55.24	-2.27	YES
MO71	0.0483	0.0013	0.35358	0.01802	0.05306	0.00294	304.1	7.97	307.4	13.52	331.5	120.75	1.07	YES
MO72	0.10337	0.0022	0.89388	0.02906	0.06268	0.00223	634.1	12.85	648.5	15.58	697.4	74.19	2.22	YES
MO73	0.22555	0.00454	4.07115	0.10399	0.13085	0.00375	1311.1	23.89	1648.5	20.82	2109.4	49.38	20.47	NO
MO74	0.15817	0.00776	1.52894	0.17446	0.07008	0.00858	946.6	43.21	942.1	70.05	930.6	233.02	-0.48	YES
MO75	0.10255	0.00226	0.90053	0.03118	0.06367	0.00244	629.3	13.2	652	16.66	730.7	79.19	3.48	YES
MO76	0.04921	0.00151	0.42977	0.02615	0.06333	0.00421	309.7	9.29	363	18.57	719.2	135.29	14.68	NO
MO77	0.10671	0.00326	0.79359	0.05025	0.05393	0.0037	653.6	18.98	593.2	28.45	367.9	147.49	-10.18	YES
MO78	0.04923	0.00141	0.36066	0.02049	0.05313	0.0033	309.8	8.67	312.7	15.29	334.3	134.14	0.93	YES
MO79	0.0949	0.00221	0.88243	0.03384	0.06743	0.00288	584.5	13.02	642.3	18.26	851.1	86.4	9.00	YES
MO80	0.04978	0.00163	0.36504	0.02441	0.05318	0.00389	313.2	10.01	316	18.16	336.6	157.23	0.89	YES
MO81	0.05574	0.00162	0.55353	0.02875	0.07202	0.00418	349.7	9.91	447.3	18.79	986.6	113.84	21.82	NO
MO82	0.15825	0.00385	1.87614	0.07299	0.086	0.00378	947	21.4	1072.7	25.77	1338	82.73	11.72	NO
MO83	0.13344	0.00309	1.2699	0.04906	0.06904	0.003	807.4	17.6	832.3	21.95	899.8	87.35	2.99	YES
MO84	0.16347	0.00366	2.37749	0.08539	0.10551	0.0043	976	20.28	1235.9	25.67	1723.3	72.93	21.03	NO
MO85	0.04704	0.00131	0.38233	0.01992	0.05897	0.00342	296.3	8.09	328.7	14.63	565.9	121.61	9.86	YES
M01	0.06295	0.00242	1.1171	0.16999	0.12699	0.0136	393.5	14.7	761.6	81.53	2056.7	177.77	48.33	NO
M02	0.39548	0.00422	6.30305	0.24143	0.12443	0.00227	2148.2	19.52	2018.9	33.57	2020.6	32.04	-6.40	YES
M03	0.10387	0.00113	0.82884	0.02731	0.05944	0.00152	637.1	6.58	613	15.16	583.1	54.48	-3.93	YES
M04	0.058	0.00064	0.38961	0.01246	0.05242	0.00146	363.4	3.87	334.1	9.1	303.6	62.01	-8.77	YES
M05	0.11825	0.00164	0.96381	0.05504	0.06419	0.00265	720.5	9.48	685.3	28.46	747.9	84.81	-5.14	YES
M06	0.05027	0.00053	0.37131	0.01038	0.05353	0.00131	316.2	3.28	320.6	7.69	351.1	54.61	1.37	YES
M07	0.05381	0.00072	0.34957	0.0177	0.04996	0.00221	337.9	4.38	304.4	13.32	193.2	99.65	-11.01	NO
M08	0.0549	0.00071	0.40369	0.01894	0.05482	0.0022	344.5	4.36	344.3	13.7	404.8	86.93	-0.06	YES
M09	0.0499	0.00069	0.3591	0.01872	0.05396	0.00245	313.9	4.24	311.5	13.99	369.3	98.39	-0.77	YES
Guaso system														
GU1	1.00276	0.00915	16.91179	0.68775	0.12201	0.00168	4477.2	29.45	2929.8	38.99	1985.8	24.31	-52.82	NO
GU2	0.84279	0.00694	20.19392	0.31513	0.17967	0.00199	3940.6	24.29	3100.7	15.1	2649.8	18.27	-27.09	NO
GU3	0.06309	0.00054	0.44156	0.00743	0.05193	0.00082	394.4	3.28	371.3	5.23	282.4	35.76	-6.22	YES
GU4	0.45157	0.00393	7.38384	0.17437	0.12863	0.00167	2402.2	17.47	2159	21.12	2079.4	22.61	-11.26	NO
GU5	0.05305	0.00045	0.38774	0.00547	0.05275	0.00074	333.2	2.75	332.7	4	317.8	31.53	-0.15	YES
GU6	0.12407	0.00104	1.09706	0.01233	0.06563	0.00076	753.9	5.94	751.9	5.97	794.6	24.26	-0.27	YES

	Isotope ratios						Estimated ages (Ma)							
Grain	$^{206}Pb/^{238}U$	1 σ	$^{207}Pb/^{235}U$	1 σ	$^{207}Pb/^{206}Pb$	1 σ	$^{206}Pb/^{238}U$	1σ	$^{207}Pb/^{235}U$	1σ	$^{207}Pb/^{206}Pb$	1σ	Discordant%	Use raw age?
GU7	0.14491	0.00123	1.37031	0.01838	0.07092	0.00088	872.4	6.92	876.3	7.87	955.1	25.24	0.45	YES
GU8	0.33513	0.00305	5.1762	0.13585	0.1188	0.00172	1863.2	14.74	1848.7	22.33	1938.2	25.65	-0.78	YES
GU9	0.05053	0.00045	0.35565	0.00606	0.05282	0.00086	317.8	2.74	309	4.54	321	36.41	-2.85	YES
GU10	0.17801	0.00153	1.72644	0.02385	0.07337	0.00091	1056.1	8.38	1018.4	8.88	1024.1	25.02	-3.70	YES
GU11	0.05137	0.00049	0.37466	0.00914	0.0547	0.0012	322.9	3.03	323.1	6.75	400.1	47.99	0.06	YES
GU12	0.04959	0.00044	0.35045	0.00536	0.05328	0.00079	312	2.7	305.1	4.03	340.5	33.14	-2.26	YES
GU13	0.04943	0.00047	0.34182	0.00765	0.053	0.00109	311	2.88	298.5	5.79	328.9	45.69	-4.19	YES
GU14	0.18292	0.0018	1.72511	0.05042	0.07257	0.00143	1082.9	9.78	1017.9	18.79	1002	39.43	-6.39	YES
GU15	0.09816	0.0009	0.7666	0.01411	0.06007	0.00096	603.6	5.28	577.8	8.11	606	34.09	-4.47	YES
GU16	0.12581	0.00116	1.08532	0.02025	0.06408	0.00099	763.9	6.62	746.2	9.86	744.3	32.37	-2.37	YES
GU17	0.13709	0.00125	1.16536	0.01922	0.0655	0.00093	828.2	7.08	784.5	9.01	790.4	29.53	-5.57	YES
GU18	0.05192	0.00048	0.36856	0.00667	0.05377	0.0009	326.3	2.97	318.6	4.95	361.3	37.53	-2.42	YES
GU19	0.0514	0.00049	0.36814	0.00702	0.05368	0.00094	323.1	2.97	318.3	5.21	357.6	39.15	-1.51	YES
GU20	0.11495	0.00108	0.93068	0.01784	0.06142	0.00099	701.4	6.26	668	9.38	654.1	34.05	-5.00	YES
GU21	0.11398	0.00108	0.942	0.01743	0.06199	0.00097	695.8	6.27	673.9	9.11	673.8	33.08	-3.25	YES
GU22	0.05042	0.00049	0.35221	0.00679	0.05294	0.00093	317.1	2.99	306.4	5.1	326.3	39.18	-3.49	YES
GU23	0.10925	0.00109	0.85406	0.02015	0.05952	0.00113	668.4	6.33	626.9	11.03	586.3	40.79	-6.62	YES
GU24	0.05138	0.0005	0.35886	0.0067	0.0531	0.0009	323	3.06	311.4	5.01	333.1	37.69	-3.73	YES
GU25	0.05169	0.00051	0.36064	0.0075	0.05252	0.00098	324.9	3.14	312.7	5.6	308	41.67	-3.90	YES
GU26	0.05319	0.00053	0.36791	0.00781	0.05297	0.001	334.1	3.26	318.1	5.8	327.4	42.08	-5.03	YES
GU27	0.16841	0.00172	1.63241	0.04141	0.07362	0.00135	1003.3	9.51	982.8	15.97	1031.2	36.75	-2.09	YES
GU28	0.32796	0.00319	6.94044	0.11632	0.15258	0.00208	1828.5	15.47	2103.8	14.87	2375	23.06	13.09	NO
GU29	0.17279	0.00177	1.66734	0.04096	0.07208	0.00129	1027.5	9.74	996.2	15.59	988	36.4	-3.14	YES
GU30	0.0526	0.00054	0.38115	0.00836	0.05436	0.00104	330.5	3.3	327.9	6.15	385.8	42.2	-0.79	YES
GU31	0.35218	0.00335	5.28507	0.19864	0.1192	0.00205	1945	15.96	1866.5	32.09	1944.3	30.42	-4.21	YES
GU32	0.11774	0.0012	0.96778	0.03628	0.06218	0.00167	717.5	6.9	687.3	18.72	680.3	56.35	-4.39	YES
GU33	0.27858	0.00308	3.61108	0.18163	0.10551	0.00253	1584.2	15.54	1552	40	1723.2	43.31	-2.07	YES
GU34	0.08255	0.00144	0.74694	0.1058	0.07022	0.00847	511.3	8.59	566.4	61.5	934.8	229.44	9.73	YES
GU35	0.13444	0.0012	1.33514	0.03534	0.07583	0.00155	813.1	6.84	861.1	15.37	1090.5	40.38	5.57	YES
GU36	0.08117	0.00071	0.66113	0.01413	0.06231	0.00115	503.1	4.24	515.3	8.64	684.8	38.85	2.37	YES
GU37	0.04802	0.00042	0.35898	0.00762	0.05676	0.00113	302.4	2.6	311.5	5.7	481.6	43.62	2.92	YES
GU38	0.104	0.00098	0.84435	0.02428	0.06116	0.00135	637.8	5.72	621.5	13.37	644.7	46.72	-2.62	YES
GU39	0.04954	0.00056	0.80146	0.02593	0.12341	0.00313	311.7	3.43	597.7	14.62	2006.1	44.35	47.85	NO
GU40	0.07197	0.00062	0.5313	0.00959	0.05628	0.00093	448	3.71	432.7	6.36	462.6	36.45	-3.54	YES

	Isotope ratios						Estimated ages (Ma)							
Grain	$^{206}Pb/^{238}U$	1 σ	$^{207}Pb/^{235}U$	1 σ	$^{207}Pb/^{206}Pb$	1 σ	$^{206}Pb/^{238}U$	1σ	$^{207}Pb/^{235}U$	1σ	$^{207}Pb/^{206}Pb$	1σ	Discordant%	Use raw age?
GU41	0.38055	0.00316	6.43746	0.0987	0.12692	0.00148	2078.9	14.77	2037.4	13.48	2055.8	20.41	-2.04	YES
GU42	0.09946	0.00089	0.77845	0.01973	0.06042	0.00135	611.2	5.22	584.6	11.27	618.5	47.44	-4.55	YES
GU43	0.11883	0.001	1.02671	0.01488	0.06506	0.00086	723.8	5.76	717.3	7.46	776.3	27.64	-0.91	YES
GU44	0.21274	0.0018	4.20093	0.06251	0.15025	0.0018	1243.4	9.55	1674.2	12.2	2348.8	20.31	25.73	NO
GU45	0.09246	0.00079	0.7205	0.01144	0.06007	0.00087	570	4.67	551	6.75	606.1	31.12	-3.45	YES
GU46	0.1398	0.00134	1.29942	0.03975	0.06946	0.00155	843.5	7.56	845.5	17.55	912.4	45.36	0.24	YES
GU47	0.08266	0.00118	0.64074	0.04129	0.05774	0.00291	512	7	502.8	25.55	519.7	107.31	-1.83	YES
GU48	0.07539	0.00068	0.57236	0.01227	0.05684	0.00107	468.5	4.07	459.5	7.92	484.8	41.45	-1.96	YES
GU49	0.05384	0.00058	0.39513	0.01405	0.05536	0.0017	338	3.53	338.1	10.23	426.5	66.62	0.03	YES
GU51	0.17386	0.00278	1.8525	0.15631	0.07457	0.00362	1033.4	15.29	1064.3	55.64	1056.7	95.03	2.90	YES
GU52	0.07829	0.00069	0.58437	0.01052	0.05608	0.00092	485.9	4.15	467.3	6.74	455.1	35.57	-3.98	YES
GU53	0.10312	0.00092	0.81765	0.01529	0.06037	0.00098	632.7	5.36	606.7	8.54	616.7	34.62	-4.29	YES
GU54	0.16122	0.00143	1.54089	0.02784	0.07147	0.00104	963.6	7.93	946.9	11.13	971	29.5	-1.76	YES
GU55	0.54391	0.00532	12.48253	0.46235	0.18525	0.00273	2799.8	22.22	2641.4	34.82	2700.5	24.14	-6.00	YES
GU56	0.0487	0.00064	0.37432	0.01957	0.0547	0.00245	306.5	3.96	322.9	14.46	400.1	96.64	5.08	YES
GU57	0.05044	0.00068	0.33279	0.0178	0.05368	0.0025	317.2	4.18	291.7	13.56	357.7	101.37	-8.74	YES
GU58	0.04828	0.00064	0.32966	0.01708	0.05359	0.00243	303.9	3.93	289.3	13.05	353.6	99.13	-5.05	YES
GU59	0.05129	0.00066	0.3726	0.0185	0.05469	0.00234	322.5	4.06	321.6	13.69	400.1	92.11	-0.28	YES
GU61	0.13259	0.00202	1.09629	0.0794	0.06307	0.00313	802.6	11.47	751.6	38.46	710.6	102.02	-6.79	YES
GU62	0.08211	0.0025	0.65451	0.0987	0.06308	0.00734	508.7	14.89	511.3	60.57	711.1	229.78	0.51	YES
GU63	0.04925	0.0007	0.3736	0.02133	0.05649	0.00277	309.9	4.32	322.3	15.77	471.1	105.8	3.85	YES
GU64	0.05251	0.00082	0.35794	0.02376	0.05337	0.00306	329.9	5	310.7	17.77	344.5	124.1	-6.18	YES
GU65	0.04978	0.00064	0.34116	0.01652	0.0528	0.00223	313.2	3.91	298.1	12.51	320.3	93.33	-5.07	YES
GU66	0.05093	0.00057	0.32623	0.01229	0.04811	0.00161	320.2	3.48	286.7	9.41	104.8	77	-11.68	NO
GU67	0.10561	0.00126	0.89427	0.04064	0.06277	0.00211	647.2	7.37	648.7	21.78	700.6	69.84	0.23	YES
GU68	0.05162	0.00064	0.35408	0.01613	0.05276	0.00209	324.5	3.93	307.8	12.09	318.6	87.65	-5.43	YES
GU69	0.45058	0.00492	10.33732	0.48381	0.17164	0.00307	2397.9	21.86	2465.5	43.33	2573.7	29.61	2.74	YES
GU70	0.18461	0.0021	1.79153	0.08026	0.06952	0.00193	1092.1	11.42	1042.4	29.19	914.1	55.98	-4.77	YES

APPENDIX – II

Fission-Track age calculation

Fission-Track Age Calculation

Details			*Summary*						
Sample No.	Mo/3		**Central age**		**239.2**	**±**	**25.2**	**Ma**	
Irrad. No.	HF 49		**age dispersion**		**52.7**	**%**			
Position	0								
Date	08/08/06		**Pooled age**		249.2	±	8.3	Ma	
Analyst	AC								
			Mean age		283.8	±	21.0	Ma	
zeta (CN5)	127								
zeta error	5		**Chi squared**		388.15	with	27	df	
No. of grains	28		**P(chi-sq)**		0.00	%			
Total Ns	10496	tr							
Total Ni	1474	tr							
Total Nd	3093	tr							
rho-d (CN5)	5.620E+05	tr/cm^2							
mean rho-s	2.386E+07	tr/cm^2							
mean rho-i	3.149E+06	tr/cm^2							
mean U	218.5	ppm							

crystal	*Ng*	*Ns*	*rho-s*	*Ni*	*rho-i*	*Ns/Ni*	*U*	*age*	*error*
1	10	284	2.049E+07	37	2.670E+06	7.6757	185.3	268.26	47.13
2	10	283	2.042E+07	34	2.453E+06	8.3235	170.2	290.40	52.97
3	10	520	3.752E+07	61	4.401E+06	8.5246	305.4	297.26	40.58
4	10	358	2.583E+07	79	5.700E+06	4.5316	395.5	159.73	20.06
5	15	534	2.569E+07	125	6.013E+06	4.2720	417.2	150.68	15.22
6	14	584	3.010E+07	91	4.690E+06	6.4176	325.4	225.05	25.68
7	14	744	3.834E+07	60	3.092E+06	12.4000	214.6	427.99	57.95
8	9	464	3.720E+07	38	3.046E+06	12.2105	211.4	421.66	71.55
9	12	440	2.646E+07	46	2.766E+06	9.5652	191.9	332.62	51.89
10	8	296	2.670E+07	23	2.074E+06	12.8696	143.9	443.65	96.37
11	14	430	2.216E+07	61	3.144E+06	7.0492	218.2	246.78	34.05
12	10	430	3.102E+07	39	2.814E+06	11.0256	195.3	381.93	64.24
13	28	241	6.210E+06	139	3.582E+06	1.7338	248.6	61.58	6.65
14	15	424	2.039E+07	84	4.040E+06	5.0476	280.4	177.66	21.46
15	10	190	1.371E+07	37	2.670E+06	5.1351	185.3	180.70	32.63
16	9	154	1.235E+07	35	2.806E+06	4.4000	194.7	155.14	29.18
17	10	340	2.453E+07	41	2.958E+06	8.2927	205.3	289.35	48.12
18	15	354	1.703E+07	48	2.309E+06	7.3750	160.2	257.96	39.95
19	14	546	2.814E+07	47	2.422E+06	11.6170	168.1	401.79	61.50
20	12	348	2.092E+07	32	1.924E+06	10.8750	133.5	376.86	69.95
21	10	406	2.929E+07	30	2.165E+06	13.5333	150.2	465.73	88.51
22	14	340	1.752E+07	42	2.165E+06	8.0952	150.2	282.61	46.50
23	10	314	2.266E+07	40	2.886E+06	7.8500	200.3	274.23	46.30
24	10	227	1.638E+07	36	2.597E+06	6.3056	180.2	221.19	39.88
25	8	399	3.598E+07	33	2.976E+06	12.0909	206.5	417.66	76.02
26	10	422	3.045E+07	36	2.597E+06	11.7222	180.2	405.32	70.75
27	10	210	1.515E+07	42	3.030E+06	5.0000	210.3	176.01	29.92
28	10	214	1.544E+07	58	4.185E+06	3.6897	290.4	130.35	19.44

Details			*Summary*						
Sample No.	Ai I		**Central age**		**277.6**	**±**	**17.7**	**Ma**	
Irrad. No.	HF 49		**age dispersion**		**33.56**	**%**			
Position	0								
Date	09/08/06		**Pooled age**		285.6	±	14.4	Ma	
Analyst	Carter								
			Mean age		309.0	±	23.2	Ma	
zeta (CN5)	127								
zeta error	5		**Chi squared**		91.29	with	37	df	
No. of grains	38		**P(chi-sq)**		0.00	%			
Total Ns	13639	tr							
Total Ni	1664	tr							
Total Nd	3093	tr							
rho-d (CN5)	5.610E+05	tr/cm^2							
mean rho-s	2.804E+07	tr/cm^2							
mean rho-i	3.420E+06	tr/cm^2							
mean U	75.0	ppm							
crystal	***Ng***	***Ns***	***rho-s***	***Ni***	***rho-i***	***Ns/Ni***	***U***	***age***	***error***
1	10	228	1.645E+07	49	3.535E+06	4.653	77.5	163.7	26.7
2	10	499	3.600E+07	58	4.185E+06	8.603	91.8	299.40	43.5
3	10	322	2.323E+07	52	3.752E+06	6.192	82.3	216.9	33.7
4	10	556	4.012E+07	48	3.463E+06	11.583	75.9	400.0	62.6
5	10	244	1.760E+07	58	4.185E+06	4.207	91.8	148.1	22.6
6	10	286	2.063E+07	42	3.030E+06	6.810	66.4	238.1	40.7
7	10	450	3.247E+07	34	2.453E+06	13.235	53.8	455.0	83.3
8	15	352	1.693E+07	21	1.010E+06	16.762	22.1	571.1	130.6
9	10	332	2.395E+07	48	3.463E+06	6.917	75.9	241.8	38.8
10	15	612	2.944E+07	85	4.088E+06	7.200	89.6	251.5	31.1
11	10	484	3.492E+07	52	3.752E+06	9.308	82.3	323.3	49.2
12	10	398	2.872E+07	39	2.814E+06	10.205	61.7	353.7	61.3
13	8	580	5.231E+06	33	2.976E+06	17.576	65.3	597.5	110.0
14	6	217	2.609E+07	26	3.126E+06	8.346	68.5	290.7	61.6
15	10	354	2.554E+07	47	3.391E+06	7.532	74.3	262.9	42.4
16	8	301	2.715E+07	36	3.247E+06	8.361	71.2	291.2	52.9
17	8	436	3.932E+07	46	4.149E+06	9.478	91.0	329.1	53.0
18	10	434	3.131E+07	49	3.535E+06	8.857	77.5	308.0	48.3
19	8	392	3.535E+07	23	2.074E+06	17.043	45.5	580.2	127.0
20	6	185	2.225E+07	40	4.810E+06	4.625	105.5	162.7	29.2
21	6	241	2.898E+07	19	2.285E+06	12.684	50.1	436.7	105.8
22	10	428	3.088E+07	51	3.680E+06	8.392	80.7	292.2	45.1
23	8	103	9.289E+07	38	3.427E+06	2.711	75.1	95.8	18.7
24	15	591	2.843E+07	90	4.329E+06	6.567	94.9	229.8	27.8
25	6	114	1.371E+07	15	1.804E+06	7.600	39.5	265.2	73.7
26	6	158	1.900E+07	15	1.804E+06	10.533	39.5	364.7	99.8
27	6	314	3.776E+07	47	5.652E+06	6.681	123.9	233.7	37.9
28	10	424	3.059E+07	47	3.391E+06	9.021	74.3	313.6	50.1
29	6	232	2.790E+07	25	3.006E+06	9.280	65.9	322.4	69.3
30	8	252	2.273E+07	28	2.525E+06	9.000	55.4	312.9	63.8
31	8	348	3.139E+07	27	2.435E+06	12.889	53.4	443.5	90.7
32	8	438	3.950E+07	47	4.239E+06	9.319	92.9	323.7	51.6
33	20	896	3.232E+07	146	4.239E+06	6.137	115.5	215.0	21.3
34	6	232	2.790E+07	33	3.968E+06	7.030	87.0	245.7	46.9

35	12	548	3.295E+07	67	4.028E+06	8.179	88.3	285.0	38.9
36	6	222	2.670E+07	24	3.608E+06	9.250	63.3	191.9	39.0
37	6	164	1.972E+07	30	3.608E+06	5.467	79.1	191.9	39.0
38	10	272	1.962E+07	29	2.092E+06	9.379	45.9	325.8	65.2

Details			*Summary*						
Sample No.	B/2		**Central age**		**200.3**	**±**	**16.6**	**Ma**	
Irrad. No.	HF 37		**age dispersion**		**33.2**	**%**			
Position	0								
Date	30/11/2005		**Pooled age**		201.5	±	8.6	Ma	
Analyst	AC								
			Mean age		227.8	±	19.7	Ma	
zeta (CN5)	127								
zeta error	5		**Chi squared**		95.85	with	21	df	
No. of grains	22		**P(chi-sq)**		0.00	%			
Total Ns	6051	tr							
Total Ni	786	tr							
Total Nd	2589	tr							
rho-d (CN5)	4.186E+05	tr/cm^2							
mean rho-s	2.069E+07	tr/cm^2							
mean rho-i	2.663E+06	tr/cm^2							
mean U	248.1	ppm							

crystal	*Ng*	*Ns*	*rho-s*	*Ni*	*rho-i*	*Ns/Ni*	*U*	*age*	*error*
1	12	274	1.647E+07	32	1.924E+06	8.5625	179.3	223.67	42.02
2	10	284	2.049E+07	16	1.154E+06	17.7500	107.6	455.35	117.34
3	6	171	2.056E+07	23	2.766E+06	7.4348	257.7	194.66	43.40
4	10	222	1.602E+07	36	2.597E+06	6.1667	242.0	161.87	29.26
5	6	232	2.790E+07	16	1.924E+06	14.5000	179.3	374.34	97.04
6	10	288	2.078E+07	34	2.453E+06	8.4706	228.5	221.31	40.37
7	10	186	1.342E+07	28	2.020E+06	6.6429	188.2	174.20	35.48
8	10	322	2.323E+07	21	1.515E+06	15.3333	141.2	395.21	89.35
9	15	360	1.732E+07	67	3.223E+06	5.3731	300.3	141.26	19.00
10	6	182	2.189E+07	24	2.886E+06	7.5833	268.9	198.49	43.28
11	10	392	2.828E+07	73	5.267E+06	5.3699	490.7	141.18	18.21
12	10	232	1.674E+07	54	3.896E+06	4.2963	363.0	113.20	17.25
13	10	298	2.150E+07	23	1.659E+06	12.9565	154.6	335.51	72.91
14	10	278	2.006E+07	37	2.670E+06	7.5135	248.7	196.69	34.64
15	10	260	1.876E+07	25	1.804E+06	10.4000	168.1	270.68	56.93
16	15	462	2.222E+07	53	2.549E+06	8.7170	237.5	227.64	33.32
17	10	294	2.121E+07	30	2.165E+06	9.8000	201.7	255.37	49.20
18	9	246	1.972E+07	50	4.008E+06	4.9200	373.4	129.47	20.25
19	10	366	2.641E+07	42	3.030E+06	8.7143	282.3	227.57	37.34
20	6	184	2.213E+07	21	2.525E+06	8.7619	235.3	228.79	52.89
21	8	152	1.371E+07	39	3.517E+06	3.8974	327.7	102.77	18.56
22	10	366	2.641E+07	42	3.030E+06	8.7143	282.3	227.57	37.34

Details			*Summary*						
Sample No.	G/T		**Central age**		**226.7**	**±**	**45.5**	**Ma**	
Irrad. No.	HF 37		**age dispersion**		**60.8**	**%**			
Position	0								

Date	12/03/05		**Pooled age**		232.0	±	13.2	Ma	
Analyst	AC								
			Mean age		297.4	±	44.5	Ma	
zeta (CN5)	127								
zeta error	5		**Chi squared**		139.97	with	9	df	
No. of grains	10		**P(chi-sq)**		0.00	%			
Total Ns	3489	tr							
Total Ni	392	tr							
Total Nd	2589	tr							
rho-d (CN5)	4.180E+05	tr/cm^2							
mean rho-s	2.486E+07	tr/cm^2							
mean rho-i	2.686E+06	tr/cm^2							
mean U	250.6	ppm							

crystal	*Ng*	*Ns*	*rho-s*	*Ni*	*rho-i*	*Ns/Ni*	*U*	*age*	*error*
1	8	260	2.345E+07	49	4.419E+06	5.3061	412.3	139.32	21.87
2	10	414	2.987E+07	21	1.515E+06	19.7143	141.4	503.12	112.97
3	10	287	2.071E+07	16	1.154E+06	17.9375	107.7	459.35	118.34
4	10	392	2.828E+07	30	2.165E+06	13.0667	202.0	337.82	64.34
5	10	284	2.049E+07	23	1.659E+06	12.3478	154.8	319.69	69.59
6	10	601	4.336E+07	44	3.175E+06	13.6591	296.2	352.72	55.52
7	9	372	2.982E+07	27	2.165E+06	13.7778	202.0	355.71	71.24
8	10	198	1.429E+07	56	4.040E+06	3.5357	377.0	93.17	14.22
9	10	232	1.674E+07	21	1.515E+06	11.0476	141.4	286.76	65.59
10	15	449	2.160E+07	105	5.051E+06	4.2762	471.2	112.52	12.40

Details			*Summary*						
Sample No.	Ar/B		**Central age**		**235.3**	**±**	**18.3**	**Ma**	
Irrad. No.	HF 37		**age dispersion**		**36.9**	**%**			
Position	0								
Date	30/11/2005		**Pooled age**		238.0	±	9.2	Ma	
Analyst	AC								
			Mean age		262.8	±	15.3	Ma	
zeta (CN5)	127								
zeta error	5		**Chi squared**		161.62	with	30	df	
No. of grains	31		**P(chi-sq)**		0.00	%			
Total Ns	9807	tr							
Total Ni	1052	tr							
Total Nd	2271	tr							
rho-d (CN5)	4.096E+05	tr/cm^2							
mean rho-s	2.111E+07	tr/cm^2							
mean rho-i	2.203E+06	tr/cm^2							
mean U	209.7	ppm							

crystal	*Ng*	*Ns*	*rho-s*	*Ni*	*rho-i*	*Ns/Ni*	*U*	*age*	*error*
1	10	380	2.742E+07	27	1.948E+06	14.0741	185.5	356.05	71.31
2	20	630	2.273E+07	138	4.978E+06	4.5652	474.0	117.66	11.33
3	10	462	3.333E+07	32	2.309E+06	14.4375	219.8	364.98	67.16
4	8	118	1.064E+07	8	7.215E+05	14.7500	68.7	372.66	136.37
5	20	640	2.309E+07	52	1.876E+06	12.3077	178.6	312.42	45.53
6	8	60	5.411E+06	23	2.074E+06	2.6087	197.5	67.50	16.61

7	8	234	2.110E+07	23	2.074E+06	10.1739	197.5	259.33	56.93
8	8	220	1.984E+07	30	2.706E+06	7.3333	257.6	187.97	36.80
9	15	195	9.380E+06	42	2.020E+06	4.6429	192.4	119.64	20.51
10	8	266	2.399E+07	27	2.435E+06	9.8519	231.9	251.28	51.03
11	8	258	2.327E+07	27	2.435E+06	9.5556	231.9	243.86	49.59
12	9	154	1.235E+07	10	8.017E+05	15.4000	76.3	388.60	127.07
13	8	194	1.750E+07	17	1.533E+06	11.4118	146.0	290.18	73.65
14	10	194	1.400E+07	27	1.948E+06	7.1852	185.5	184.23	38.04
15	10	298	2.150E+07	31	2.237E+06	9.6129	213.0	245.30	46.58
16	8	302	2.724E+07	39	3.517E+06	7.7436	334.9	198.33	34.00
17	10	314	2.266E+07	25	1.804E+06	12.5600	171.7	318.67	66.56
18	10	270	1.948E+07	42	3.030E+06	6.4286	288.5	165.07	27.60
19	12	453	2.724E+07	40	2.405E+06	11.3250	229.0	288.03	47.89
20	12	482	2.898E+07	37	2.225E+06	13.0270	211.8	330.22	56.76
21	8	264	2.381E+07	26	2.345E+06	10.1538	223.3	258.83	53.48
22	10	348	2.511E+07	25	1.804E+06	13.9200	171.7	352.25	73.31
23	15	399	1.919E+07	47	2.261E+06	8.4894	215.3	217.11	33.79
24	10	280	2.020E+07	32	2.309E+06	8.7500	219.8	223.66	42.00
25	12	333	2.002E+07	23	1.383E+06	14.4783	131.7	365.99	79.28
26	12	398	2.393E+07	36	2.165E+06	11.0556	206.1	281.32	49.32
27	12	392	2.357E+07	44	2.646E+06	8.9091	251.9	227.65	36.51
28	12	343	2.062E+07	42	2.525E+06	8.1667	240.4	208.99	34.45
29	10	320	2.309E+07	19	1.371E+06	16.8421	130.5	423.81	100.47
30	10	290	2.092E+07	32	2.309E+06	9.0625	219.8	231.50	43.40
31	10	316	2.280E+07	29	2.092E+06	10.8966	199.2	277.36	54.13

List of Publications

- Das Gupta, K., and Pickering K.T., 2008, Petrography and temporal changes in petrofacies of deep-marine Ainsa-Jaca basin sandstone systems, Early and Middle Eocene, Spanish Pyrenees, *Sedimentology*, v. 55, p. 1083-1114.

- Das Gupta, K., and Pickering K.T., 2007, Understanding the evolution of clastic sediments from the deep-marine Ainsa-Jaca basin, Spanish Pyrenees: a petrographic approach, *AAPG Annual Convention & Exhibition*, Long Beach, California, USA.

- Das Gupta, K., Carter, A., Pickering K.T., and Hurford A.J., 2006, Provenance studies of the deep-marine Ainsa basin, Spanish Pyrenees using combined U-Pb and fission track techniques, *Geochimica et Cosmochimica Acta*, Volume 70, Issue 18, Supplement 1, Page A127.

- Das Gupta, K., Carter, A., and Pickering K.T., Provenance of deep-marine Ainsa basin clastic systems, Eocene, Spanish Pyrenees: constraints from petrography, geochemistry and detrital zircon geochronology, *Sedimentary Geology* (to be submitted).